

DISS. ETH No. 26184

**Additive manufacturing of metals at small length scales –
microstructure, properties and novel multi-metal electrochemical
concepts**

A thesis submitted to attain the degree of

DOCTOR OF SCIENCES of ETH ZÜRICH

(Dr. sc. ETH Zürich)

presented by

Alain Stefan Reiser

MSc in Materials Science, ETH Zürich

born on 11.11.1987

citizen of Zürich ZH

Accepted on the recommendation of:

Prof. Dr. Ralph Spolenak, examiner

Prof. Dr. Markus Niederberger, co-examiner

Prof. Dr. Julia Greer, co-examiner

2019

Summary

Many emerging applications in microscale engineering demand the fabrication of three-dimensional architectures in inorganic materials. Small-scale additive manufacturing (AM) aspires to provide access to these geometries with feature sizes in the micro- and submicrometer range. Yet, the synthesis of device-grade inorganic materials is still a challenge for AM, and the properties of additively manufactured materials are typically inferior to those of materials deposited via traditional, subtractive 2D fabrication routes – a major handicap for incorporating AM in advanced micro- and nanofabrication processes. Materials engineering is thus necessary to improve the quality of printed inorganic materials.

This thesis revolves around the materials science of small-scale AM of metals, focusing on both, contemporary techniques and novel concepts introduced in this thesis. The work covers two major topics: first, it establishes a comprehensive overview of the microstructure and properties of metals synthesized by modern additive methods. Second, it explores new techniques that enable facile electrochemical AM of high-quality metals and unlock multi-metal printing of chemically architected geometries with spatially modulated properties at the submicron-scale. In combination, these studies present a further step towards the integration of AM into modern microfabrication routines.

The first part of the thesis defines the state of the art of small-scale metal AM, providing a detailed literature review of current techniques and an experimental survey of their materials' properties. Note that the thesis in general concentrates on the study and development of methods that enable direct additive deposition of metals. Thus, it considers indirect concepts based on the fabrication of organic templates by two-photon lithography in combination with subsequent metallization procedures in little detail only. Today, almost a dozen different methods are available for the direct deposition of metal 3D geometries with a resolution better than 10 μm . As these approaches build

on different physico-chemical principles, their characteristics such as feature size, speed and complexity of printable geometries, as well as the synthesized metals and their microstructure, vary greatly. A discussion of the individual principles and capabilities puts the concepts in perspective to each other and projects their potentials. The thesis then presents an experimental study on the "quality" of metals deposited by these methods. In collaboration with most of the groups active in the field of small-scale metal AM, the thesis explores the microstructure and resulting mechanical properties of today's materials. On one hand, we show that metals with a wide range of microstructures and elastic and plastic properties are synthesized. Especially electrochemical methods deposit dense and crystalline metals with excellent mechanical properties that compare well to those of thin-film nanocrystalline materials. On the other hand, the results reveal large variations in materials performance that can be related to the microstructure of the individual materials. Thus, the study provides practical guidelines for users of small-scale additive methods and establishes a baseline for the necessary optimization of printed metals.

The second part of the thesis presents novel electrochemical AM methods that offer a spatial resolution $\ll 1 \mu\text{m}$. First, two chapters introduce electrohydrodynamic redox printing (EHD-RP). This technique enables the direct, ink-free fabrication of polycrystalline multi-metal 3D structures with a resolution of 250 nm and a feature size of ≈ 100 nm. The electrochemical concept enables outstanding as-printed materials properties (for example a strength of copper that competes with highest values reported for nanocrystalline copper) printed at speeds that outperform current electrochemical techniques by one order of magnitude. Although neither its speed, its resolution nor its overall materials properties are unrivaled by competing methods, EHD-RP excels in an advantageous combination of these characteristics, readily permitting applications in microfabrication. Additionally, as a most unique feature, EHD-RP enables multi-metal printing with unprecedented detail. As shown, the additive control of the chemical architecture of metals with a chemical feature size < 400 nm unlocks the synthesis of 3D bi-metal structures with spatially varying microstructure and thus locally modified properties.

The last chapter discusses the potential of tip-induced deposition in the electrochemical scanning tunneling microscope (STM) for nanoscale AM. A strong confinement of deposition below the nanometer-sized probe enables 2D patterning of cobalt with a feature size of ≈ 50 nm. The potential for 3D printing is demonstrated, but reliable 3D fabrication is hampered by unsatisfactory stability of employed gold STM probes. Consequently, the chapter concludes with the development of more stable Pt and Pt-20at.%Ir probes, readying the designed setup for true 3D deposition. Nevertheless, a low deposition speed, a narrow processing window and a comparably complex instrumentation are identified as significant challenges for the proposed concept.

In conclusion, the thesis experimentally identifies materials challenges for contemporary small-scale AM of metals but at the same time presents a potential solution by introducing EHD-RP – an electrochemical concept that offers ink-free printing of high-quality metals. Additionally, the demonstrated multi-metal printing with submicrometer resolution sketches a route towards the bottom-up fabrication of chemically designed 3D devices and materials with properties tuned at single-voxel level – staking out a niche for small-scale AM as an enabling technology for chemically architected, inorganic materials that could spark the development of novel materials for *e.g.* catalysis, active chemical devices, sensors, or metamaterials that combine architected geometry and chemistry.

Zusammenfassung

Diverse neuartige Anwendungen in der Mikrotechnik erfordern die Herstellung dreidimensionaler Architekturen aus anorganischen Materialien. Die additive Fertigung auf kleinen Längenskalen bietet grosses Potential, den Zugang zu diesen Geometrien mit minimalen Strukturgrössen im Mikro- und Submikrometerbereich zu ermöglichen. Jedoch ist die Abscheidung von qualitativ hochwertigen anorganischen Materialien nach wie vor eine Herausforderung für die additive Fertigung – ein erheblicher Nachteil für den Einsatz von additiven Produktionstrategien in modernen Mikro- und Nano-Fertigungsroutrinen. Eine forcierte Materialentwicklung, welche die Qualität von gedruckten anorganischen Materialien zu verbessern vermag, ist daher unerlässlich.

Diese Dissertation stellt die Materialwissenschaft kleinskalig additiv gefertigter Metalle in den Mittelpunkt, und fokussiert dabei auf die zeitgenössischen Fabrikationstechniken sowie auf neue, im Rahmen dieser Arbeit entwickelte additive Verfahren. Vereint werden dabei zwei Hauptthemen: Es wird erstens ein umfassender Überblick über das Gefüge und die resultierenden Eigenschaften von additiv gefertigten, mikroskaligen Metallstrukturen präsentiert. Zweitens werden neue elektrochemische Verfahren etabliert, welche zum einen die einfache additive Fertigung von Metallen in hoher Qualität ermöglichen, und zum anderen den Multimetalldruck von Strukturen mit lokal modulierten Eigenschaften auf der Submikrometer-Skala erschliessen. In Kombination präsentieren sich diese Studien als einen weiteren Schritt auf dem Weg zur Integration von additiven Fertigungsprozessen in modernste Mikrofabrikationsverfahren.

Der erste Teil der Arbeit definiert den aktuellen Stand der Technik bei der kleinskaligen additiven Fertigung von Metallen, inklusive einer detaillierten Literaturübersicht aktueller Verfahren sowie einer experimentellen Überprüfung der von diesen Techniken abeschiedenen Metalle. Dabei ist zu beachten, dass sich die Arbeit im Wesentlichen auf das Studium und die Entwicklung von Methoden konzentriert, die eine direkte additive Abscheidung von Metallen ermöglichen. Daher werden

indirekte Konzepte, die auf der Herstellung von organischen Formkörpern durch Zwei-Photonen-Lithographie in Kombination mit nachfolgenden Metallisierungsverfahren basieren, weitestgehend ausser Betracht gelassen. Von den direkten Verfahren ermöglichen heute beinahe ein Dutzend verschiedene Ansätze eine Auflösung kleiner als 10 μm . Da diese Methoden auf verschiedenen physikalisch-chemischen Prinzipien aufbauen, variieren die Prozesseigenschaften wie Strukturgrösse, Geschwindigkeit und Komplexität der druckbaren Geometrie, sowie die synthetisierten Metalle selbst und ihr Gefüge, stark. Eine Diskussion der einzelnen Prinzipien und Fähigkeiten stellt die Konzepte ins Verhältnis zueinander und erörtert ihr jeweiliges Potenzial. Anschliessend präsentiert die Dissertation eine experimentelle Studie zur "Qualität" von Metallen, die mit diesen Verfahren abgeschieden wurden. In Zusammenarbeit mit der Mehrzahl der weltweiten Forschungsgruppen aus dem Bereich der kleinskaligen Fertigung von Metallen untersucht diese Arbeit das Gefüge und die daraus resultierenden mechanischen Eigenschaften der heutigen Materialien. Einerseits wird gezeigt, dass Metalle mit einem breiten Spektrum an Gefügebildern und elastischen sowie plastischen Eigenschaften synthetisiert werden können. Hierbei garantieren insbesondere elektrochemische Verfahren eine dichte und kristalline Gefügestruktur mit hervorragenden mechanischen Eigenschaften, vergleichbar mit jenen von nanokristallinen Dünnschichtmaterialien. Auf der anderen Seite zeigen die Ergebnisse grosse Unterschiede in den Eigenschaften der Werkstoffe, die jeweils mit dem Gefüge der einzelnen Materialien in Zusammenhang gebracht werden können. Damit vermittelt die Studie praktische Leitlinien für Anwender von kleinskaligen additiven Verfahren und schafft eine Grundlage für die zukünftig notwendige Optimierung von gedruckten Metallen.

Im zweiten Teil der Arbeit werden neu entwickelte elektrochemische additive Methoden vorgestellt, welche eine räumliche Auflösung $\ll 1 \mu\text{m}$ bieten. Zunächst werden in zwei Kapiteln der elektrohydrodynamische Redox-Druck (EHD-RP) vorgestellt. Diese Technik ermöglicht die direkte, tintenfreie Herstellung von polykristallinen multimetallischen 3D-Strukturen mit einer Auflösung von 250 nm und einer minimalen Strukturgrösse von $\approx 100 \text{ nm}$. Das elektrochemische Konzept garantiert herausragende Materialeigenschaften (z.B. eine Festigkeit von Kupfer, die der von nanokristallinen Dünnschichten ebenbürtig ist). Zudem ist die Prozessgeschwindigkeit um eine Grössenordnung höher als bei herkömmlichen elektrochemischen Verfahren. Obwohl weder die hohe Geschwindigkeit noch die hohe Auflösung oder die allgemeinen Materialeigenschaften konkurrenzlos sind, zeichnet sich EHD-RP durch eine gute Kombination ebendieser Eigenschaften aus. Dies ermöglicht eine direkte Anwendung in der Mikrofertigung. Einzigartig unter den heutigen Methoden ist der durch EHD-RP gezeigte Multimetalldruck mit unvergleichlicher Detailtreue. Eine chemische Strukturgrösse von $< 400 \text{ nm}$ gestattet das hochauflösende Design chemischer Architekturen

und gestattet die Synthese von 3D-Bi-Metallstrukturen mit programmiertem lokalen Gefüge und daraus resultierenden lokal modulierten Eigenschaften.

Im letzten Kapitel wird das Potential der lokalen Abscheidung im elektrochemischen Rastertunnelmikroskop (STM) für nanoskalige additive Fertigung erörtert. Insbesondere wird gezeigt, dass die starke Lokalisation der Abscheidung unterhalb der nanometergrossen Sonde eine 2D-Strukturierung von Cobalt mit einer Strukturgrösse von ≈ 50 nm ermöglicht. Obwohl das prinzipielle Potential für die additive Abscheidung demonstriert wird, verhindert die unzureichende Stabilität der eingesetzten Goldspitzen die zuverlässige 3D-Fertigung. Folglich schliesst das Kapitel mit der Entwicklung von stabileren Pt- und Pt-20at.%Ir-Spitzen. Trotz dieser Fortschritte, welche die additive Fertigung prinzipiell ermöglichen würden, lassen sich die niedrige Prozessgeschwindigkeit, ein schmales Prozessfenster und eine vergleichsweise komplexe Instrumentierung als wesentliche Herausforderungen für das vorgestellte Konzept identifizieren.

Zusammenfassend stellt die vorliegende Dissertation experimentell die Herausforderungen bezüglich Werkstoffqualität der zeitgenössischen additiven Fertigung von Metallen auf Mikro- und Nanoskalen heraus. Gleichzeitig präsentiert die Arbeit eine mögliche Lösung durch die Entwicklung von EHD-RP – ein elektrochemisches Konzept, das den tintenfreien Druck von hochwertigen Metallen ermöglicht. Darüber hinaus skizziert der gezeigte Multimetalldruck mit Submikrometer-Auflösung einen Weg zur bottom-up-Fertigung von 3D-Bauteilen und Materialien mit chemisch graduierten Gefügen und auf Voxel-Level modulierten Eigenschaften. Damit etabliert die Arbeit die kleinskalige additive Fertigung als Basistechnologie für chemisch graduierte, anorganische Materialien welche Anwendung in neuartigen Katalysatoren, in der Batterietechnik, in Sensoren oder als Metamaterialien finden könnten.

Contents

| | |
|---|------------|
| Title | I |
| Summary | III |
| Zusammenfassung | VII |
| 1 Introduction | 1 |
| 1.1 Motivation | 1 |
| 1.2 Aim of the Thesis | 4 |
| 1.3 A readers guide | 5 |
| 2 A review of state-of-the-art microscale metal additive manufacturing techniques | 7 |
| 2.1 Introduction | 9 |
| 2.2 Metal AM techniques for the microscale | 13 |
| 2.3 Discussion | 49 |
| 2.4 Conclusion and general outlook | 69 |
| 2.5 Implementations for this thesis | 70 |
| 3 Metals by micro additive manufacturing: a comparison of microstructure and mechanical properties | 73 |
| 3.1 Introduction | 75 |
| 3.2 Objective of this chapter | 78 |
| 3.3 Methods | 80 |
| 3.4 Results | 87 |
| 3.5 Discussion | 95 |
| 3.6 Conclusion and outlook | 103 |

| | |
|---|------------|
| 4 Electrohydrodynamic redox 3D printing – accelerating electrochemical submicron-scale AM | 107 |
| 4.1 Introduction: Electrochemistry versus colloidal inks for small-scale AM – advantages and disadvantages | 108 |
| 4.2 Objective of this chapter | 113 |
| 4.3 Methods | 114 |
| 4.4 Results | 119 |
| 4.5 Discussion | 141 |
| 4.6 Conclusion and outlook | 151 |
| 5 Multi-metal electrohydrodynamic redox 3D printing for voxel-by-voxel materials design | 153 |
| 5.1 Introduction: multi-material 3D printing | 154 |
| 5.2 Objective of this chapter | 156 |
| 5.3 Methods | 158 |
| 5.4 Results | 161 |
| 5.5 Discussion | 171 |
| 5.6 Conclusion and outlook | 177 |
| 6 Electrochemical additive deposition with nanosecond voltage pulses in a STM – a route towards smallest feature sizes | 179 |
| 6.1 Introduction: Scanning-probe microscopy for electrochemical patterning – potential for smallest feature sizes | 180 |
| 6.2 Objective of this chapter | 186 |
| 6.3 Methods | 187 |
| 6.4 Results | 191 |
| 6.5 Discussion | 204 |
| 6.6 Conclusion and outlook | 207 |
| 7 General discussion, conclusion and outlook | 209 |
| 7.1 From qualitative concepts to quantitative understanding | 210 |
| 7.2 Is there a future for small-scale AM? | 213 |
| 7.3 Consequences: the future of EHD-RP | 219 |
| A Appendix to Chapter 1 | 221 |
| B Appendix to Chapter 2 | 223 |

| | |
|--|------------|
| C Appendix to Chapter 3 | 225 |
| C.1 Morphology: LIFT (melt) | 225 |
| C.2 Microstructure and chemical composition | 225 |
| C.3 Mechanical data for all tested samples of all techniques | 230 |
| C.4 Mechanical literature data for thin films | 247 |
| D Appendix to Chapter 4 | 249 |
| D.1 Deposition mechanism | 249 |
| D.2 Influence of oxygen on the microstructure | 252 |
| D.3 FIB-flattening of pillars for microcompression | 253 |
| E Appendix to Chapter 6 | 255 |
| E.1 Anodic degradation of the Au tip | 255 |
| E.2 Setup: circuit diagram | 256 |
| E.3 Nanoscale deposition with the "Hofmann" approach | 257 |
| Bibliography | 259 |
| Declaration | 297 |
| Acknowledgements | 301 |
| Curriculum Vitae | 305 |
| List of Figures | 311 |
| List of Tables | 315 |

Chapter 1

Introduction

1.1 Motivation

3D printing revolutionizes the way we design and fabricate. Today, additive manufacturing (AM), *i.e.*, building objects in a voxel-by-voxel fashion, is an established extension of conventional manufacturing techniques. AM has enabled the fabrication of personalized implants, efficient conformal cooling systems or lightweight and cost-saving components for the aviation and automotive industry^{1,2}, while more advanced applications such as bioprinting of tissue³ and bone⁴, integration of electronics and sensors⁵ or manufacturing of biologically inspired, shape-morphing materials^{6,7} are under development. Further, the concept of AM does not only span fields, but also length scales – AM enables printed buildings⁸ as well as nanometric metamaterials⁹.

For manufacturing at small scales, AM's potential impact is immense: the established subtractive routes based on lithography are by nature two-dimensional – hardly any techniques exist for true 3D fabrication at all. In addition, a rapidly expanding area of research in materials science and engineering demands the fabrication of complex three-dimensional structures with feature sizes in the micro- and submicrometer range. 3D geometries are often superior to their established, planar counterparts, and enable a wide range of emerging applications in, for example, microelectromechanical systems (MEMS)^{10,11}, electronics^{12–19}, optics^{20,21} and optoelectronics^{22,23}, energy storage^{24–26} and biomedicine^{27–29} (Fig. 1.1). Additionally, materials based on 3D architectures offer properties and functionalities that are a result of not only their chemistry and microstructure, but

also their geometry. These materials, often categorized as architected materials^{30,31} or metamaterials^{9,32}, can access fundamentally novel properties not typically found in nature. Thus, such 3D designs offer powerful options for optical^{33–37} and mechanical metamaterials^{38–44} (Fig. 1.1).

As progress in 3D architected materials follows from the ability to realize respective structures from suitable materials, the development of small-scale 3D fabrication methods is necessary⁴⁵. Here, AM could play a prominent role. The most widespread approaches for the realization of deterministic 3D geometries with microscale resolution are self assembly, stress-controlled deformation, and AM⁴⁵. Of these fundamental strategies, AM promises largest variation and closest control of the synthesized geometries. Hence, a large number of microscale AM techniques with a minimum feature size $<10\mu\text{m}$ have emerged in the past decade^{46–48}, paving the way to additively manufactured 3D metamaterials^{34,35,38,40,49,50}, printed electrical circuit elements^{12–14,16,17}, or small-scale sensors^{51,52}.

Despite their potential, contemporary additive methods face a major challenge: materials and materials performance. In order to enable above-mentioned progress, AM techniques must provide the materials today's state-of-the-art microfabrication processes require: combinations of device-grade, inorganic materials that can serve structural, electronic and optical functions. This need is illustrated by the widespread use of two-photon lithography (TPL) as a mere templating tool: after building a template using TPL, the photosensitive materials are exchanged with state-of-the-art materials necessary for proper functioning of the final structure, that is, materials with a high dielectric constant for optical metamaterials^{34–36}, or materials with a high stiffness or strength for mechanical metamaterials^{38,40,43,50}. These materials are invariably deposited by established microfabrication processes such as atomic layer deposition^{40,50} or electrodeposition^{34,38,40}.

While the symbiosis of TPL and proven deposition techniques is an ideal approach for many applications, direct patterning of high-performance materials would be preferable for a number of reasons: a reduction in processing steps, geometries that are not dictated by requirements for subsequent template inversion (proper filling of complex templates can be demanding⁵³) and, maybe most interesting for advanced designs of devices and materials, the possibility of spatially varying properties (which is not accessible with homogeneous coating or filling). Unfortunately, direct printing of inorganic materials typically suffers from unknown or inferior materials properties. Although printed materials are functional, their performance varies considerably and can typically not yet compete with traditional fabrication routes such as PVD or electrodeposition⁴⁸. This shortcoming, in combination with challenging scalability^{54–57}, is a major handicap for incorporating AM in advanced micro- and nanofabrication routines.

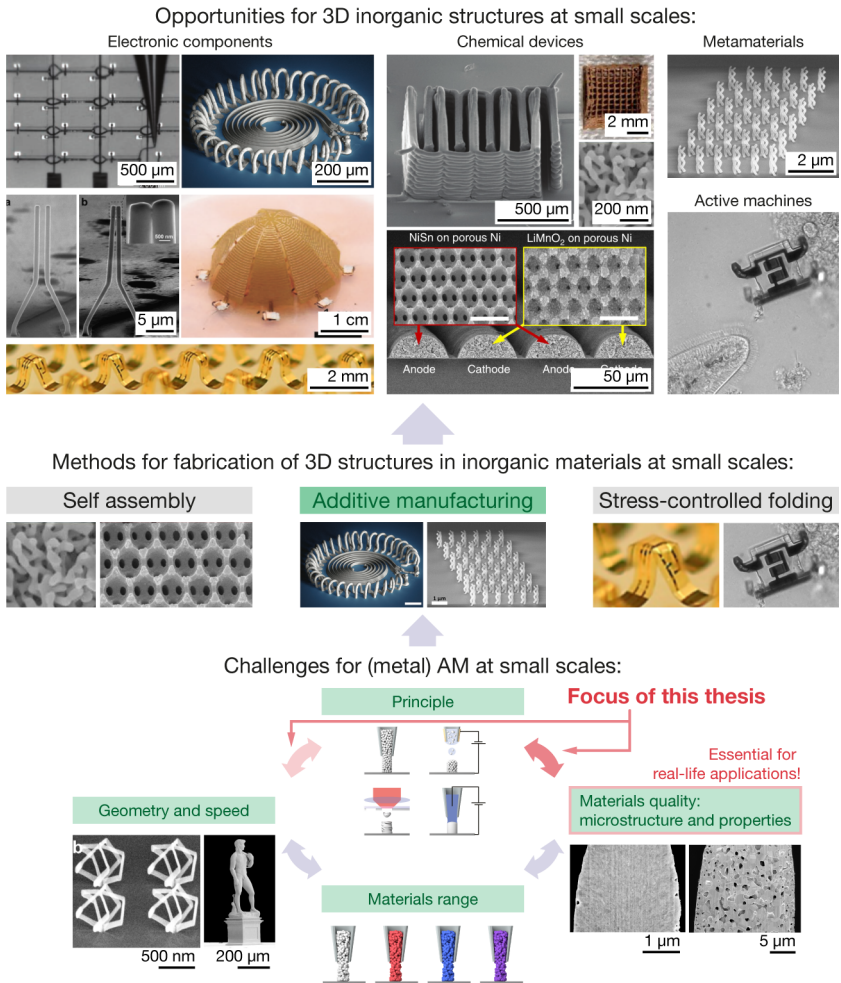


Figure 1.1 – Small-scale additive manufacturing of inorganic materials – opportunities and challenges. Complex three-dimensional structures fabricated in high-performance inorganic materials enable a wide range of emerging applications. Here, progress relies on advanced fabrication methods for 3D geometries with microscale resolution: self assembly, AM and stress-controlled deformation. Of these, AM techniques offer most complex geometries, but face multiple challenges: low speed, a limited range of materials and often inferior materials quality. In an effort to solve some of these challenges, a first part of this thesis focuses on the interplay between the various physico-chemical principles employed for small-scale metal AM and the resulting materials' microstructure and properties. The second part targets the development of novel electrochemical AM methods that enable multi-metal printing with a resolution $<1\ \mu\text{m}$ for tuning the local microstructure and properties. Individual panels reproduced with permission. See Fig. A.1 for references and copyrights. 3

1.2 Aim of the Thesis

Outlined in coarse strokes, this thesis aims at studying but also advancing contemporary small-scale metal AM from a materials point of view. This involves two main foci: first, a survey of microstructures and properties of metals synthesized today. Second, based on these observations, the development of new techniques that enable the facile synthesis of high-quality metals and thereby – hopefully – benefit the incorporation of direct AM into state-of-the-art microfabrication routines.

In a first part, the thesis should develop an overview of current techniques for small-scale metal AM (Literature review in Chapter 2) and the microstructure and resulting mechanical properties of metals deposited by these methods (Chapter 3). The latter study is motivated by the low number of microstructural analyses in the community and my conviction that additive techniques can only benefit microfabrication if they provide high-performance materials.

The second part of the thesis targets the development of novel AM methods that utilize electrochemical synthesis principles and offer a spatial resolution $\ll 1 \mu\text{m}$. On one hand, this work is stimulated by the fact that electrochemical techniques generally guarantee high-performance metals but lack practicability as their deposition rate is low (Chapter 4). On the other hand, this thesis should make first steps towards the active control of the synthesized microstructure of each single voxel (chemical composition, grain size, porosity), facilitating local microstructure optimization in three dimensions (Chapter 5). Such control in pure metals is currently only available through electrochemical strategies, as these are the only methods that facilitate on-the-fly manipulation of the printed microstructure by variation of the deposition parameters.

In contrast, this thesis does not aim at the following objectives: first, optimization of the materials synthesized by the techniques studied in Chapter 3. Strategies for a potential optimization are discussed, but not actively pursued. Second, the techniques developed in Chapters 4, 5 and 6 do not strive to build the most complex 3D geometries at highest speeds – geometries as those typically fabricated by TPL in polymers are not intended. Rather, the thesis focuses on the synthesized materials and their microstructure. Third, and most importantly, only the direct deposition of metals is considered. Consequently, the thesis acknowledges the potential of indirect concepts based on the fabrication of organic templates by TPL in combination with subsequent metallization procedures, but treats them in little detail for most of the part. Additionally, the necessity of venturing beyond metals is noted. Functional devices are always combinations of multiple materials classes – electronic applications require conductive, semi-conductive and insulating materials; optical devices need materials of high and low reflectivity or absorption; chemical devices need inert and reactive

materials. State-of-the-art deposition techniques used in modern microfabrication are often characterized by their compatibility with a large range of materials. For example, PVD provides access to high-quality films of polymers, ceramics and metals alike. In analogy, the ultimate small-scale additive technology needs to offer a large range of materials should it be practical for real-world applications – at least some electrical conductors, semiconductors and insulators should be available. However, this ultimate goal is beyond the scope of this thesis, but the issue will be revisited in the discussion (Chapter 7).

1.3 A readers guide

Chapter 2 will provide a detailed overview of the state of the art of small-scale metal AM. Today, almost a dozen different methods are available for the deposition of 3D geometries with a resolution better than 10 μm . The fabrication capabilities of these methods as well as the synthesized metals and their microstructure vary greatly, as all approaches build on different physico-chemical principles. For example, the reader can imagine that the range of materials and the compatibility with various substrates differ between methods that extrude nanoparticle inks and methods that synthesize metals electrochemically. Likewise, the accessible geometries but also the purity and microstructure of the respective materials and hence their properties change. Consequently, the chapter will summarize the principles of all contemporary methods, the limits of their fabrication capabilities (geometry, feature size, speed), the accessible metals and materials and – if available – materials properties data and representative applications. The chapter will also discuss the strengths, weaknesses, prospects and limitations of the individual techniques and, in general, metal AM at the microscale. Lastly, after overviewing the state of the art, conclusions for this thesis are drawn.

Chapter 3 will present a comprehensive study of the "materials quality" of metals synthesized by most of the techniques currently available. In a collaboration with most of the groups active in the field of small-scale AM, I studied the microstructure and resulting mechanical properties of metals synthesized today. On one hand, the chapter shows that metals with a wide range of microstructures and elastic and plastic properties are synthesized by current microscale AM techniques, including materials of dense and crystalline microstructure and excellent mechanical properties that compare well to those of thin-film nanocrystalline materials. On the other, the chapter reveals large variations in materials performance that can be related to the individual materials' microstructure, which in turn are coupled to the various physico-chemical principles exploited by the different

printing methods. The study provides practical guidelines for users of small-scale additive methods and establishes a baseline for the future optimization of the properties of printed metals – a first step towards the potential establishment of AM techniques in microfabrication.

Chapters 4 and 5 introduce a novel electrochemical method: electrohydrodynamic redox printing (EHD-RP). This technique enables the direct, ink-free fabrication of polycrystalline multi-metal 3D structures with a resolution of 250 nm. Importantly, EHD-RP outperforms typical speeds of state-of-the-art electrochemical techniques by more than an order of magnitude, significantly improving one of the drawbacks of contemporary electrochemical AM (Chapter 4). Additionally, as a most unique feature, EHD-RP enables fast on-the-fly switching and mixing of two metals printed from a single multichannel nozzle, facilitating a chemical feature size of <400 nm. As shown, the additive control of the chemical architecture of materials provided by EHD-RP unlocks the synthesis of 3D bi-metal structures with programmed local microstructure and thus properties (Chapter 5).

The last result Chapter 6 discusses the potential of tip-induced deposition in the electrochemical scanning tunneling microscope as a route towards electrochemical nanoscale AM with feature sizes <100 nm (a resolution that is out of reach of current electrochemical techniques). The results suggest some potential for the approach, but a low deposition speed, oxidation of the tip material, a comparably complex instrumentation and a narrow range of accessible metals present significant challenges.

An overarching conclusion and an outlook to future work are given in Chapter 7, reviewing the main findings of the thesis and extrapolating the technical consequences for EHD-RP. Additionally, the chapter puts the present work in perspective to ongoing research in the field of small-scale AM and small-scale fabrication of 3D structures in general. Essentially, the chapter will try to convince the reader of three fundamental insights I earned during my PhD years: conceptual development of a new techniques needs to be followed by quantitative studies of underlying processes; probably not all small-scale AM methods are practical and user-friendly – only those that are will leave their laboratory environment; small-scale AM is not the ideal solution for a number of applications, but for some – AM thus needs to find its niche in advanced micromanufacturing.

Chapter 2

A review of state-of-the-art microscale metal additive manufacturing techniques

Currently, the focus of additive manufacturing (AM) is shifting from simple prototyping to actual production. One driving factor of this process is the ability of AM to build geometries that are not accessible by subtractive fabrication techniques. While these techniques often call for a geometry that is easiest to manufacture, AM enables to build the geometry required for best performance by freeing the design process from restrictions imposed by traditional machining. At the micrometer scale, the design limitations of standard fabrication techniques are even more severe, and AM thus promises to be a valuable addition to traditional methods. This potential is confirmed by the rapid success of commercial two-photon lithography tools as an enabling technology for a broad range of scientific applications. For metals however, there is still no established AM solution at small scales. Nevertheless, considering the importance of metals in microtechnology, there is a need for microscale metal AM techniques. To tackle the limited resolution of standard metal AM methods (a few tens of micrometers at best), various new techniques aiming at the micrometer scale and below are presently under development. Here, we review these recent efforts. Specifically, we feature the techniques of direct ink writing, electrohydrodynamic printing, laser-assisted electrophoretic deposition, laser-induced forward transfer, local electroplating methods, laser-induced photoreduction and focused electron or ion beam induced deposition. Additionally, we touch on

This chapter is an updated version of: Reiser, A., Hirt, L., Spolenak, R. & Zambelli, T. Additive Manufacturing of Metal Structures at the Micrometer Scale. *Adv. Mater.* **29**, 1604211 (2017). All content is reproduced with permission from John Wiley and Sons.

the two most novel approaches to small-scale AM, two-photon lithography combined with post-print carbothermal reduction and implosion fabrication. Although all these methods have proven to facilitate the additive manufacturing of metals with feature sizes in the range of 0.01 – 10 μm , they are still in a prototype stage and their potential is not fully explored yet. For instance, comprehensive studies of material availability and materials properties are often lacking, yet compulsory for actual applications. We address these items while critically discussing and comparing the potential of current microscale metal AM techniques. A final section outlines the consequences for this thesis.

2.1 Introduction

Additive manufacturing (AM) is currently transforming the way we design and produce components at the macroscale. AM has enabled the fabrication of innovative products such as personalized implants, more efficient conformal cooling systems or lightweight and cost-saving components for the aviation and automotive industry^{1,2}, while more advanced applications, *e.g.*, the bioprinting of tissue³, AM in the construction industry⁵⁸, integration of electronics and sensors⁵ or manufacturing of biologically inspired, shape-morphing materials^{6,7} are under development. One reason for the success of AM is its ability to realize almost any desired geometry. This markedly contrasts with design limitations imposed by subtractive manufacturing techniques. Before AM, generations of engineers had to accept non-ideal geometries dictated by the geometrical shortcomings of subtractive manufacturing techniques. Now, AM enables the design of architectures required for best performance rather than ease of manufacturing.

As metals are indispensable in state-of-the-art engineering, *e.g.*, for structural support, electrical conductivity or heat dissipation, extensive research has been conducted to develop AM processes for metals, resulting in a range of metal AM techniques for the macro and mesoscale, many of which are commercially available today. The most established methods are selective laser melting (SLM) and electron beam melting (EBM), two techniques that rely on the local fusion of metal particles to form a solid material^{59–62}. Whereas these technologies play a major role in the commercialization of AM at the macroscale, they are not suited for the microscale and below. The minimum line width of powder fusing methods is several tens of micrometers^{63,64}, limited by the finite particle size of the metal powder and the high heat dissipation in metals, resulting in a low confinement of the heating pulse.

This limitation is unfortunate because metal AM with micrometer and submicrometer resolution has the potential to expand the capabilities of established techniques to an extent unmatched by macroscopic AM: the design limitations imposed by traditional fabrication processes at small scales are considerably more restrictive than those imposed at the macroscale. Subtractive manufacturing by various lithography processes is by nature two-dimensional, and thus is not well suited for the fabrication of complex three-dimensional (3D) parts. Since the additive approach of AM does not suffer from these drawbacks, AM will be a valuable addition to traditional microfabrication methods. For polymers, this promise has been met by the ascent of two-photon lithography (TPL, also known as direct laser writing, two-photon lithography or 3D μ -printing)^{47,65}. While TPL-created templates may be used for later metallization by coating or templated electrodeposition^{34,66,67}, no mask-free metal AM technique has been established for these scales.

Consequently, ongoing research aims to develop routes for metal AM at the micro- and sub-micrometer scale. The approaches to obtain micrometer-sized metallic structures are manifold, and a variety of principles have been proposed recently. Some of these approaches have already been presented in comprehensive review articles of micro AM in general^{64,68,69}, individual techniques^{46,70–75}, or specific applications of AM at the microscale^{76,77}. However, to our knowledge, no reports are available that focus exclusively on the microscale AM of metals. In addition, materials properties are rarely considered in the available articles. This provided the motivation to discuss contemporary AM techniques for metal fabrication at the micrometer scale, including a consideration of materials properties, such as the composition or microstructure of the resulting deposits.

2.1.1 Metal AM at the microscale

We begin our discussion with a definition of the term "metal AM at the microscale". In general, AM is a family of techniques that produce 3D objects by the successive addition of material in a layer-by-layer fashion. To differentiate 3D AM from 2D lithography, we define 3D as a stack of two or more layers. Additionally, we expect an AM technique to be able to fabricate structures with an out-of-plane aspect ratio of at least two. Furthermore, we interpret AM as a process that produces the required material, in our case the metal, in a single direct-write step. Hence, we disregard all approaches that rely on the use of masks, such as the LIGA process, where 2D layers created by photolithography and subsequent electrodeposition are stacked to produce complex 3D parts⁷⁸. The single-step criterion also excludes the popular approach of utilizing TPL to synthesize polymeric templates that are subsequently metallized^{34,67,79}. For a review of this major technology, we recommend the recent articles of Fischer *et al.*⁸⁰, Sugioka *et al.*⁶⁵ and Hohmann *et al.*⁴⁷.

Next, we must specify the term "metallic" materials. Many microscale metal AM techniques synthesize metal-organic composites rather than pure metals. We will include these processes because the composites often show metallic characteristics, *e.g.*, high electrical conductivity or magnetic susceptibility. Since post-deposition annealing is usually performed to achieve these metallic characteristics, the single-step criterion is violated. Nevertheless, we incorporate these techniques but explicitly mention any post-deposition treatments required.

Finally, the vague term "micrometer scale" must be delineated. Because SLM approaches line widths of tens of micrometers^{63,64}, we establish a benchmark feature size of 10 μm for any technique that qualifies as a microscale metal AM technique. This last criterion led us to disregard both localized electrochemical deposition (LECD) and laser assisted chemical vapor deposition

(LCVD) from the main part of this report. Both techniques are capable of metallic freeform synthesis, with minimum feature sizes approaching 10 μm . Better performance has been demonstrated for 1D and 2D LCVD^{81,82}, and 3D LECD⁸³. Still, most common 3D metal deposits have diameters between 10 – 100 μm . For an introduction to these techniques, we refer to the following references for LECD^{83–88} and LCVD^{89–92}.

In summary, we will compare AM techniques that enable the synthesis of metallic or metal-containing structures in a one-step process with a minimum feature size better than 10 μm and an aspect ratio of at least two. Based on our literature search, we will include the following methods:

- Direct ink writing (DIW)
- Electrohydrodynamic printing (EHD printing)
- Local electrophoretic deposition
- Laser-induced forward transfer (LIFT) of melts
- Laser-induced forward transfer (LIFT) of nanoparticle inks
- Meniscus-confined electrodeposition
- Concentration-confined electrodeposition (FluidFM / SICM)
- Laser-induced photoreduction
- Focused electron/ion beam induced deposition (FEBID / FIBID)

Further, a brief description of two very recent techniques is added: TPL-based synthesis of organic-inorganic composites with subsequent pyrolysis to produce metal-containing architectures⁹³ (In contrast to photoreduction techniques, the reduction seems to occur upon pyrolysis. Thus, the approach is not considered under photoreduction) and the so-termed implosion fabrication⁹⁴. As only one paper per technique has been published so far, a detailed discussion is difficult and the two techniques are treated in less depth in the general discussion. However, although not yet established, both approaches should be kept in mind as powerful options for micro- and nanoscale 3D patterning of metals.

The first part of this article reviews the following aspects of each technique:

- **Principle:** the physico-chemical mechanism underlying the local metal deposition

- **Setup:** the components of typical instrumentation and demands on the substrate
- **Geometry:** the range of feasible geometries
- **Feature size:** typical in-plane dimensions of deposits
- **Speed:** typical in- or out-of-plane deposition rates
- **Microstructure:** purity and internal structure of deposits
- **Materials:** demonstrated range of metallic elements
- **Applications:** relevant prototype geometries

Please note that some methods have been pioneered only recently and consequently, some data concerning the listed points might be missing. Additionally, we do not address the resolution of the techniques, *i.e.*, the minimal obtainable spacing between two single deposits, due to a lack of available studies. Finally, we note that most of the reviewed techniques were originally developed for 2D applications. Without these pioneering studies, research and progress of 3D applications would clearly be impossible; however, for the sake of conciseness, we generally do not refer to any of the initial 2D work.

Apart from major criteria for all AM techniques, *e.g.*, the geometric complexity of the build, the minimum feature size and the fabrication speed, we would like to emphasize the material characteristics. The traditional material science paradigm also applies for AM: the performance of a component is an interplay of its design, its elemental composition and its microstructure. AM may enable optimized control over geometrical factors such as the topology of a part or the architecture of composite materials^{6,7}; nevertheless, the composition and microstructure still have a decisive influence on the materials properties and consequently the performance of any component fabricated by AM. Macroscopic metal AM is mostly employed for structural applications, and thus the materials properties are dictated by mechanics. In contrast, metal AM at the micrometer scale is expected to benefit the design of microelectronics^{17,95,96}, optical and mechanical metamaterials⁹⁷, microelectromechanical systems (MEMS)⁹⁸, plasmonics⁹⁹, catalysis¹⁰⁰ and hierarchical materials^{79,93}, and the requested materials properties differ widely for the individual applications. These needs can only be met if metal AM is capable of handling a variety of compositions and microstructures.

Finally, we stress the importance of the substrate: it is an often disregarded though crucial element in any AM process at the micrometer scale because fabricated structures are usually not isolated units, but rather functional parts of a more complex system.

In the second part of this review article, we compare the techniques with respect to the listed items and discuss the strengths, weaknesses, prospects and limitations of metal AM at the microscale.

2.2 Metal AM techniques for the microscale

The techniques presented in this report are summarized in Fig. 2.1. From an engineering point of view, it is reasonable to group such techniques according to the tools employed, for example, lasers, electron beams or micropipettes. However, in our opinion, a classification according to the material synthesis principles is more suitable to emphasize the fundamental similarities that determine the properties of the resulting materials. The techniques in Fig. 2.1 are thus grouped in two main categories: **metal transfer** and ***in-situ* synthesis** techniques. The techniques of the first class require the previous synthesis of metallic materials before the actual AM process, while the subsequent deposition simply transfers the pre-synthesized material to the location of interest. In contrast, the *in-situ* methods rely on the synthesis of the metal at the location of interest during the AM process. The metal transfer category is further divided into **transfer of nanoparticles** and **transfer of melt droplets**, whereas the *in-situ* category contains the subgroups **chemical reduction** and **dissociation of metal precursors**.

2.2.1 Direct ink writing

Direct ink writing (DIW) is a well-studied technique for the additive deposition of a variety of materials at the micrometer scale. For a detailed overview, we recommend referring to references⁴⁶ and¹⁰¹. The application of DIW to metals was pioneered by the Lewis group^{12,95}.

Principle. Direct ink writing (DIW) of metals is based on the extrusion of concentrated metal nanoparticle inks from micrometer-sized nozzles (Fig. 2.2a). In a process similar to macroscopic filament extrusion, 3D structures can be fabricated in a layer-by-layer fashion (Fig. 2.2d). The viscoelastic properties of the employed inks must be carefully tuned to enable additive deposition. The inks must exhibit a pronounced shear-thinning behavior, *i.e.*, a decrease in the shear modulus over several orders of magnitude under an applied shear stress (Fig. 2.2b). By applying an overpressure, a shear-thinning ink filament exits the nozzle with a rigid, unyielding core and a more fluid, heavily sheared shell. While the solid core guarantees shape retention, the fluid shell allows the individual layers to fuse¹⁰¹. This unique filament profile enables the printing of self-supporting and spanning structures (Fig. 2.2c)¹².

Setup. The main components of a DIW setup are a glass pipette with a micrometer-sized nozzle (usually 1 – 10 μm in diameter)¹², a pump to control the ink flow rate and a translational stage. The

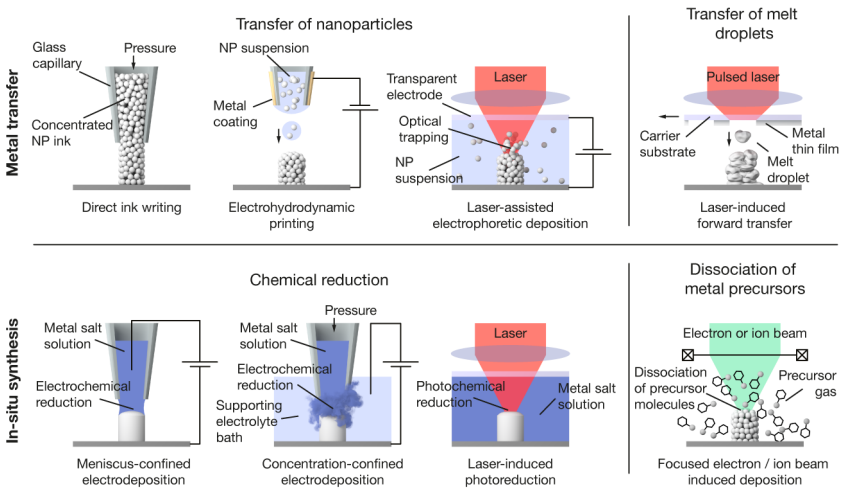


Figure 2.1 – State-of-the-art microscale metal AM techniques. Top row: techniques that rely on the transfer of pre-synthesized material. Bottom row: Techniques that synthesize metals upon the deposition process. **Direct ink writing.** A shear-thinning nanoparticle ink is extruded through a micrometer-sized glass capillary. **Electrohydrodynamic printing.** Submicrometer-sized droplets of a nanoparticle ink are ejected by electrohydrodynamic forces. After evaporation of the solvent, a confined volume of particles is left at the point of impact. **Laser-assisted electrophoretic deposition.** An optical trap locally concentrates nanoparticles in a solvent. Additionally, an electric field is applied to deposit and densify the particles. **Laser-induced forward transfer.** The absorption of a laser pulse in a metal thin film provokes the ejection of a droplet of molten metal. The droplet solidifies on the substrate placed below the donor. The same concept can be used with films of ink. **Meniscus-confined electrodeposition.** A meniscus of a metal salt solution is maintained between the substrate and a glass capillary. The application of a cathodic potential to the substrate induces the electrochemical reduction of the metal ions in the meniscus. **Concentration-confined electrodeposition.** A solution of metal ions is locally dispensed through a submicrometer sized nozzle immersed in a supporting electrolyte bath. The local confinement of the ion concentration results in localized electrochemical deposition upon the application of a cathodic potential to the substrate. **Laser-induced photoreduction.** The local photoreduction of metal ions in a photosensitive solution is triggered by two-photon-absorption. **Focused electron/ion beam induced deposition.** A precursor gas is dissociated into its metallic and organic components by local interactions with an electron or ion beam. Ideally, metallic products deposit, whereas volatile organic products evaporate.

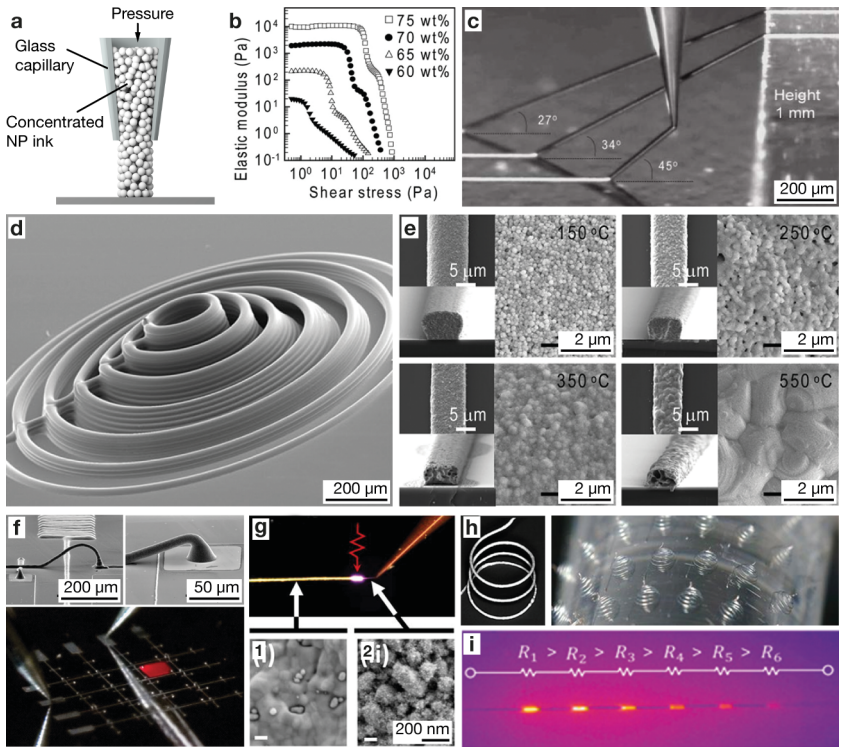


Figure 2.2 – Direct ink writing (DIW). **a**, Principle. A shear-thinning Ag nanoparticle ink is extruded from a glass micropipette. **b**, Influence of the particle concentration on the inks' viscoelastic and shear-thinning properties¹². The elastic modulus increases sharply at low shear stresses. Thus, the ink deposit is stable after extrusion from the nozzle. **c**, The printing process in action: thanks to the high stiffness of the ink in the absence of shear stress, spanning features can be deposited¹². **d**, SEM micrograph of 3D Ag-structures fabricated using layer-by-layer printing¹². **e**, Top view and cross-sectional SEM micrographs of Ag-lines annealed at different temperatures¹². The total volume decreases by $\approx 30\%$ due to evaporation of organic content and coalescence of the nanoparticles that form grains of up to 3 μm in diameter. **f**, SEM images and photograph of DIW-fabricated electric interconnects on a 4×4 LED array¹². **g**, Laser-DIW process. Top: photograph of the extruded ink being annealed *in situ* using an IR laser. A change in surface reflectivity (dull to shiny) and microstructure (bottom, **1**, as deposited, **2**, annealed) is observed⁹⁵. **h**, Ag coils fabricated on a plastic substrate with laser-DIW⁹⁵. Coil diameter: 500 μm . **i**, By varying the laser intensity in laser-DIW, the degree of annealing and the resulting local resistivity may be tuned. The picture shows the infrared emission due to varying Joule heating in a laser-DIW-fabricated wire⁹⁵. **b – i**, Reprinted with permission from **b – f**,¹² ©2009 AAAS; **g – i**,⁹⁵.

nozzles are made from glass capillaries using a laser-pulling system, where local heating under a tensile load results in a tapered, plastic fracture of the capillary. Micropipettes of desired nozzle sizes are reproducibly prepared by controlling both the heating process and pulling rate.

The highly concentrated inks are made of Ag nanoparticles coated with poly(acrylic acid) dispersed in water and ethylene glycol. Depending on the particle concentration, these inks exhibit strong shear thinning. A typical ink configuration is 75 wt.% of (20 ± 5) nm Ag nanoparticles. This ink has an elastic modulus of $G' = 10^4$ Pa (at no shear stress, see Fig. 2.2b). At particle concentrations below 70 wt.%, the extruded ink spreads on the substrate, while concentrations above ≈ 85 wt.% lead to clogging of the micrometer-sized nozzle¹².

The single limitation that the original system imposed on the choice of the substrate was the material stability at post-deposition annealing temperatures¹². However, the Lewis group recently presented a novel setup equipped with an *in-situ* 5 W laser annealing system (laser-DIW) to anneal the extruded nanoparticle ink directly after leaving the nozzle⁹⁵ (Fig. 2.2g). This *in-situ* annealing not only allows printing on thermally sensitive substrates such as flexible polymers but also enables freestanding architectures due to enhanced filament stability.

Geometry. DIW has been used to create a large range of geometries. The technique is best suited for the layer-by-layer fabrication of continuous filaments (Fig. 2.2d) and individual traces (Fig. 2.2e). While the stiff core of the extruded filaments allows the fabrication of out-of-plane arcs and spanning wires (Fig. 2.2c), larger portions of freestanding geometries, for example springs, have not been possible with the original setup¹². Laser-DIW overcomes this limitation by annealing the inks right after extrusion, enabling the fabrication of self-supporting, freestanding geometries (Fig. 2.2h)⁹⁵.

Feature size. The filament thickness mainly depends on the nozzle size, extrusion pressure and translation speed. For conventional DIW, a minimum filament diameter of $2 \mu\text{m}$ was achieved with a $1 \mu\text{m}$ nozzle¹². With the same nozzle and laser-DIW, Skylar-Scott *et al.*⁹⁵ fabricated wires with smallest diameters of 600 nm.

Speed. The reported extrusion speeds are in the range of $20 - 500 \mu\text{m s}^{-1}$ for DIW¹² and $0.5 - 1 \text{ mm s}^{-1}$ for laser-DIW⁹⁵.

Microstructure. The as-deposited structures have the same composition as the ink. Due to the organic content of the ink, the printed features require thermal annealing to become more mechanically stable and electrically conductive¹². At temperatures above 400°C , the residual organic constituents are removed (Fig. 2.2e). Additionally, the nanoparticles sinter to form a dense, metallic microstructure with grain sizes of up to $3 \mu\text{m}$ at 550°C . As the organic content evaporates and

the structure densifies, the volume decreases by $\approx 30\%$. After annealing, the filaments show a drop in electrical resistivity, reaching values as low as $5.2 \times 10^{-7} \Omega \text{ m}$ (bulk Ag: $1.6 \times 10^{-8} \Omega \text{ m}$) with the conventional method and even $5.4 \times 10^{-8} \Omega \text{ m}$ with laser annealing. Moreover, laser-DIW offers the ability to tune the annealing parameters and consequently the local materials properties⁹⁵. This capability is demonstrated in Fig. 2.2i, where individual segments of a printed wire were annealed at different laser intensities, resulting in different local resistances.

Materials. So far, DIW of metals is exclusively based on Ag nanoparticles. In contrast, DIW of ceramics and polymers has been studied more extensively⁴⁶.

Applications. The method was applied to fabricate flexible 3D interconnects on an array of micro-solar cells and connections of individual pixels of a 4×4 LED chip array (Fig. 2.2f)¹².

2.2.2 Electrohydrodynamic printing

Electrohydrodynamic (EHD) printing (also known as e-jet printing) is a method based on the electrohydrodynamic ejection of an ink jet or individual ink droplets from a nozzle. The technique was first applied for 2D printing of polymers, proteins, Si nanowires, carbon nanotubes¹⁰², and coarse patterns of metal particle dispersions¹⁰³. The high-resolution deposition of 2D and 3D structures with metal nanoparticle inks has been established in the last few years. For more detailed insights into EHD printing, please consult the recent review articles by Onses *et al.*⁷¹ and Zhang *et al.*⁷⁴.

Principle. The key element of 3D EHD printing is the controlled electrohydrodynamic ejection of submicrometer droplets of organic nanoparticle dispersions from micrometer sized glass pipettes (Fig. 2.3a). To initiate printing, a voltage of 100 – 1000 V is applied between the capillary and the substrate. Driven by the high electric field, the mobile ions or charged particles in the solvent meniscus migrate to the solvent-air interface. The mutual electrostatic repulsion between the ions generates a tangential stress on the surface. This stress eventually overcomes the surface tension of the solvent and causes the ejection of a jet or a droplet, which can be significantly smaller than the nozzle diameter. Due to the accumulated ions, each droplet is charged.

Different ejection modes are observed as a function of the field strength, size of the nozzle, flow rate and viscous properties of the ink¹⁰⁷. If we generalize, we can distinguish between jetting and dripping modes. The most prominent continuous jet is the cone-jet, a thin, continuous stream of liquid that is ejected from a sharply converging liquid meniscus, referred to as the Taylor cone. The cone-jet guarantees a feature size of a few micrometers and high volume flow rates and is sometimes applied for continuous 2D patterning^{108,109}. Nonetheless, reproducible printing with the cone-jet mode is challenging due to its proximity to unstable modes in the parameter space¹⁰².

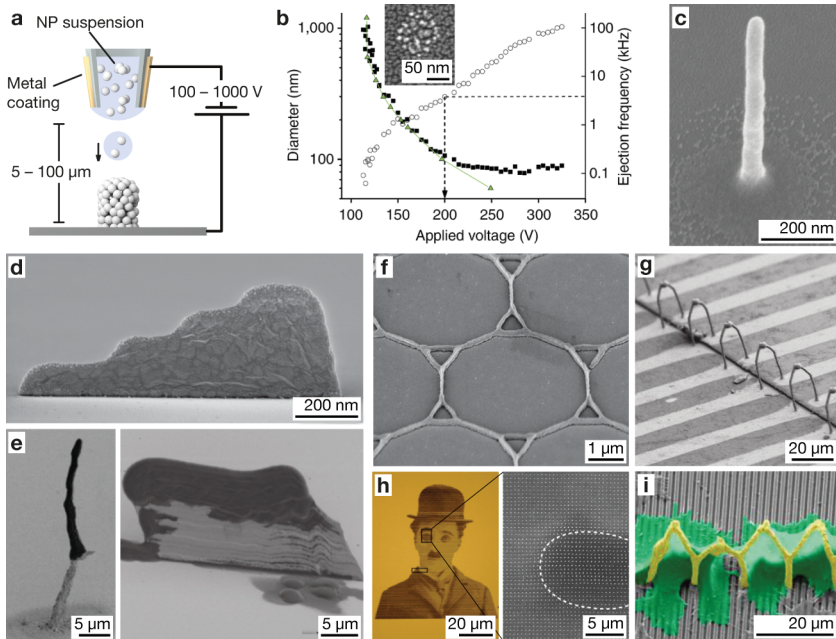


Figure 2.3 – Electrohydrodynamic (EHD) printing. **a**, Principle. Droplets of a metal nanoparticle dispersion are electrohydrodynamically ejected from a glass nozzle. The solvent evaporates in flight or upon impingement on the substrate, leaving an aggregation of nanoparticles at the site of droplet impact. The stacking or layering of the droplets results in 3D fabrication. **b**, Droplet diameter and ejection frequency versus the applied ejection voltage⁹⁹. In dripping mode, the droplet size, and hence the width of the deposit, are a function of the ejection voltage. Inset: SEM micrograph of a Au nanoparticle deposit formed by a single droplet⁹⁹. Upon solvent evaporation, metal nanoparticles and surfactant molecules are left behind. **c**, SEM micrograph of a Au pillar printed on an ITO-coated glass slide⁹⁹. The concentration of electric field lines at the growing deposit focuses incoming droplets towards its tip and facilitates the fabrication of wire-like structures. **d**, SEM micrograph of a Au wall printed in a layer-by-layer fashion¹⁶. The number of layers increases from left to right from three to five, seven and nine. **e**, SEM micrographs of EHD-printed multi-material structures made of anthracene (black) and Ag (gray)¹⁰⁴. The Ag parts had to be annealed prior to the anthracene deposition. **f – i**, Applications of EHD printing. **f**, Transparent electrode built from Au walls with an aspect-ratio of 2.3 and a line diameter of 80 nm¹⁶; **g**, 3D Ag interconnects printed on pre-fabricated traces to bridge two flexible substrates¹⁰⁴; **h**, 200 × 175 μm² large absorption contrast image made of Au pillars 120 nm in diameter¹⁰⁵. The height of the pillars governs the degree of absorption. **i**, Out-of-plane arches with different pore sizes for the study of cell migration plasticity¹⁰⁶. **b – i**, Reprinted with permission from **b**, **c**,⁹⁹ ©2012 Springer Nature; **d**, **f**,¹⁶ ©2015 John Wiley and Sons; **e**, **g**,¹⁰⁴ ©2015 John Wiley and Sons; **h**,¹⁰⁵ ©2016 ACS; **i**,¹⁰⁶ ©2016 ACS.

Moreover, the high flow rate usually does not allow enough time for solvent evaporation when used for 3D deposition. Thus, dripping modes are more commonly used^{99,102,104}. In the dripping mode, single droplets are ejected at a given frequency under a constant electric field. The diameter of the droplet scales with the nozzle size and can be as small as 50 to 100 nm for a 1 μm nozzle⁹⁹. The change from a constant electric field, where the ejection frequency is a function of the applied voltage, to a pulsed field, where the ejection frequency can be controlled by the pulse frequency, allows for on-demand printing of individual droplets¹¹⁰.

Upon emission, the droplets transfer the dispersed nanoparticles from the nozzle to the substrate. After the droplet lands on the substrate, the evaporating solvent leaves a well-defined deposit consisting of loosely packed nanoparticles with a coverage of usually <1 (inset Fig. 2.3b). Given that all of the solvent evaporates between two impacts, the deposits can be stacked to form 3D structures⁹⁹. To increase their mechanical stability and electrical conductivity, post-deposition annealing is required^{16,99,104}.

Setup. A typical ink contains metallic nanoparticles that are a few nanometers in size, surfactants and an organic solvent. The particle loading is $\approx 0.1 - 1$ vol.% to avoid clogging of the nozzle^{16,71,99,104}. The print head is made of a tapered glass capillary optionally connected to a flow system. The opening of the capillary can be as small as 100 nm but is usually micrometer-sized to avoid clogging. To enable the application of an electric potential to the nozzle, the outside of the capillary is coated with a thin metal film, or the ink is directly biased by a thin wire inside the nozzle. Often, the surface of the nozzle is chemically treated to avoid wetting of the ink on the outside of the capillary. The substrate is placed on a grounded electrode and brought within a distance of 5 – 100 μm of the nozzle. To initiate liquid extraction, a constant or pulsed voltage of 100 – 1000 V is applied. Often, optical microscopes are used to monitor the process. High resolution direct video feedback of the printing process can be achieved using a laser confocal microscope with interferometric scattering detection (iSCAT)⁹⁹.

When choosing a substrate material, two aspects must be considered. First, the surface chemistry and the resulting wetting behavior of the ink determines the spreading of the liquid droplet and the evaporation of the solvent. Good wetting is beneficial for fast solvent evaporation and consequently the deposition of 3D structures^{16,99}. Second, some electrical conductivity of the substrate is beneficial because incoming droplets may otherwise be repelled due to accumulated charges⁹⁹. However, although conductive substrates are preferred to guarantee a fast charge removal from the printed structures, 3D deposition on non-conductive substrates is also possible¹⁶. To reduce the electrostatic charging effects, the ejection voltage polarity can be alternated¹¹¹.

Most demonstrations of EHD printing were performed on planar substrates. 2D^{109,112} and 3D¹⁰⁵ fabrication on non-planar substrates is nevertheless feasible; however, possible electric field distortions must be taken into account.

Geometry. EHD printing is well suited for printing of out-of-plane wire-like structures in a sequential manner, but also satisfies the criteria for layer-by-layer printing. Examples of EHD printing include the sequentially printed pillars in Fig. 2.3h, the layer-by-layer printed wire-like structures in Fig. 2.3g, i and the Au wall in Fig. 2.3d. Overhangs of up to 56° were demonstrated⁹⁹. More extreme overhangs can be formed by exploiting the dielectrophoretic bending of pillars towards each other¹¹³.

Feature size. The droplet diameter often translates directly into the diameter of the deposit. Galliker *et al.*⁹⁹ showed that the width of a single spot of Au nanoparticles is equal to the spherical diameter of the ejected ink droplet. The smallest deposits observed were 35 nm in width, ejected from a 600 nm nozzle. Further factors affecting the obtained feature size include droplet charge¹¹⁴ and, particularly, the wettability of the ink on the substrate⁷¹.

Primarily, the droplet diameter is a function of the fixed nozzle size. Additionally, the diameter can be changed *in situ* by varying the amplitude of the pulsed or constant electric field. For example, doubling the voltage can cause a change of droplet size from 1 μm to 100 nm (Fig. 2.3b)⁹⁹. Pulsed setups allow for additional control of the diameter by changing the ejection pulse length¹¹⁰.

A peculiarity of EHD printing is the fact that the ink droplets carry charges. Consequently, the droplets can be guided by electric fields¹¹⁵, which is advantageous for depositing high-aspect-ratio structures. Any protrusion on the substrate, such as a growing deposit, acts as an antenna, concentrating the electric field lines at its tip and thus attracting the incoming droplets. This auto-focusing guarantees an outstanding stacking accuracy of single droplets. Galliker *et al.* printed Au pillars 50 nm in diameter with an aspect ratio of 17 (Fig. 2.3c)⁹⁹. However, the process requires the swift removal of any charges in the deposit; otherwise, the accumulated charge will repel arriving droplets. This problem is circumvented by utilizing conductive substrates and volatile solvents to quickly remove the excess ionic charge. As another application of the focusing effect, the precise deposition of 2D and 3D structures on the apex of a wedge has been reported^{105,112}. On the other hand, the attraction of droplets to a protrusion can be detrimental if it is not intended. Kress *et al.* demonstrated the severe deflection of 2D linear features close to a pyramid¹¹⁶, and Schneider *et al.* found that unwanted droplet autofocusing can result in unconnected junctions in high-aspect-ratio grid electrodes¹⁶.

Speed. Ejection frequencies of several kilohertz for the dripping⁹⁹ and drop-on-demand¹¹⁰ modes compensate for the relatively small volume deposited by a single droplet. A typical in-plane print velocity for layer-by-layer deposition by dripping is $1 - 10 \mu\text{m s}^{-1}$ ¹⁶. Single pillars can be fabricated at z-growth speeds of a few $\mu\text{m s}^{-1}$ ^{99,104}. For 2D deposition with a cone-jet, the printing of Ag lines can be as fast as tens of cm s^{-1} ^{108,109}.

Microstructure. The deposited structures are composed of loosely aggregated nanoparticles, surfactant molecules and residual solvent molecules. The structures are fragile^{111,113} and not yet electrically conductive¹⁶ because each nanoparticle is surrounded by adsorbed surfactant molecules. To remove the residual organic content and coalesce the nanoparticles, the deposits must be annealed at 150 to 400 °C. The Young's modulus of as-deposited EHD-printed Au pillars was estimated to be smaller than 0.2 MPa¹¹³. After one minute of annealing at 140 °C, the stiffness of Au structures was measured to be 6 GPa in another study¹¹¹. Annealing also improves the conductivity of the deposits: Ag structures became conductive at temperatures as low as 150 °C^{16,104}, whereas Au deposits required annealing temperatures of up to 250 °C¹⁶. The volume loss upon annealing can be as large as 60 %⁹⁹. This may introduce mechanical stresses, which will cause warping or fracturing at susceptible points of stress concentration, such as the junctions in printed grid electrodes¹⁶.

Materials. Au and Ag nanoparticles are commonly used for metal EHD printing^{16,99,109}. In addition, the 2D and 3D deposition of Cu^{104,117,118}, Co¹⁰⁴ and Al^{119,120} have been demonstrated. Apart from metals, other materials such as semiconductors, polymers, ceramics, carbon nanotubes and graphene can be printed⁷¹.

The sequential use of different nozzles filled with different inks enables the deposition of multiple materials. Recently, An *et al.*¹⁰⁴ demonstrated the 3D deposition of two inks combined in one structure. Fig. 2.3e shows a pillar and a wall with a Ag bottom and an anthracene top. The Ag parts had to be annealed before the anthracene deposition took place.

Applications. Selected examples of the diverse applications of EHD printing are given in Fig. 2.3f – i. A promising field is the printing of electronics, either for transparent grid electrodes^{16,108,109} or 3D interconnects on flexible substrates (Fig. 2.3g)¹⁰⁴. The printing of Ag and Au grid electrodes with high aspect ratios significantly increases the sheet conductivity of the electrode without deteriorating its optical transmittance (Fig. 2.3f)¹⁶. The flexibility of EHD printing permits a simple tuning of the grid density, geometry and aspect ratio to optimize the performance for either high conductivity or high transmittance. EHD-printed optical metamaterials were demonstrated by Richner *et al.*¹⁰⁵. They printed a $200 \times 175 \mu\text{m}^2$ large grey-scale image made of an array of Au-dielectric composite pillars, each 120 nm in diameter and 500 nm apart (Fig. 2.3h).

The local degree of absorption in this metamaterial was governed by the height of the single pillars. By controlling the height of each individual pillar, different shades of grey were fabricated. 3D pore structures printed directly onto basal scaffolds were used to study the migration and pore penetration of cancer cells (Fig. 2.3i)^{106,111}.

2.2.3 Laser-assisted electrophoretic deposition

Electrophoresis is the movement of charged particles in liquid under the influence of an electric field. Recently, Iwata and coworkers^{121,122} proposed two methods that make use of local electrophoretic deposition to additively assemble metallic nanoparticles. While the first technique utilizes a glass capillary to locally supply the nanoparticles¹²¹, the second method employs an optical trap for the same purpose¹²². Here, we focus on this second, more advanced technique.

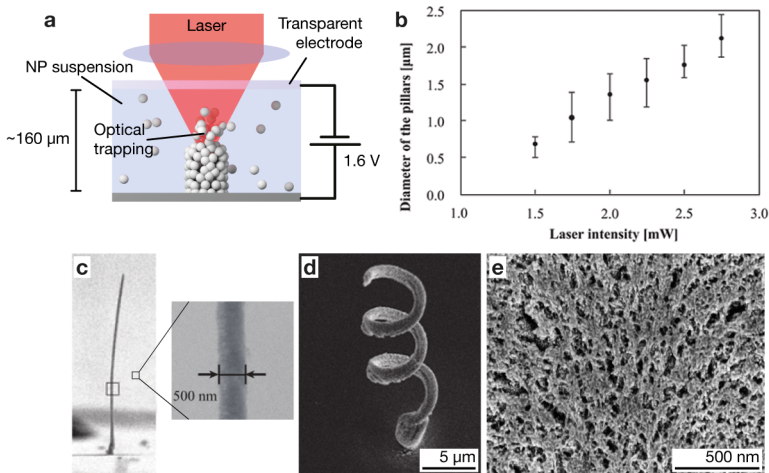


Figure 2.4 – Laser-assisted electrophoretic deposition. **a**, Principle. A nanoparticle solution is confined between a conductive substrate and a transparent flat cover electrode. Optical trapping of particles in the focal spot of a laser beam accumulates particles locally. The additional application of an electric potential across the solution results in electrophoretic deposition of the trapped nanoparticles. **b**, The obtained feature size is a function of the laser intensity¹²². **c**, The technique enables the fabrication of nanowires 500 nm in diameter. **d**, SEM micrograph of a Au coil fabricated by laser-assisted electrophoretic deposition¹²². **e**, FIB cross-section of an as-deposited, porous microstructure (sample kindly provided by Iwata *et al.*). **b – d**, Reprinted from¹²² ©2014 OSA.

Principle. Laser-assisted electrophoretic deposition is based on the optical trapping of nanoparticles combined with their electrophoretic deposition (Fig. 2.4a)¹²². A tightly focused laser beam

is directed into a suspension of negatively charged metallic nanoparticles and optically traps and accumulates particles in its focal spot, drastically increasing the local particle concentration. In addition, a constant electric field is established across the suspension, forcing the particles to coagulate and settle on the positively polarized substrate¹²³. With an appropriate movement of the laser spot, the particles can be assembled into 3D objects.

Setup. Iwata *et al.*¹²² used a continuous-wave laser beam with a wavelength of 488 nm operated at powers of 1.5 – 2.75 mW for optical trapping. The laser beam was focused into a 0.26 wt.% aqueous suspension of negatively charged 3 nm Au nanoparticles confined by two planar, transparent indium tin oxide (ITO) electrodes with an electrode spacing of 160 μm . An electric field of $\approx 10 \text{ kV m}^{-1}$ was established across these electrodes for electrophoretic deposition. The conductive ITO-coated substrate was mounted on a piezo stage.

Geometry. Because processing occurs in solution, no restrictions are imposed on the growth direction, and overhanging structures such as coils can be fabricated (Fig. 2.4d). Layer-by-layer fabrication has not been demonstrated yet, but will be shown in Chapter 3.

Feature size. The authors indicate a minimum wire diameter of 500 nm achieved with the laser trapping technique. This corresponds to the approximate size of the focal spot¹²². The diameter of the fabricated wires scales linearly with the laser power (Fig. 2.4b), and wires between 500 nm (Fig. 2.4c) and several micrometers in width can be fabricated¹²².

Speed. The coil shown in Fig. 2.4d was assembled in approximately 2 min, with vertical and horizontal velocities of 300 nm s^{-1} and 400 nm s^{-1} , respectively. A maximum vertical growth rate of 670 nm s^{-1} was reported for 1.5 mW laser power¹²².

Microstructure. The deposits are built from loosely aggregated nanoparticles (Fig. 2.4e). Whereas the surface morphology is usually smooth, significant internal porosity may exist. The loose packing of as-deposited structures results in a low elastic modulus of approximately 1.5 GPa¹²². No studies of the microstructure after thermal annealing have been performed to date.

Materials. So far, laser-assisted electrophoretic deposition has exclusively been demonstrated with Au nanoparticles.

2.2.4 Laser-induced forward transfer

Laser-induced forward transfer (LIFT) is a technique for the direct transfer of various types of materials by ablation. For an overview of the general concept of LIFT, we would like to point out

the review articles by Huis in 't Veld *et al.*⁷⁰, Piqué *et al.*⁷² and Serra *et al.*⁷⁵. LIFT was introduced for 2D metal patterning in 1986¹²⁴ but has only recently been studied for metal AM^{125–128}.

Principle. A schematic of the LIFT procedure for metals is shown in Fig. 2.5a. A focused laser pulse is absorbed by a thin film of metal (donor) coated onto a glass slide (carrier) and induces local melting of the metal film as well as the potential evaporation of low-melting-point carriers such as soda lime glass¹³². The resulting pressure at the carrier-donor interface causes the ejection of a liquid metal droplet and its transfer to the substrate placed below the carrier. Upon impact, the droplet quickly cools and solidifies (Fig. 2.5b). Subsequently, the carrier is translated laterally to expose an intact region of the film where the next droplet is created. With appropriate substrate movement, the droplets can be stacked to build 3D objects (Fig. 2.5c,d, e).

Setup. The carrier and the substrate are both mounted on XYZ-stages. Typically, the laser is stationary but can optionally be translated with the help of scanning mirrors¹³⁰. In the most common setup, the laser illuminates the donor film from the backside through the carrier glass slide^{126,130}. Accurate positioning of individual droplets becomes increasingly difficult for larger donor-substrate gaps. Therefore, the gap is usually limited to $\approx 10 - 200 \mu\text{m}$ and needs to be precisely controlled using a distance meter¹²⁸. An optical microscope facilitates tuning of the parameters for optimal ejection conditions and observation of the fabrication process.

The substrate should be flat because of the small separation to the planar donor. Since the adhesion of the metal droplets is often an issue, surface oxides of non-noble metal substrates have to be removed and the surface of plastic or ceramic substrates has to be roughened¹³³. Alternatively, metal adhesion layers can be used. Furthermore, substrates with a high heat conductivity are beneficial because they avoid a splashing of the impacting droplets¹²⁵.

Geometry. LIFT is best suited for the deposition of vertical wires and layer-by-layer fabrication. In contrast, the fabrication of overhangs is difficult due to the vertical impact of the droplets. Nevertheless, overhanging Cu pillars with tilt angles of up to 30° were printed (Fig. 2.5d, g)^{52,127}. Horizontal overhangs and hollow features are enabled by the deposition of sacrificial support materials that are removed in a post-processing step^{130,131} (Fig. 2.5e, f, h).

Feature size. The reported 3D structures usually have minimal lateral dimensions of several micrometers^{126–128}. The smallest reported X-Y feature size of 3D structures is $3 \mu\text{m}$ ¹²⁶. Whereas the diameter of single droplets can be in the submicrometer range¹²⁵, insufficient landing accuracy broadens the features. The most important parameter for influencing the droplet ejection and hence the landing accuracy is the energy input per pulse (fluence, $[\text{J m}^{-2}]$). If the fluence is too low, no droplet ejection occurs. Near a threshold fluence, the process is prone to local donor variations,

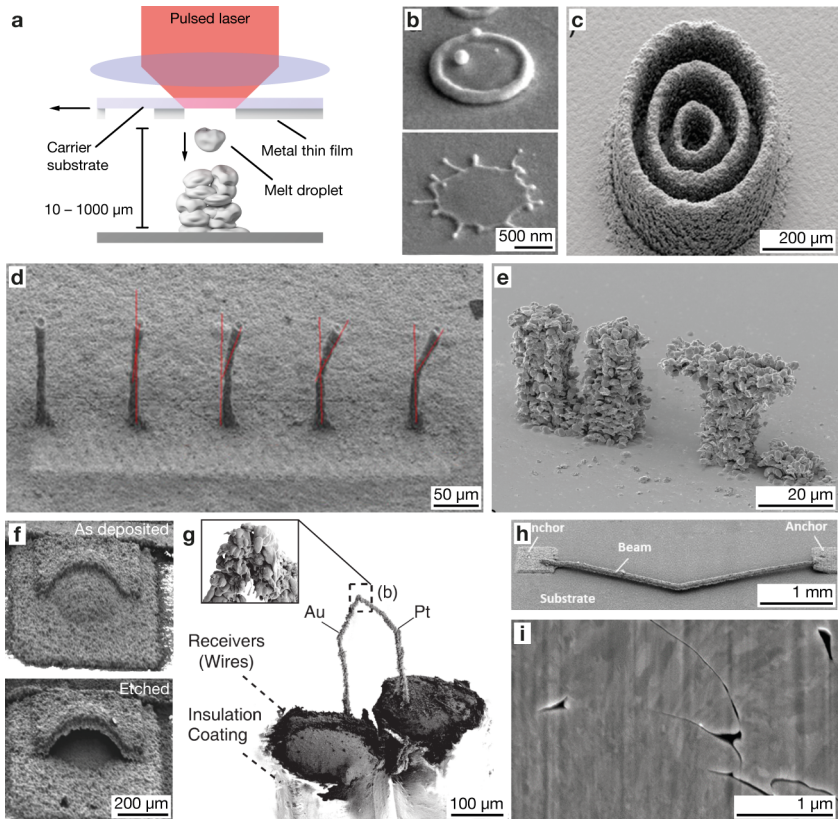


Figure 2.5 – Laser-induced forward transfer (LIFT) of metal melts. **a**, Principle. A glass slide (carrier) coated with a metal thin film (donor) is placed within hundreds of micrometers above a substrate. A high-power picosecond laser pulse is focused onto the donor and absorbed. The local overpressure generated upon melting of the donor leads to the ejection of a micrometer-sized metal droplet which lands on the substrate and re-solidifies. **b**, Solidified Cu droplets for low (top) and high (bottom) ejection speeds, showing a different impact and solidification behavior.¹²⁶ **c**, Concentric cylinders fabricated in a layer-by-layer fashion.¹²⁷ **d**, Vertical and tilted Cu pillars grown by stacking droplets diagonally.¹²⁷ **e**, **f**, Overhanging structures can be printed with the help of sacrificial support structures: **e**, SEM micrograph of overhanging Au structure printed on a sacrificial layer of Cu (shown after etching of Cu)¹²⁹. **f**, LIFT-printed Cu-Ag dome before (top) and after removal of the sacrificial Cu material (bottom).¹³⁰ **g**, LIFT-printed miniature thermocouple deposited onto a macroscale thermocouple.⁵² **h**, Freestanding electrothermal actuator fabricated by printing Au on top of a sacrificial Cu support layer and post-print etching of Cu.¹³¹ **i**, FIB cross-section of a Cu structure fabricated with LIFT.¹³⁰ Boundaries and voids between single droplets as well as a polycrystalline microstructure are visible. **b – i**, Reprinted with permission from **b**,¹²⁶ ©2015 John Wiley and Sons; **c**, **d**, **i**,¹²⁷ CC BY 4.0 (<https://creativecommons.org/licenses/by/4.0/>); **e**,¹²⁹ CC BY 4.0 (<https://creativecommons.org/licenses/by/4.0/>); **f**,¹³⁰ ©2015 John Wiley and Sons; **g**,⁵² ©2016 John Wiley and Sons; **h**,¹³¹ ©2018 Elsevier.

e.g., inhomogeneous thickness or surface contamination. This typically results in unstable ejection angles. When the fluence is increased beyond the threshold, the so-called thermally-induced-nozzle regime (TIN) is reached¹²⁷. In this regime, the thermal diffusion length during the pulse is smaller than the layer thickness. Therefore, the donor is not liquefied across its entire thickness, but a wave of molten material travels from the interface to the donor surface. The intersection of the spherical wavefront and the surface forms a disruption of the surface smaller than the actual diameter of the liquid pool. All the liquid metal is ejected through this small quasi-nozzle. According to Zenou and Kotler¹²⁷, the most stable and well-directed jetting occurs in the TIN regime, allowing for metal transfer over donor-substrate gaps of up to 1000 μm . Further prolongation of the laser pulses once more results in unstable ejection with the simultaneous generation of multiple droplets. Additional parameters of the printing process are the donor film thickness and the donor-substrate gap. For example, the optimal laser fluence to achieve a stable and well-directed jetting depends on the donor thickness¹²⁷.

A surface roughness between 0.5 and 2 μm is generally observed for LIFT deposits (Fig. 2.5c – f)^{130,133}, but can also be higher, especially for Au¹²⁹ (Fig. 2.5e). The roughness is caused by the sequential solidification of single melt droplets and was identified by Zenou and Kotler as one of the main drawbacks of metal AM by LIFT¹²⁸.

Speed. The deposition speed of LIFT is determined by the droplet ejection frequency and the droplet volume. The ejection frequency is mainly limited by the maximum velocity at which the donor can be translated¹²⁶. A recent system by Visser *et al.*¹²⁶ has an ejection rate of ≈ 200 Hz, corresponding to a z growth rate of several tens of $\mu\text{m s}^{-1}$.

Microstructure. LIFT-printed structures are generally polycrystalline and of high purity, although the oxidation of non-noble metal droplets can lead to the inclusion of oxides^{126,127,134}. Visser and coworkers¹²⁶ showed that printing in inert argon atmosphere instead of air reduced the resistivity of Cu deposits from 22 to 12 times the bulk resistivity. The internal morphology is mostly compact. However, as a result of the sequential solidification of individual droplets, often as a spherical or torus-like voxel rather than as a compact, cylindrical voxel¹²⁶, voids and gaps are difficult to eliminate and interfaces between the single droplets are usually present (Fig. 2.5i). Additionally, the rapid quenching of the droplets upon impact can result in high internal mechanical stresses which are a major cause for poor adhesion to the substrate⁷².

Materials. AM with LIFT has been demonstrated for a variety of metals, including Al¹³³, Cu^{126,127,130,135}, Au^{125–127}, and metal alloys¹³⁰. Moreover, the review articles of Huis in 't Veld *et al.*⁷⁰ and Piqué *et al.*⁷² list the following materials that have been used for 2D LIFT: Ag, Cr,

Ge, Ni, Pd, Pt, Sn, Ti, V, W, Zn, Ge/Se, various oxides and polymers. Even heat-sensitive materials, for example, multiphase systems that would undergo irreversible changes upon melting and re-solidification, can be transferred using either dynamic release layers or the matrix-assisted pulsed laser evaporation technique^{70,72}. Multi-material printing can be performed using a carrier patterned with donor layers of different materials. This multi-material printing capability allows for the printing of sacrificial support material, as discussed above (Fig. 2.5f)¹³⁰.

Laser decal transfer. Additional to solid films, films of nanoparticle pastes – hundreds of nanometers to $\approx 10\ \mu\text{m}$ in thickness – can be transferred with LIFT^{14,136,137} (Fig. 2.6a). The paste voxels can easily be stacked using a layer-by-layer approach. Fig. 2.6b shows a pyramid made of individual square voxels¹⁴.

The pastes are highly concentrated suspensions of Ag nanoparticles, usually smaller than 10 nm in diameter, suspended in an organic solvent. In contrast to LIFT, the pressure required for ejection is not provided by the melting of the metallic particles but rather by rapid solvent evaporation. Therefore, the transferred voxel sheets retain their shape and can be much larger than those for pure metal films, with reported voxel widths ranging from $2\ \mu\text{m}$ to 1 mm¹³⁷.

The shape of the voxels can be defined by either patterning the donor layer⁹⁶ or using apertures to shape the laser beam accordingly (Fig. 2.6a)¹⁴. Circular, square and various custom-shaped voxels have been demonstrated¹⁴. The technique is therefore also referred to as laser decal transfer (LDT)¹³⁶. Complex shapes can be transferred at once using a digital mirror device (DMD) for shaping of the laser profile (Fig. 2.6c). With a dynamic shaping of the beam and various donor thicknesses, the voxel shape can be varied *in situ*: Fig. 2.6d shows two small circular voxels (radius $3\ \mu\text{m}$, height $1\ \mu\text{m}$) printed next to one large rectangular voxel ($13\ \mu\text{m} \times 65\ \mu\text{m}$, height $5\ \mu\text{m}$). Patterned donor layers enable parallel transfer (Fig. 2.6e)¹³⁹.

It is important to note that the transfer distances are considerably smaller for LDT than for LIFT because the flat, sheet-like voxels are prone to rupture or folding in flight⁹⁶. Furthermore, the non-metallic nature of the donor triggers two additional processing steps: first, before deposition, the paste needs to be aged (dried) to render an optimal viscosity¹⁴. Second, post-print thermal sintering is needed for conductive and mechanically stable structures. Upon annealing, the single particles coalesce into a partially porous structure¹⁴⁰ and grain growth occurs. Fig. 2.6h shows an increase in the grain size of a Ag deposit from $\approx 70\ \text{nm}$ to $\approx 200\ \text{nm}$ at annealing temperatures of up to $250\ ^\circ\text{C}$ ¹⁴. After annealing, an electrical resistivity of $1.9 \times 10^{-8}\ \Omega\ \text{m}$, 20% above the value for bulk Ag, was achieved¹⁴. Young's moduli of 40 – 57 GPa^{140–142} and a yield stress of 110 MPa¹⁴² both approximately half the bulk values of Ag, were found for annealed structures. LDT has been primarily applied for printed electrical interconnects¹⁴ (Fig. 2.6f, g).

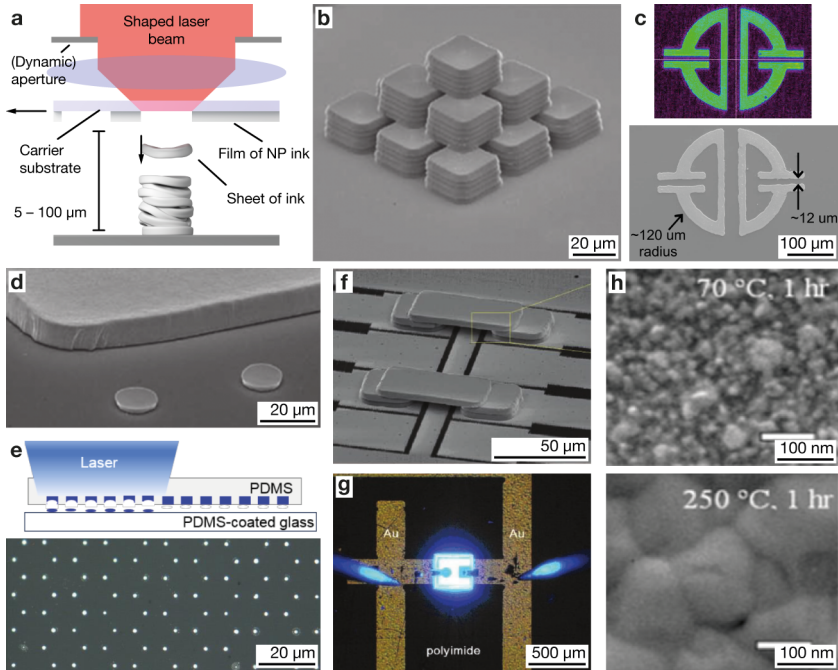


Figure 2.6 – LIFT (laser decal transfer) of nanoparticle inks. **a**, Schematic of the laser decal transfer process for the transfer of nanoparticle pastes. The shape of the laser beam determines the shape of the transferred voxels. **b**, Stacks of square voxels of Ag paste ejected with a laser beam shaped by a square aperture¹⁴. **c**, The use of a digital mirror device (DMD) instead of an aperture enables more complex modulation of the laser beam. Top: measured beam profile corresponding to the laser beam after shaping with a DMD. Bottom: SEM imaging showing the corresponding transferred shape: a single D-ring meta-antenna deposited in one shot¹³⁸. **d**, Two small circular voxels next to a large square voxel, demonstrating the potential to dynamically change the voxel size and shape during printing of metal pastes¹⁴. **e**, The parallel transfer of pre-patterned shapes further increases fabrication speed. Bottom: SEM micrographs of Ag ink dots transferred in one shot¹³⁹. **f**, Applications: **f**, bridging interconnects built from five voxels with variable shape¹⁴, and **g**, operational LED contacted by two printed interconnects¹⁴. **h**, SE micrographs of the surface morphology of transferred Ag pastes after annealing at two different temperatures. An increase in grain size with increased annealing temperature is apparent¹⁴. **b – h**, Reprinted with permission from **b**, **d**, **f – h**,¹⁴ ©2010 John Wiley and Sons; **c**,¹³⁸ ©2013 SPIE; **e**,¹³⁹ ©2019 SPIE.

2.2.5 Meniscus-confined electrodeposition

Electroplating is a technique widely used in industry and research and is usually performed as a homogeneous surface reaction. To localize the reaction, meniscus-confined electrodeposition makes use of glass pipettes to confine the electroplating solution to a specific point on the substrate^{13,143–146}.

Principle. A nanopipette filled with a metal salt solution is approached to a conductive substrate. A liquid meniscus forms between the pipette and the substrate upon contact of the electrolyte (Fig. 2.7a). To initiate electrochemical reduction, the substrate is negatively polarized versus a counter electrode placed in the pipette. The liquid meniscus defines the lateral extension of the electrochemical reaction and hence nucleation and growth of the metallic deposit. Finally, the controlled retraction of the pipette promotes the 3D growth of a metal wire. Suryavanshi *et al.*^{145,146} first demonstrated the capability of this method to fabricate arrays of freestanding Cu pillars (Fig. 2.7c).

Setup. Glass pipettes with micrometer- to submicrometer wide apertures are employed to deliver the electrolyte solution. A counter electrode, typically a metal wire mounted inside the pipette and connected to a potentiostat, serves to control the electrochemical reactions. Controlled wire fabrication requires retraction of the pipette at appropriate speeds to avoid breaking the meniscus. Without a feedback mechanism in place, the retraction velocity has to be calibrated (Fig. 2.7b). For a controlled approach to the substrate, the ionic current may be observed, where a sharp increase in the current indicates contact with the substrate¹³. As for all electrodeposition processes, a conductive or semiconductive substrate is required.

Feature size. The use of a liquid meniscus is a straightforward way to confine the electroplating reaction. Hence, the X-Y feature size depends mainly on the meniscus size, which can be as small as half the diameter of the pipette used¹³. Solid vertical nanowires as thin as 100 nm may be fabricated using this approach. However, establishing a stable liquid bridge under a nanopipette is not trivial. In general, the meniscus size depends on many parameters, such as the air humidity, wetting properties of the substrate, and retraction speed (Fig. 2.7b)^{13,146,150,151}.

Geometry. To date, meniscus-confined approaches have predominantly been used for the continuous growth of wire-like structures. The synthesis of vertical wires of high aspect ratios (>50 ¹⁴⁷) and wires with moderate overhangs¹⁵² is straightforward. Point-by-point printing enables the synthesis of more complex structures, such as the intertwined helices or arrays of high-aspect-ratio wires (Fig. 2.7d). Horizontal wires can be grown using pipettes with custom-shaped apertures (usually by FIB milling) that establish a horizontal meniscus. Using such pipettes, overhanging

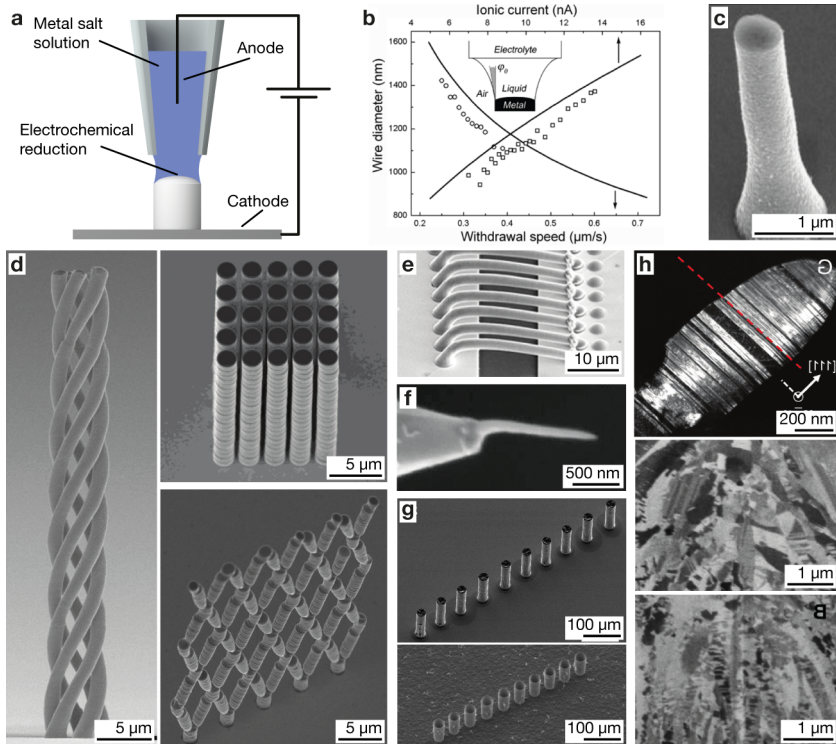


Figure 2.7 – Meniscus-confined electrodeposition. **a**, Principle. A micropipette filled with a metal salt solution and containing a wire electrode is approached to a conductive surface. Upon contact with the substrate, a liquid meniscus is established. The application of a suitable potential between the wire electrode and the substrate initiates the electrochemical reduction of the metal ions in the area confined by the meniscus. The linear retraction of the pipette builds a wire-like structure. **b**, Influence of the withdrawal speed and the ionic current on the obtained wire diameter. Slower withdrawal or a higher current result in bigger wire diameters¹³. **c**, SEM image of a Cu pillar fabricated by meniscus-confined electrodeposition¹⁴⁵. **d**, Layer-by-layer printing instead of simple retraction of the nozzle enables the deposition of intricate geometries¹⁴⁷. **e – f**, Applications: **e**, Cu wire bonds fabricated by meniscus-confined electrodeposition¹³. **f**, The meniscus-confined deposition of a Pt nanowire onto the apex of a regular AFM probe renders a high-aspect ratio probe¹³. **g**, Parallel printing with multiple nozzles. SEM micrographs of an array of ten Cu pillars printed in parallel (top) using a microfabricated nozzle array with ten nozzles (bottom)¹⁴⁷. **h**, The microstructure of the deposits can be varied by adjusting the deposition potential profile. Top: Dark-field TEM micrograph of nanotwinned Cu¹⁴⁸. Middle and bottom: FIB micrographs of printed Cu with different grain sizes¹⁴⁹. **b – h**, Reprinted with permission from **b**, **e**, **f**,¹³ ©2010 AAAS; **c**,¹⁴⁵ ©2006 AIP Publishing; **d**, **g**,¹⁴⁷ ©2018 John Wiley and Sons; **h**, top:¹⁴⁸ ©2017 John Wiley and Sons, bottom:¹⁴⁹ ©2018 John Wiley and Sons.

spirals and horizontal wire bonds were fabricated (Fig. 2.7e)¹³. Finally, the combination of the controlled evaporation of the meniscus and the application of appropriate potential profiles allows the growth of hollow tubes¹⁴⁴.

Speed. The reaction rate of electrochemical reactions is mass transport limited above a critical potential. At too high potentials, side effects such as hydrogen evolution occur and impede the process^{145,146}. As a result, the fabrication speed is generally relatively low; typical growth rates are 250 nm s^{-1} (Fig. 2.7e) or 170 nm s^{-1} (Fig. 2.7d). Simulations by Morsali *et al.*¹⁵⁰ suggest that deposition rate is a strong function of pipette diameter, as small pipettes profit from enhanced evaporation rates. The resulting increase in convection towards the growth area increases the maximum out-of-plane growth speed: maximum simulated out-of-plane growth values were $\approx 520 - 2300 \text{ nm s}^{-1}$ and $\approx 15 - 45 \text{ nm s}^{-1}$ for pipette openings of 100 nm and $5 \mu\text{m}$, respectively. However, experiments show only a moderate increase of growth rate: 200 nm s^{-1} for grown wires of 450 nm in diameter compared to 100 nm s^{-1} for wires of 650 nm in diameter¹⁵⁰. In an effort to increase the throughput, Lin *et al.*¹⁴⁷ recently demonstrated parallelization of the deposition using a microfabricated nozzle-array with ten nozzles (Fig. 2.7g).

Microstructure. Electrochemical deposition generally enables the synthesis of pure metals without the need of additional post-processing steps. Suryavanshi *et al.*¹⁴⁶ showed that synthesized Pt wires are polycrystalline. An as-deposited resistivity of $\approx 3 \times 10^{-8} \Omega \text{ m}$, only 80% higher than the resistivity of bulk Cu, indicates the metallic nature of the deposits. The electrochemical principle further offers direct control of the synthesized microstructure. It has been shown that the microstructure of Cu pillars is changed with a variation in deposition parameters (Fig. 2.7h), and that the resulting yield strength can be tuned within a range of $630 \pm 15 - 909 \pm 23 \text{ MPa}$ ¹⁴⁹. The deposition of nanotwinned Cu with high twin density (Fig. 2.7h) results in excellent mechanical properties, with a reported Young's modulus of $128.2 \pm 10.9 \text{ GPa}$, a hardness of $2.0 \pm 0.19 \text{ GPa}$ ¹⁴⁸, and a yield strength of 960 MPa ¹⁵².

Materials. Meniscus-confined electrodeposition has been used almost exclusively for AM of Cu^{13,144,145,147-149}. Additionally, the 3D deposition of Pt¹⁴⁶ and 2D patterning of Ag¹⁵³ was shown.

Applications. The technique was used to fabricate high aspect ratio extensions on commercial AFM probes (Fig. 2.7f)¹³.

2.2.6 Concentration-confined electrodeposition

To enhance the geometric freedom of meniscus-confined electrodeposition, we recently introduced a method based on the localized delivery of metallic ions through hollow atomic force microscopy (AFM) cantilevers in solution¹⁵⁴. In the meantime, an additional technique based on the same principle but relying on glass capillaries in scanning ion conductance microscope (SICM) configuration has been demonstrated by Momotenko *et al.*¹⁵⁵. In analogy to meniscus-confined electrodeposition, the two methods are summarized under the umbrella term concentration-confined electrodeposition, as the deposition is localized by a concentration gradient rather than a liquid meniscus.

Principle. A schematic of localized electroplating with a confined concentration field of precursor ions is shown in Fig. 2.8a. The metal ions are only present in the pipette and not in the surrounding solution. The localization of the electroplating reaction is achieved by spatial confinement of the metal ion supply through the nano-sized pipette aperture. For 3D deposition, the pipette is approached to a cathodically polarized substrate, usually to a separation of $\approx 15 - 500$ nm. Subsequently, controlled dispensing of metal ions from the pipette aperture is induced. The ions exiting the aperture are electrochemically reduced on the cathodic substrate, and the localized nucleation and growth of a metal deposit is initiated. A feedback is employed to detect the growth of the deposit and maintain a constant separation of pipette and deposit.

Setup. Two basic setups have been reported up to date. These mainly differ in the pipettes employed, schematically depicted in Fig. 2.8b. The original setup, called FluidFM^{157,158}, is a variation of on an AFM equipped with cantilevers featuring a fluidic microchannel that ends in an aperture at the apex of the AFM tip. An SEM image of a FluidFM cantilever is shown as an inset in Fig. 2.8b. Typical tip openings are 300 nm but can range from 100 nm to 2 μ m. The second setup is based on a SICM and uses a dual-barreled glass capillary to dispense the metal ions¹⁵⁵. Only one of the barrels is filled with the metal salt solution, whereas the other barrel is filled with supporting electrolyte and used for SICM feedback. The aperture diameters of the pulled glass pipettes are between 30 and 50 nm (Fig. 2.8b, inset).

The pipette and the substrate are both immersed in a supporting electrolyte bath. A potentiostat controls the potential of the substrate through a reference electrode and a counter electrode placed in the bath. In the case of SICM, an additional electrode is placed in each barrel: one serves to induce the ion current for the SICM feedback, whereas the other, placed in the barrel with the metal salt solution, is used to regulate the metal ion flux via electromigration. In contrast, FluidFM uses

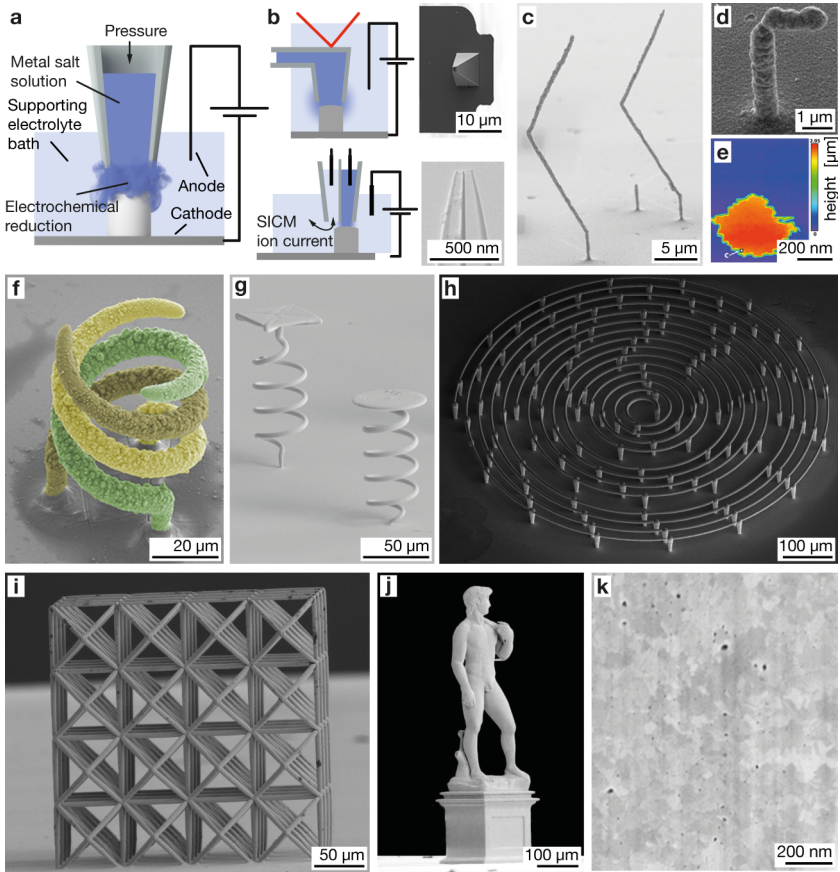


Figure 2.8 – Concentration-confined electrodeposition. **a**, Principle. A nanopipette serves as a local source of metal ions immersed in an electrochemical cell. The dispensing of a metal salt solution through the pipette results in a confined concentration field of metal ions. These ions are reduced locally upon the application of a cathodic potential to the substrate. **b**, Different feedback mechanisms. Top: FluidFM system. Hollow AFM cantilevers detect the growing deposit via the deflection signal of the cantilever¹⁵⁴. Bottom: SICM system with dual-barreled pipette. One barrel serves as the metal ion source whereas the ionic current through the other barrel is used for SICM feedback¹⁵⁵. **c**, High aspect ratio structures and **d**, an overhanging wire produced with the SICM system¹⁵⁵. **e**, Both methods allow for an *in-situ* topography scan (here: SICM)¹⁵⁵. **f**, Triple helix printed with the FluidFM system¹⁵⁴. **g – j**, SEM micrographs of Cu structures printed with the commercial CERES printer (Exaddon¹⁵⁶), which is based on the original FluidFM concept. The geometrical feedback loop provided by the system enables accurate reproduction of complex structures (i, j) and support-free deposition of horizontal features (g, h). **k**, FIB cross-section of a Cu structure deposited with the FluidFM¹⁵⁴. The polycrystalline, mostly dense nature of the deposit is evident. **b – k**, Reprinted with permission from **b**, (dual-barreled pipette), **c – e**,¹⁵⁵ ©2016 ACS; **b**, (FluidFM cantilever), **f**,¹⁵⁴ ©2016 John Wiley and Sons; **g – j**, ©Exaddon¹⁵⁶.

a pressure controller connected to the FluidFM cantilever for controlled dispensing of the metal ion solution.

The FluidFM utilizes the force between tip apex and substrate in the standard AFM contact-mode as feedback. During the deposition process, the tip is positioned at a given distance above the substrate. When the growing reaches the tip, pushing against its apex, the respective deflection signal indicates the successful fabrication of a voxel, whereupon the tip is moved to its next position. In contrast, the SICM setup is based on the ionic current measured between an auxiliary electrode and an electrode immersed in one of the two barrels of the capillary, and thus contactless. This enables a continuous positioning feedback during deposition and avoids contact between the deposit and the pipette. As with any electrodeposition process, the choice of the substrate is limited to conductive or semiconductive materials.

Geometry. The absence of a liquid meniscus and the growth in solution simplifies the variation of growth direction. Wire-like structures as in Fig. 2.8c, d can be grown at variable angles, and support-free printing of horizontal wires, plates and hollow geometries is possible (Fig. 2.8g – j, Michelangelo’s David in (j) is hollow). Additionally, overhangs of more than 90° have been demonstrated¹⁵⁴. In general, the feedback that signals completion of individual voxels ensures accurate reproduction of complex geometries (Fig. 2.8f – j).

Feature size. The enhanced geometric freedom comes at the cost of larger feature sizes compared to meniscus-confined electrodeposition. Because the metal ions are dispensed into the bath surrounding the pipette, the deposits are generally larger than the aperture size. The smallest deposits produced with a 300 nm FluidFM aperture have a diameter of ≈ 800 nm¹⁵⁴. Pillars fabricated with glass capillaries with openings of 30 – 50 nm have diameters of 400 – 600 nm¹⁵⁵. In both cases, the structures are typically slightly broader at their base. Additionally, the surface of printed features can be rough (Fig. 2.8f), possibly due to the unwanted deposition of diffusing ions onto previously printed structures.

Speed. Analogous to the meniscus-confined approach, the speed is limited by the electroplating rate. Thus, it is a function of the applied overpotential and the mass transport conditions. With typical parameters, the hollow David statue shown in Fig. 2.8j is printed over night. The z increment between each layer, *i.e.*, the voxel height, is usually 250 nm for FluidFM. Such voxels can be deposited in approximately 0.5 s; however, the growth speed depends on process conditions, such as the aperture size, liquid flow, and ion concentration¹⁵⁴. Typical growth speeds of metal structures deposited with the SICM system are in the range of 20 – 100 nm s⁻¹¹⁵⁵. Exaddon, the company that offers a commercial system based on the FluidFM concept (CERES), claims highest growth rates of $\approx 3 \mu\text{m s}^{-1}$ without relating it to a feature size¹⁵⁶.

Microstructure. A FIB cross-section of a FluidFM Cu deposit is shown in Fig. 2.8h. While some pores can be observed, the obtained microstructure is dense and polycrystalline with grain sizes of $\approx 10 - 100$ nm. Energy-dispersive X-ray spectroscopy confirmed the purely metallic nature of the as-deposited structures¹⁵⁴.

Materials. So far, the technique has only been used for the 3D deposition of Cu^{154,155}. However, Pt and a Cu-Ni alloy were 2D-patterned using regular glass pipettes on a larger scale by Whitaker *et al.*¹⁵⁹.

2.2.7 Laser-induced photoreduction

Laser irradiation of photosensitive metal salt solutions can initiate local photochemical reduction. Moving the focal point or the substrate in three dimensions enables the creation of 3D metal structures.

Principle. The method relies on simple aqueous¹⁶⁰ or non-aqueous¹⁶¹ metal salt solutions of AgNO_3 or AuHCl_4 , often containing additional photosensitizing dyes and sacrificial donors¹⁶²⁻¹⁶⁶. The confinement of the photoreduction to the focal spot is a prerequisite for 3D deposition. Hence, two-photon absorption (TPA) processes are typically exploited because they require a high photon flux which is available in the focal spot only¹⁶⁴. The electrons required for photoreduction are usually excited in the dye molecules and subsequently transferred to the metal ions. The reduction of ions to their zero-valence state initiates the nucleation and growth of metallic crystallites in solution or on a nearby surface (Fig. 2.9a). After electron transfer, the neutral state of the dye is restored by the sacrificial donor^{164,165}.

Setup. The high photon flux required for TPA necessitates the use of mode-locked femtosecond lasers^{160,162,163,166,168,169}. An oil immersion objective focuses the laser onto the photosensitive solution confined by two glass cover slips. The focal point is translated by a combination of motor stages and galvanometer mirrors. The electrolyte can either be an aqueous solution of metal ions^{160,162,163} or a solid, polymeric electrolyte^{164,170,171}.

For the fabrication of fine features, the substrate must be transparent at the laser wavelength to avoid thermal photoreduction, as discussed below. Most studies were performed with planar glass substrates, but 2D deposition on PMMA¹⁶⁹ and non-planar SU8¹⁶⁶ have been shown.

Geometry. Laser-induced photoreduction offers a high geometric freedom for structure design. Overhanging structures are easily fabricated (Fig. 2.9d, g). A variant of photoreduction involves

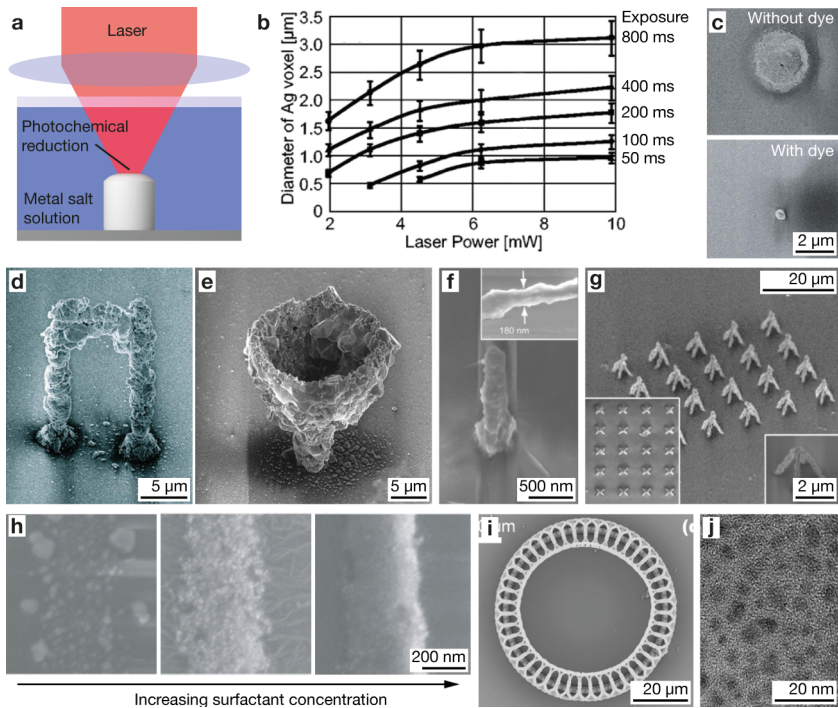


Figure 2.9 – Laser-induced photoreduction. **a**, Principle. A photosensitive metal salt solution is exposed to a pulsed femtosecond laser. Metal ions are photochemically reduced upon a two photon absorption process. Nucleation and growth either occurs in free solution, followed by particle aggregation, or at a nearby surface. **b**, The dimension of 1D Ag-deposits is a function of the laser-power and the exposure time: the lower the power or the exposure time, the smaller the diameter of individual dots¹⁶⁰. **c**, SEM micrographs of Ag dots reduced from a AgNO₃ solution without (top) and with (bottom) a photosensitizing dye. The addition of a photosensitizing dye avoids additional thermal reduction, thus increasing the confinement and control of the reaction¹⁶³. **d – g**, SEM micrographs of 3D Ag structures on glass substrates synthesized from **d**, a pure AgNO₃ solution¹⁶⁰, **e**, a solution of AgNO₃ and a photosensitizing dye¹⁶³, **f, g**, a solution of AgNO₃ and the surfactant n-decanoylsarcosine sodium (NDSS)¹⁶². Extensive growth of single nuclei causes a coarse surface morphology in solutions without surfactant. The use of the surfactant results in the deposition of smoother 3D structures. **h**, SEM micrographs of Ag lines deposited from a Ag(NH₃)₂⁺ electrolyte containing increasing concentrations of the surfactant NDSS¹⁶². The surfactant readily adsorbs to the synthesized metal nuclei and prevents their growth, resulting in a lower surface roughness. **i**, SEM-micrograph of a 3D Au-containing metal-polymer composite material fabricated by simultaneous two-photon polymerization and photoreduction¹⁶⁷. **j**, BF-TEM micrograph of an Au-containing polymer as synthesized in **i**. The Au nanoparticles are ≈5 nm in diameter and isolated from each other¹⁶⁷. **b – j**, Reprinted with permission from **b**, **d**,¹⁶⁰ ©2006 AIP Publishing; **c**, **e**,¹⁶³ ©2006 AIP Publishing; **f – h**,¹⁶² ©2009 John Wiley and Sons; **i, j**,¹⁶⁷ CC BY 4.0 (<https://creativecommons.org/licenses/by/4.0/>).

writing into solid polymers to create 3D-structured metal-polymer composites. Hu *et al.*¹⁶⁷ demonstrated the combination of two-photon polymerization and photoreduction for the sculpting of highly intricate Au-containing polymer-metal composites (Fig. 2.9i), and Kang and Vora *et al.* synthesized Ag particles at specified locations in gelatin¹⁷⁰ and PVP^{172,173}. However, due to the lack of connectivity of the particles, the structures collapsed when the matrix was dissolved. By adding pre-synthesized Ag nanoparticles to a Ag-ion-containing PMMA matrix, Stellacci *et al.*¹⁶⁴ were able to fabricate connected Ag structures.

Feature size. The dimensions of the deposits scale with the laser power and the exposure time (Fig. 2.9b)^{160,163}. At low laser intensities, the typical minimal feature size in systems without dyes is 1 μm ¹⁶⁰. At higher intensities, an additional thermal reduction deteriorates both the confinement of the deposition and the control of the process and should be avoided^{160,163}. Ishikawa *et al.*¹⁶³ showed that thermal reduction becomes the dominant mechanism at higher laser power, leading to coarse deposits.

Adding a photosensitizing dye enhances the confinement by preventing thermal reduction. First, the efficiency of photoreduction is increased and thus the laser power can be reduced. Second, the dye absorbs some of the radiation that would otherwise be absorbed by the deposit. The addition of a dye typically improves the minimal 1D feature size to a few hundred nanometers^{162,163}. For example, Fig. 2.9c shows the effect of coumarin 440 on the photoreduction of a AgNO_3 solution. The Ag dot deposited with 15 mW, the minimum laser power that still enabled photoreduction in a solution without a photosensitizing dye, is 3 μm in diameter. In contrast, the use of the dye decreased the required laser power to 2 mW and the spot diameter to 500 nm.

Even though the diameter of 1D deposits can be small, the surface of 3D deposits is comparably rough. 3D Ag structures grown both without and with the addition of a sensitizing dye each clearly show a coarse-grained morphology (Fig. 2.9d, e). This is attributed to an excessive growth of single crystallites. Cao *et al.*¹⁶² showed that the coarsening of the surface can be suppressed by the addition of surfactants that cover the surface of Ag particles immediately after nucleation, suppressing any further growth and forcing the generation of new nuclei. As shown in Fig. 2.9h, the homogeneity of 2D deposits increases with an increasing amount of surfactant. The surfactant also decreases the width of 3D fabricated wires to ≈ 200 nm and results in improved surface quality (Fig. 2.9f).

Speed. The maximum writing speed of 3D photoreduction is a few tens of $\mu\text{m s}^{-1}$. The cup in Fig. 2.9e was synthesized in 50 s¹⁶³, and the arch in Fig. 2.9d was produced using a scan speed of 24 $\mu\text{m s}^{-1}$ ¹⁶⁰. 2D deposition experiments have shown that the addition of pre-synthesized metal nanoparticles can increase the reaction rate by overcoming material transport limitations and

facilitating nucleation¹⁶⁹. Writing speeds for the synthesis of nanoparticles contained in a polymer matrix (Fig. 2.9i, j) can be up to $5000 \mu\text{m s}^{-1}$ ¹⁶⁷.

Microstructure. The deposits usually consist of coarse, metallic crystallites (Fig. 2.9d, e)¹⁶⁰. However, the nucleation of metallic particles in solution and their subsequent growth, aggregation and possible further growth provide a way to manipulate the microstructure of the deposited metal. The addition of surfactants and the associated suppression of the grain growth result in structures that resemble an agglomerate of nanoparticles (Fig. 2.9h). The metallic nature of the as-deposited structures is confirmed by a resistivity of the Ag structures that is only 3 times higher than the bulk value¹⁶⁰. The conductivity is slightly worse if the deposits consist of particle agglomerates¹⁶⁸.

Materials. Studies of photoreduction have concentrated almost exclusively on the deposition of Ag structures^{160,162,163,166,169,170}. Additionally, reports of 2D and 3D deposition of Au^{164,168} and Cu¹⁶⁴ exist. The simultaneous deposition of metallic and polymeric structures in one system¹⁷⁴ or metal-polymer composites^{167,175} is also possible (Fig. 2.9i, j).

Applications. Recently, Focsan *et al.*¹⁷⁶ fabricated 3D Ag objects in a microfluidic channel to study their potential for volumetric surface-enhanced Raman scattering. They found that the efficiency of detecting a probe molecule is higher for $5 \mu\text{m}$ cubes than for $10 \mu\text{m}$ pillars with a diameter of $2 \mu\text{m}$. The AM approach allows for facile variation of the object geometry to study such effects. In another demonstration, Xu *et al.*¹⁶⁶ fabricated a 2D micro-heater inside a microfluidic channel.

2.2.8 Focused electron/ion beam induced deposition

Focused electron and ion beams have been widely applied for deposition and machining processes for years. For a detailed discussion of the theory and the manifold applications of ion and electron beams, we recommend the review article by Utke *et al.*⁷³ or the book by Utke, Moshkalev and Russel¹⁷⁷. We intend to limit this section to the focused electron/ion beam induced deposition (FEBID and FIBID) of metals. Many similar concepts and problems apply for both FEBID and FIBID. Generally, FIBID offers a higher yield but introduces irradiation damage and Ga^+ contamination, while FEBID delivers deposits of lower metal content but largely avoids damage and contamination by the beam species.

Principle. Deposition with an ion or electron beam requires the beam-induced dissociation of suitable precursor molecules (Fig. 2.10a). These molecules are usually supplied in the gas-phase and adsorb, desorb and diffuse on the substrate surface. It is important to note that the interaction of the beam with the precursor molecules happens mainly in an indirect way. The impingement of the high-energy beam on the substrate generates low-energy secondary electrons, which subsequently

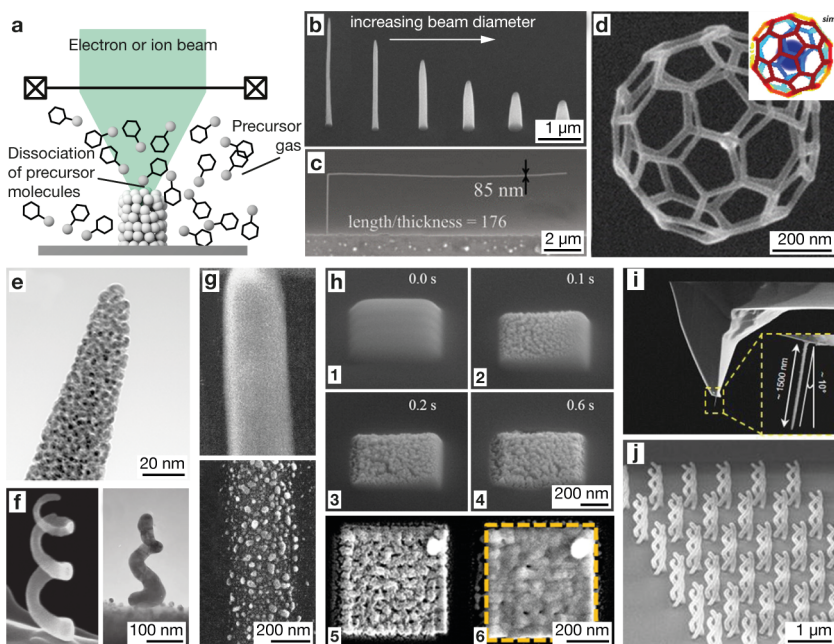


Figure 2.10 – Focused electron/ion beam induced deposition (FEBID and FIBID). **a**, Principle. A focused electron or ion beam interacts with the substrate and adsorbed precursor molecules. As a result, the precursor dissociates into metallic and organic products. The resulting nonvolatile dissociation products form the deposit, while volatile fragments ideally desorb. **b**, SEM micrograph of Pt rods deposited with different beam diameters¹⁷⁸. Increasing the size of the focus increases the width of the deposits. **c**, SEM micrograph of a horizontal DLC wire grown in free space with real-time feedback. Monitoring the SE-current enables the maintaining of a stable growth angle¹⁷⁹. **d**, SEM micrograph of a Pt icosahedron fabricated with simulation-guided FEBID. Inset: the simulation anticipates beam-deposit interactions as well as locally varying precursor concentrations and guides the beam accordingly to compensate for such effects¹⁸⁰. **e**, TEM micrograph of a Pt-containing deposit ($C_9H_{16}Pt$)¹⁷⁸. Typically, FEBID and FIBID deposits are not purely metallic but consist of metal nanoparticles embedded in a carbonaceous matrix. **f**, Au helix deposited using a $Me_2Au(acac)$ precursor before (SEM, left) and after annealing at 175 °C in ozone/water atmosphere (TEM, right) After annealing, the microstructure is polycrystalline and free of organic residues. However, a shrinkage due to volume loss and an imperfect shape retention are obvious. **g**, SEM micrographs of 2D FEBID deposits synthesized from a standard organometallic precursor $Me_2Au(tfa)$ (top) and a carbon-free precursor PF_3AuCl (bottom)¹⁸¹. Whereas the deposit from $Me_2Au(tfa)$ contains only 15 at.% Au embedded in an organic matrix, the deposit from PF_3AuCl is made of pure Au crystallites. **h**, *In-situ* annealing to improve shape retention. SEM micrographs of a FEBID-made Pt-structure (PtC_5): **1**, As-deposited; **2 – 5**, After laser-induced photothermal annealing with residual H_2O for various exposure times; **6**, After a laser induced smoothing cycle to coalesce the Pt grains¹⁸². **i**, **j**, Applications: **i**, Fe nanowire grown by FEBID onto the tip of commercial AFM probe to render a high-aspect-ratio MFM probe⁵¹. **j**, An optical metamaterial formed by an array of 6×6 helix assemblies, each made of three intertwined Pt helices¹⁸³. **b – j**, Reprinted with permission from **b**, **e**,¹⁷⁸ ©2008 IOP Publishing; **c**,¹⁷⁹ ©2013 AIP Publishing; **d**,¹⁸⁰ ©2016 ACS; **f**,¹⁸⁴ ©2011 John Wiley and Sons; **g**,¹⁸¹ ©2000 AIP Publishing; **h**,¹⁸² ©2015 ACS; **i**,⁵¹ ©2014 ACS; **j**,¹⁸³ ©2016 Springer Nature.

dissociate the precursor molecules. The resulting non-volatile dissociation products, typically a mixture of organic and metallic materials, form the solid deposit, whereas the volatile fragments leave the surface.

Setup. FEBID systems are based on a scanning electron microscope (SEM) equipped with a gas injection system (GIS) to supply the precursor gas. Most contemporary systems feature only a single-electron beam; however, machines with multiple beams are in development^{55,185,186}. Standard FIBID machines are dual beam setups, combining an SEM with an FIB column that usually contains a liquid gallium source. Thus, an electron beam for imaging and a Ga⁺-ion beam for deposition are available simultaneously.

The choice of the precursor is crucial for the success of FEBID and FIBID – its chemical nature and dissociation behavior determine the composition of the deposit. A high precursor stability, complete and efficient dissociation upon irradiation, and a facile desorption of non-metallic products are desired, but hardly achieved in combination. The most widely used precursors are metal carbonyls, organometallic compounds and acetylacetonates⁷³. The first category yields relatively pure deposits (>50 at.%)^{187,188}, but the metal carbonyls are toxic. Organometallic compounds are less problematic, but they result in the poorest metal content for all precursors (10 – 25 at.%)⁷³, whereas acetylacetonates, widely used for conventional CVD processes, have intermediate results^{189,190}. The highest purity deposits are synthesized from metal halides¹⁹¹, but these gases are both toxic and corrosive.

For feedback, dual-beam machines allow the optical observation of the FIBID process in real time. Additionally, monitoring of the SE current can be used to anticipate and actively control the growth angle of the deposit (Fig. 2.10c)^{179,192–194}. Recently, simulations of the deposition process have been proven a powerful approach for the exact fabrication of complex 3D structures^{180,195,196}.

FEBID and FIBID can be performed on metallic¹⁸⁴ and semiconducting^{197,198} substrates. To avoid charging under irradiation, some electrical conductivity of the substrate is recommended, even though the deposition on insulators such as polycarbonate has been demonstrated as well¹⁹⁹. FEBID and FIBID can be applied to any type of substrate geometry. For example, the customization of pre-fabricated AFM tips is routinely performed by these methods^{51,200}.

Geometry. FEBID and FIBID enable the processing of almost arbitrary geometries, and a range of intricate designs has been demonstrated (Fig. 2.10d)^{49,180,193,195,196,201,202}. Originally, most of the complex geometries have been realized with precursors for diamond-like carbon, for instance emitters complete with a tip and an anode cage²⁰³, horizontal ladders in free space²⁰⁴ and even movable rotors²⁰⁵.

It should be noted that the fabrication of such complex structures is not straightforward; the growth process needs to be carefully controlled or simulated since both the growth rate²⁰⁶ and the growth angle²⁰⁷ are functions of the growth direction relative to the gas-flow. Additionally, electron range effects often result in unwanted proximal deposition²⁰⁸. Guo *et al.*¹⁷⁹ demonstrated a real-time growth feedback for stable deposition of overhanging features (Fig. 2.10c). Fowlkes and Winter *et al.*^{180,195,196} demonstrated that a simulation of the electron-solid interaction and the temporal and spatial distribution of adsorbed precursor molecules can successfully predict the growth of FEBID structures. Hence, dwell-times and coordinates of the beam can be calculated prior to the experiment to fabricate the desired shape precisely. Fig. 2.10d shows a deposited Pt icosahedron deposited with simulation guidance and the geometry predicted by the simulation.

Feature size. The typical minimum feature size of FEBID and FIBID is a few tens of nanometers and is partially a function of the beam diameter. Wider structures can be fabricated by deliberate broadening of the beam (Fig. 2.10b)¹⁷⁸. Thinner deposits however are challenging to synthesize. Even though beam diameters of a modern instrument are 1 – 10 nm for FEBID and 10 nm for FIBID⁷³, the minimum feature size is fundamentally limited by the width of the interaction volume of the primary beam with the substrate, which is several times larger than the beam focus itself^{208,209}.

The interaction volume can be reduced by using a substrate considerably thinner than the beam penetration depth or by writing into free space. In these cases, the interaction volume is limited by the volume of the structure itself and can become as small as the beam diameter. Van Dorp *et al.*²¹⁰ managed to deposit W dots and lines of 0.7 and 2 nm widths, respectively, on a 30 nm-thin SiN membrane in a transmission electron microscope (TEM). Shimojo *et al.*²⁰² also fabricated horizontal, freestanding W wires with a diameter of 8 nm in a TEM. Under such free-space writing conditions, the obtained wire diameter is often a function of the scanning speed²⁰².

Speed. FEBID of metals typically achieves growth rates of tens of nm s^{-1} ^{181,192,193,202}. FIBID of DLC can be performed at speeds of up to 200 nm s^{-1} ^{179,204}. The growth rate of FEBID and FIBID is proportional to the dissociation rate of the adsorbed precursor molecules, which in turn is a function of the surface density of both the molecules and the electrons or ions. The concentration of adsorbed molecules can be increased by an enhanced precursor flux, that is, by using high-speed gas jets^{211,212}, whereas the density of electrons or ions can be controlled by the beam current. Nonetheless, the most effective way to increase the population of precursor molecules is to change from gaseous to liquid precursors (cryo-FEBID, see below).

Microstructure. As a consequence of the non-ideal precursors currently available, FEBID and FIBID-fabricated metal structures are generally contaminated with organic material. Some deposits can contain as little as 10 – 20 at.% metal^{190,213,214}. The high carbon content is reflected in the inferior elastic²¹⁵ as well as electrical²¹⁶ properties of the as-deposited structures. In addition, FIBID systems often introduce Ga⁺ into the deposit²⁰⁴, which may be unfavorable for Ga-sensitive materials such as aluminum²¹⁷. The TEM bright-field image in Fig. 2.10e shows a representative microstructure for FEBID and FIBID deposits. The deposit was synthesized from a C₉H₁₆Pt precursor and consists of crystalline Pt nanoparticles embedded in an amorphous, organic matrix¹⁷⁸.

The precursor has a pronounced influence on the microstructure. For example, pure Au crystallites can be synthesized from the carbon-free but unstable and rarely used precursor Au-trifluorophosphine-chloride (AuClPF₃, Fig. 2.10g, bottom)^{181,218}. In contrast, the deposit from an organic precursor, dimethyl-Au(III)-trifluoro-acetylacetonate (Me₂Au(tfa)), contains only 15 at.% Au and displays a smooth contrast typical of the organic matrix (Fig. 2.10g, top)¹⁸¹.

Post-deposition purification procedures, *e.g.*, thermal annealing in an oxidizing atmosphere^{184,214,219}, vacuum²²⁰ or air²²¹, electron-beam assisted annealing^{178,222,223}, laser annealing in oxygen¹⁸², and plasma treatment²²⁴ have been extensively studied, and were thoroughly reviewed by Botman *et al.*²¹⁶. An example of thermal annealing is presented in Fig. 2.10f, showing a Au helix before (left) and after annealing for 3 h at 175 °C in an oxidative ozone/water atmosphere¹⁸⁴. While the as-deposited structure contains approximately 30 at.% Au, the purified deposit is composed of polycrystalline Au without residual carbon. However, severe shrinkage and deformation have to be accepted. For example, the third pitch of the helix in Fig. 2.10f is completely lost. To improve the shape preservation, intermittent *in-situ* annealing during the deposition process was proposed^{182,225}. Stanford *et al.*¹⁸² cycled between FEBID and pulsed laser reactive gas anneals to obtain relatively dense, pure deposits of Pt (Fig. 2.10h). However, the intermittent purification steps are time-consuming and not regularly performed because they usually require the use of reactive gases and hence a change in the chamber pressure.

Materials. Precursors for a wide range of metallic, organic and semiconducting materials are available. Here, we reproduce an updated list of all elements that can be deposited by FEBID, as originally composed by Botman *et al.*²¹⁶. The maximum metal content achieved without post-processing is given in brackets: Al (claimed to be pure, but no quantitative analysis), Au (100 at.%), C (100), Co (100)²²⁶, Cr (claimed to be pure), Cu (60), Fe (100), Ga (50), Ge (100), Ir (33), Mn (n/a), Mo (10), Ni (36), Os (n/a), Pb (n/a), Pd (>50), Pt (83), Rh (66), Ru (n/a), Si (100), Sn (58),

Ti (35) and W (95)²¹². The synthesis of binary systems such as Pt-Si²²⁷, Co-Si²²⁸, Co-Pt²²⁹ and Fe-Si²³⁰ is possible when separate GISs are available for each precursor.

Applications. Both FEBID and FIBID are regularly employed in research, and a multitude of applications have been demonstrated. A limited selection includes: customized magnetic force microscopy tips (Fig. 2.10i)⁵¹, optical metamaterials¹⁸³ (Fig. 2.10j), photonic crystals²³¹, scanning probe single electron transistors²³² and nanoscale electron sources²³³.

Cryo-FEBID. Cryo-FEBID is a variant of FEBID that enables enhanced deposition speeds at the cost of minimal feature size and geometrical flexibility^{234–236}. The high growth rates are enabled by a marked increase in the precursor density due to the condensation of the gaseous precursor on the cooled substrate (Fig. 2.11a). The $22 \times 25 \mu\text{m}^2$ wide Pt square in Fig. 2.11b was deposited in just 30 s using cryo-FEBID, whereas a shape the size of the red square in Fig. 2.11b took 5 min using room temperature (RT)-FEBID and identical beam parameters. Bresin *et al.*²³⁵ measured a volumetric growth rate of $10^{10} \text{ nm}^3 \text{ s}^{-1}$ for cryo-FEBID, which is four orders of magnitude higher than the growth rate for RT-FEBID at comparable current densities. However, since cryo-FEBID is not a continuous process, the time to grow a precursor layer should be considered when estimating a practical 3D growth rate. A typical growth rate for the condensate is $10 - 70 \text{ nm s}^{-1}$ ²³⁵.

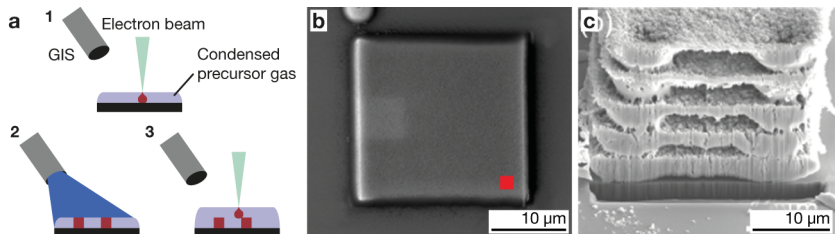


Figure 2.11 – cryo-FEBID. **a**, Principle of Cryo-FEBID. **1**, The precursor gas condensates on the cooled substrate and forms a liquid precursor layer. Upon e-beam exposure, precursor molecules are dissociated across the entire interaction volume of the e-beam. **2, 3**, A 3D structure is built by repeated cycles of precursor condensation and e-beam exposure. **b**, SEM micrograph of a Pt square fabricated with cryo-FEBID in 30 s²³⁵. The red square marks the area that can be deposited with conventional FEBID with the same beam parameters in 5 min. Due to the significantly higher precursor density, cryo-FEBID offers much higher volume growth rates at the cost of lower resolution. **c**, 3D Pt structure fabricated with cryo-FEBID in five consecutive condensation-exposure-cycles²³⁵. **b, c**, Reprinted with permission from²³⁵ ©2013 IOP Publishing.

The electron interaction with a liquid precursor is much stronger than the interaction with a gaseous precursor. Consequently, the dissociation of precursor molecules occurs in the whole interaction volume of the beam with the liquid layer and not exclusively on the substrate (as opposed to RT-FEBID). Therefore, cryo-FEBID requires a special 3D fabrication procedure (Fig. 2.11a). First, a

liquid layer of precursor molecules, several micrometers in thickness, condensates on the substrate. Second, the e-beam exposure forms a metal-carbon composite in the precursor film. This can occur across the whole film or only in the upper portion of the layer, depending on the layer thickness and the beam energy. Finally, a subsequent precursor coating is applied and e-beam writing is continued in this layer. The influence of the beam energy in cryo-FEBID is demonstrated in Fig. 2.11c which shows a stack of Pt squares fabricated in five cycles²³⁵. In each cycle, the middle part of the square was exposed with lower beam energy than the outer part. Furthermore, the beam energy used for the inner portion was decreased after each cycle. Because the penetration depth of the e-beam was thus diminished with each successive cycle, the gap in the middle of the layers increases from the bottom to the top.

2.2.9 The two most recent approaches to small-scale AM

Most of the standard methods for metal AM currently rely on the deposition or synthesis of metallic materials in air or vacuum. Nevertheless, the photoreduction of metal salts in polymers has shown the potential for high geometrical freedom and high spatial resolution of two-photon structuring in a host medium^{164,167,170,172–175} (Section 2.2.7). However, the photoinduced nucleation in a polymeric material usually led to disconnected metal particles and a collapse of the structures when the matrix was dissolved.

Now, two different concepts based on two-photon structuring in functionalized host media have been proposed that solve the issue of isolated particles by post-print shrinkage of the matrix. A first approach presented by Vyatskikh *et al.*⁹³ utilizes the shrinkage of a metal-loaded photoresist upon thermal pyrolysis. A second method, implosion fabrication introduced by Oran *et al.*⁹⁴, is based on the shrinkage of a hydrogel upon drying. The following sections will briefly introduce the two approaches. Yet, as only one paper per technique has been published so far, a detailed discussion is difficult and the two techniques are not treated in much detail in the general discussion.

2.2.9.1 Carbothermal reduction of organic-inorganic composites

Principle. The method is based on TPL for the fabrication of 3D structures from a metal-rich photoresist and the subsequent carbothermal reduction to obtain metal structures. A carbothermic reaction involves the reduction of substances, often metal oxides, using carbon as the reducing agent^{237,238}. The photosensitive resist used by Vyatskikh *et al.*⁹³ contained an acrylic resin, a photoinitiator and Ni acrylate as a metal precursor. 3D lithography of this resist renders a polymeric structure containing the metal precursor (Fig. 2.12a). Pyrolysis of the cross-linked geometries removes most organic materials and synthesizes metallic Ni. The volatilization of the organic matrix

results in an isotropic shrinkage of $\approx 80\%$. The method is different from previously introduced photoreduction techniques (section 2.2.7) as the reduction to elemental metal presumably occurs upon pyrolysis and not upon photoreduction.

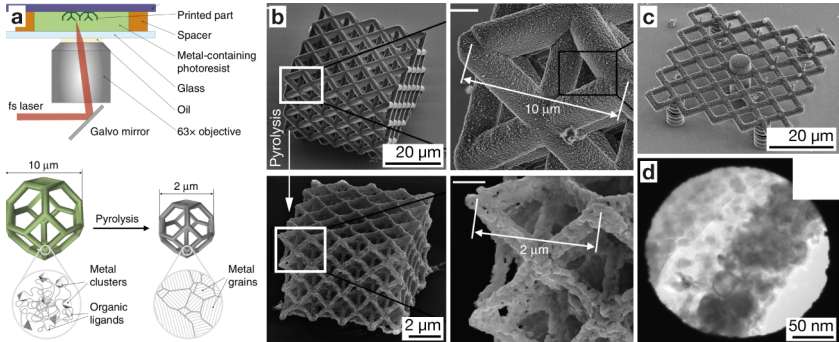


Figure 2.12 – Carbothermal reduction of organic-inorganic composites synthesized by TPL. **a**, Principle. A metal-containing photoresist (green) is patterned by TPL⁹³. Subsequent carbothermal pyrolysis of the scaffold removes most organic materials and results in the formation of metallic Ni. The volatilization of the organic matrix results in an isotropic shrinkage. **b**, SEM micrographs of a lattice before (top) and after pyrolysis (bottom)⁹³. After pyrolysis, the beams of the structure are made of crystalline Ni and feature a porosity of 10–30%. **c**, SEM micrograph of a support structure made from four springs (corners) and a pedestal (middle)⁹³. An isotropic shrinkage of $\approx 80\%$ necessitates the use of dilatible support structures that enable unconstrained shrinkage of the printed geometry. **d**, BF TEM micrograph of a Ni beam after pyrolysis⁹³. **a – d**, Reprinted from⁹³ under CC BY 4.0 (<https://creativecommons.org/licenses/by/4.0/>).

Setup. The developed resist is compatible with commercially available TPL systems. Vyatskikh *et al.*⁹³ used a Nanoscribe Photonic Professional GT system. Pyrolysis is performed in a tube furnace at 1000 °C for 1 h in inert atmosphere and at 600 °C under reducing atmosphere.

Geometry. As the approach relies on TPL for structuring, intricate 3D geometries such as the lattice structure shown in Fig. 2.12b are accessible. However, the excessive shrinkage upon pyrolysis demands the use of support structures that facilitate isotropic shrinkage of the geometries that are attached to the substrate. The lattice in Fig. 2.12b was supported by vertical springs at each corner and by a vertical pillar in the center (Fig. 2.12c).

Feature size. Beam diameters of 3D lattices are 300 – 400 nm in diameter after pyrolysis. Line widths of 100 nm were claimed for 2D structures.

Speed. As with all TPL approaches, writing speeds and thus the size of geometries printed are a key advantage. Typical features sizes of 300 – 600 nm are structured at scanning speeds of 4 – 6 mm s⁻¹, corresponding to 6700 – 20 000 voxel/s.

Microstructure. The fabricated Ni beams are nanocrystalline and nanoporous, with a 20 nm mean grain size and a porosity of 10 – 30 % (Fig. 2.12b). The TEM micrograph in Fig. 2.12d suggests a microstructure that is not fully coalesced, with multiple isolated nuclei. EDS analysis showed a chemical composition of 91.8 wt.% Ni, 5.0 wt.% O, and 3.2 wt.% C after pyrolysis. This corresponds to a metal content of 72.9 at.%.^a The metallic and crystalline microstructure with nanoscale feature size result in a strength of 6.9 – 18.2 MPa (corresponding to a specific strength of 2.1 – 7.2 MPa g⁻¹ cm³) and a stiffness of 47 – 174 MPa for lattices as the one in Fig. 2.12b.

Materials. The method has so far been demonstrated for Ni only⁹³. Due to the post-print pyrolysis step, the method is restricted to substrates that are compatible with temperatures ≥ 1000 °C.

2.2.9.2 Implosion Fabrication

Principle. Implosion fabrication (ImpFab) is based on 3D patterning of molecules with available reactive groups into an expanded (hydrated) hydrogel by two-photon excitation (Fig. 2.13a)⁹⁴. Subsequently, the reactive groups can be functionalized with a desired molecule or material, for example metal nanoparticles, by using an appropriate conjugation chemistry and by diffusing the respective molecules / particles into the wet gel. If metal particles are introduced into the gel, their volume can be increased after functionalization by electroless deposition in an intensification step. Dehydration of the functionalized gel shrinks the pattern by a factor of 10× or 20×. Sintering of the patterned particles after shrinkage results in connected tracks of metal. As the modular approach of ImpFab decouples the patterning and the functionalization steps, the specific physical properties of the molecules or nanoparticles used for functionalization do not affect the patterning.

Setup. Multiphoton patterning is compatible with any femtosecond IR laser setup. Oran *et al.*⁹⁴ used a confocal microscope with a femtosecond pulsed IR laser set to 780 nm. For patterning, fluoresceins with reactive sites suitable for the subsequent functionalization were utilized (Fig. 2.13a). The functionalization step is compatible with a wide variety of hydrophilic reagents. For metal patterning, the gel is incubated in a solution of 5-aminomethyl fluorescein prior to patterning. After binding the fluorescein to the gel, the pattern was stained with biotin-NHS and subsequently, fluoronanogold-streptavidin (Au nanoparticles 1.4 nm in diameter) was diffused into the gel. Intensification of the Au nanoparticles with Ag was performed using an electroless Ag plating solution

^aPer 100 g: $\frac{91.8 \text{ g}}{58.7 \text{ g mol}^{-1}} + \frac{5.0 \text{ g}}{16.0 \text{ g mol}^{-1}} + \frac{3.2 \text{ g}}{12.0 \text{ g mol}^{-1}} = 2.14 \text{ mol}$. Thus, the mol fraction of Ni is $\frac{91.8 \text{ g} / 58.7 \text{ g mol}^{-1}}{2.14 \text{ mol}} = 0.729$.

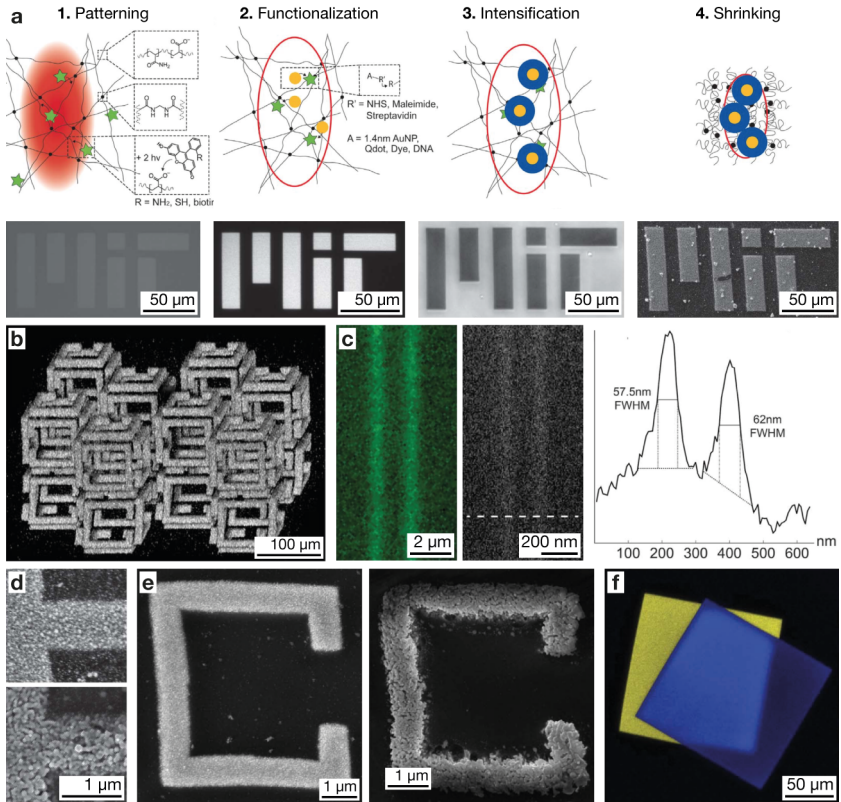


Figure 2.13 – Implosion fabrication. **a**, Principle. **1. Patterning:** upon two-photon excitation, fluorescein (green stars, with reactive groups R) binds covalently to a hydrated hydrogel (black lines and dots). Bottom: Optical micrograph of fluorescent pattern of fluorescein. **2. Functionalization:** the patterned gel is functionalized by attaching molecules, proteins, DNA or nanoparticles to reactive R groups. Bottom: Optical micrograph of fluorescent Au nanoparticle conjugates attached to the pattern in (2). **3. Intensification:** Ag is grown on top of Au nanoparticles within the hydrogel matrix. Bottom: Transmission optical micrograph of Ag deposited onto the pattern in (3). **4. Shrinking:** the hydrogel is shrunken and dehydrated to coalesce the pattern⁹⁴. **b**, Reflected light image of 3D Ag structures deposited within a gel (prior to shrinking)⁹⁴. **c**, Left: fluorescent image of two patterned lines of Au nanoparticles before shrinkage. Right: SEM micrograph of the Au lines after shrinkage. The corresponding intensity profile suggests a line width of ≈ 60 nm⁹⁴. **d**, Laser-sintering of Ag patterns deposited at the surface of a gel results in coalescence of particles and grain growth. SEM micrograph of shrunken Ag deposits before (top, non-conductive) and after laser sintering (bottom, electrically conductive). **e**, SEM micrograph of a 2D Ag structure (before and after sintering) fabricated at the surface of a gel. **f**, Due to the modular approach, nanoparticles of different material can be deposited in two subsequent patterning and deposition steps. Optical image of a gel patterned with Au nanoparticles (yellow) and CdTe quantum dots (blue)⁹⁴. **a – f**, Reprinted with permission from⁹⁴ ©2018 AAAS.

(light insensitive Ag solution). The shrinking step is usually performed by exposing the hydrated gel to hydrochloric acid. After shrinkage, the Ag patterns are sintered using the IR laser.

Geometry. As ImpFab patterns reactive groups into a host matrix using two-photon lithography, arbitrary 3D geometries are easily produced (Fig. 2.13b). Importantly, the decoupling of patterning and post-patterning functionalization avoids any interference of the materials to be attached to the pattern, for example the Au nanoparticles, with the patterning process itself. However, ImpFab is currently limited to 3D deposits within a gel or 2D deposits on the surface of a gel, and no freestanding geometries have been demonstrated.

Feature size. The minimal line width achieved with patterned Au nanoparticles after $10\times$ shrinkage is ≈ 60 nm, and the spatial resolution in X-Y direction seems to be better than ≈ 100 nm (Fig. 2.13c).

Speed. The reported setup operates at a scan-speed of 4 cm s^{-1} (post-shrink dimensions)⁹⁴. With typical lateral dimensions of $\approx 1\text{ }\mu\text{m}$ for conductive metal patterns (Fig. 2.13d, e), this corresponds to an in-plane speed of $40\,000\text{ pixel/s}$. A volumetric growth speed cannot be calculated as the height of the printed lines is unknown.

Microstructure. Shrunken metal patterns are not reproducibly conductive. Thus, it is to be assumed that the microstructure consists of still isolated Ag-coated Au nanoparticles. Upon laser-sintering, the particles coalesce and form a conductive path (Fig. 2.13d, e). However, the sintered metals are not fully dense (Fig. 2.13e).

Materials. Thanks to its modular synthesis approach, ImpFab can access a wide range of materials: small molecules, bio-molecules, semiconductor nanoparticles, and metal nanoparticles. Multi-material deposition is possible by repeated patterning and functionalization steps. Fig. 2.13f shows a pattern consisting of Au (yellow) and CdTe (blue) nanoparticles. Yet, ImpFab is limited to deposition into gels and does not allow for deposition into dense materials – a certain porosity is necessary to allow for diffusion of the reactants into the patterned volume. Further, the extensive shrinkage is incompatible with any solid substrate. Thus, ImpFab is limited to applications that require 3D structures within a polymeric matrix or that ask for a release of the synthesized structures into solution. Synthesis of 3D structures attached to a substrate seem to be inaccessible at the moment (although post-shrink transfer of 2D patterns can be imagined).

2.3 Discussion

In the previous section, we described the various methods that were proposed for metal AM at the micrometer scale. Since these methods rely on diverse physical and chemical mechanisms as well as fabrication setups, each technique has different capabilities, advantages, prerequisites and limitations. In this section, we provide a critical comparison of the techniques according to their **fabrication possibilities** (accessible geometries, feature size, speed), **range of materials** (deposit and substrate) and obtained **microstructure** and resulting materials properties. These major characteristics are compared in Fig. 2.14, while a comprehensive data collection with the respective references can be found in Table 2.1.

2.3.1 Fabrication capabilities

A main advantage of template-free metal AM techniques is the capability to fabricate truly three-dimensional metal structures that are otherwise difficult to obtain. Yet, similar to macroscopic AM, the geometrical capabilities are limited for most methods. Such constraints are imposed by the technical setup or by the underlying physico-chemical fabrication principle. Furthermore, large geometric freedom is to no purpose if the desired structures cannot be deposited with the desired dimensions in a reasonable time. Hence, the minimal feature size of the process and its speed are also important factors determining the potential of AM techniques.

2.3.1.1 Geometric flexibility

To evaluate the geometric freedom of each method, we compare the capability of the presented techniques to print a selection of basic 2.5D geometries that can be considered as the building blocks for more intricate 3D superstructures. These building blocks include a pillar, a wall, and overhangs at an angle of 45° and 90° relative to the z-axis (Fig. 2.14a). The pillar represents the capability to stack voxels and fabricate out-of-plane shapes beyond 2D, whereas the wall extends this capability to the X-Y direction and is the basic prerequisite for layer-by-layer fabrication. While these first two geometries are mere projections of 2D shapes, the fabrication of overhangs indicates the capability to fabricate truly 3D structures, such as coils. As a further indicator of geometric freedom, we list the capability of voxel-on-demand printing, *i.e.*, the ability to print individual, disconnected voxels in a non-continuous process. This is a requirement for the layer-by-layer fabrication of intricate and intertwined designs such as trusses.

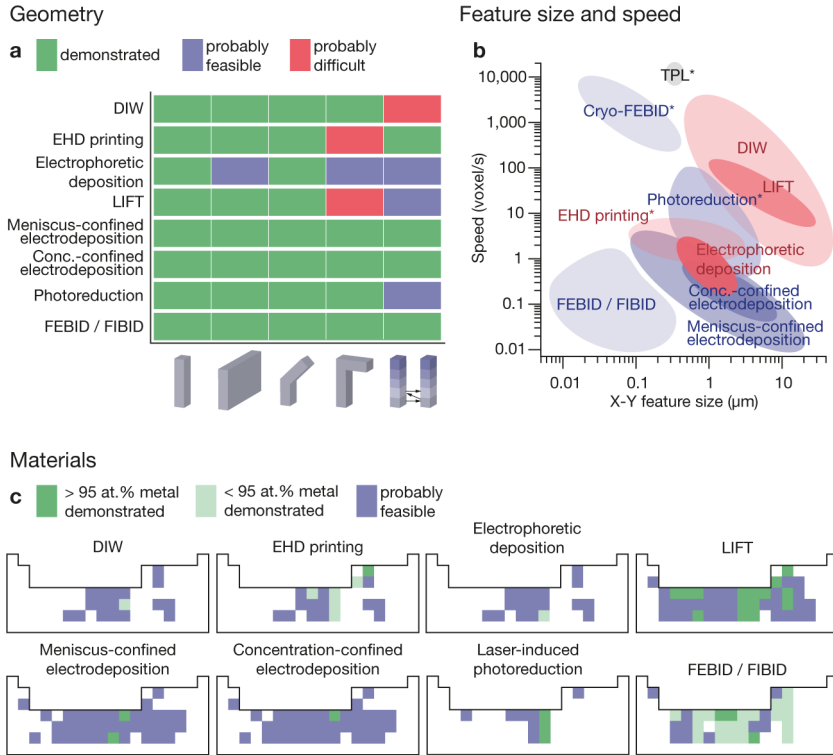


Figure 2.14 – Small-scale metal AM methods in comparison: fabrication capabilities. **a**, Graphic representation of the geometric freedom enabled by each technique. Green indicates that the respective basic building block has been demonstrated. Blue represents building blocks that are most likely feasible. Red signals that we assume the technique will hardly be able to fabricate the corresponding building block. **b**, Speed versus X-Y feature size of all techniques. The speed has been normalized by the voxel size. *: EHD printing: only 3D deposition speeds are considered. 2D speeds can be pronouncedly higher. Photoreduction: only deposition speeds in liquid solvents are represented. Cryo-FEBID: the time to form each precursor layer was included for calculation of the speed. TPL: TPL of metal-containing photoresists with subsequent pyrolysis. **c**, Schematized periodic tables showing the elements that have been deposited with the respective technique. Dark green squares represent pure deposits whereas light green squares indicate that the as-deposited materials were metal-organic composites. Blue squares denote elements we assume could be deposited with the technique. For labeled periodic tables, see Fig. B.1. References for feature size, speed and elements are given in Table 2.1.

Table 2.1 – Collection of published data on X-Y feature size, speed, deposited metals, employed substrates and annealing. Except for FEBID / FIBID and the list of elements for LIFT, the data is summarized for individual publications. If published, a range instead of a maximum value is given. Whether thermal annealing was performed or not is indicated by Y (yes) or N (no), respectively. Abbreviations: out-of-plane (oop), in-plane (ip), not available (n/a).

| | X-Y feature size (μm) | Speed ($\mu\text{m s}^{-1}$) | Metal | Annealing | Substrate | Year and Ref. |
|----------------------------|---|---|--|---|---|---|
| DIW | 0.6 – 20 2 – 30 | 500 – 2000 20 – 500 | Ag Ag | Y Y | Glass, PET, Si Au, glass, polyimide, Si | 2016 ⁹⁵ 2009 ¹² |
| EHD printing | 0.07 – 0.12 0.08 – 0.5 0.7 – 3 0.5 – 3 0.05 – 0.12 | 0.4 (oop) 1 – 10 (ip) 0.16 – 3.3 (oop) n/a n/a | Au Au, Au Ag, Co, Cu Au Au, Ag | Y Y Y Y Y | Al ₂ O ₃ , glass Glass, polyimide Au, glass, Si Cyclic olefin copolymer Silane on glass | 2016 ¹⁰⁵ 2016 ¹⁶ 2015 ¹⁰⁴ 2013 ¹¹¹ 2012 ⁹⁹ |
| LIFT | ≈4 – 10 12 5 – 7 6.5 7 – 40 3.6 – 4.4 4 – 6 1 n/a | repetition rate 1.5 Hz $7 \times 10^{-12} \text{ g s}^{-1}$ n/a n/a n/a n/a $3000 \mu\text{m}^3 \text{ s}^{-1}$ n/a n/a | Cu, Au Au, Pt Cu Cu, Cu-Ag Au, Cu Al Au, Cu Au Cu, Ag, V, Cr; Al, Au, Ni, Pd, Ti, Ge, Sn, W, Zn, Pt | N N N N N N N N n/a | Au-coated Si Au, thermocouple wires Epoxy glass laminate Epoxy glass laminate Al, Cu, polymers, ceramics Glass, paper, PET Cu Au, glass n/a | 2018 ¹²⁹ 2017 ⁵² 2016 ¹³⁵ 2015 ¹³⁰ 2015 ¹²⁷ 2015 ¹³³ 2015 ¹²⁶ 2010 ¹²⁵ Review ⁷⁰ |
| Laser decal transfer | 1 – 2 (2D only) 2.5 – 500 (2D only) 10 – 400 8 – 75 | Parallel transfer n/a Parallel transfer n/a | Ag Ag Ag Ag | N Y Y Y | PDMS Sapphire, Si Si Glass, polyimide, Si | 2019 ¹³⁹ 2015 ⁹⁶ 2013 ¹³⁸ 2010 ¹⁴ |
| Electrophoretic deposition | 0.5 – 2 | 0.3 – 0.67 | Au | N | ITO | 2014 ¹²² |

Table 2.1 continued.

| | X-Y feature size (μm) | Speed ($\mu\text{m s}^{-1}$) | Metal | Annealing | Substrate | Year and Ref. |
|--|------------------------------------|---|------------------------------|-----------|-----------|---------------------|
| Meniscus-confined electrodeposition | $\approx 0.2 - 25$ | $0.17 - 0.25$ | Cu | N | Au | 2019 ¹⁴⁷ |
| | $0.5 - 1$ | $0.015 - 0.25$ | Cu | N | Au | 2018 ¹⁵² |
| | $0.45 - 0.65$ | $0.1 - 0.2$ | Cu | N | n/a | 2017 ¹⁵⁰ |
| | $12 - 15$ | $0.18 - 0.4$ | Cu | N | Pt | 2015 ¹⁴⁴ |
| | $0.08 - 1.6$ | $0.25 - 0.35$ | Cu, Pt | N | Au | 2010 ¹³ |
| Concentration-confined electrodeposition | $0.15 - 0.5$ | $0.05 - 0.1$ | Pt | N | Pt-Ir | 2007 ¹⁴⁶ |
| | $0.2 - 0.95$ | 0.25 | Cu | N | Au | 2006 ¹⁴⁵ |
| | $0.4 - 0.8$ | $0.002 - 0.115$ | Cu | N | Au | 2016 ¹⁵⁵ |
| Laser-induced photoreduction | $0.8 - 5$ | $0.25 - 0.5$ | Cu | N | Au | 2016 ¹⁵⁴ |
| | 0.097 | 5000 | Au in PETA | N | Glass | 2017 ¹⁶⁷ |
| TPPL + carbothermal reduction | 2 | 50 | Ag in PSS | N | Glass | 2016 ¹⁷⁶ |
| | $0.18 - 1$ | $2.5 - 3$ | Ag | N | Glass | 2009 ¹⁶² |
| | $0.2 - 1.7$ | $1 - 100$ | Ag in PVVP | N | Glass | 2008 ¹⁷⁴ |
| | $0.4 - 5$ | $3.4 - 50$ | Ag | N | Glass | 2006 ¹⁶³ |
| | $0.5 - 3$ | 24 | Au, Ag | N | Glass | 2006 ¹⁶⁰ |
| | ≥ 0.5 | 25 | Ag in PVK, Au and Cu in PMMA | N | Glass | 2002 ¹⁶⁴ |
| | $0.3 - 0.4$ | $4000 - 6000$ | Ni | Y | Si | 2018 ⁹³ |
| Implulsion fabrication | 0.06 | 4 cm s^{-1} (post-shrink dimensions) | Ag and Au in hydrogel | Y | n/a | 2018 ⁹⁴ |

Table 2.1 continued.

| | X-Y feature size (μm) | Speed ($\mu\text{m s}^{-1}$) | Metal | Annealing | Substrate | Year and Ref. |
|---------------|---|---|------------------------------------|----------------------|---|--|
| FEBID / FIBID | ≈ 0.05 Lines (on bulk Si): $0.01 - 0.05$ $0.15 - 0.23$ $0.008 - 0.04$ (TEM) | $0.01 - 0.125$ n/a $0.2 - 0.9 \times 10^{-3} \mu\text{m}^3 \text{s}^{-1}$ $\approx 0.034 - 0.026 \mu\text{m s}^{-1}$ $0.0005 - 0.005$ | Pt, W, Au Co Pt W | N N N N | Si SiO ₂ /Si HOPG C, Si (membranes) n/a | 2018 ¹⁹⁶ 2014 ²²⁶ 2008 ¹⁷⁸ 2004 ²⁰² Review ^{73,177,216,239} |
| cryo-FEBID | $0.022 - 0.31$ | $10 \mu\text{m}^3 \text{s}^{-1}$ $\approx 100 - 400 \mu\text{m s}^{-1}$ | Pt | N | Si | 2013 ²³⁵ |

Figure 2.14a indicates whether a technique has already demonstrated the capability to deposit individual building blocks. Additionally, we try to anticipate whether each technique is capable of fabricating the missing building blocks.

Pillars, walls and moderate overhangs can be fabricated by all techniques. Walls or other bulky structures have not been demonstrated with **electrophoretic deposition**, but we do not see any principle limitation to it.

On the other hand, strongly overhanging features are generally difficult to obtain when using the droplet-based approaches **EHD printing** and **LIFT**. Moderate overhangs may be obtained by lateral translation while printing. Above a given angle however, the droplets, arriving normal to the substrate, will fly past the overhanging feature and impinge on the substrate below. Changing the jetting angle relative to the substrate could extend the overhang capabilities. Yet, this is hardly possible with the current configurations. For LIFT, the lateral extension of the carrier substrate and its short distance to the substrate prohibit such a solution. In EHD printing, changing the impact vector is not possible because droplets are guided by electric field lines that are always perpendicular to the substrate. Thus, the fabrication of sacrificial support materials, as has already been applied by LIFT^{130,131}, will be the easiest and most versatile approach for fabricating overhangs with both LIFT and EHD printing.

The ability to stack single voxels on demand has been demonstrated by EHD printing^{106,111}, LIFT¹³⁰, **meniscus**-¹⁴⁷ and **concentration-confined electrodeposition**¹⁵⁴ and **FEBID / FIBID**^{205,240}. In principle, electrophoretic deposition and **photoreduction** should have the same capability since the laser can be blanked on demand. In contrast, DIW is less suited for this task because it is based on the continuous deposition of ink filaments.

Overall, microscale metal AM can already access a substantial range of geometries. Among the techniques presented here, FIBID and FEBID as well as concentration-confined electrodeposition have been used for the fabrication of the most complex designs. Here, it is important to note that all complex geometries were printed with some sort of a geometrical feedback (mainly in the FluidFM system) or guided by simulations that predict growth instabilities (FEBID). This feedback is an essential factor for high fidelity printing. Laser-induced photoreduction and meniscus-confined electrodeposition demonstrated similar basic capabilities as FEBID and the FluidFM system, but do not offer a feedback and have shown less complex geometries only. The metal transfer methods EHD and LIFT are especially suited for creating 2.5D deposits while DIW excels in the fabrication of continuous wires and layer-by-layer grown geometries such as woodpile lattices.

Besides extending the range of accessible geometries, future efforts will also have to focus on increasing the accuracy of shape replication. Present techniques often generate crude geometries, sometimes with large surface roughness or unwanted proximal deposition. Additionally, annealing and resulting shrinkage are challenging for shape preservation. Simulation-guided fabrication will be beneficial to tackle these challenges, as already demonstrated for FEBID^{180,195,196}. For example, simulating the shrinkage upon annealing could result in as-deposited structures designed to compensate for the expected volume loss and geometrical distortion.

2.3.1.2 Feature size and speed

Both the minimal feature size and the speed are key aspects of AM techniques: On one hand, speed is the notorious drawback of any serial technique such as AM, and its improvement is usually a prerequisite to apply the technique in an economic way. On the other hand, the minimal feature size is an important characteristic of all (micro-)fabrication processes because it determines the geometrical accuracy of fabricated structures as well as their surface roughness. Furthermore, small dimensions are often a prerequisite for enabling novel applications; for example, optical metamaterials require geometric features that are considerably smaller than the targeted wavelengths.

The accessible feature sizes and the speed of each method are compared in Fig. 2.14b. The two quantities are mutually dependent: printing with smaller voxels often necessitates a tradeoff in the volumetric growth rate because a given geometry will consume more voxels. Thus, we normalize the velocity by the feature size. This leads to an estimation of the fabrication speed in units of voxels per time rather than absolute volume per time. The absolute volumetric rate can be obtained by multiplying the two axes. Thus the processes in the top right corner have the highest deposition rates.

Using voxel/s as a unit requires the definition of a voxel. First, LIFT and EHD printing are the only techniques that sequentially deposit discrete volumes; all other methods produce structures in a continuous fashion. Second, the aspect ratio of a single unit of deposit is different for each technique. To enable a comparison of the different processes, we define a single voxel as a cylinder with a diameter and height equal to the X-Y feature size of the respective technique.

Based on this assumption, we calculate the speed using the available data of growth rates as a function of feature sizes. Unfortunately, this data is sparse, therefore Fig. 2.14b should be regarded as a qualitative comparison. Please note that we used the geometric data of the as-deposited structures and that a possible inhomogeneous volumetric shrinkage due to thermal annealing is not considered. We also included the time required for the intermittent steps, i.e., the time to form each precursor layer in cryo-FEBID, into our growth speed calculations.

2.3.1.3 Feature size

The minimum feature sizes among the techniques range from single nanometers to tens of micrometers, with most techniques enabling a minimum lateral dimension of at least 1 μm (Fig. 2.14b). **FEBID and FIBID** are capable of fabricating the finest structures, with demonstrated feature sizes of only tens of nanometers. Ultimately, this value is limited by the focal spot, which can be smaller than 1 nm²⁴¹. In practice however, the resolution is dominated by the size of the interaction volume of the beam species with the substrate and by proximity effects at lower beam energies²⁰⁸. The ultimate FEBID resolution calculated for a zero-diameter electron beam of 20 kV and a thin target of 10 nm was 0.23 nm²⁰⁹. Effectively, 2D structures with resolutions of a few nanometers have been demonstrated on both thin²¹⁰ and bulky substrates²⁴². Nevertheless, the confinement decreases once the deposits grow thicker than a few monolayers due to scattering in the deposit itself^{208,209}. Because feature sizes close to the ultimate limit can already be achieved, no significant improvement can be expected from FEBID and FIBID.

A high-resolution method related to FEBID is the decomposition of the precursor molecules by the tunneling current of a scanning tunneling microscope (STM). This approach enables fabrication of features smaller than 10 nm even on bulky substrates^{243–247}. However, we found only one report of a high-aspect-ratio metal structure fabricated in an STM, a 9 nm-wide and 880 nm-high fiber made of crystalline bcc Fe²⁴⁴.

The majority of the other techniques is based on the use of micro- and nanometer sized capillaries. The resolution of **DIW, EHD printing, meniscus-confined electrodeposition, FluidFM and SICM** is determined in first approximation by the diameter of the capillary opening. Nozzle diameters smaller than 20 nm can be manufactured²⁴⁸; nevertheless, the resolution of all these techniques is in practice constrained by other limitations, as discussed hereafter.

DIW offers robust fabrication with filament diameters down to 1 μm . Since DIW is a nanoparticle-based technique, its resolution is ultimately limited by the size of available nanoparticles: the single particles should be significantly smaller than the structure they build. Additionally, the shear-thinning properties are based on the cumulative interaction of single particles in a nanoparticle network^{46,101}. Thus, a critical number of particles is required in each filament, restricting its minimal diameter. Typically used particles are ≈ 20 nm in size⁹⁹, but particles down to a few nanometers can be synthesized, which could enable a further increase of the resolution.

Similar to DIW, the smallest feature size of EHD printing has to be markedly larger than the transferred nanoparticles. However, using 3 – 7 nm particles, the minimal feature size of EHD printing comes second only to FEBID and FIBID: 80 nm-wide 3D and 35 nm-wide 1D features

were reported⁹⁹. An advantage of EHD printing is the fact that droplet sizes are typically much smaller than nozzle openings. For instance, 50 – 100 nm droplets can be ejected from a 1 μm nozzle¹⁰⁵. Hence, moderate pipette diameters can be used, minimizing the danger of clogging⁹⁹. Nevertheless, a further decrease in pipette diameter to increase the resolution will require further lowering of the ink concentration. This will eventually create a situation where some droplets do not contain any particles.

The **electrochemical deposition methods** achieve submicrometer resolution. Here, the meniscus-confined approach is advantageous since the only parameter affecting the size of the deposit is the meniscus diameter. In contrast, transport of metal ions into the supporting electrolyte impairs the confinement of FluidFM and SICM deposits. This is reflected in the demonstrated wire diameters fabricated with pipettes of similar size: ≈ 100 nm for meniscus-confined electrodeposition¹³ and 400 – 600 nm for SICM¹⁵⁵. Generally, the diameter of wires that can be grown with meniscus confinement is half the pipette diameter¹³, hence a minimum feature size in the 10 nm range can be envisioned. However, the control over ambient conditions to avoid clogging becomes more critical with smaller pipettes^{146,151}.

In concentration-confined electrodeposition, the feature size depends on the concentration profile of metal ions under the aperture. This profile is the result of a combined diffusional and hydrodynamic mass transport and can be minimized by smaller flow rates as well as smaller tip apertures. However, in the SICM-based method, even with apertures of 30 – 50 nm and no convective transport, the feature size is in the range of 400 – 600 nm¹⁵⁵. Hence, the X-Y dimensions of electroplating with nanopipettes in a liquid bath will probably not be able to exceed the feature size enabled by the meniscus-confined approach.

The remaining techniques that cope without pipettes are electrophoretic deposition, LIFT and local photoreduction. The resolution of **laser-assisted electrophoretic deposition** is not limited by the trap size, since trapping of single nanoparticles is possible as long as the solution is dilute enough²⁴⁹. The resolution will on the one hand be limited by thermal fluctuations that work against the trapping forces and thus limit the precision of placing a single particle²⁴⁹. On the other hand, a structure built by single particles must consist of a large enough number of particles in order to be well defined, which is a limitation that applies to all nanoparticle-based AM methods.

LIFT currently achieves a minimal feature size of ≈ 5 μm , which results from a combination of the droplet size and landing accuracy. The size of the ejected droplets can be reduced by using a lower laser fluence, but this entails unwanted side effects: first, the droplets tend to solidify in as spheres rather than disks because the ejection velocity is lower at low fluence¹²⁶. Second, the landing accuracy is reduced for a fluence near the ejection threshold¹²⁷. An alternative approach

to improve the feature size might be the patterning of single donor voxels on the carrier. This was demonstrated for square voxels of Ag pastes down to a side length of $2.5\ \mu\text{m}$ ⁹⁶ or circular droplets of $1 - 2\ \mu\text{m}$ in diameter¹³⁹. Overall, we estimate that 3D LIFT could reach minimal feature sizes in the range of $1\ \mu\text{m}$. Because smaller voxel sizes will impose stricter tolerances for the landing accuracy, operating the process at even smaller donor-substrate distances might become necessary.

In analogy to TPL, feature sizes below the diffraction limit should be accessible with **laser-induced photoreduction**. Depletion techniques have enabled the fabrication of features smaller than $100\ \text{nm}$ with TPL⁸⁰. Similar approaches might be applicable to the photoreduction of metal ions. However, in light of the fact that wire diameters of approximately $200\ \text{nm}$ have already been achieved by photoreduction¹⁶², a significant improvement cannot be expected. A focus on the decrease of unwanted surface roughness as well as thermal reduction due to absorbance of the laser by synthesized metal structures might be more important for this technique to be routinely applied. An alternative approach for decreasing the feature size of laser-written structures has been demonstrated by post-print shrinkage of exposed patterns^{93,94}.

2.3.1.4 Speed

Commercial TPL tools can fabricate polymeric structures that are millimeters in size with submicrometer features at a writing speed of $20\ \text{mm s}^{-1}$, corresponding to several $10^4\ \text{voxel/s}$ ⁴¹. Such deposition speeds are reached by TPL-based fabrication of metal structures (Photoreduction in polymers^{164,167,170,172-175}, TPL of metal-containing photoresists with subsequent pyrolysis⁹³, and ImpFab⁹⁴), but is currently out of reach for all other state-of-the-art micro metal AM techniques, although cryo-FEBID may reach maximum values that are only one order of magnitude smaller (but at a severely lower geometric precision). This raises the question of why the metal AM techniques have such limited speeds and whether any of the processes can be accelerated substantially.

Two concepts to increase the throughput of AM techniques are usually suggested: higher rate of deposition or parallelization of the writing. Parallelization is a promising solution for upscaling but still at its dawn. Parallel 2D deposition was demonstrated with multi beam FEBID⁵⁵, with a multi-nozzle printhead for EHD-printing⁵⁴, with patterned donor layers for LIFT of inks¹³⁹ and dip-pen nanolithography²⁵⁰, a technique that is not suited for 3D fabrication yet. Demonstrations in 3D are rare, but recently Lin *et al.*¹⁴⁷ successfully deposited an array of ten Cu pillars with a multi-nozzle printhead using meniscus-confined electrodeposition (Fig. 2.7g). Additionally, beam-shaping in decal transfer should be considered parallel deposition, as complete layers can be transferred at once¹³⁸. Yet, the following discussion focuses on increasing the deposition rate of individual voxels only, as parallelization is merely a technical challenge.

Transfer techniques that rely on forced mass transport (DIW, EHD printing and LIFT) are generally about one order of magnitude faster than *in-situ* techniques (Fig. 2.14b). For **DIW**, the extrusion rate determines the translation speed of the printing process. When aiming for faster extrusion, the ink rheology is a critical factor that has to be considered. Viscoelastic fluids require a finite amount of time to arrive at equilibrium viscosity after a change in the shear rate. As described by Lewis and coworkers, this time span is ≈ 1 s⁴⁶. During this period, the extruded filament is partially fluid and hence unstable, although it is supported by the more solid core. On the one hand, ink instabilities during high-speed extrusion may become an issue especially for thin filaments because the required equilibration time increases with higher shear stresses²⁵¹ and the fraction of the solid core decreases with smaller filament diameters. On the other hand, laser-DIW might render these thoughts obsolete. At speeds of 1 mm s^{-1} , the laser is typically placed $100 \mu\text{m}$ after the nozzle, but it can be moved closer to the nozzle if the printing speed is increased⁹⁵. Thereby, an unstable filament would have to bridge a distance of only a few tens of micrometers between the nozzle and the annealed part of the deposited structure.

High-resolution 3D **EHD printing** is limited to the dripping mode^{99,104}, where the deposition rate is proportional to the ejection frequency. Although droplet ejection can be sustained at up to 100 kHz ⁹⁹, in-plane EHD printing typically operates at $0.1 - 10 \text{ kHz}$, which corresponds to growth rates of $2 - 5 \mu\text{m s}^{-1}$ or $\approx 10 - 50 \text{ voxel/s}$ ^{16,115}. For out-of-plane printing, complete evaporation of the residual solvent must occur between single droplet impacts. Galliker *et al.*⁹⁹ estimated a time of approximately 0.2 ms for the evaporation of a 100 nm solvent droplet. This would impose a limiting frequency of 5 kHz for 3D fabrication, which is comparable to above-mentioned in-plane ejection frequencies. To enable higher deposition rates, substrate heating could be applied to increase the solvent evaporation rate¹⁰⁶. In contrast to out-of-plane deposition, in-plane printing of layer-by-layer structures should be feasible at higher frequencies; because sequential droplets will not land at the same location, more time is available for proper solvent evaporation. Additionally, the growth rate is directly proportional to the particle loading of the ink. To avoid clogging of the nozzle, typical inks are diluted to $0.1 - 5 \text{ wt.}\%$ ^{16,99,104}. Nevertheless, ink loadings of up to $15 \text{ wt.}\%$ for capillary diameters of $\approx 1 \mu\text{m}$ have been demonstrated¹⁰⁴. Thus, a combination of more concentrated inks and higher ejection frequencies, possibly accompanied by a means of enhancing the solvent evaporation rates, could further increase the volumetric growth rate of EHD printing.

Analogous to EHD printing, **LIFT** builds 3D structures by the ejection of discrete volumes of material, and similarly, the ejection frequency is the main lever for improving the growth speed. In setups with static lasers, the ejection frequency is currently limited by the maximum translation velocity of the donor¹²⁶. Therefore, alternative setups with a translating laser spot and carriers have been introduced^{130,133}. Zenou and coworkers reasoned that current laser technology, *i.e.* high

repetition rate fiber lasers operating at 100 – 1000 kHz repetition rates, could permit a throughput on the order of $10^7 \mu\text{m}^3 \text{s}^{-1}$ ¹³⁰. This corresponds to $\approx 8 \times 10^4$ voxel/s for a feature size of 5 μm , which is two orders of magnitude higher than current deposition rates.

Although **electrophoretic deposition** is a metal transfer technique, its transport limitations resemble those of *in-situ* techniques discussed below. We assume that the growth rate is dominated by the mass transport of nanoparticles into the focal spot of the trapping laser. In optical trapping, the transport to the focal spot is assisted by the radiation pressure that pushes the particles down the optical axis, but these forces are usually kept at a minimum by a strongly diverging beam²⁵². Thus, the main methods of speeding up the deposition are similar to those used for *in-situ* deposition: an increase in concentration and an increase in convection. The Iwata group used suspensions with a solid loading of up to 0.3 wt.%¹²². If a significant increase in particle concentration were to be sustained, the absorption and scattering of the laser by the particles would have to be considered. For example, both the absorption and Rayleigh scattering of Au solutions are significant at the employed wavelength of 500 nm and below^{253,254}. Enhanced mass transport could be envisioned by deposition in a flow cell as long as the hydrodynamic forces acting on the nanoparticles do not surpass the trapping force²⁵⁵.

For the *in-situ* techniques, mass transport is probably the primary limitation of the growth speed. So far, means to increase mass transport have only been successfully explored for **FEBID**. Even without considering the extreme case of cryo-FEBID, the use of gas jets has led to a tenfold increase in the growth rate of conventional FEBID²¹¹. The fact that laser-induced photoreduction performs surprisingly fast indicates the possible enhancement of mass transport by temperature effects which has previously been observed in laser-enhanced electroplating²⁵⁶.

Under typical conditions, **electrodeposition** rates are capped by the mass transport limited current, which is a function of diffusion, migration and convection of the ionic species²⁵⁷. Diffusion could be enhanced by deposition at higher temperature. Yet, the influence of temperature on the growth rate is marginal compared to the amount of enhancement required^b. The limiting current is also directly proportional to the concentration of the electrolyte²⁶². Since concentrations used for metal AM are sometimes far below the solubility limit, one can expect to enhance the growth rates in these cases by approximately one to two orders of magnitude by simply increasing the

^bThe limiting current j_L is directly proportional to $D^{1/2}$, whereas the diffusion coefficient D is a function of temperature. Upon a temperature increase from 25 to 65 °C, D of cupric ions in concentrated solutions was measured to increase from approx. $6 \times 10^{-6} \text{ cm}^2 \text{ s}^{-1}$ ^{258,259} to $12 \times 10^{-6} \text{ cm}^2 \text{ s}^{-1}$ ²⁶⁰. Such an enhanced diffusivity would not even double j_L . Gladysz *et al.*²⁶¹ have measured an increase of the diffusional current at a microelectrode in commercial Cu electrolytes by a factor of ≈ 2 for temperatures of 60 °C compared to 25 °C, taking into account other temperature effects such as amplified charge-transfer rates and activity of additives.

concentration of metallic salts^c. However, specific limitations may apply, such as the clogging risk of micropipettes or a minimum transparency of the electrolyte in photoreduction. Yet, the most efficient measure to increase electroplating rates is enhanced convection. Forced convection reduces the diffusion layer thickness, which in turn increases the limiting current²⁶³. Concepts for boosting the deposition rates in conventional electroplating are stirring²⁶³, ultrasonic fields²⁶⁴, liquid jets²⁶⁵, laser-induced convection²⁵⁶ or combinations of these methods²⁶⁶. Liquid jets and laser-induced convection were shown to be particularly effective. An enhancement in speed by a factor of 10^3 has been reported for laser-assisted electroplating²⁵⁶. If such methods are to be applied for AM, the possible interference of the agitation method with the localization mechanism has to be considered. Of all the techniques, photoreduction is probably the least sensitive to disturbances, and even liquid jets or the deposition in flow cells can be imagined. Pipette-based electroplating in liquid offers a straightforward way to increase the convection by using higher flow rates. Unfortunately, this usually leads to larger feature sizes because of increased and less focused hydrodynamic transport¹⁵⁴.

We conclude with two remarks. First, we would like to stress the potential of enhancing fabrication speeds by dynamically changing the voxel size during deposition. Such potential has been demonstrated to some extent by nanopipette-based electroplating in liquid, EHD printing, but most clearly by laser decal transfer (Fig. 2.6). The growth speed expressed in voxel/s usually drops with an increasing voxel size because the z-growth rate is, at best, constant (electroplating) or is even decreased (EHD printing, because of the lower ejection frequency). Nevertheless, the absolute volume growth rate is higher with larger voxels: let us consider a technique that can dynamically switch between an X-Y feature size of 1 and $10\mu\text{m}$ but has a fixed z-growth rate of $1\mu\text{m s}^{-1}$. The voxel speeds are thus 1 and 0.1 voxel/s, respectively. Nevertheless, the time to fabricate a $10\mu\text{m}$ -wide cube with small voxels is 10^3 s and it scales with the cube of the volume. Using the large voxel, the fabrication time is only 10 s, and it scales linearly with the volume as long as the voxel area can be made as large as required. If printing algorithms were free to scale the voxel size, using large voxels for coarse features and small voxels only when required, the volumetric printing speed could be significantly increased. Laser decal transfer is a method that already demonstrated variable voxel size and could directly implement such a strategy^{14,138}. As decal transfer also showed the transfer of complete sheets of complex shapes, the method could even be used to transfer whole layers instead of single voxels.

^cPhotoreduction: 0.2 M¹⁶⁰, 0.05 M¹⁶² AgNO_3 . Solubility limit of AgNO_3 : 12.7 M at 20°C . Meniscus-confined plating: 0.05 M¹³, 1 M⁸⁸, 0.5 M¹⁴⁷ CuSO_4 . Solubility limit of CuSO_4 : 1.26 M at 20°C . The inverse dependence of D on the concentration has been ignored, since it alters D by only 10 – 20 %²⁵⁸.

Second, the maximum speeds will eventually be capped by hardware limitations, although most techniques are still far from reaching this limit. In general, translation of motorized stages is slower than the translation of particle beams. Galvanometric mirror systems can deflect lasers at speeds of cm s^{-1} to m s^{-1} ⁴⁷, and thanks to the absence of any moving parts, the translation of electron beams is even faster²⁶⁷. Therefore, beam-based techniques have an intrinsic advantage for ultimately achieving the highest throughput.

2.3.2 Materials

The variety of potential applications of metal AM at the microscale requires the consideration of a broad range of materials properties, including for example electrical conductivity, magnetic properties or mechanical strength and stiffness. These properties will be defined by the elemental composition and the microstructure of the manufactured deposits. In this section, we discuss the range of additively manufactured metals, their microstructures and the resulting properties. Additionally, we will briefly touch on the substrate requirements.

2.3.2.1 Materials range

In order to evaluate the materials range offered by microscale metal AM techniques, we should clarify what materials are desired. In a first approximation, we assume that metal AM must be compatible with state-of-the-art microfabrication processes. Hence, standard elements for integrated circuits and MEMS should be accessible: Al, Au, Ti, W, Cu, Cr and Ni-Fe alloys, and, less commonly, Zr, Ta, Ir, C, Pt, Pd, Ag, Zn and Nb²⁶⁸. MEMS processes are heavily focused on the use of Si²⁶⁹; however, metals such as Cu, Ni, Ni-Fe and Ni-P are employed with the LIGA technique⁷⁸.

Figure 2.14c presents an overview of the metallic and non-metallic elements that have been deposited with the different micro metal AM techniques (See Fig. B.1 for the same schematic with labeled periodic tables). A complete list of the deposited metals can be found in Table 2.1. Dark green squares in the schematized periodic tables denote elements that have been deposited in pure metallic form (>95 at.% metal), without post-deposition treatments. In contrast, light green squares indicate elements that were co-deposited with organic additives (<95 at.% metal). Subsequent purification steps have been ignored in the figure, but we note that they are often applied. Elements that could possibly be used but have not been demonstrated are marked with blue squares. We assume that nanoparticle-based techniques can be extended to all conventionally available metallic particles, as compiled from references^{270–272}. For LIFT, we include all materials that can

be fabricated as a donor film, taken from reference²⁷³. For electrodeposition, we consider all metals that can be plated in conventional processes^{274,275}, and for photoreduction, we add all metal ions that can undergo photoreduction to the zero-valence state, taken from references²⁷⁶ and²⁷⁷. Because FEBID and FIBID can, in principle, be performed with every CVD precursor¹⁷⁷, we include all CVD materials reported from references^{278,279} and²⁸⁰. In general, metallic elements, metalloids, and carbon as a placeholder for various organic materials, are included, whereas highly unstable metals, such as lithium and sodium, are ignored. For the sake of clarity, we exclude intermetallics, alloys and multi-element semiconductors, and all ceramic materials.

FEBID and FIBID were used for the deposition of the largest number of metals, and commercial systems enable the facile exchange of a large variety of precursors^{281,282}. The main problem of FEBID and FIBID is no longer the availability of different materials but rather their maximal purity²¹⁶.

In contrast, no other approach except LIFT has been used to deposit more than a few metals. Clearly, the respective research groups have concentrated on the development of their techniques and thus used the metals easiest to handle, that is, Au nanoparticles for particle transfer or Cu for electrodeposition. Now that all techniques have brought forth at least a proof-of-principle, we can start to fathom the limits of the materials that can be processed. The two categories of techniques face different challenges regarding the materials they can process. For all metal transfer techniques, the required base material can be prepared with any appropriate method, but has to be stable and suitable for the respective transfer technique. *In-situ* techniques are generally more restricted in the choice of materials because the synthesis has to be compatible with the process environment.

Most **transfer techniques** are based on the delivery of metallic nanoparticles. Hence, stable, non-oxidizing nanoparticles are required. However, zero-valent metal nanoparticles are challenging to synthesize and use due to their inclination to oxidation²⁷⁰. Noble metals such as Au and Ag have therefore attracted the most attention and were widely used for metal AM with **DIW**^{12,95}, **EHD printing**^{16,99} or **electrophoretic transfer**¹²³. Metal particles with higher oxidation susceptibility can be utilized with suitable capping. For example, conductive lines of Cu^{104,117,118} and Al^{119,120} have been fabricated by EHD printing. As long as appropriate measures are taken, we believe that DIW, EHD printing and electrophoretic deposition can also be applied to other standard metallic nanoparticles such as Fe, Co, Ni, Cu, Ru, Rh, Pd, Ag, Sn, Sb, Re, W, Pt, Au, Bi and Ir^{270–272}. In addition to metallic nanoparticles, the range of non-metallic and organic particles is vast and also accessible to nanoparticle-based AM techniques^{101,112,116,283}. A route to significantly increase the range of metallic elements would be the use of metal oxide nanoparticles combined with subsequent annealing in a reducing atmosphere. Dunand and coworkers^{284,285} developed a method

of macroscopic 3D printing with oxide particles and showed that most oxides can be reduced to their metallic state after printing. Yet, the significant volume loss upon reduction of the oxide is a considerable drawback of this approach.

LIFT, the only transfer method that does not rely on nanoparticles, shows the potential for printing a multitude of metals. The prime criterion to print a material with LIFT is the possibility of fabricating a thin film of the material in question¹²⁸. Because several thin film deposition technologies such as evaporation, sputtering or CVD are established, almost any material combination can be deposited as a thin film. During the subsequent transfer process, the evaporation of the carrier material is common¹³². Yet, the carrier itself does not limit the choice of metals; even W, with the highest melting point of all metals (3422 ± 15 °C²⁸⁶), can be transferred from a carrier with a glass transition temperature of only ≈ 700 °C²⁸⁷. However, for the large number of metals susceptible to oxidation, an inert or reducing gas setup will be mandatory. Droplet oxidation has been observed for the transfer of Cu as well as Al under atmospheric conditions^{134,135}. In addition to metals, the deposition of ceramics⁷², polymers, bio-molecules and living cells is feasible²⁸⁸. Finally, LIFT is well suited for the deposition of multiple materials, and the transfer of a combination of metals¹³⁰ or layered materials²⁸⁹ has been shown. In principle, switching the material for each individual voxel by using a carrier patterned with different materials can be imagined.

Most *in-situ* techniques rely on the reduction of metal ions to their metallic state. A straightforward way to drive such a reaction is the use of an electric potential. **Electrochemical approaches** promise high flexibility for the selection of metals because the number of elements that can be deposited with standard plating baths is large²⁷⁴. **Local photoreduction** has been reported for Ag^{160,162,163,166,169,170}, Au^{164,168} and Cu¹⁶⁴ only. Although conventional photoreduction has been additionally performed with Co, Fe, Ni, Pd, Pt and Ti^{276,277}, we presume that photoreduction is the least promising technique for the synthesis of a wide selection of metals. Nevertheless, photochemical reactions of both inorganic and organic materials are manifold and can be combined with the photoreduction of metals^{167,175}.

In summary, it is likely that present metal AM techniques for the microscale will be able to cover a wide range of metals frequently used in microfabrication. Transfer techniques are potentially very flexible in choice of materials. For the synthesis of mono-elemental precursor materials but also fine-tuning of alloys, transfer techniques can draw upon a vast knowledge base for nanoparticle and thin film synthesis. More importantly, the concept of the transfer techniques is universal and the approaches are not limited to metals but can also be applied to the deposition of polymers and ceramics. Nonetheless, the prospects of most discussed techniques have hardly been explored up

to now, and the choice of demonstrated material systems is presently limited. FEBID and FIBID currently offer the largest selection of elements by far.

2.3.2.2 Substrate materials

We believe that the compatibility with a large range of substrate materials (*e.g.*, Si, SiO₂, glass, polymers²⁹⁰) is crucial if a micro AM process is to be integrated with standard microfabrication techniques. Yet, the range of compatible substrates is limited for several of the techniques.

The single most important requirement of a substrate used for small-scale metal AM is often its electrical conductivity. The electrochemistry-based techniques, electrophoretic deposition as well as FEBID and FIBID require conductive substrates, whereas some conductivity is at least beneficial for EHD. In contrast, DIW, LIFT and local photoreduction can also fabricate structures on non-conductive substrates.

For metal AM techniques that demand thermal annealing (DIW, EHD, electrophoresis, and FEBID and FIBID), one should consider the substrate stability at elevated temperatures. Annealing may be performed at temperatures as low as 150 °C, but the best results are often achieved at temperatures between 300 – 500 °C^{12,111}. The *in-situ* laser annealing brought forward by Skylar-Scott *et al.*⁹⁵ circumvents this issue and enables annealing even on sensitive substrates. While similar concepts have been explored for FEBID and FIBID^{182,216}, it will be interesting to see whether *in-situ* annealing will be adapted by other nanoparticle-based techniques.

Other substrate limitations for different methods include their transparency to the laser (photoreduction), their compatibility with electrolyte solutions (FluidFM and SICM), their planarity due to the required small donor-substrate gap (LIFT), the ability to control their surface roughness and the adhesion of the deposit (LIFT)¹³³.

In conclusion, the variety of substrates compatible with the transfer techniques is large and compatible to standard microfabrication techniques. In contrast, the *in-situ* techniques suffer from certain restrictions, like the limitation of electrochemical methods to conducting and semiconducting substrates.

2.3.2.3 Microstructure

The microstructure of a material is a major factor influencing its properties. For example, both the electric conductivity and the mechanical yield strength of metals are a function of the grain size, the solid solution content and the dislocation density. Furthermore, the materials properties of binary

composites are usually a function of the volume fraction of each component²⁹¹. Consequently, the knowledge of the microstructure is key for understanding and optimizing a material's behavior.

Figure 2.15a summarizes the available microstructure data for metals deposited by the discussed AM techniques (see our respective study in Chapter 3 for a more comprehensive overview). Additionally, the figure plots typical electrical resistivity values of the corresponding microstructures. The microstructure and resistivity data often originate from different sources; thus, the figure should be observed as a qualitative comparison of the available data.

An obvious difference between techniques that require annealing and those that do not is observed. The first category is populated by all the **nanoparticle transfer techniques** as well as **FEBID** and **FIBID**. The micrographs in the upper row of Fig. 2.15a indicate that the printed structures consist of agglomerated nanoparticles embedded in an organic matrix. Admittedly, the carbonaceous fraction is only visible in the TEM micrograph for FEBID and FIBID, and a quantitative analysis of the organic content has not been published for all techniques. Ahn *et al.*¹² report the Ag content of typical DIW inks to be 70 – 85 wt.%. The high organic fraction is reflected in the pronounced drop of electric resistivity upon annealing for deposits fabricated by DIW¹², EHD-printing¹⁶ as well as FEBID²¹⁶. The composite nature is also confirmed by mechanical data, where elastic moduli of 0.2 MPa¹¹³ (EHD-printing) to 1.5 GPa¹²² (electrophoretic deposition) were estimated (polycrystalline bulk Au: 78 GPa). During heat treatment at up to 400 – 550 °C, the organic matrix decomposes and the metallic phase undergoes densification and grain growth^{12,16}. Single grains can be perceived in the annealed microstructures. The volumetric shrinkage of several tens of percent^{12,16,177} can cause pronounced porosity (Fig. 2.15a, EHD printing).

LIFT and all **reduction-based approaches** generate deposits with a metallic, crystalline microstructure in a single step without the need for post-print processing. The metallic nature of the materials is reflected in the generally lower electric resistivity of the as-deposited structures as well as their mechanical properties. For example, a strength that compares well to that of nanocrystalline Cu films was reported for electrodeposited structures^{149,152,154}. Differences between the single techniques are apparent: the microstructure of the electrochemical deposits evolves gradually upon growth and is thus homogeneous. In contrast, the single melt droplets that solidified upon impact are clearly discernible in the LIFT microstructure. Special care has to be taken to avoid oxidation of the droplet surfaces when metals prone to oxidation are transferred^{134,135}: the inset in the LIFT micrograph shows an amorphous layer of Al oxide at the interface of two individual droplets.

Being aware of the microstructure is only a first step towards the improvement of the materials properties. To achieve optimized properties, the microstructure has to be engineered accordingly. Options for tailoring the final microstructure are limited for techniques that rely on annealing.

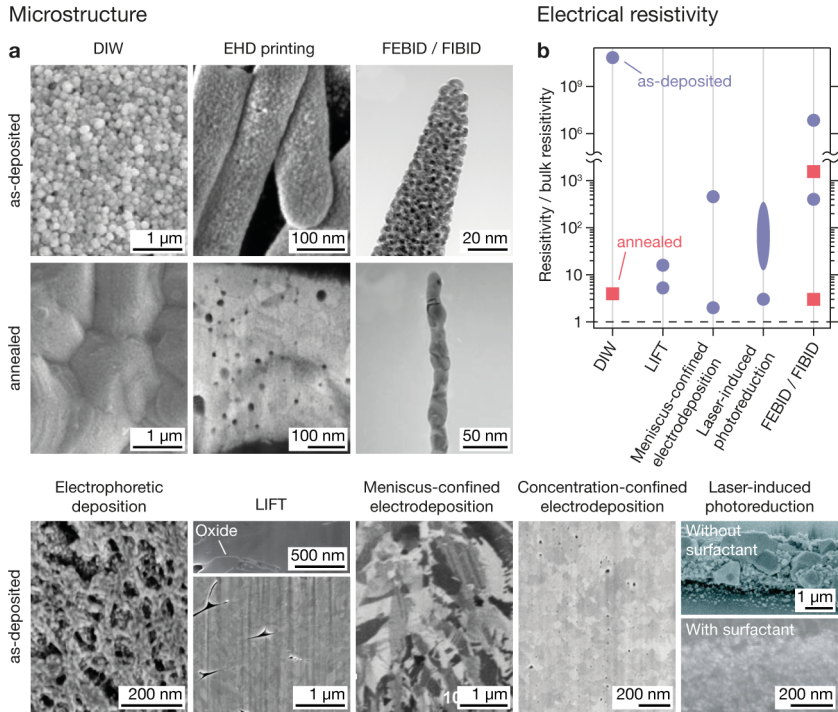


Figure 2.15 – Small-scale metal AM methods in comparison: microstructures. **a**, The as-deposited and annealed microstructure of additively deposited metals. Both images for DIW, the as-deposited image for EHD printing and the top image of laser-induced photoreduction are top-view SEM images. The bottom image of photoreduction is an AFM topology map. Both images for FEBID and FIBID are TEM micrographs. All other images are SEM micrographs of FIB cross-sections. **b**, Representative resistivity values normalized to the bulk resistivity for each technique, if available. If several data points for a single technique exist (FEBID and FIBID), extremes are plotted. The resistivity values reflect the corresponding microstructure: particle agglomerates suffer of a high resistivity that can be decreased upon annealing. On the other hand, the crystalline, dense as-deposited microstructures of LIFT and the techniques focused on reduction of metal ions exhibit smaller resistivity ratios. References: DIW^{12,95}; FEBID / FIBID²¹⁶; LIFT¹³⁵; meniscus-confined electrodeposition^{13,144}; laser-induced photoreduction^{160,174}. Micrographs in (a) reprinted with permission from: DIW¹², ©2009 AAAS; EHD as-deposited¹⁰⁵, ©2016 ACS; EHD annealed: sample kindly provided for this work by Rohner *et al.*; FIBID as-deposited¹⁷⁸, ©2008 IOP Publishing; FEBID annealed¹⁸⁴, ©2011 John Wiley and Sons; Laser-assisted electrophoretic deposition: sample kindly provided for this work by Iwata *et al.*; LIFT: top¹³⁴, ©2016 IOP Publishing, bottom¹³⁰, ©2015 John Wiley and Sons; Meniscus-confined electrodeposition¹⁴⁹, ©2018 John Wiley and Sons; Laser-induced photoreduction: top¹⁶⁰, ©2006, AIP publishing, bottom¹⁶², ©2009 John Wiley and Sons.

Thermal treatment will invariably lead to grain-growth and annihilation of defects, which increases conductivity, but can be undesired for applications that require a high mechanical strength. For increased mechanical strength, grain growth could be inhibited by the addition of appropriate alloying elements that segregate to the grain boundaries or form voids in the grain boundaries^{292,293}.

If no annealing is necessary, as for LIFT and the reduction-based *in-situ* techniques, the structural properties can be varied via the deposition parameters. The microstructure of LIFT-fabricated deposits is defined by voids between the single droplets and grain boundaries within single droplets. The presence of voids can be influenced by the distance between the donor and substrate as well as the laser power. For example, porosity can be adjusted between 10 and 15%¹³⁵. The defect density within the single droplets is a function of the cooling rate. Hence, substrate cooling or heating could be employed to influence the cooling rate and the resulting microstructure.

Electrochemical techniques facilitate a straightforward tuning of the microstructure. A multitude of strategies originating from conventional electroplating, such as pulsed plating and the use of additives, are applicable for electrochemical metal AM techniques. For example, different morphologies, grain sizes and twin densities have already been synthesized by varying the potential pulse profile in meniscus-confined electrodeposition^{148,149,152,294}. Earlier and at larger scales, the manipulation of the morphology and microstructure of wires synthesized using microelectrodes has been studied^{85,295,296}. Similarly, the microstructure of photoreduced deposits can be influenced by the use of surfactants¹⁶².

An interesting feature of metal AM techniques could be the voxel-by-voxel engineering of the metal microstructure and chemical composition during the fabrication process. Spatially graded architectures have been proposed to synthesize materials with inhomogeneous and highly anisotropic properties²⁹⁷. The most recent results obtained by the Lewis group⁹⁵ can be deemed as a first step towards this direction: a local variation in annealing temperatures results in deposits with a locally varying microstructure and hence an inhomogeneous electrical resistance. The LIFT fabrication of materials with engineered porosity at the voxel scale has also been suggested¹²⁷. *In-situ* synthesis techniques might show the ability to perform such variations on a more elaborate level because the local synthesis conditions can be varied with more degrees of freedom than local annealing or the introduction of pores (see Chapter 5 for our demonstration of voxel-by-voxel design of microstructures by control of the local composition).

In conclusion, LIFT and electrochemical and photochemical methods enable the fabrication of as-deposited structures with materials properties that are comparable to bulk values. Other techniques require an annealing process to decrease the organic fraction as well as the porosity and to render

acceptable performance for most applications. However, annealing routines that can be performed during the deposition process may circumvent this disadvantage. Yet, *in-situ* synthesis techniques will be more suitable for local engineering of the microstructure due to the larger range of tunable process parameters.

2.4 Conclusion and general outlook

This chapter reviewed the diverse research activities towards the additive manufacturing of metals at the micrometer scale. A multitude of techniques currently allow the true 3D fabrication of metals, and exciting developments such as *in-situ* annealing or simulation-guided deposition promise to advance the field significantly in the near future. Yet, none of the techniques reviewed in this article can currently be applied without expert knowledge, and the majority of research is still focused on the understanding and optimization of the single processes. Consequently, 3D metallic microstructures are still predominantly fabricated by the popular combination of TPL and a metalization process^{34,66,67,79}, a multi-step approach well suited for a range of applications. However, once micro metal AM techniques become established, they will enable the fabrication of more complex geometries and material architectures, for example functionally graded materials.

The main criteria for the widespread adaption of a micro AM technique have been demonstrated by TPL and its expansion into diverse branches of research: structuring speed, maximum available sample volume, minimum feature size and facile pre- and post-processing⁴⁷. Additionally, a large range of available materials is beneficial for broad applicability, and a growth feedback as offered by concentration-confined electrodeposition and FEBID will probably be essential for the user-friendliness of many techniques. Considering these criteria, we believe that DIW, EHD printing, LIFT, meniscus- as well as concentration-confined electrodeposition and FEBID and FIBID are at the verge of transitioning from development to application. This selection is based on the number of publications for each technique, the demonstrated reliable operation of the systems, the apparent ease of use, and the flexibility in choice of substrate. Nevertheless, no single technique is able to combine high resolution, high purity and intricate geometry yet, and future users will have to decide which process best serves their needs.

Concerning future applications, micro AM should not be perceived as a disruptive technique that seeks to replace traditional microfabrication. Rather, we envision further development to occur in synergy with existing technology: first, metal AM could be used as a prototyping tool for design optimization of microscale geometries produced with time- and resource-intensive micro-fabrication processes such as the LIGA technique. Yet, current metal AM methods still struggle to guarantee high material quality and low surface roughness, both of which are required properties

for most LIGA applications⁷⁸. Here, meniscus- and concentration-confined electrodeposition are probably the most competitive AM techniques. Second, a combination of micro metal AM with traditional microfabrication techniques is within reach. We have shown in our review that some of the micro metal AM procedures are readily compatible with standard microfabrication techniques, as demonstrated by the deposition of single sensor elements on top of conventional AFM probes¹³ or additively manufactured actuators in pre-fabricated microfluidic channels¹⁶⁶. In order to gain the full benefit of the fusion of AM and established techniques in the future, a transition from such sequential fabrication to a complete integration of metal AM into existing process workflows will be essential. Finally, the integration of micro metal AM into existing macroscopic AM could advance current attempts^{298,299} to fabricate electronics, actuators and sensors inside macro AM builds. Additionally, the combination of micro and macro metal AM could enable unique features, for instance an extreme voxel scaling that would permit highly resolved details in critical areas combined with large volume growth rates in less critical sections of a part. With the same strategy, the issue of poor surface quality of macroscale metal AM may be overcome.

Functional structures fabricated exclusively by a single microscale metal AM technique will probably require another leap forward in the deposition speed and process reliability. Yet, once a technique leaves the prototyping niche, eliminating geometric constraints at the micrometer- and submicrometer scale, we will observe a paradigm change for microfabrication, foreshadowed by the present success of macroscopic AM.

2.5 Implementations for this thesis

Multiple challenges for both, the users and developers of techniques, are highlighted after overviewing the wide range of principles and capabilities of the methods available for small-scale AM. The potential user needs to select the approach that fits his application best, considering the strengths and weaknesses of the individual techniques. If a large range of materials or large build volumes are required, particle-based methods are the methods of choice. In contrast, nanometer-scale resolution asks for ion- and electron-beam-based methods, and purest metals for electrochemical approaches – no technique offers highest geometrical complexity in combination with highest speed and best materials quality yet. Thus, practitioners need comparative data of all techniques to make a well founded choice – data that is often not available yet.

For developers of AM techniques, a set of core challenges can be identified. A first group of tasks is centered around geometrical attributes: complexity, feature size, deposition speed, total build volume. A second class of challenges involves materials, their microstructure and resulting properties. Generally, most techniques were developed with a focus on the geometrical features – a

reasonable priority considering the main advantage of 3D printing: geometry. However, in my opinion, the emphasis on geometry resulted in a lack of materials characterization and materials optimization. Many examples contradicting this statement exist, as some groups certainly studied the deposited metals in detail – but in general, microstructural data is hard to find. Nevertheless, it is my belief that materials quality will be one of the crucial factors for the incorporation of additive microfabrication into modern small-scale manufacturing. Consequently, the microstructure and properties of additively synthesized metals will be an important part of this thesis.

This thesis aspires to tackle some of the mentioned challenges. First, the choice of a technique for a given application should be simplified and simultaneously, the focus on materials' microstructures should be strengthened: the next Chapter 3 provides a comparison of "materials quality" of metals deposited by modern small-scale AM methods, presenting a comprehensive study of the microstructures and mechanical properties of metals synthesized by most of the techniques introduced here.

The subsequent Chapters 4 – 6 will concentrate on the development of novel electrochemical AM methods. Primarily, this motif is motivated by the high quality of metals synthesized by electrodeposition (Fig. 2.15) and the wide range of microstructures accessible by tuning the electrochemical deposition parameters, providing extended options for performance optimization. Provoked by the comparably low speed of electrochemical AM (Fig. 2.14b), a new method for high-speed electrochemical AM is introduced in Chapter 4. The subsequent Chapter 5 demonstrates that the same method enables multi-metal AM with sub-micrometer resolution (including tuning of local microstructures and hence properties) – a feature that is unique amongst all the methods presented in this overview. The last Chapter 6 will discuss how to obtain feature sizes <100 nm with electrochemical deposition (a resolution that is out of reach of current electrochemical techniques).

Chapter 3

Metals by micro additive manufacturing: a comparison of microstructure and mechanical properties

Many emerging applications in microscale engineering rely on the fabrication of three-dimensional architectures in inorganic materials. Small-scale additive manufacturing (AM) aspires to provide access to these geometries. Yet, the synthesis of device-grade inorganic materials is still a key challenge towards the implementation of AM in microfabrication. Here, we present a comprehensive overview of the microstructural and mechanical properties of metals fabricated by most contemporary AM methods that offer a spatial resolution $\leq 10\ \mu\text{m}$ (including the EHD-RP technique introduced in the next chapter). For each technique, a standardized set of samples was studied by cross-sectional electron microscopy, nanoindentation and microcompression. This study shows that metals with a wide range of microstructures and elastic and plastic properties are synthesized by current microscale AM techniques, including materials of dense and crystalline microstructure with excellent mechanical properties that compare well to those of thin-film nanocrystalline materials. The large variations in materials performance can be related to the individual microstructure, which in turn is coupled to the various physico-chemical principles exploited by the different printing methods. The study provides practical guidelines for users of small-scale additive methods and

This chapter is based on: Reiser, A., Koch, L., Dunn, K. A., Iwata, F., Fogel, O., Kotler, Z., Zhou, N., Shi, Q., Lewis, J., Charipar, K., Piqué, A., Rohner, P., Poulikakos, D., Lee, S., Seol, S. K., Utke, I., van Nesselroy, C., Zambelli, T., Wheeler, J. M., Spolenak, R. Metals by micro additive manufacturing: a comparison of microstructure and mechanical properties. To be submitted to *Small*.

establishes a baseline for the future optimization of the properties of printed metals – a first step towards the potential establishment of AM techniques in microfabrication.

3.1 Introduction

Complex three-dimensional structures with feature sizes in the micro- and nanometer range currently enable new areas of exciting growth in materials science and engineering. 3D geometries are often superior to their established, planar counterparts and are demanded by a wide range of emerging applications for microelectromechanical systems (MEMS)^{10,11}, electronics^{12,13,17,18}, optics^{20,21} or metamaterials^{9,37–39}. Progress in these fields relies on fabrication methods that can provide the required 3D architectures from suitable materials. Here, small-scale AM of inorganic materials⁴⁸ is one of three major fabrication strategies (the two others are self assembly and stress-controlled buckling⁴⁵). While AM has potential for the most intricate geometries, it faces a major challenge: the materials and their performance provided by additive methods are typically inferior to those deposited by traditional fabrication routes such as PVD or electrodeposition⁴⁸. This shortcoming, in combination with challenging scalability^{54–57}, is a major handicap for incorporating AM in advanced micro- and nanofabrication routines.

Materials engineering is thus necessary to improve the quality of printed inorganic materials. A first and crucial step towards this goal is the knowledge of the deposited materials' microstructure and its relation to the properties of additively manufactured materials. Here, we identify a deficit in knowledge – for many techniques, characterization and optimization of microstructure-property relationships is in its infancy. For metals, a number of studies on electrical properties exist, reporting typical conductivities of $10^{-3} - 0.55 \times$ bulk conductivity^{12,13,95,135,160,174,216}. In contrast, only a few mechanical properties are found in literature. Yet, the mechanical performance of small-scale 3D metal structures cannot be neglected in many current MEMS applications³⁰⁰, for example in RF switches³⁰¹ or in digital micromirror devices³⁰², and neither can it be ignored for many projected implementations of printed metals, *e.g.*, unsuspended interconnects for flexible electronics¹², out-of-plane, high-aspect-ratio switches^{76,303}, sensors⁵² and probes⁵¹, printed actuators and manipulators^{76,131}. Thus, mechanical properties of additively manufactured metals are a key for many applications at small scales.

3.1.1 Metal AM at small scales – a brief review of techniques, materials' microstructure and mechanical properties

Metals are essential for the microfabrication of high-performance devices. Consequently, a multitude of direct AM process for metals have been developed in the past decade⁴⁸, including long-standing methods such as laser-induced forward transfer (LIFT) and focused electron induced

deposition (FEBID), or more novel techniques such as direct ink writing (DIW) or electrohydrodynamic printing (EHDP). From a materials-science point of view, it is useful to classify the techniques according to their underlying principle of material synthesis, as it emphasizes the fundamental similarities and differences that determine the properties of the resulting materials. The techniques are thus grouped in two main categories: *transfer* and *synthesis* techniques (Fig. 3.1). Transfer techniques require the previous synthesis of metallic materials before the actual AM process – the subsequent deposition simply transfers the pre-synthesized material to the location of interest. In contrast, the synthesis methods rely on the growth of the metal at the location of interest during the AM process. Both categories can further be divided into the sub-groups of methods that do or do not use colloidal inks (transfer techniques), and methods that use wet electrochemistry or electron-initiated gas-phase reactions similar to CVD (synthesis methods).

A list of the techniques included in this study is presented in Section 3.2. For a detailed description of their working principle and performance characteristics, please refer to Chapter 2. Additionally, see Chapter 4 for an introduction to EHD-RP. In brief, printing metals from colloidal inks is typically a two-step process that requires a post-print thermal annealing step to render metallic materials characteristics, burning off organic residues and sintering the particles. The process of transferring the ink to the location of interest varies between the techniques (DIW, EHDP, LIFT (ink) and EPD^a), but materials characteristics are typically comparable: an agglomeration of loosely packed, surfactant-coated micro- or nanoparticles in the as-deposited state, a crystalline, sintered microstructure in the annealed state. LIFT of metallic melts is an ink-free transfer method that does not demand any post-print treatment, as it transfers molten droplets of metals that solidify as pure metals on the substrate. Electrochemical methods (MCED, FluidFM, EHD-RP) use different approaches to localize growth, but generally offer as-deposited dense and crystalline metals. They typically require electrically conductive substrates as cathodes for the electrochemical reduction process. Focused particle beam methods (FIBID, FEBID, cryo-FEBID) make use of electron-induced dissociation of gaseous precursors (typically organometallic compounds) to synthesize metal-carbon composites with metallic characteristics – as the process can be likened to a localized CVD process, we use the term "electron-induced CVD" to summarize the working principle.

As all techniques explore different physico-chemical principles, the microstructure of the deposited metals varies greatly – each of the methods results in metals of different purity, defect density and porosity. As a result, a large variance in materials performance can be expected. Previous studies suggest that the elastic and plastic properties of state-of-the-art metals varies over a large range

^aAbbreviations are explained in the list of techniques in Section 3.2

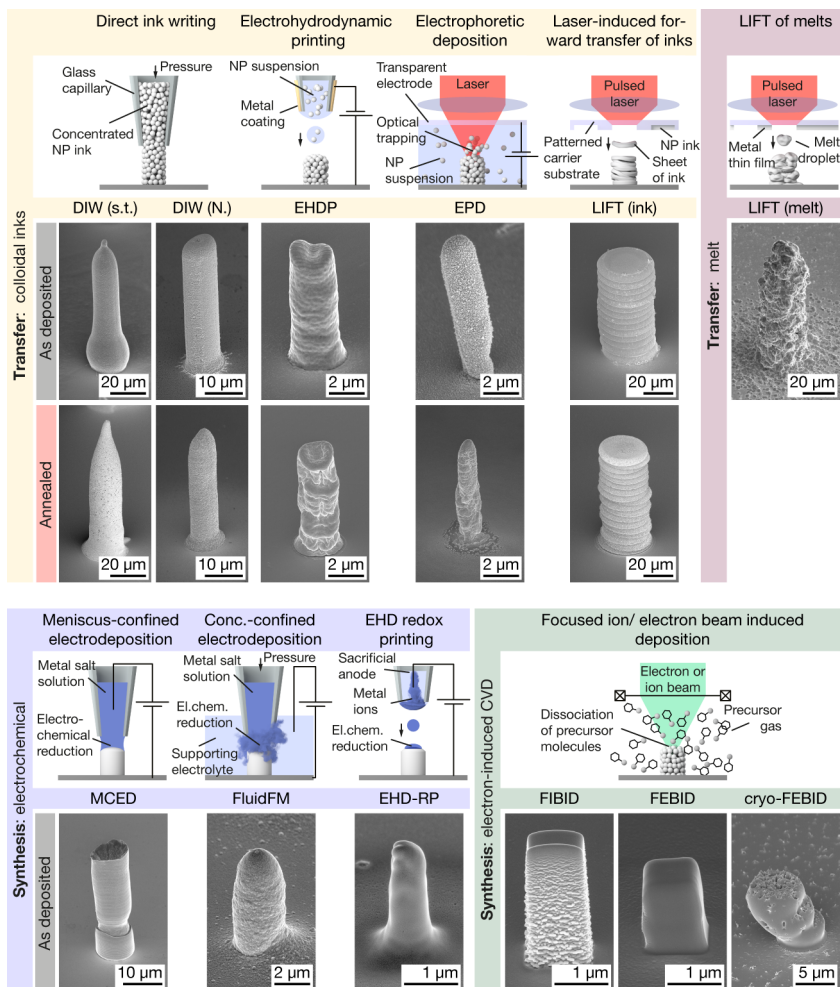


Figure 3.1 – Small-scale metal AM methods included in this study and pillars printed by these techniques. Small-scale additive techniques can be grouped into *transfer* and *synthesis* methods based on their approach to metal deposition. Subgroups include: Transfer of colloids, transfer of melts, electrochemical synthesis and synthesis via electron-induced CVD. The SE micrographs show representative pillars printed with each of the techniques and tested in this study. As-printed and annealed pillars are shown if thermal annealing was conducted (not the same samples). Samples for DIW and LIFT (ink) are printed from Ag inks, and samples from EHPD and EPD from suspensions of Au nanoparticles. The LIFT (melt) pillar is Cu (for Au, see Fig. C.1), as are the structures for MCED, the FluidFM and EHD-RP. FIBID and (cryo-)FEBID pillars were deposited from MeCpPt(Me)₃. Tilt angle of the micrographs: 55°.

of $\approx 0.05 - 1 \times$ bulk values: measurements of Young's moduli E and hardnesses H of various printed Ag inks derived values of 10 – 100 GPa and 0.03 – 1.4 GPa, respectively^{140,304–306}; The elastic modulus of EHD-printed Au inks was reported to be 0.2 MPa (as printed)¹¹³ and 6 GPa (annealed)¹¹¹, while a modulus of 1.5 GPa was measured for as-printed Au nanoparticle wires deposited by electrophoretic deposition (EPD)¹²²; Studies of meniscus-confined electrodeposited Cu pillars derived values of 128 GPa for E , 2 GPa for H ¹⁴⁸ and a flow stress σ of 630 – 962 MPa^{149,152}; Young's moduli of metals deposited by laser-induced forward transfer (LIFT) were 12 GPa (Cu) and 9 GPa (Au)¹³¹; and metal-containing deposits grown by focused ion and electron beam-induced deposition (FEBID / FIBID) showed moduli of 10 – 100 GPa^{215,307,308}, a hardness of 3.6 – 7.6 GPa^{308,309}, and a tensile strength σ_{tensile} of 1 – 2 GPa³⁰⁷. However, despite these studies, it is difficult to present a properly founded overview of the quality of the metals deposited by small-scale AM today – the size of the dataset is too limited, and the large variation in sample geometries and the different techniques used for its compilation prevent a fair comparison.

3.2 Objective of this chapter

With the intention to present a comprehensive overview of state-of-the-art materials, this chapter compares the microstructure of metals synthesized by most of the contemporary small-scale AM approaches (including EHD-RP, the AM method introduced in this thesis, see Chapters 4 and 5) and relates the materials' microstructure to the mechanical properties of the deposits. The following techniques are included in this study:

- Direct ink writing of shear-thinning inks (DIW (s.t.))¹²
- DIW of Newtonian inks (DIW (N.))³¹⁰
- Electrohydrodynamic printing of nanoparticle inks (EHDP)⁹⁹
- Laser-assisted electrophoretic deposition (EPD)¹²²
- Laser-induced forward transfer of nanoparticle inks (LIFT (ink))¹⁴
- LIFT of melts of thin films (LIFT (melt))^{126,127}
- Meniscus-confined electrodeposition (MCED)¹³
- Concentration-confined electrodeposition (FluidFM)¹⁵⁴
- Electrohydrodynamic redox printing (EHD-RP)³¹¹ (Chapters 4 and 5)

- Focused ion beam deposition (FIBID)⁷³
- Focused electron beam deposition (FEBID)⁷³
- FEBID at cryogenic temperatures (cryo-FEBID)²³⁵

Not covered in this study are the methods of photoreduction¹⁶⁰, pyrolysis of metal-containing resins structured by two-photon lithography (TPL)⁹³, and implosion fabrication⁹⁴.

For each technique, a standardized set of samples was studied by cross-sectional electron microscopy, nanoindentation and microcompression. We show that a large variety of microstructures results from the different principles exploited by the different printing methods. As a consequence thereof, the elastic and plastic properties of the synthesized metals vary within one order of magnitude. The study highlights general challenges of current approaches, but also shows that some methods already provide a dense and crystalline microstructure with mechanical properties that compare to those of metals deposited by standard thin-film techniques. On one hand, the standardized approach used in this study allows a fair comparison of the capabilities of the various small-scale AM methods (within the boundaries discussed) – consequently, this study can serve as the base for matching future applications with the appropriate AM method that offers the most suitable materials properties. On the other hand, the presented overview is the groundwork for future optimization of materials performance.

3.3 Methods

3.3.1 Sample preparation

A standardized set of samples containing pads and pillars was printed with each technique to assess both the microstructural as well as the mechanical properties of the printed metals (Fig. 3.1, 3.2). Due to the variation in geometrical resolution and volumetric print speed of the individual techniques, the dimensions of the samples varied. Pads ranged from 10 to 200 μm in width and 400 nm to $>10\ \mu\text{m}$ in thickness. Pillar diameters were typically $\geq 1\ \mu\text{m}$, with maximum diameters of $\approx 45\ \mu\text{m}$. A set of as-deposited and annealed samples was prepared if thermal annealing is generally required for functional performance of the metals (nanoparticle inks). In contrast, no annealed FIBID and FEBID structures were included, because the vast majority of reported usage of those techniques restricts itself to as-deposited materials^{48,73} and existing purification and annealing procedures²¹⁶ are not yet applied by a broad range of practitioners.

3.3.1.1 DIW of shear-thinning Ag inks

The concept and setup for DIW of Ag structures, as well as the synthesis of the shear-thinning Ag inks, have been described earlier^{12,17}. Pads and pillars were printed on a Regenovo Bio-Architect WS printer at speeds of 30 – 80 $\mu\text{m s}^{-1}$ and extrusion pressures of 17 – 24 bar. Pads were printed with a layer-by-layer approach, while pillars were deposited by continuously retracting the nozzle from the substrate. G-code was generated manually (software: CIMCO). All samples were printed directly onto soda lime glass substrates (Taitan). After printing, samples were heated on a hotplate (IKA RCT basic) in air. As-deposited samples were dried at 100 °C (30 min), and annealed samples were sintered at a final temperature of 300 °C after a controlled temperature ramp (100 °C (10 min), 150 °C (10 min), 200 °C (10 min), 250 °C (10 min), and finally, 300 °C for 30 min or 2 h). All samples were sputter-coated with a conductive layer of Pt-Pd (8 nm, CCU-010 safematic) prior to SEM imaging and mechanical testing to avoid charging in the electron microscope.

3.3.1.2 DIW of Newtonian Ag inks

The basic process and setup for printing, as well as the synthesis of the Ag inks, was previously described by Lee *et al.*³¹⁰. The synthesized ink (Polyacrylic acid (PAA)-coated Ag particles, 25 wt.% in DI water) shows Newtonian fluid characteristics at shear rates of 0 – 10³ s⁻¹, with a viscosity of 6.8 × 10⁻³ Pa s. Glass nozzles with an opening of 10 μm were fabricated with a P-97

pipette puller (Sutter Instruments). Pads were printed with a layer-by-layer strategy (hatch distance $10\ \mu\text{m}$, layer height $10\ \mu\text{m}$) at a speed of $10\ \mu\text{m s}^{-1}$. Pillars were printed by retracting the nozzle at $10\ \mu\text{m s}^{-1}$. All samples were printed on (111) Si wafers coated with a $1\ \mu\text{m}$ thick Pt film. Annealing was performed in an ambient-atmosphere furnace (ov-11, JEIO-Tech), either at $150\ ^\circ\text{C}$ for 1 hour or $450\ ^\circ\text{C}$ for 12 hours.

3.3.1.3 EHDP of Au inks

The printing procedure was previously described by Galliker *et al.*⁹⁹ Similarly, the ink has been reported elsewhere.¹⁰⁵ In brief, Au nanoparticles with Decanethiol ligands, $\approx 5\ \text{nm}$ in diameter, were synthesized with the Stucky method³¹² and dispersed in Tetradecane. The maximum ink concentration was $\approx 10\ \text{mg mL}^{-1}$. All samples were printed on diced SiO_2 wafers (University-Wafer, USA). The printing parameters are similar to the process presented by Schneider *et al.*¹⁶. Yet, the printing process was optimized for high mass flow for printing the large structures presented herein. Therefore, the 250 Hz AC actuation voltage was increased to $260 - 360\ \text{V}_p$ and larger nozzles with an aperture diameter of $1.8 - 2\ \mu\text{m}$ were used. These parameters resulted in an ejection frequency of $\approx 1\ \text{kHz}$ of droplets $\approx 200\ \text{nm}$ in diameter. In general, the samples were printed in a layer-by-layer fashion, where each layer was deposited in a serpentine-like printing path. With a translation speed of $5\ \mu\text{m s}^{-1}$ and a hatch distance (line pitch) of $300\ \text{nm}$, approximately 30 layers are required to deposit a pad of $5\ \mu\text{m}$ in height. In tendency, pillars (especially small pillars) were printed with lower mass flow, thus lower actuation voltages and smaller nozzles. As-printed samples were annealed for 10 min at $400\ ^\circ\text{C}$ in a constant gas flow of O_2 at ambient pressure in a rapid thermal processing furnace (As-One 150, Annealsys, France).¹⁶

3.3.1.4 Laser-assisted EPD of Au nanoparticles

The principle, setup and typical printing parameters for laser-assisted electrophoretic printing have been described in detail in literature^{122,123}. For deposition of Au structures, an aqueous solution of Au nanoparticles (0.25 wt.%, $3\ \text{nm}$ dia., Tanaka Kikinzoku Kogyo K. K.) was dispensed between an ITO-coated cover glass and an ITO-coated glass substrate ($200\ \text{nm}$ ITO on soda lime glass, Gematec inc.). An electric field of $12\ \text{kV m}^{-1}$ was applied between these electrodes for electrophoresis (electrode distance: $160\ \mu\text{m}$). A CW Nd:YVO₄ laser ($532\ \text{nm}$, Spectra physics, Millennia Pro) was used for optical trapping of the Au particles (Objective lens: $\times 60$, $\text{NA}=1.2$, Olympus, UPLSAPO 60XW). For printing of pillars, the stage was lowered at $0.67\ \mu\text{m s}^{-1}$. Printed structures were annealed for 1 h at $300\ ^\circ\text{C}$ in ambient atmosphere in a furnace (AFM-10, ASWAN).

3.3.1.5 LIFT of Ag nanoparticle inks

The details of the method have been described earlier^{14,136,313}. Donor substrates were prepared via doctor-blading a commercial Ag ink (80 wt.%, particle dia.: 7 – 12 nm, NPS Nanopaste, Harima Chemicals Group) onto glass substrates with lithographically-defined, circular wells (8 μm deep). The viscosity of the ink was 90 Pa s. Pads were printed by laser-transferring individual, circular disks of ink, and pillars were deposited by stacking multiple individual disks³¹³. All samples were printed onto diced (100), p-type Si wafers (University Wafer, Inc.). Thermal annealing was performed in a furnace (ambient atmosphere) for one hour at temperatures in the range of 150 – 230 °C.

3.3.1.6 LIFT of melts of Au and Cu thin films

The printing setup for LIFT and the general principle have been reported in literature^{127,128}. A 3 W laser with a pulse duration of 0.8 ns and a wavelength of 532 nm (Picospark, Teem Photonics) is used for the LIFT process. The laser was deflected by a scanning mirror, and its spot size was $(28.0 \pm 0.5) \mu\text{m}$ (4-sigma) at the donor interface. Soda lime glass slides coated with 500 nm of either Cu or Au were used as donors. Substrates were soda lime glass coated with 10 nm Ti / 100 nm Au. Printing was performed in ambient atmosphere with a donor-substrate gap of 300 μm . All samples were printed with droplet overlaps of 3 μm ¹²⁸ and a total of five layers. The pulse energy used was 5.5 – 7.5 μJ for Cu and 4 – 6.5 μJ for Au.

3.3.1.7 Meniscus-confined electrodeposition of Cu

The method and setup was described by Seol *et al.*¹⁴⁴. In short, Cu was deposited from an electrolyte of 1.05 M $\text{CuSO}_4 \cdot 5\text{H}_2\text{O}$ (99 %, Samchun Chem.) in an aqueous solution of 0.8 M H_2SO_4 (95 %, Daejung Chem.) using a two-electrode setup with a Pt anode. All samples were grown by pulsed electrodeposition (pulse profile: -1.7 V (1 s), 1 V (0.5 s)) at growth rates of $0.02 \mu\text{m s}^{-1}$ and $0.4 \mu\text{m s}^{-1}$ for pads and pillars respectively. Both, pads and pillars, were printed by retracting the nozzles ($\varnothing 25 \mu\text{m}$ for pads, $\varnothing 10 \mu\text{m}$ for pillars) from the substrate in steps of 10 μm . All samples were deposited on a 1 μm -thick film of Pt on cut (111) Si wafers. No thermal annealing was performed.

3.3.1.8 FluidFM deposition of Cu

The FluidFM principle and general printing parameters have been reported by Hirt *et al.*¹⁵⁴. Structures were printed with a FluidFM BOT (Cytosurge AG) using a FluidFM Nanopipette probe

(300 nm opening, Cytosurge). For printing, the pipette was filled with a Cu electrolyte solution (1 M CuSO₄ (Sigma Aldrich) in aq. 0.8 M H₂SO₄ (Sigma Aldrich), filtered using a Millex-VV Syringe filter (0.1 μm, PVDF, Sigma Aldrich)) and immersed in a supporting electrolyte bath (aq. H₂SO₄, pH 3). The electrochemical cell was equipped with a graphite counter electrode and a Ag/AgCl reference electrode. Samples were deposited onto Ti(3 nm)/Au(25 nm) films coated either on soda lime glass (Menzel Gläser, ThermoScientific) in the case of pillars, or Si substrates ((100), Microchemicals) in the case of pads. Pads were printed with a layer-by-layer strategy at a potential of -0.45 – -0.6 V vs. Ag/AgCl, an applied pressure of 4 – 8 mbar and a layer height of 0.4 – 0.8 μm. Pillars were grown by gradually retracting the stationary pipette at a potential of -0.67 V vs. Ag/AgCl, an applied pressure of 7 mbar and a voxel height of 0.25 μm. No thermal annealing was performed.

3.3.1.9 EHD redox printing of Cu

The basic concept and setup for EHD-printing is described in detail in chapter 4. In brief, a Cu wire (0.1 mm dia., 99.9985 %, Alfa Aesar) is immersed in a printing nozzle filled with acetonitrile (Optima, Fisher Chemical). The nozzles are pulled (P-2000 micropipette puller system, Sutter Instrument) from quartz capillaries (QF100-70-15, Sutter Instrument) to an aperture diameter of 135 – 145 nm. A Cu wire (∅0.1 mm, 99.9985 %, Alfa Aesar, etched in pure nitric acid (Sigma Aldrich) for 20 s) was used as the sacrificial anode. Printing is conducted in Ar-atmosphere (<40 ppm O₂, as measured by a Module ISM-3 oxygen sensor (PBI Dansensor)). Samples were printed onto Si substrates ((100), SiMat) with a Ti(3 nm)/Au(20 nm) coating (deposited in our laboratory sputter facility by DC magnetron sputtering (PVD Products Inc.)). 15 × 15 μm pads were printed layer by layer, with a serpentine-like print path, a hatch distance (line pitch) of 100 nm and a rotation of the hatch direction by 90° in every subsequent layer. The voltage applied to the sacrificial anode was 110 – 150 V and the nozzle-substrate separation 7.5 μm. The nozzle is retracted in every layer by a distance equal to an estimated layer height. Different combinations of in-plane speed, layer height and number of layers were used. Typical values were: in-plane speed: 10 – 40 μm s⁻¹; layer height: 25 – 100 nm; layers: 10 – 80. Nominally 1 × 1 μm wide, square pillars were printed with the same protocol as the pads. Printing parameters were: hatch distance: 100 nm; voltage: 100 V; nozzle-substrate separation: 7.5 μm; in-plane speed: 5 μm s⁻¹; layer height: 200 nm; layers: 14. Two pillars 160 and 170 nm in diameter were printed with the same electric field but with no relative motion between substrate and nozzle.

3.3.1.10 FIBID and FEBID of Pt

A Tescan Lyra FIB-SEM (background pressure 9×10^{-6} mbar, operating pressure 1×10^{-5} mbar) with electron field emission gun, Orsay Physics Ga-ion source, and Orsay Physics gas injection system (GIS) was used for FIBID and FEBID of Pt deposits. The GIS nozzle exit (inner $\varnothing 350 \mu\text{m}$) was placed at a distance of approximately $200 \mu\text{m}$ to the area of deposition. We used Methylcyclopentadienyl platinum (IV) trimethyl ($\text{MeCpPt}(\text{Me})_3$) as a precursor gas, heated to 80°C . The local precursor pressure was calculated by Empa's freeware GIS simulator to be 0.4 and 0.8 Pa (2×10^3 and 4×10^3 ML/s) for FIB and FEB deposition, respectively. All samples were deposited onto diced (100) Si wafers (Semiwafer). The deposition parameters for FIBID and FEBID pillars and pads are given as (beam current, beam energy, beam size, scan pattern, dwell time, pixel distance, refresh time, total time, and deposition rate). FIBID pillars: (5 pA, 10 kV, 32 nm, fly back, 80 ns, 25.6 nm, 122 μs , 10 min 28 s, $0.7 \mu\text{m}^3 \text{nA}^{-1} \text{s}^{-1}$). FIBID pads: (285 pA, 10 kV, 32 nm, fly back, 80 ns, 25.6 nm, 12 ms, 19 min 34 s, $0.3 \mu\text{m}^3 \text{nA}^{-1} \text{s}^{-1}$). FEBID pillars: (1 nA, 5 kV, 29 nm, rotating leading edge (RLE), 80 ns, 29 nm, 92.5 μs , 16 min 38 s, $0.0026 \mu\text{m}^3 \text{nA}^{-1} \text{s}^{-1}$). FEBID pads: (3.9 nA, 5 kV, 180 nm, RLE, 1 μs , 180 nm, 6.9 ms, 70 min, $0.0064 \mu\text{m}^3 \text{nA}^{-1} \text{s}^{-1}$).

3.3.1.11 cryo-FEBID of Pt

The set-up has been described in detail by Bresin *et al.*^{234,235}, including the important processes governing morphology, size, microstructure and composition. All experiments were conducted in a FEI Nova 600 Nanolab dual beam system (base pressure 6.7×10^{-5} Pa). For deposition, the $\text{MeCpPt}(\text{Me})_3$ precursor gas is condensed on the substrate at -190°C (custom-built cryogenic stage cooled by liquid nitrogen in a heat exchanger) and subsequently patterned with the electron beam. Square pads were printed by injecting the precursor gas for 30 s (crucible temperature: 27°C) and scanning the electron beam (0.62 nA, 20 kV) in a normal imaging raster with a pixel dwell time of 100 ns. Pillars were deposited by three cycles of condensation and e-beam patterning. In contrast to the pads, the precursor was injected for 60 s, and beam parameters were 0.6 nA, 18 kV. Further, the individual layers were exposed with a stationary rather than a scanning beam, exposing a nominal area of 10 nm for 30 s. All structures were deposited onto p-type (100) silicon with 100 nm of thermal oxide (plasma cleaned prior to deposition (20 % O_2 in Ar, Fischione Model 1020)).

3.3.2 Analysis

The morphology of the printed samples was studied with a FEG-SEM (Magellan 400, FEI, USA). Cross-sections of samples for microstructure analysis were cut and imaged with a dual-beam FIB-SEM (NVision40, Zeiss, Germany) using the InLens detection mode and an acceleration voltage of 5 kV and final polishing currents of 40 – 80 pA. The chemical composition was qualitatively analyzed by SEM EDX spectroscopy (Quanta 200F, FEI, equipped with an Octane Super EDX system, EDAX, software: Genesis, EDAX). All spectra were recorded with identical acquisition conditions: acceleration voltage: 10 kV, amplification time: 7.68 μ s, live time: 60 s, dead time: 25 – 30 %, scan size: $5 \times 5 \mu\text{m}^2$ for small pads, $15 \times 15 \mu\text{m}^2$ for large pads, no specimen tilt. In general, all samples were stored either under vacuum in a desiccator or at atmospheric pressures in a low-humidity Ar cabinet.

The mechanical properties of the printed materials were measured by nanoindentation of pads and microcompression of micropillars. Nanoindentation was performed with three different testing setups: a Ultra Nanoindentation Tester (Anton Paar TriTec SA, Switzerland) or a iNano Nanoindenter (Nanomechanics, Inc., USA) were used to test samples of low surface roughness. Both systems were fitted with a diamond Berkovich indenter (Synton-MDP, Switzerland). An Alemnis indenter (Alemnis GmbH, Thun, Switzerland)³¹⁴ fitted with either a Berkovich or a cube-corner indenter (Synton-MDP, Switzerland) was used for indentation of LIFT (melt)-printed pads, as these samples showed higher surface roughness and thus required higher indentation depths. Typical linear loading rates were 5000 – 10 000 $\mu\text{N min}^{-1}$ and 10 mN min^{-1} for the Anton Paar TriTec and the Alemnis systems, respectively. The Nanomechanics system was used in constant strain rate mode, with a target strain rate of 0.1. Hardness and elastic modulus were recorded as a function of depth, either by performing progressive load-unload cycles (Anton Paar TriTec and Nanomechanics system) or a continuous measurement by superimposing a sinus oscillation on the load profile (110 Hz, Nanomechanics system). Reported values are as-measured hardness and modulus values averaged over a depth range adjusted to the thickness, width and roughness of the tested pads. No model to account for substrate effects was applied. The following Poisson's ratios were used for the conversion of indentation modulus to Young's modulus: Ag: 0.37, Au: 0.42, Cu: 0.36³¹⁵. For all Pt FIBID and FEBID samples, we calculated with the Poisson's ratio of the matrix material (glassy carbon, 0.2) instead of the value for Pt. A constraint factor of 2.8³¹⁶ was used for conversion of hardness to strength.

Microcompression testing was performed using an in-situ SEM Indenter (Alemnis GmbH, Thun, Switzerland)³¹⁴ mounted in a Vega3 SEM (Tescan, Brno, Czech Republic). This facilitated both sample positioning and direct observation of the deformation process. The indenter was fitted with

diamond flat punches of 1.5 – 50 μm in diameter, depending on the width of the tested pillars. Pillars were compressed in progressive loading-unloading cycles to a total strain of 10 – 25 %. Compression was performed under displacement control at a rate proportional to the pillar's height to produce a strain rate on the order of $1 \times 10^{-3} \text{ s}^{-1}$. For determination of the yield stress, load-displacement curves were converted to stress-strain curves based on the average diameter of the deformed portion of the pillar. Due to the non-uniform pillar diameter and the blurred onset of yield, no classic yield criterion was applied. Instead, we report the flow stress at 7 % strain, which corresponds directly to the representative strain under a Berkovich indenter³¹⁷. For the calculation of the Young's modulus, stress-strain curves based on the average load-bearing cross-section of the whole pillar were used. The Young's modulus was usually measured from the first unloading segment after the plastic yield point. No volume conservation was applied. Sneddon's model³¹⁸ was used to correct for pillar sink-in, using the following elastic moduli of the different substrates: soda lime glass: 72 GPa; fused silica: 73 GPa; Si <100>: 130 GPa; Si <111>: 186 GPa. Metallic coating layers between pillar and substrate were ignored in the model, as the elastic field was expected to extend far beyond those layers. Prior to testing, the top portions of most pillars were cut using a dual-beam FIB-SEM (NVision40, Zeiss, Germany) to produce flat pillar tops and to trim the pillars to an aspect ratio 2 – 3. This helped to avoid buckling and to achieve a clearer plastic yield point which is less influenced by the rounded top of the pillars. Final Ga^+ -ion milling currents of 80 pA – 3 nA were used, depending on the diameter of the pillars.

The measured mechanical data were normalized to literature values of polycrystalline thin films deposited by PVD or electrochemical deposition to decouple microstructural from chemical influences on the mechanical properties (To allow a comparison between the different chemical elements used by different AM methods) and to enable a facile comparison of the quality of printed metals to that of thin-film materials synthesized by established deposition techniques. The following values were used (Table C.2): E_{Ag} : 80.5 GPa, H_{Ag} : 1.2 GPa, E_{Au} : 80.2 GPa, H_{Au} : 1.2 GPa, E_{Cu} : 125 GPa, H_{Cu} : 2 GPa, E_{Pt} : 174 GPa, H_{Pt} : 4 GPa. Literature data for E of Co and W FEBID deposits were normalized to E_{Co} : 204 GPa and E_{W} : 369 GPa, while the hardness values were not normalized. The measured flow stress $\sigma_{0.07}$ was normalized by literature values for $H/2.8$. All FEBID and FIBID values were normalized to literature data of Pt to highlight the difference in mechanical behavior compared to metals, although we acknowledge that FEBID and FIBID deposits are mostly composed of amorphous carbon.

3.4 Results

3.4.1 Morphology

Representative samples printed with each of the studied techniques are shown in Fig. 3.1 and 3.2. If multiple annealing states were prepared, the sample annealed the longest at the highest temperature is shown. Cu and Au structures were tested for LIFT (melt), but only Cu is shown here. For Au, refer to Fig. C.1. In general, please note the marked difference in scales.

Before comparing the geometry of the printed structures (including volume, shape reproduction and surface roughness), it is important to note that the shown geometries and their dimensions were dictated by the requirements of mechanical testing: pads had to be at least a few hundred nanometers in thickness and in minimum 10 μm in width (without any upper boundaries for thickness and size) and should feature a minimum surface roughness. Pillars had to be at least 1 μm in diameter and 2 – 3 μm in height (with a maximum diameter of 50 μm). No flat top was required. Any conclusions regarding resolution and smallest printable geometries should be made with these boundary conditions in mind – none of the methods strived to synthesize the smallest geometries for this study.

In general, the geometry of the printed pads and pillars clearly reflect the individual techniques' deposition principles. FEBID and FIBID geometries show highest resolution and lowest surface roughness (due to a combination of smallest feature size and the fact that an amorphous, smooth carbon matrix is deposited), but the build volume is limited to a few cubic micrometers. In contrast, structures printed by LIFT (melt) feature the highest microscale surface roughness due to incomplete compaction upon solidification of the impacting droplets, but the build volume of LIFT is only rivaled by DIW. DIW manages to deposit smooth pillars drawn from a single filament, but pads clearly reflect the hatch pattern and thus a pronounced roughness on a scale of tens of micrometers. In general, pads fabricated without in-plane hatching show lowest surface roughness (LIFT (ink), MCED). For cryo-FEBID, drift during cycling of precursor deposition and patterning caused a shift between individual layers in pillars.

Thermal annealing of nanoparticle-inks caused shrinkage and warping of EHDP and EPD structures. In the case of EHDP, the shrinkage even resulted in suspended pads that prohibited reliable indentation testing (Fig. C.8). The warping of EHDP pillars was less pronounced for small diameters (printed without in-plane hatching and at lower flow rates, Fig. C.9). In contrast, annealing of DIW and LIFT (ink) printed geometries showed better shape retention.

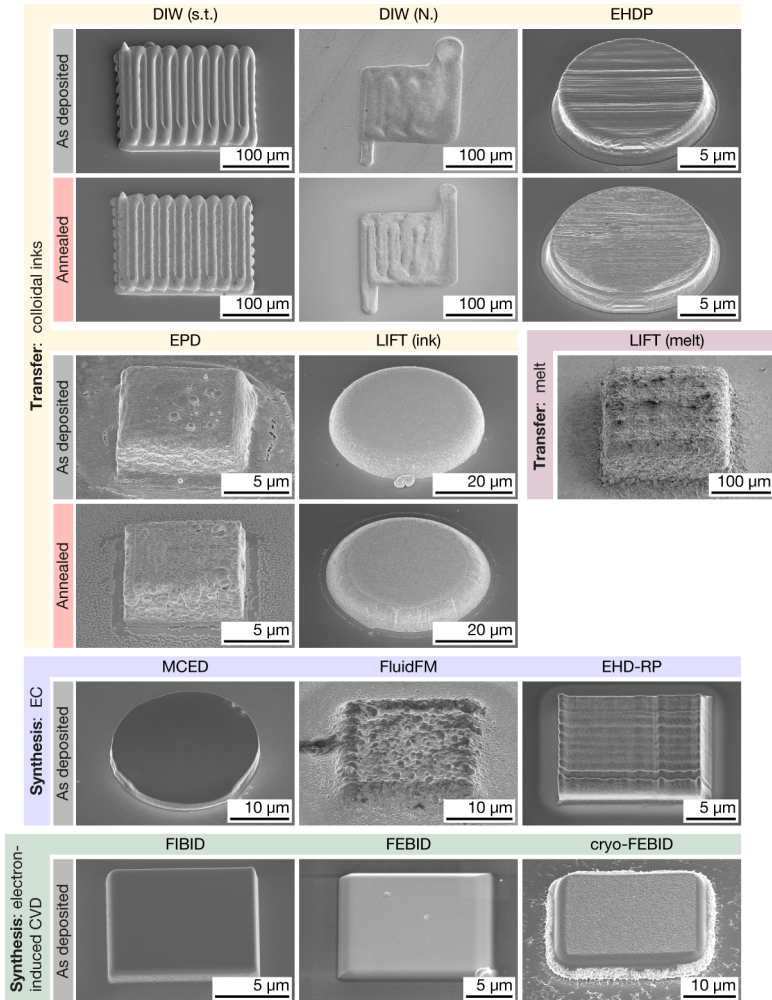


Figure 3.2 – Printed pads. SE micrographs of representative pads printed with each of the techniques. If thermal annealing was performed, samples of as-printed and annealed pads are shown. Metals: DIW, LIFT (ink): Ag; EHDP, EPD: Au. LIFT (melt), MCED, FluidFM, EHD-RP: Cu. FIBID, (cryo-)FEBID: MeCpPt(Me)₃. For Au deposited by LIFT (melt), see Fig. C.1. Tilt angles: 45°.

3.4.2 Microstructure

Figures 3.3 and 3.4 present an overview of the microstructure of the metals printed by the different AM techniques. If multiple annealing states were prepared, the sample annealed the longest at the highest temperature is shown. Only Cu is shown for LIFT (melt). Please refer to Fig. C.2 for micrographs of lower magnification for pads, and Section C.3 for a complete collection of all microstructures. Figure C.4 provides a qualitative overview of the chemical composition of printed pads analyzed by EDX spectroscopy.

Four types of microstructure can be identified in an effort to reduce the observed microstructures to their common denominators: (1) loose agglomerations of metal colloids and organic surfactants, (2) polycrystalline and porous metals, (3) polycrystalline and dense metals, and (4) dense carbon-metal composites. All as-printed colloidal inks belong to category (1). The non-metallic contrast (dark) in the micrographs in Fig. 3.3 and 3.4 is interpreted as organic components, based on the chemical analysis that suggests significant amounts of carbon in as-printed inks (Fig. C.4) and the fact that all inks in this study are composed of micro- and nanoparticles coated with organic surfactants and mixed with organic solvents. All transfer methods eventually synthesize materials of category (2), although the degree and homogeneity of the observed porosity is subjected to large variations: the microstructure synthesized upon thermal consolidation of colloidal inks is pronouncedly porous. The pore size ranges from tens of nanometers to approximately one micron, and the porosity is usually homogeneous without a preferential orientation. Metals printed by LIFT of Au and Cu melts are also porous, although the density of Cu is higher than that of Au (Fig. C.13). In contrast to annealed inks, the pore distribution is pronouncedly inhomogeneous, the pore size in the microscale range, and the pore shape non-spherical (often elongated inter-droplet gaps). Additionally, the grain size can vary by one order of magnitude within a printed structure (Fig. C.13). Category (3) is populated by Cu synthesized by additive electrochemical methods, with a typically microstructure that is nano- to microcrystalline and dense (*i.e.* no obvious porosity is detected at the studied length scale). Yet, Cu synthesized by EHD-RP features nanoscale voids in the pillars, and pads show the evolution of mostly vertical gaps at a height of ≈ 500 nm (Fig. 3.3) or already after a few layers (not shown). Below that height, the grown Cu is dense. The gaps are ≤ 50 nm in width. Room-temperature FEBID and FIBID deposits belong to category (4), *i.e.* they are dense, but as known from literature, they consist of metal nanoparticles embedded in an amorphous carbon matrix⁷³. The typical metal contents achieved with commercial setups at room temperature is approx. 10 – 15 at.%²¹⁶ for MeCpPt(Me)₃, the precursor used in this study. FEBID deposits grown at cryogenic temperatures presumably feature a similar composition, but namely the pillars feature pronounced, vertically elongated pores (Fig. 3.4).

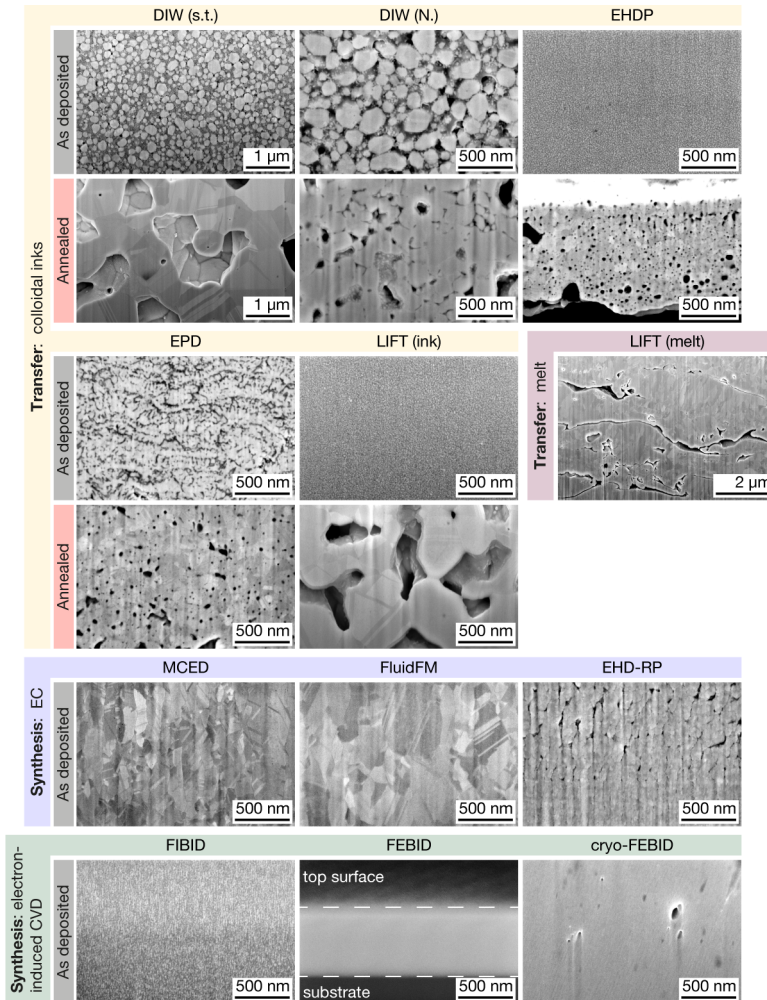


Figure 3.3 – Microstructure of printed pads. Representative cross-section micrographs of printed pads. Four distinctive microstructures are observed: (1) Loose agglomerations of metal colloids (as-deposited inks), (2) polycrystalline and porous metals (transfer techniques), (3) polycrystalline and dense metals (electrochemical techniques), and (4) dense metal-carbon composites (FIBID and FEBID). All images are tilt-corrected. FIB curtaining effects are observed in the following micrographs and are imaging artefacts rather than real features: DIW (N.), EPD, LIFT (ink), LIFT (melt), EHD-RP and cryo-FEBID. For micrographs of lower magnification, see Fig. C.2.

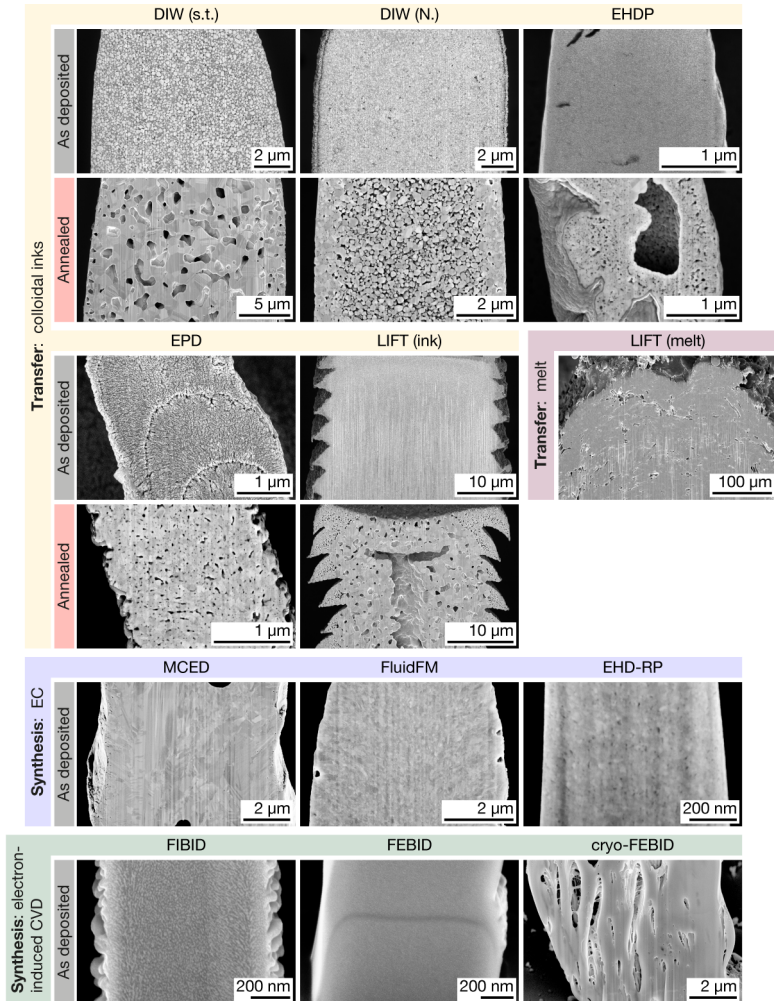


Figure 3.4 – Microstructure of printed pillars. Representative cross-section micrographs of printed pillars. The microstructure of printed pillars is generally comparable to the microstructure of the corresponding pads. However, radial microstructure gradients are obvious in most annealed pillars printed from colloidal inks (DIW, EHDP, LIFT (ink)), whereas pillars printed by synthesis methods and LIFT (melt) are more homogeneous. All images are tilt-corrected.

The homogeneity of the deposited microstructure, *i.e.* the spatial distribution of grain size or porosity, varies between techniques and also printed geometries. Annealed inks often feature gradients in porosity and variations of grain sizes within a deposit. This phenomena is observed mostly in pillars (Fig. 3.4), and less frequently in pads (Fig.C.3). The micrographs in Fig. 3.4 specifically suggest that the outer region of pillars is often denser and features smaller pore sizes (DIW, EHDP, LIFT (ink)). In extreme cases, annealed pillars developed hollow centers (EHDP, LIFT (ink)). In contrast, synthesis techniques produce a homogeneous microstructure in both pads and pillars (apart from the large pores observed in the pillars by MCED, cryo-FEBID, and the change in microstructure as a function of height in the pads by EHD-RP).

3.4.3 Mechanical properties

Fig. 3.5 presents indentation and microcompression data of samples printed by three representative techniques: DIW (s.t.) (representing transfer techniques), FluidFM (electrochemical synthesis) and FIBID (electron-induced CVD). The complete set of data from indentation and compression tests of all samples of all techniques is provided in Section C.3. The averaged values of E , H and $\sigma_{0.07}$ are plotted in Fig. 3.6a, b (together with data for previously measured properties of 3D printed metals) and listed in Table C.1. Additionally, Fig. 3.6c, d normalizes the measured values to literature values of thin films fabricated by traditional deposition techniques (PVD and electrodeposition, Table C.2) to enable a comparison between different printed metals and a general assessment of the overall quality of the printed materials. The comparison to thin-film instead of bulk metals is motivated by the fact that these are the materials and properties established in microfabrication routines.

Both the elastic and plastic properties vary by two orders of magnitudes between the individual techniques if all as-printed samples are included, and by one order of magnitude if only annealed ink-samples are considered. The normalized modulus $E/E_{\text{thin film}}$ of annealed inks and samples printed by LIFT is always < 1 , while their hardness $H/H_{\text{thin film}}$ can be ≥ 1 . Electrochemical techniques enable $E/E_{\text{thin film}} = 1$ (except EHD-RP with $E/E_{\text{thin film}} < 1$) and $H/H_{\text{thin film}} \geq 1$. Room-temperature FEBID and FIBID structures show a lower elastic modulus than Pt, but enable a high hardness of 6 – 9 GPa. As this is higher than the strength of most metals routinely used in microfabrication (typical hardness of Pt thin films $\approx 1.5 - 5$ GPa^{319,320}), $H/H_{\text{thin film}} > 1$ although $E/E_{\text{thin film}} < 1$ (A comparison to hardest metals, for example W with a hardness of 6 – 18 GPa^{321,322} would yield a normalized hardness ≤ 1). An exception are cryo-FEB deposits, which are pronouncedly more compliant and softer than their room-temperature counterparts.

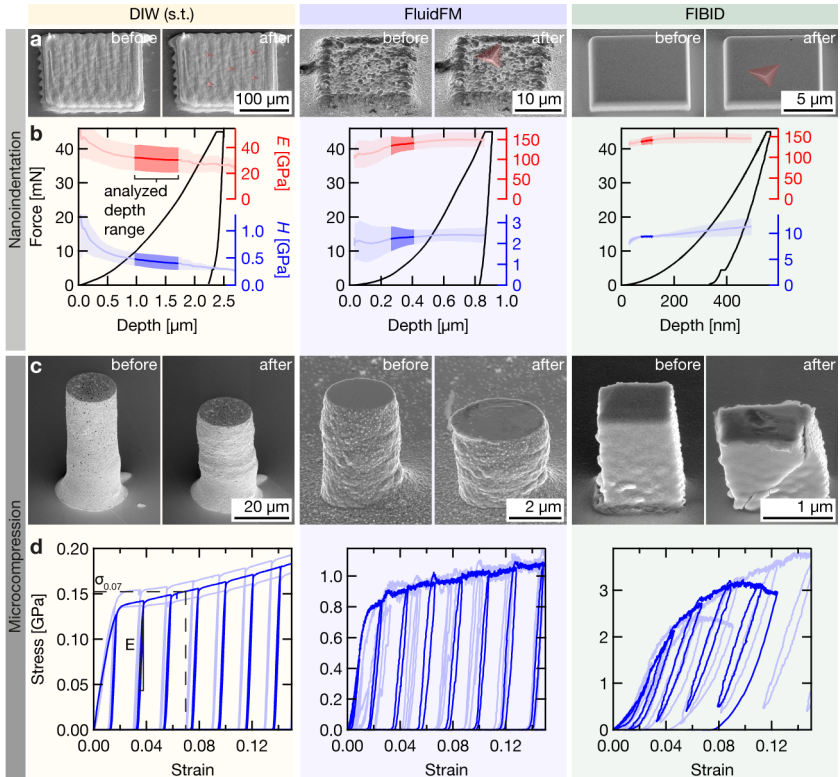


Figure 3.5 – Mechanical testing. Nanoindentation and microcompression data of samples printed by three techniques representing the main categories of small-scale metal AM: DIW (s.t.) (transfer techniques), FluidFM (electrochemical techniques), and FIBID (electron-induced CVD). **a.** Representative pads before (left) and after (right) nanoindentation. The indents are highlighted in red. **b.** Single indentation curves (black) and average Young's modulus E (red) and hardness H (blue) as a function of indentation depth. The solid line is the mean value derived from all indents, the shaded area represents the standard deviation. Elastic and plastic properties are reported from the highlighted depth range. **c.** Pillars before (left) and after (right) microcompression. **d.** Three representative stress-strain curves. One curve per technique is highlighted for clarity.

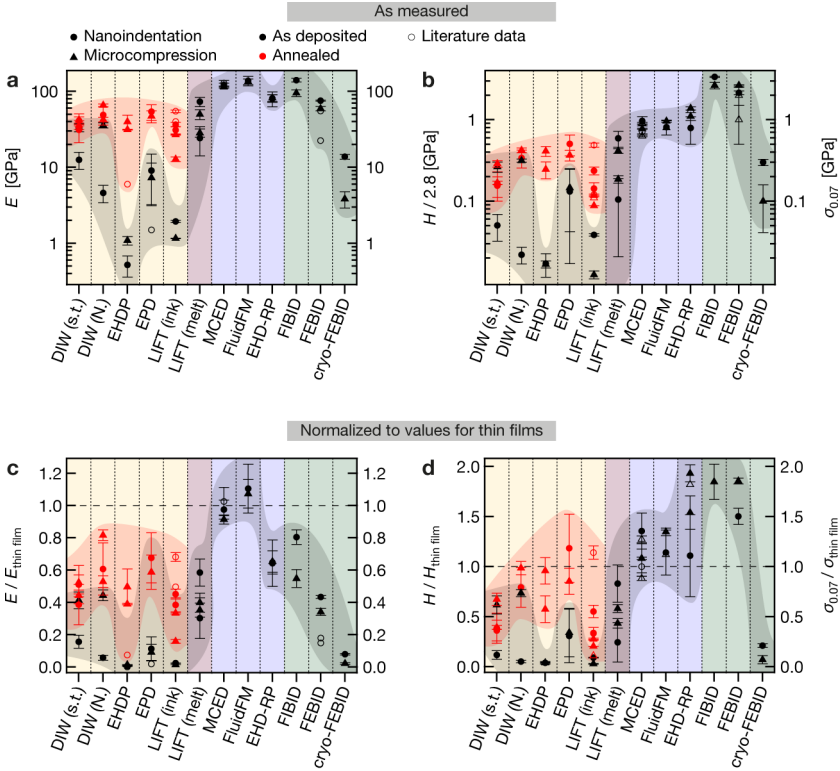


Figure 3.6 – Young’s modulus E , hardness H and flow stress $\sigma_{0.07}$ of printed metals. **a.** E measured by nanoindentation (circles) and microcompression (triangles) for as-deposited (black) and annealed (red) samples of all techniques. Literature data: open symbols. **b.** measured values for H (circles) and $\sigma_{0.07}$ (triangles). Hardness data is divided by a constraint factor of 2.8 for a direct comparison with the flow stress. Literature data: open symbols. **c, d.** Measured data normalized by literature data for thin films deposited by traditional microfabrication methods (Table C.2). References for literature data: EHDP¹¹¹, EPD¹²², LIFT, NP^{140–142}, MCEd^{148,149}, FluidFM¹⁵⁴, EHD-RP³¹¹ (Chapter 4), FEBID^{215,307}.

3.5 Discussion

3.5.1 Morphology

The present study is not suited for a comparison of geometrical abilities of the different small-scale AM methods. The samples were not fabricated for benchmarking the resolution or surface roughness of the techniques – our interest was entirely focused on microstructural and mechanical analysis. For a general overview of the geometries and resolutions accessible with the respective techniques, please refer to our recent review article⁴⁸.

Nevertheless, two points are noteworthy. First, thermal annealing of printed inks can result in distorted geometries due to shrinkage upon coalescence of individual particles – but it does not necessarily do so. Au pillars and pads printed by EHDP and EPD both underwent pronounced inhomogeneous shrinkage that resulted in wrinkled pillars and often poor adhesion of the annealed pads. In contrast, DIW and LIFT (ink) deposited Ag structures, especially pillars, showed a more isotropic volume loss (although cracking is evident in annealed DIW (N.) pads). The precise reason for the observed difference is unknown. The most obvious distinctions between inhomogeneously and homogeneously shrunken pillars are their size ($\approx 2\ \mu\text{m}$ dia. for the inhomogeneous pillars versus $\approx 10 - 40\ \mu\text{m}$ for the homogeneous pillars) and their material (Au and Ag, respectively). While the metal itself is probably secondary, the size might have a very simple effect: in small structures, small-scale inhomogeneities upon densification are proportionally larger compared to the size of the whole structure, and have thus a more profound effect on the resulting overall geometry. In larger structures, the same inhomogeneities are probably averaged or simply less obvious. However, as structures were printed by different methods and the as-deposited densities probably differ as well, no general conclusion should be drawn from this observation. In any case, the management of shrinkage and accompanied distortions will likely be a challenge for all ink-based methods in more complex geometries than those shown in this study.

Second, printing strategies differ between the individual techniques. For example, pillars printed by DIW, EPD, MCED and the FluidFM were deposited with a width of a single voxel, *i.e.* without in-plane hatching but simple out-of-plane growth, while pillars printed by EHDP, LIFT (melt), EHD-RP, FIBID, FEBID and cryo-FEBID are built from hatched layers. Most pads were printed with multiple hatched layers, but pads by LIFT (ink) and MCED are single entities (LIFT (ink): a single sheet of ink, MCED: a deposit grown with a large capillary). While this difference is clearly limited to geometries as simple as the ones presented here, the advantage of adapting to various shapes without the need for hatching within single layers is interesting. Tuning the shape and size of single voxels to accommodate certain geometries with as few voxels as possible is an advantage

of the respective techniques, which simplifies and accelerates the printing of the here demanded geometries and typically decreases the surface roughness (see pads by LIFT (ink) or MCED). Nevertheless, the surface finish and overall fidelity of real-life structures built from many voxels cannot be interpolated from these results (although LIFT (ink) can transfer complexly shaped, large sheets that enable smooth layers also for intricate layer designs¹³⁸).

3.5.2 Limitations of the study and validity and general applicability of the results

Generally, materials properties are a function of the materials' chemistry and microstructure. Naturally, this implies that no absolute value for any property can be assigned to the individual small-scale AM methods – each technique can synthesize metals with a range of properties by changing the chemistry and fine-tuning the synthesized microstructure. Thus, it is important to note that the generalization of the here reported microstructural and mechanical data underlies the following considerations: within the limits stated below, the reported values are representative and reproducible for each technique. Yet, these values are mere snapshots of the materials synthesized today, and should be perceived as a visualization of commonalities and differences between individual techniques rather than as absolute and static maxima for any given method.

Two factors constrain the interpretation of the reported results: First, the materials tested in this study are representative materials synthesized in the authors' laboratories, but were not optimized for high mechanical strength. Hence, within the limitations of each technique, higher modulus and strength can be expected once printing and annealing process are optimized. This applies strongly to ink-printed materials: the microstructure evolution upon annealing has an immense effect on materials properties, but is a function of many variables. Optimization of these process parameters was outside the scope of this study. In comparison, the microstructure of electrodeposited metals and FEBID / FIBID deposits is presumably closer to its optimum. Second, the accurate measurement of mechanical properties requires well defined geometries of the test specimens. In this respect, many of the used small-scale AM methods struggle to deposit samples with ideal geometries. Nanoindentation analysis was sometimes limited by a high surface roughness $\gg 100$ nm (LIFT (melt)), a sample thickness $< 1 - 2$ μm (FIBID, FEBID), or a distance from an indent to the edge of a pad $< 10\times$ the indentation depth (a combination of placing accuracy of the indent (± 5 μm) and limited pad width of $10 - 20$ μm in the case of EHDP, EPD, FluidFM, EHD-RP, FIBID and FEBID). Microcompression analysis was complicated by inhomogeneous pillar diameters and pillar tilt (EPD, EHDP (annealed only), MCED, cryo-FEBID). For some AM methods, these factors result in a pronounced scatter between individual samples (Section C.3): standard

deviations typically range between 10 – 20 % but can be as high as 40 – 80 % for a few techniques, especially for nanoindentation data.

The combination of limits imposed by available materials and test geometries underline the necessity to treat the here reported values as ranges rather than absolute numbers. Consequently, the following discussion focuses on common features or distinctions between the materials synthesized by the various methods rather than on detailed structure-property relationships.

3.5.3 Microstructure and resulting mechanical properties

Four types of microstructure can be identified if the observed results are reduced to their common denominators:

1. Loose agglomeration of metal colloids (as-printed inks)
2. Polycrystalline and porous metals (annealed inks and LIFT of melts)
3. Polycrystalline and dense metals (electrochemical synthesis)
4. Dense carbon-metal composites (electron-induced CVD)

These microstructures result in four distinctive classes of mechanical performance:

1. $E/E_{\text{thin film}} \ll 1, H/H_{\text{thin film}} \ll 1$ (as-printed inks)
2. $E/E_{\text{thin film}} < 1, H/H_{\text{thin film}} \leq 1$ (annealed inks and LIFT of melts)
3. $E/E_{\text{thin film}} \leq 1, H/H_{\text{thin film}} \geq 1$ (electrochemical synthesis)
4. $E/E_{\text{thin film}} < 1, H/H_{\text{thin film}} > 1$ (electron-induced CVD)

As a note: the Young's modulus of thin films $E_{\text{thin film}}$ is mostly consistent in literature and usually comparable to the bulk Young's modulus E , because the elastic properties are mostly independent of a metals' microstructure (apart from porosity). Hence, the normalized data for E is representative. In contrast, literature values for $H_{\text{thin film}}$ easily vary by a factor of two due to variations in microstructure of the deposited films (for example, H_{Ag} : 0.7 – 1.5^{323,324}, H_{Au} : 1 – 2 GPa^{325,326}, H_{Cu} : 1.6 – 3.5 GPa^{295,327–329}, H_{Pt} : 1.5 – 8.6^{319,320,330}). Consequently, the normalized H data should be treated with care, although we tried to select a value that is most representative of the available literature (Ag: 1.2 GPa, Au: 1.2 GPa, Cu: 2 GPa, Pt: 4 GPa) to normalize our data.

3.5.3.1 Transfer techniques: inks

As-deposited inks are composed of loosely packed micro- or nanoparticles. Due to organic capping layers and residual solvent, the filling factors of these colloidal systems are necessarily below the theoretical maximal values for equal spheres (random loose packing: 0.55³³¹, random close packing: 0.64³³¹, close packing: 0.74). For illustration, Richner *et al.*¹⁰⁵ have calculated theoretic volume filling factors as little as 0.21 – 0.26 for nanoparticle inks (Random loose packing, 5 nm particle dia.). Nevertheless, inks can be compared to colloidal crystals in first approximation, despite their lower filling factors. The mechanical behavior of all as-deposited inks (E : 0.5 – 10 GPa, H : 30 – 600 MPa) is similar to that of nanoparticle colloidal crystals (E : 0.1 – 6 GPa^{332,333}, H : 10 – 450 MPa³³²). The considerable variation is presumably owed to the large difference in particle packing density (presumably higher in DIW than in EHDP for example), the differences in particle shape and size distribution which will both affect the flow properties, the chemical instability of as-printed inks (and thus changing properties over time, also when kept in inert atmosphere) and the differences in ink preparation (some inks were actively dried after printing, others not). Two exceptions from this general picture of colloidal inks were observed. First, for colloidal DIW inks the strength determined by microcompression was significantly higher than the strength derived from hardness of nanoindentation of the same materials (briefly discussed in Section C.3). Second, electrophoretically deposited Au nanoparticles seem to be fused upon laser-assisted deposition rather than loosely assembled (Fig. 3.3). Such an in-situ sintering is plausible, as Au nanoparticles show a high absorption around the employed laser wavelength of 532 nm²⁵⁴, and would explain the comparably high strength of these samples.

The microstructure of annealed inks is dominated by inter-granular porosity resulting from incomplete densification upon sintering, although the absolute pore fraction varies between techniques (Fig. 3.3) and annealing states (Section C.3), and can range from $\approx 10 - 35\%$ (estimated areal fraction by threshold analysis of cross-section micrographs). Additional to the mere presence of porosity, its inhomogeneous distribution is often observed in printed pillars (Fig. 3.4). These gradients in pore fraction, pore size and grain size are probably a result of local variations in sintering conditions (heat conductance and heat capacitance) in combination with mechanical constraints exerted by both the substrate and previously sintered material (as discussed below). Apart from the microstructure, the shrinkage upon annealing can affect the printed geometries by warping or partial delamination.

In general, the observed behavior of printed inks is in qualitative and quantitative agreement with previous mechanical studies of Ag inks reporting moduli and hardnesses of 10 – 100 GPa and

0.03 – 1.4 GPa, respectively^{140,304,305} and decreasing strength with longer annealing due to coarsening of the porosity (ligament size effect)³⁰⁶. The porosity and its characteristic length scale in combination with the nanoscale grain size results in the peculiar observation that the modulus of annealed inks is invariably inferior to that of dense thin films, but their normalized hardness can be close to unity or larger. As the elastic properties of a porous material is independent of its defect density and is only influenced by the fraction and shape of its pores^{334,335}, the measured moduli are naturally lower than those of dense bulk materials. In contrast, the yield strength is additionally modulated by the grain size as well as the ligament size (in highly porous solids such as inks after short annealing^{306,336}). Consequently, a porous material can be strong if the grain size or ligament size is sufficiently small so that Hall-Petch strengthening or ligament size effects compensate the loss in strength due to the lower density. The strength of these materials typically decreases upon prolonged annealing and coarsening of grains and ligaments (compare microcompression results in Fig. C.5 and C.6, and nanoindentation hardness in Fig. C.11 and C.12).

The pronounced porosity and the large spread in elastic and plastic properties reported in this study as well as in the literature highlight a major challenge for ink-based techniques: shrinkage upon annealing is inherent to the concept of colloidal inks. Accompanying effects such as the evolution of porosity, warping of printed geometries or stress-induced failure predominantly characterize the properties of the printed materials and structures. Thus, the management of the densification and coarsening processes upon annealing is inevitable for most applications. The same conclusions apply to metals synthesized by pyrolysis of metal-containing resists structured by TPL⁹³, one of the metal AM methods not included in this study. Here, a linear shrinkage of 80 % upon pyrolysis highlights the challenge for dealing with volume loss in extremis.

The observed porosity of the annealed geometries contrasts with the low residual porosity usually reported for macroscale structures fabricated by DIW or templating of metal and metal oxide inks (with 50 % isotropic linear shrinkage)²⁸⁴. Nearly 100 % density is achieved in a range of sintered metal colloids, including Fe and Ni³³⁷, W^{285,338}, or CoCrFeNi high-entropy alloys³³⁹. To explain the marked differences, a comparison of the micro- and macroscale sintering strategies is insightful. For prevention of residual porosity, the absence of mechanical constraints is a most important factor: in sintering of large-scale DIW structures, friction reduction to the substrate facilitates unconstrained, homogeneous shrinkage and thus densification. In contrast, printed microscale objects are not free to shrink and densify – they are (and usually need to be) invariably attached to a substrate. Consequently, shrinkage is constrained by their support but also the material that has been sintered before and is already firmly attached to the substrate (such as the outer regions of annealed ink pillars or the surface of EHDP pads). Hence, complete densification cannot be

achieved, as the evolving stresses counteract the coalescence of pores or result in failure or delamination. In this light, other concepts that typically enable high densification at larger scales are probably also decreased in effectiveness at small scales, including higher sintering temperatures (homologous temperatures used for sintering of large-scale structures are typically in the range of $\approx 0.35 - 0.9$ ^{337,338}, and were $\approx 0.2 - 0.4$ for the present study) and the use of sintering aids²⁸⁵.

Consequently, a compromise between maximum densification and minimal shrinkage is probably necessary for ink-printed geometries at small scales. For highest strength combined with best shape retention (*i.e.* without complete densification), a brief annealing that guarantees neck formation between individual nanoparticles but avoids coarsening of the microstructure is probably the most promising approach, as it avoids large shrinkage but offers high strength via ligament size effect strengthening. High densification via thermal sintering will in most cases be accompanied by pronounced grain growth and hence a weakening of the metal. Thus, alternative strengthening mechanisms such as precipitation hardening should be considered for high strength if nanoporous structures are not an option. Unfortunately, it is likely that sintering protocols need to be adjusted to every geometry and ink-substrate combination: the observed gradients in microstructure and differences between the microstructure of pillars and pads subjected to the same thermal treatment (Fig. C.3) suggest that the local densification is influenced by local boundary conditions that vary for every geometry and materials combination. Nevertheless, although this optimization is not a trivial task, a large body of established sintering knowledge from powder metallurgy could in principle guide strategies for improved annealing of printed inks.

3.5.3.2 Transfer techniques: LIFT of melts

LIFT of metal melt droplets renders as-printed functional materials that do not require any post-print processing. Nevertheless, as with inks, residual porosity is a characteristic feature of the synthesized materials. This observation is in agreement with literature reports of porosities of 5 – 15 % in Cu^{129,130,135} and up to 50 % in Au¹²⁹. Grain and pore sizes are large compared to inks of early annealing states, and cannot easily be reduced. The porosity in combination with a medium grain size result in normalized elastic and plastic properties that are lower than those of dense thin films, although the measured elastic moduli of 50 – 75 GPa (Cu) and 25 – 30 GPa (Au) are higher than previously reported values (Cu: 12 GPa, Au: 9 GPa¹³¹).

The large pore size, the inhomogeneous pore distribution and the comparably high surface roughness are a challenge for the use of these materials in mechanical applications at small scales. To some extent, the porosity and roughness can be minimized at higher laser fluence, which increase the impact energy and temperature of the droplets¹³⁵. As this changes the wetting upon impact,

cooling rate and hence the grain size and grain morphology are probably also coupled to the laser fluence. As a complication, the observed microstructural inhomogeneities (variations in density and grain size) suggest that the boundary conditions for solidification are subjected to strong local variations. Consequently, microstructure engineering is a task with many variables. Nevertheless, especially Cu with its comparably low porosity could be optimized for higher strength by increasing the defect density of the melt-solidified metal. Because direct control of the local cooling rates and hence the evolving grain size is inaccessible, alternative approaches to microstructure engineering should be considered. As the LIFT process facilitates alloying¹³⁰, solid solution hardening or precipitation of an immiscible phase for hardening or grain boundary pinning could be a viable path to increase the defect density and thus the strength more independently of local cooling rates.

3.5.3.3 Synthesis techniques: electrochemical

Cu synthesized by MCED and the FluidFM, the two techniques that use classical aqueous electrochemistry, is dense and crystalline, with crystallite sizes of <100 – 500 nm. Comparable microstructural data for electrochemical AM techniques has been published earlier^{145,146,148,149,154}. As a result of the high density, the measured elastic and plastic properties (E : 114 – 138 GPa, H : 2.3 – 2.7 GPa) can easily compete with properties of Cu films prepared by sputtering or electroplating (E : 130 GPa, H : 2 GPa (grain size: 100 nm)²⁹⁵). The high materials quality of electrochemically 3D printed Cu is confirmed by previous studies of mechanical^{148,149,152,154} and electrical^{13,146} properties.

Pillars printed by EHD-RP are homogeneous and mostly dense, but they feature nanoscale pores. All pads developed vertical gaps (often resembling columnar growth), either after a few layers or only after an initially dense growth (Fig. C.2). Grain sizes in both geometries are <50 nm and thus pronouncedly smaller than those by the other electrochemical techniques. The combination of residual porosity and nanoscale grain size results in a high strength (H : 2.2 GPa, $\sigma_{0.07}$: 1.1 – 1.38 GPa) but a lowered elastic modulus (E : \approx 80 GPa). These findings are in line with previously reported mechanical data (Chapter 4). Despite the use of an organic solvent, the measured carbon content is as low as for MCED and FluidFM (Fig. C.4). Thus, it is assumed that the porosity or potentially oxide phases rather than residual organic solvents are responsible for the low stiffness. Previous results also suggest that the synthesized microstructure depends on the deposition parameters, especially the electric field (Chapter 4). The present study adds the observation that the final microstructure is further influenced by the printing strategy itself. The evolution of vertical gaps in pads is likely the result of growth instabilities in combination with preferred growth at protrusions due to field-focusing effects. The reason for the exclusive presence

of these instabilities in the pads is unclear. Yet, the initially dense growth of the pads indicate that the synthesis of dense Cu is possible given the printing parameters are optimized. Interestingly, the modulus of the denser pillars is as low as that of the pads (only the scatter is larger for the pads). It follows that also the nanoscale pores need to be eliminated to enable moduli as high as those measured for the other electrochemical methods. Thermal annealing would possibly promote densification but has not yet been studied.

In general, electrochemical synthesis of thin films offers extended options for microstructure engineering. First steps in this direction have already been made with electrochemical small-scale AM, demonstrating a range of grain sizes¹⁴⁹, twin densities^{148,152} and even local alloying and tuning of local porosity within printed geometries (Chapter 5). In its extent, the range of microstructures that could be accessed with electrochemical AM is unique amongst all small-scale AM methods. This advantage could and should be exploited for maximizing materials properties and adjusting the synthesized microstructure to the specific needs of different applications (for example electrical conductivity versus mechanical strength).

In principle, the high density and purity and resulting stiffness and strength of electrodeposited metals makes these materials the obvious choice for mechanical and also electrical applications. Unfortunately, electrochemical methods are limited in broad applicability: first, the electrochemical reduction necessitates an electrically conductive substrate, and second, the techniques are usually restricted to small build volumes due to a low deposition speed compared to transfer methods (although EHD-RP improves deposition speeds by one order of magnitude, see Chapter 4). Further, the electrochemical strategies are currently limited to metals only, while ink-, laser-transfer- and ion/electron-beam-based techniques allow for the deposition of all materials classes⁴⁸. Consequently, electrochemical methods are – for the time being – restricted to applications that demand highest materials properties in metals but can adjust to the mentioned limitations.

3.5.3.4 Synthesis techniques: electron-induced CVD

It is generally accepted that FEBID and FIBID deposits obtained from carbon-containing organometallic gases (as the precursor used in this study, MeCpPt(Me)₃) feature a composite structure, *i.e.* metal nanoparticles embedded in an amorphous hydrogenated carbon (a-C:H) matrix⁷³. Typical metal contents achieved with commercial setups at room temperature is approx. 10 – 15 at.% for MeCpPt(Me)₃²¹⁶, although systems that achieve much higher metal content have been suggested³⁴⁰.

As a result of the low metal content, the mechanical behavior is dominated by the carbonaceous matrix. The properties of a-C:H is highly dependent on its sp²/sp³ ratio, with the stiffness and

strength increasing with increasing sp^3 content^{341,342}. In FEBID and FIBID, this ratio as well as the density of the matrix are variable with the primary electron or ion energy and dose²¹⁵. Consequently, our measurements (E : 60 – 140 GPa, H : 6 – 9.4 GPa, $\sigma_{0.07}$: 2.6 GPa) as well as reported mechanical properties of FIBID and FEBID deposits (E : 10 – 100 GPa^{215,307,308}, H : 3.6 – 7.6 GPa^{308,309}, tensile strength σ_{tensile} : 1 – 2 GPa³⁰⁷) cover a large range. Yet, they are considerably lower than data of a-C:H synthesized by conventional plasma deposition techniques (E : 40 – 760 GPa^{341–343}, H : 5 – 30 GPa^{341,342}, σ_{tensile} : 7 GPa³⁴³), probably due to the contained softer Pt phase and potentially a lower sp^2/sp^3 ratio.

In general, the low volume fraction of metal is no disadvantage for mechanical performance – the stiffness compares well to that of metals synthesized with the other small-scale AM techniques, and the strength outperforms the electrochemically deposited metals by a factor 2 – 3. Further, variation of the sp^2/sp^3 ratio enables optimization of the stiffness and strength for a given application. A drawback of amorphous carbon is its brittleness compared to metals. However, as long as fracture toughness is not an issue, there is no need to increase the metal loading from a mechanical perspective. Of course, an increase of the metallic volume fraction is inevitable for electrical conductivities that can compete with those of metals, as the resistance of the carbonaceous matrix is typically high ($6.8 \times 10^{-6} - 10^{-1} \Omega \text{ m}$, which corresponds to $\approx 10^2 - 10^6 \times$ the resistivity of bulk metals.)²¹⁶.

The pronouncedly lower mechanical properties measured for cryo-FEB deposits are likely owed to the porosity of the structures (especially of the pillars). This porosity results from evaporation of nonirradiated precursor-gas upon heating the deposits from cryogenic to room temperature²³⁴. As the amount of nonirradiated precursor is a function of total fluence²³⁴, optimization of the exposure parameters could probably result in an increased density and thus improved mechanical properties.

3.6 Conclusion and outlook

We have studied the microstructure and the resulting mechanical properties of metals fabricated by almost all contemporary small-scale AM methods. The study provides a comprehensive overview of metals available today, and thus provides groundwork for optimization of the materials required tomorrow. Although none of the printing and annealing processes have been specifically optimized for this study, common similarities and differences between the synthesized metals were found: metals deposited by transfer techniques (from colloidal inks or metal melts) are typically nano- to microporous. In contrast, materials produced by synthesis techniques are usually dense, and in the case of electrochemical methods, often nanocrystalline. Thus, modern microscale AM techniques

synthesize metallic materials with a wide range of microstructures and can supply materials for various potential applications: dense and nanocrystalline metals for mechanical applications, dense and microcrystalline metals for high electrical or thermal conductivity, or highly porous materials for the use in catalysis or optical metamaterials.

The best mechanical performance is guaranteed by electrochemical techniques, FEBID and FIBID. These techniques deliver materials with dense microstructure and excellent mechanical properties, equal to those of metals used in state-of-the art microfabrication. In contrast, ink-based transfer methods and LIFT of melts typically result in materials with moduli of $0.3 - 0.8\times$ and strengths of $0.2 - 1\times$ the values for dense thin films. For inks, annealing procedures that render small ligament and pore size will likely be the optimal compromise for high strength.

Two consequences are drawn from the demonstrated limitations of modern additive materials synthesis. First, 3D printed metals are not equal to 3D printed metals – the characteristic microstructure of metals deposited by the different techniques vary considerably. Consequently, practitioners that require specific materials properties need to select the appropriate method. For good mechanical properties, electrochemical techniques or FEBID and FIBID are recommended. Applications that require low defect density should probably also rely on electrochemical methods (potentially in combination with thermal annealing for grain coarsening), while porous microstructures are most easiest printed with colloidal inks.

Second, today's challenges for the performance of metals synthesized from colloids or printed by LIFT should be tackled – relying on electrochemical and electron/ion-beam techniques is no option. Although these techniques offer high performance metals, they suffer from other drawbacks: both, electrochemical methods as well as FEBID and FIBID provide distinctly lower volumetric growth rates compared to transfer techniques⁴⁸ (partial exceptions are cryo-FEBID and EHD-RP, see Chapter 4). Additionally – and most importantly for a broad applicability – all transfer techniques offer a much wider range of accessible materials that also include non-metals, which are not available with electrochemical techniques yet. Thus, for many applications, transfer-methods are and will remain first choice for small-scale printing, despite their shortcomings in materials quality. Consequently, there is a strong need to improve the materials synthesized by these methods in order to guarantee levels of performance requested in typical applications. Hence, we urge for more detailed studies of printed materials' microstructure and, most importantly, optimization of thermal post-print processing. To this end, the large body of established sintering strategies employed in powder metallurgy should be tapped to guide attempts to improved densification of printed inks. On the other end, electrochemical and electron-beam based methods need to expand

the available materials, their compatibility with non-conductive substrates, and their volumetric growth rate.

In summary, some small-scale AM methods can already provide device-grade materials, but the narrow range of accessible chemistries and the comparably small build volumes of these methods still limit the application of additive techniques in modern microfabrication. However, if the porosity of ink-derived metals and the limited applicability of electrochemical and electron-beam-based methods are addressed, it is likely that microscale AM of inorganic materials will eventually be able to offer a large range of device-grade materials and will become a versatile and powerful alternative to lithography-based 3D manufacturing at small scales.

Chapter 4

Electrohydrodynamic redox 3D printing – accelerating electrochemical submicron-scale AM

An extensive range of metals can be dissolved and potentially re-deposited in liquid organic solvents using electrochemistry, including standard metals used in microfabrication such as Cu^{344,345}, Co³⁴⁶, Al^{347,348} or Si³⁴⁹. We harness the concept of electrochemical dissolution and redeposition for additive manufacturing, demonstrating the focused electrohydrodynamic ejection of metal ions dissolved from sacrificial anodes and their subsequent reduction to elemental metals on the substrate. This technique, termed electrohydrodynamic redox printing (EHD-RP), enables the direct, ink-free fabrication of polycrystalline 3D structures without the need for post-print processing. EHD-RP offers a minimal feature size of <100 nm and maximum printing speed of 10 voxel/s, outperforming the deposition rate of alternative electrochemical methods by one order of magnitude. The ink-free synthesis results in as-deposited functional metals with excellent mechanical and good electrical properties printed at competitive speeds and ambient pressures – readily permitting applications such as small-scale wire bonding, optical or mechanical metamaterials and printed sensors or actuators.

This chapter is based in part on: Reiser, A., Lindén, M., Rohner, P., Marchand, A., Galinski, H., Sologubenko, A. S., Wheeler, J. M., Zenobi, R., Poulikakos, D., Spolenak, R. Multi-metal electrohydrodynamic redox 3D printing at the submicron scale. *Nat. Commun.* **10**, 1853 (2019), licensed under a CC BY 4.0 license.

4.1 Introduction: Electrochemistry versus colloidal inks for small-scale AM – advantages and disadvantages

Materials performance will be a critical criterion for establishing inorganic AM in state-of-the-art microfabrication – small-scale AM will not appeal to a broad range of practitioners without access to device-grade, inorganic materials that can serve structural, electronic and optical functions and compare in quality to those materials synthesized by established techniques (PVD, CVD, electrodeposition). Unfortunately, the quality of printed metals is a major challenge for most techniques. For example, colloidal-ink-based methods are undoubtedly the most widespread and versatile class of small-scale AM techniques, because inks offer most choice of printable materials and highest compatibility with various substrates⁴⁸. However, the quality of materials synthesized from colloids is invariably inferior to metals deposited by standard deposition techniques: the required thermal annealing necessary for the consolidation of the printed inks typically results in shrinkage, residual porosity and inhomogeneous microstructure that corrupt a wide range of materials properties (Fig. 4.1c).

As concluded in the previous chapter, localized electrochemical deposition is the only concept that guarantees high materials performance. Yet, the electrochemical approach is generally not competitive with ink-based methods because it is at least one order of magnitude slower than most techniques (Fig. 4.1a) and the deposition in a wet electrochemical environment is excruciatingly complicated compared to the pronouncedly simpler ink setups (for example DIW). While optimization of equipment and processes might simplify the use of electrochemical techniques, the low speed is closely linked to an intrinsic disadvantage of today's electrochemical AM techniques: they are not compatible with vigorously forced mass-transport.

4.1.1 Mass-transport limitations of modern electrochemical AM

Comparing the deposition speed of all small-scale AM methods in Fig. 4.1a, it is obvious that transfer techniques are generally at least one order of magnitude faster than synthesis methods. This discrepancy is intrinsically linked to the difference in mass-transport limitations of these two fundamental approaches: transfer techniques rely on highly forced mass transport, and the material flux is only limited by technical parameters (maximum extrusion pressure in DIW, highest repetition rate of shots in LIFT). In contrast, *in-situ* synthesis techniques, including the electrochemical methods, primarily rely on slower forms of mass transport (diffusion, migration, very limited convection, see Section 2.3.1.4). These limitations results in comparably low deposition speeds.

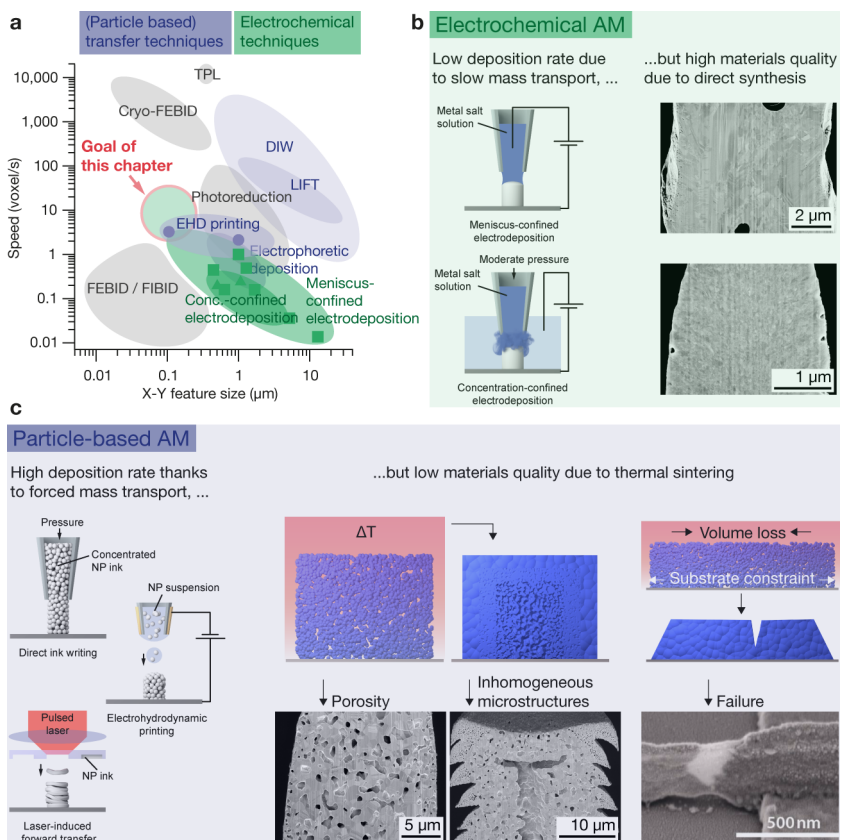


Figure 4.1 – Motivation: colloidal-ink-based AM versus electrochemical AM: deposition speed and microstructure. **a**, Speed versus X-Y feature size of contemporary small-scale metal AM techniques. Blue: transfer techniques (mostly particle-based). Green: conventional electrochemical techniques (excluding photoreduction). Grey: others. Discrete data points highlight the state-of-the-art of electrochemical techniques and EHD-printing: Squares: Meniscus-confined electrodeposition^{13,144,147,150}. Triangles: FluidFM¹⁵⁴, SICM¹⁵⁵. Circles: EHD printing^{104,105}. **b**, Electrochemical techniques. Slow mass transport (diffusion and migration, little convection) results in a low deposition rate. Yet, the direct synthesis of dense metal offers materials with excellent as-deposited properties. **c**, Particle-based transfer techniques. Forced mass transport (extrusion via pressure, ejection in an electric field, laser transfer) guarantees a high deposition rate. However, the consolidation of the printed particles in a thermal post-print process required to achieve functionality invariably results in a low materials quality. Examples: cross-sections of printed and annealed Ag pillars reveal extensive and inhomogeneous internal porosity (Chapter 3). In addition, shrinkage of several tens of percent often results in warping or failure. Example: sintered wall of printed Ag nanoparticles¹⁶. The micrograph of the sintered Ag wall in (c) is reproduced with permission from¹⁶ ©2015 John Wiley and Sons.

Please note that I ignore photoreduction in this discussion. The clear advantage in speed of the technique is acknowledged. Nevertheless, in my opinion, its potential for the synthesis of high-quality materials is not yet comparable to standard electrochemical techniques: either the synthesized structures are very rough¹⁶³ (and presumably porous to some degree) or, if surfactants are used, merely consist of agglomerated nanoparticles¹⁶². Consequently, I decided to focus on standard electrochemical approaches only (meniscus-confined electrodeposition and the FluidFM/SICM), which guarantee the synthesis of dense, crystalline and pure metals.

In analogy to transfer techniques, electrochemical printing rates could be enhanced by forced mass-transport, *i.e.* convection. Forced convection reduces the diffusion layer thickness, which in turn increases the limiting current and facilitates a higher deposition rate. Established concepts for boosting the deposition rates in macroscale electroplating are stirring²⁶³, ultrasonic fields²⁶⁴, liquid jets²⁶⁵, laser-induced convection²⁵⁶ or a combination of these methods²⁶⁶. Liquid jets and laser-induced convection were shown to be particularly effective. An enhancement in speed by a factor of 10^3 has been reported for laser-assisted electroplating²⁵⁶.

However, none of these strategies are easily implemented with established electrochemical AM methods – the agitation would interfere with the localization mechanisms. The FluidFM concept already relies on forced liquid flow, and higher flow rates are easily enforced by increasing the pressure in the dispensing probe. However, this enlarges the minimal feature size because of increased and less focused hydrodynamic transport¹⁵⁴ and is not an option for high-resolution printing. In meniscus-confined electrodeposition, the fragile balance of evaporation rate and surface tension that stabilizes the meniscus prohibits any forced liquid flow towards the tip of the pipette. Thus, control of the mass transport rate is entirely passive. For example, simulations by Morsali *et al.*¹⁵⁰ suggested that deposition rate is a strong function of pipette diameter, as small pipettes ($\varnothing 100$ nm) profit from enhanced evaporation rates which in turn increase convection towards the growth area and hence the maximum out-of-plane growth speed by a factor of 50 compared to large pipettes ($\varnothing 5 \mu\text{m}$). However, high evaporation rates in combinations with small nozzles probably increase the clogging risk, and experimentally shown growth rates were only $100 - 350 \text{ nm s}^{-1}$ ^{13,147,150}.

Thus, I propose a radically different approach to increase the deposition rate of electrochemical AM, circumventing the complications involved when enforcing a significant increase in convection in established electrochemical small-scale AM principles. Instead of modifying an existing electrochemical method to tolerate high convection rates, I suggest to turn an existing transfer technique – that is, a method proved high mass flow in combination with high resolution – into an electrochemical method.

4.1.2 Background: deposition of metals by electro spraying of their cations

A transfer technique that can tolerate the suggested change in character (from ink-based to electrochemical) is electrohydrodynamic (EHD) printing of nanoparticles. EHD 3D printing^{71,99,102} is based on jetting of charged, nanoscale liquid droplets loaded with nanoparticles. As will be shown, the replacement of these nanoparticles with solvated metal ions unlocks the combination of high mass flow and electrochemical principles, facilitating the synthesis of dense metals at high speeds.

EHD printing is a method based on the electrohydrodynamic ejection of jets or individual droplets of liquid (usually a colloidal ink for printing) from micrometer-sized glass pipettes (See Section 2.2.2 for more details). The phenomena of electrohydrodynamic ejection of a liquid has been first described in 1914³⁵⁰, and has since been applied in a wide range of applications, for example, electrospinning or electrospray ionization (ESI) for mass spectrometry (MS). To initiate EHD printing of colloids, a voltage of 100 – 1000 V is applied between a nozzle (filled with a suspension of particles) and the substrate. Driven by the high electric field, charged particles or other charges in the solvent migrate to the solvent-air interface at the aperture of the nozzle. The mutual electrostatic repulsion between the charges generates a tangential stress on the surface. This stress eventually overcomes the surface tension of the solvent and causes the ejection of a jet or a droplet, which can be significantly smaller than the nozzle diameter. Upon emission, the droplets transfer the dispersed nanoparticles from the nozzle to the substrate. After the droplet lands on the substrate, the evaporating solvent leaves a well-defined deposit consisting of loosely packed nanoparticles with a coverage of usually <1 .

The new printing method suggested in this chapter is based on the principle of EHD printing, but will use transfer of metal cations instead of metal nanoparticles in the ejected droplets. Here, the ejection of solvated metal cations towards a conductive substrate and their reduction to elemental metal upon impact will result in the electrochemical deposition of metals. A most crucial factor for the functioning of the technique introduced later is the source of metal cations used for printing. The electrochemical deposition of metals in solution requires solvated metal cations that are available for reduction. Traditional electrochemistry utilizes metal salts as sources for dissolved metal cations. Consequently, one could imagine EHD printing with solutions of metal salts instead of nanoparticle inks to transfer solvated cations to the substrate. Previous work by Park *et al.*³⁵¹ demonstrated the feasibility of printing aqueous salt solutions and confirmed that the ejected droplets contain a net charge, *i.e.* that there can be a surplus of positive cations over negative anions that would be available for reduction (Fig. 4.2a). Indeed we could show that EHD printing of aqueous solutions of CuSO_4 (1 mM–1 M) results in the formation of Cu particles in the impact

area of landing droplets (Fig. 4.2b). However, large amounts of CuSO_4 salts are co-deposited, surpassing the deposited Cu in volume (as judged from SEM images). The chemical nature of both the Cu particles and the CuSO_4 salts were confirmed by EDX spectroscopy (not shown here). Apparently, the majority of cations and anions recombine to form the original salt upon solvent evaporation – only the surplus of cations is deposited as elemental metal.

Electrospraying solvated metal cations – cation source:

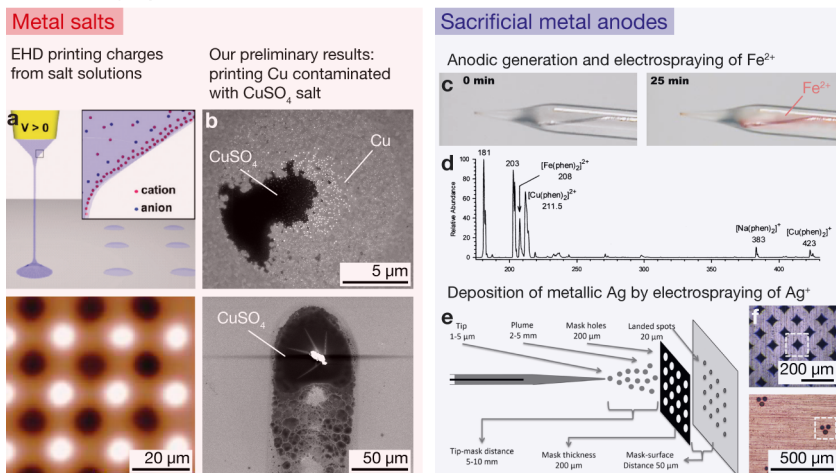


Figure 4.2 – Electro spraying of metal cations – salts vs. sacrificial anodes as sources of cations. **a – b**, Dissolved metal salts can be used as a source for solvated metal cations. However, the recombination of cations and anions results in the co-deposition of salt – only the surplus of cations is deposited as elemental metal. **a**, Charged salt droplets can be deposited by EHD ejection of aqueous salt solutions. Bottom: Potential mode Kelvin force microscopy image of positively (white) and negatively (black) charged dots of printed aqueous sodium phosphate solution³⁵¹. **b**, Our preliminary results showed that printing of 1 mM aqueous CuSO_4 solutions indeed deposits Cu particles (white), but also considerable amounts of CuSO_4 salt. Top: SE-SEM micrographs of impact area of a single droplet. Bottom: line after 50 passes. **c – f**, Solutions of cations without the accompanying anions can be produced by corrosion of sacrificial metal anodes. **c**, Time-lapsed photographs of a capillary containing an Fe(II) indicator, 1,10-phenanthroline in acetonitrile that were acquired 0 min and 25 min after application of 900 V to an Fe wire immersed in the capillary. The red color indicates the complexation of Fe^{2+} ions³⁵². **d**, The corresponding mass spectrum of the sprayed solvent confirms the formation of Fe cations (plus the formation of Cu ions due to contamination of the wire)³⁵². **e**, Electro spraying Ag^+ ions onto grounded and conductive substrates promotes the deposition of metallic nanoparticles. Spraying through a patterned shadow mask confines the deposition³⁵³. **f**, Optical micrographs of deposited Ag patterns³⁵³. **a, c – f**, Reprinted with permission from **a**,³⁵¹ ©2010 ACS, **c, d**,³⁵² ©2001 Springer Nature; **e**,³⁵³ ©2014 John Wiley and Sons.

Solutions of cations without the accompanying anions can be produced by corrosion of sacrificial metal anodes. As shown in the next sections, the absence of anions results in the deposition of

metals that are considerably purer than those deposited from electrosprayed salt solutions. The use of sacrificial anodes as precursors for metal ions is established since the late seventies for solution-based synthesis^{354,355} and since beginning of 2000 for the electrospraying of metal ions and particles^{352,353,356,357}. Fig. 4.2c demonstrates the production of Fe²⁺ cations in a electrospray capillary filled with acetonitrile and an Fe(II) indicator. Upon applying an anodic voltage to an Fe wire immersed in acetonitrile, the wire is anodically dissolved and the solvated Fe²⁺ ions form an orange [Fe(phen)₃]²⁺ complex³⁵². The corresponding mass spectrum of the solvent ejected from the capillary confirms the presence of Fe²⁺-containing clusters (Fig. 4.2d). Furthermore, the reduction of the produced cations has been shown as well: Li *et al.* have used the corrosion of sacrificial metal wires and spraying of the thereby produced cations for the synthesis of Au and Ag particles in solution³⁵⁷ or Ag particles deposited on conductive substrates³⁵³ (Fig. 4.2e, f).

Consequently, existing literature suggest that the combination of EHD printing with the anodic generation of metal cations from sacrificial sources could enable electrochemical printing of pure metals. This approach will be explored in this chapter.

4.2 Objective of this chapter

This chapter introduces a method that combines the good materials quality of electrochemical techniques and the high speed and resolution of EHD printing: electrohydrodynamic redox printing (EHD-RP). This technique is based on the *in-situ* generation and deposition of metal ions from sacrificial anodes. The ink-free, electrochemical method overcomes the previously mentioned rate limitations of electrochemical small-scale metal AM, as it enables deposition speeds that are equal to those achieved in EHD-printing and are one order of magnitude larger than typical speeds of electrochemical methods.

4.3 Methods

4.3.1 Materials

Printing nozzles. Printing nozzles were fabricated from quartz capillaries (Sutter Instrument) using the P-2000 micropipette puller system (Sutter Instrument). Pulling parameters for typical nozzle diameters are listed in Table 4.1. Heat, filament (fil), velocity (vel), delay (del), and pull refer to the five programmable parameters of the P-2000 micropipette puller system: (heat) is proportional to the output power of the laser that locally heats the glass capillary; (fil) chooses the scanning pattern (rate and scan length) of the laser beam. Larger values equal a larger scan range; (vel) is a measure of the glass temperature at which the pull is initiated; (del) is the delay between turning off the laser and start of the pull; (pull) is proportional to the force of the pull. Nozzle diameters in the range of 160 – 200 nm facilitated the most focused ejection and were thus primarily used (Fig. 4.11).

Prior to printing, the nozzles were rinsed with acetonitrile (Optima, Fisher Chemical) and subsequently filled with acetonitrile using a glass syringe (Gastight #1010, Hamilton) equipped with a syringe-filter (20 nm pore-size, Anotop 10, GE Whatman) and a non-metallic needle (MF34G-5, World Precision Instruments). In general, the overall cleanliness of the system was of high importance. Especially organic contaminants can be problematic, since many of them may dissolve in acetonitrile and are consequently co-deposited with the metallic species. Further contaminants can be leached from the glass: the use of borosilicate nozzles resulted in unusually large quantities of sodium in the case of Ag. Switching to quartz glass significantly increased the purity and strength of the printed metals.

Table 4.1 – Pulling parameters for single-channel nozzles. Pulling parameters for the fabrication of single-channel quartz nozzles with the P-2000 micropipette puller system.

| \varnothing [nm] | glass | line | heat | fil | vel | del | pull | loops |
|--------------------|-------------|------|------|-----|-----|-----|------|-------|
| 1300 \pm 100 | QF100-70-10 | 1 | 750 | 5 | 25 | 128 | 50 | |
| | | 2 | 500 | 4 | 50 | 130 | 100 | 1 |
| 170 \pm 20 | QF100-70-10 | 1 | 850 | 5 | 25 | 128 | 50 | |
| | | 2 | 700 | 4 | 50 | 130 | 100 | 1 |
| 100 \pm 20 | QF100-70-10 | 1 | 850 | 5 | 25 | 128 | 50 | |
| | | 2 | 750 | 4 | 50 | 130 | 100 | 1 |

Substrates. Substrates were usually either ITO coated glass slides (TIXZ 001, Techinstro) or Au thin-films deposited in our laboratory sputter facility by DC magnetron sputtering (PVD Products Inc.). 100 nm thick Au films (3 mTorr Ar, 200 W) on top of a 12 nm thick Ti adhesion layer (3 mTorr Ar, 250 W) were sputtered on (100)-Si wafers (SiMat). In general, the base pressure of the sputtering system was 10^{-7} Torr, and a substrate rotation of 30 rpm was used to obtain uniform film thicknesses. Au substrates covered with an electrically insulating $\text{Al}_{2+x}\text{O}_{3-x}$ layer were prepared by depositing a 1 μm thick film of the oxide by reactive sputtering (100 sscm Ar, 5.75 sscm O_2 , 5 mTorr) on previously prepared Au-substrates. Prior to reactive sputtering, the Al target was cleaned for 10 min at 300 W. For direct printing on a semiconductor substrate, an undoped Ge single crystal was used as-received ((123), 1GE 005E, Crystal GmbH, Berlin).

Sacrificial anodes. Metal wires were used as electrodes for printing. Before printing, Cu (\varnothing 0.1 mm, 99.9985 %, Alfa Aesar) and Ag wires (\varnothing 0.1 mm, 99.997 %, Alfa Aesar) were etched in pure nitric acid (Sigma Aldrich) for 20 s and 2 min respectively. Fe wires (\varnothing 0.25 mm, 99.998 %, Alfa Aesar) were etched in a 1:1:1 mixture of sulfuric acid, hydrochloric acid and water. A variety of etching procedures were tested for Zn wires (\varnothing 0.25 mm, 99.95 %, Alfa Aesar): etching in diluted nitric acid, etching in a mixture of 70% acetic acid and 30% nitric acid, or etching in a 1:1 solution of nitric acid and water with subsequent electrochemical etching in acetonitrile with approximately 0.1 M of NaClO_4 as supporting electrolyte. After etching, all wires were rinsed with deionized water and dried in air at ambient temperature (this does not apply to the last etching procedure for Zn, after which the wires were directly transferred to the nozzle). Au (\varnothing 0.1 mm, 99.998 %, Alfa Aesar), Pd (\varnothing 0.1 mm, 99.99 %, Alfa Aesar), Pt (\varnothing 0.1 mm, 99.997 %, Alfa Aesar) and Ir wires (\varnothing 0.08 mm, 99.8 %, Scientific Instrument Services, Inc.) were either used as-received or were sonicated in acetonitrile before use.

4.3.2 Printing setup

The main components of the printing setup designed and assembled during this thesis were (Fig. 4.3): a power source (B2962A, Keysight) for biasing the source electrode; a printing nozzle; an electrically grounded substrate mounted on a three-axis piezo translation stage (QNP60XY-500-C-MP-TAS, QNP60Z-500-C-TAS, Aerotech); and an optical microscope to observe the printing process. The piezo axes were mounted on an additional long-range axis (M112-1VG, PI) to enable stage translations larger than 500 μm . The nozzle was fixed to a manual three-axis micromanipulator-stage (PT3, Thorlabs) for coarse positioning, with one motorized axis (Z825B combined with a KDC101 servo motor controller, Thorlabs) for focusing the nozzle. The microscope was built from a 50 \times objective-lens (LMPLFLN, Olympus), a CMOS camera (DCC1545M,

Thorlabs), and a blue LED light source (LEDMT1E, Thorlabs). The optical axis of the lens was inclined 60° to the substrate normal. To print at low oxygen levels (200 – 1000 ppm), an acrylic chamber enclosing the printer was flushed with argon gas (4.8, PanGas). Oxygen- and humidity-levels were monitored with a gas sensor (Module ISM-3, PBI Dansensor) and a humidity sensor (SHT31, Sensirion). Usual relative humidity and temperature during printing were 30 – 50 % and 20 – 25 °C.

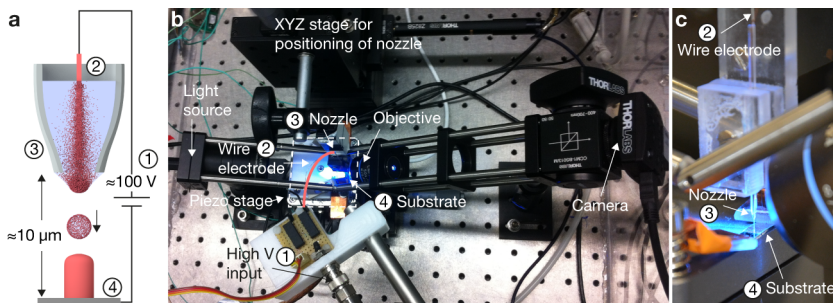


Figure 4.3 – EHD-RP setup. **a**, Schematic of the printing process with major components of the setup labelled: (1) Voltage source, (2) sacrificial metal wire anode, (3) printing nozzle, (4) grounded substrate. **b**, Main components of the printing setup, as described in the methods Section 4.3.2. Numeric labels as in (a). The wire electrode is schematically drawn in red. **c**, Zoomed image of a nozzle positioned above the substrate, with a wire anode inserted into the back of the nozzle.

4.3.3 Printing parameters

Typical electrical fields for printing were on the order of 10^7 V m^{-1} , with electrode voltages of 80 to 150 V and a typical nozzle-substrate distance of 5 – 10 μm . Throughout the text, we define the electric field as the voltage applied to the source divided by the tip-substrate distance. We use this oversimplified definition because a more precise description of the actual electric field was not attainable: the concentration of solvated ions and thus the solvent conductivity upon printing are unknown. Printing at low fields of 10^7 V m^{-1} guaranteed highest resolution, low surface roughness and facile control of the printing process. In contrast, higher fields offered increased growth rates (Fig. 4.19) and access to additional growth morphologies and microstructures (Fig. 4.14). Yet, the high speed complicated control of the overall printing process.

4.3.4 Analysis

Mass spectrometry. All mass spectrometry (MS) experiments were performed on a Synapt G2S (Waters) instrument in positive ion mode using the time-of-flight mode (ion mobility was not activated). The extraction voltage was set to 150 – 400 V using an external power supply (B2962A, Keysight). The nozzle was positioned at a distance of 2 – 4 mm from the grounded MS cone. Hence, electric fields required for EHD ejection in MS are considerably smaller compared to the fields necessary for printing. The reasons that enable electrospraying at such low voltages (typical voltages in electrospraying are often several hundred volts up to a few kV) and the reasons for higher fields necessary when printing are currently unknown. Spectra were recorded with an integration time of 1 s and summed over several acquisitions.

Microscopy. Optical microscopy was conducted using a VHX-6000 optical microscope (Keyence) equipped with a VH-Z500R and a VH-Z20T lens. Analysis of geometry and chemical composition of the printed structures were performed by scanning electron microscopy, using a Magellan 400 SEM (Thermofischer Scientific, former FEI) equipped with an Octane Super EDX-system (EDAX, software: Genesis, EDAX). EDX data were always recorded with 10 kV acceleration voltage. For preparation of cross sections and TEM lamellae of printed pillars, a dual beam FIB (NVision 40, Zeiss) was used, employing typical Ga⁺-ion-milling currents of 1 pA at 30 kV for final polishing. Transmission electron microscopy (TEM) analyses were performed on a Talos F200X TEM (Thermofischer Scientific, former FEI) operated at 200kV in both, TEM and STEM imaging modes. STEM signals were recorded using bright field (BF STEM), low-angle annular dark field (LAADF) and high angle annular dark field (HAADF) detectors simultaneously with a probe size of 0.7 nm.

Mechanical analysis. Microcompression testing was performed using an ultra-nanohardness tester (UNHT, Anton Paar Tritec SA, formerly CSM Instruments) and an *in-situ* SEM indenter (Alemnis GmbH)³¹⁴ installed in a Vega3 SEM (Tescan). Both indenters were fitted with a 8 μ m diameter diamond flat punch (Synton-MDP). Pillars were compressed either under displacement control at a rate proportional to the pillar's height to produce a strain rate of 0.01 s⁻¹, or under load-control at a rate of 0.5 mN min⁻¹, corresponding to a strain rate of 0.01 to 0.05 s⁻¹. No volume conservation was applied for analysis. Sneddon's model³¹⁸ was used to correct for pillar sink-in, using a modulus of 130 GPa for (100) Si (the substrate). To achieve a clear plastic yield point that is not influenced by the rounded top of the pillars, the top portions of the pillars were flattened by FIB-polishing prior to testing, using an ion-milling current of 10 pA.

Electrical analysis. Electrical resistance measurements were performed in a dual beam FIB microscope (NVision 40, Zeiss) using a Keithley 6430 source-meter and a Kleindiek W micromanipulator needle to establish an electrical contact to Pt pads that were deposited onto the printed line (for more detail, see Fig. 4.18). Samples for electrical measurements were printed from grounded, 75 nm thick Ag electrodes (thermally evaporated, base pressure 3.2 mbar, 1 \AA s^{-1} , Kurt J. Lesker Company) onto p-type (100) Si wafers (SiMat) covered with a 50 nm thick thermal oxide and a 50 nm thick Si_3N_4 diffusion barrier.

Analysis of speed. Out-of-plane growth rates were measured and averaged for 50 pillars per reported speed value. The speed was derived by measuring height h , diameter d and printing time t for each individual pillar. The approximate number of voxels per pillar was defined as $n_{\text{voxel}} = h/d$, and the resulting voxel-speed, that is, the growth rate normalized by the feature size, as $v_{\text{voxel}} = n_{\text{voxel}}/t$.

4.4 Results

4.4.1 The principle of electrohydrodynamic redox printing

Electrohydrodynamic redox printing (EHD-RP) utilizes basic electrochemistry to synthesize metallic deposits: *in-situ* dissolution of a metal anode M^0 immersed in a pure liquid solvent (acetonitrile in this case) generates solvated metal ions M^{z+} inside the printing nozzle (Fig. 4.4a). These ions M^{z+} are ejected towards the substrate, where they are reduced to form the metallic deposit M^0 (see Section 4.4.2 for more details regarding the growth mode). The ion source is quasi-infinite, as the volume of the anode is many orders of magnitude larger than the printed volumes. The emission of ions is accomplished by electrohydrodynamic (EHD) ejection of ion-loaded solvent droplets from the orifice of the printing nozzle³⁵⁰. An applied DC voltage of 80 to 150 V drives the EHD ejection of droplets and at the same time ensures a sufficiently high anodic surface potential for the dissolution of the source electrode. Direct printing onto metallic and semiconductive substrates as well as indirect printing across insulators is accessible with this concept (Fig. 4.6).

The use of sacrificial metal electrodes combined with the localized electrochemical reduction of the generated ions on the substrate makes this work distinct from existing AM concepts in general⁴⁸, and more specifically, from previous demonstrations of ink-based EHD micro- and nanoprinting of metals^{16,99,104}. Yet, sacrificial anodes as precursors for metal ions are well established for solution-based synthesis^{354,355} and electrospaying of metal ions and particles^{352,353,356,357}. EHD-RP differs from these experiments by enabling highly localized electrochemical growth of dense materials as opposed to the deposition of isolated particles^{353,357}.

4.4.2 Deposition mechanism – electrochemical growth via reduction of ions by charge transfer from the substrate

A key feature of EHD-RP is the electrochemical production of solvated ions and their electrochemical reduction on the substrate. In the following, we show evidence for this process and consequently establish an electrochemical growth mechanism underlying EHD-RP.

Of the two major stages of deposition, the oxidative generation of solvated ions from sacrificial electrodes is widely accepted^{354,355}, and has previously been verified in electro spray ionization experiments^{352,353,356,357}. In contrast, the reduction of ejected ions to elemental metal has received less attention. In principle, two basic mechanisms for the deposition of metallic materials from ejected metal ions can be distinguished: neutralization of ions on the substrate, followed by the

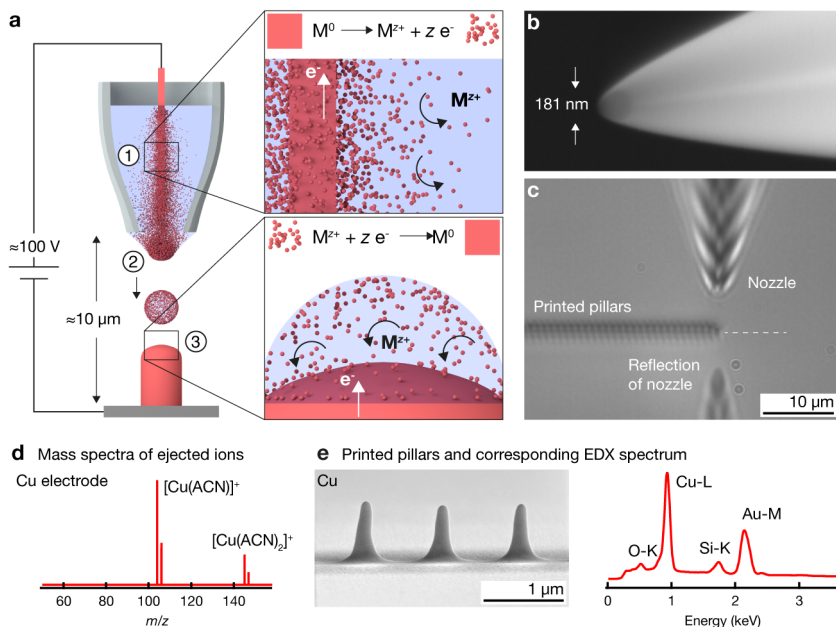


Figure 4.4 – Working principle of EHD-RP. **a** (1) Solvated metal ions M^{z+} are generated within the printing nozzle via electrocorrosion of a metal electrode M^0 immersed in a liquid solvent. (2) Ion-loaded solvent droplets are ejected by electrohydrodynamic forces. (3) Upon landing, M^{z+} ions are reduced to zero valence metal M^0 through electron transfer from the substrate (Schematic not drawn to scale: typical dimensions of the electrode wire are $100 \mu\text{m} \times 2 \text{ cm}$). **b**, Low-vacuum SE micrograph of a quartz printing nozzle. **c**, Optical micrograph of the printing process. **d**, Mass spectrum of ejected ions when using a Cu anode in acetonitrile (ACN). **e**, SE micrograph of printed Cu pillars with corresponding energy-dispersive X-ray (EDX) spectrum reflecting the chemical nature of the source electrode. The Si-K and Au-M peaks originate from the substrate. The O-K peaks likely indicates residual solvent or minor oxidation. Tilt angle of the micrograph: 85° .

bottom-up growth of a metallic deposit, or neutralization of ions in flight, followed by cluster formation and deposition of individual particles on the substrate. The first mechanism is supported by Cooks and coworkers: they suggest the neutralization of solvated ions on the grounded substrate after studying the delocalized synthesis of metals via spraying of metal cations from sacrificial sources^{353,357}. Yet, the authors only demonstrate the deposition of isolated nanoparticles and do not present evidence for fused and dense metallic materials. The second mechanism is regularly applied for the synthesis of inorganic nanoparticles by electrospray deposition³⁵⁸, but usually requires active neutralization of droplets in flight, followed by pyrolysis of the neutralized precursors

(often metal salts). To our knowledge, formation of metallic particles without active neutralization has not been reported. Nevertheless, both mechanisms are considered for the following discussion of the deposition mechanism underlying EHD-RP. Thus, the main question to be answered is: are ions reduced on the cathode and thus facilitate an electrochemical growth from the substrate, or are the ions neutralized in mid-air and deposit as loose particles onto the substrate?

Our interpretation is primarily based on a comprehensive microstructure analysis of the printed deposits and a detailed look at the nature of the ejected ions. Further support of the growth hypothesis is presented in Appendix D.1: a theoretical calculation of the maximum size of a particle formed in flight, and a study of the printing on substrates that inhibit neutralization via charge transfer from the substrate.

The polycrystalline, textured as-deposited microstructure excludes a particle-based deposition mode altogether (Fig. 4.12, 4.14). Indeed, the microstructure evolution within individual pillars along the pillar axis – grain coarsening and faceted grain boundaries accompanied by the crystallographic alignment of the grains – evidences grain formation and growth during deposition. This is best demonstrated by pillars printed in high field conditions (Fig. 4.14b, c). Pillars fabricated at lower electric fields present less obvious but nevertheless clear evidence of the same growth process occurring at somewhat lower rates. The excellent mechanical strength shown by grown pillars also excludes particle-based materials (Fig. 4.17). Thus, we conclude a mechanism based on electrochemical growth and exclude any significant contribution of particle deposition.

The electrochemical deposition is likely facilitated by the arrival of individual, solvated ad-ions on the substrate. MS data for a large range of m/z evidences the exclusive formation of mono-metallic clusters of ions containing a single metal cation only (Fig. 4.5). The absence of bi- and tri-metal clusters again indicates a very low probability for the formation of any particles: if particles were to nucleate in air, multi-metal clusters, which are intermediate stages of particle formation, must be present in the MS spectra. It should be noted that results from MS are not directly comparable to the printing process, because the time of flight in air is longer in an MS-experiment compared to printing (distance and voltage MS: 0.5 – 2 mm, 150 – 400 V, printing: 5 – 10 μm , 80 – 150 V). Nevertheless, because of the increased flight-time in MS, it can be stated with high certainty that if single-metal ion-clusters are the only species detected in MS, they are also the only species contributing to the growth upon printing.

In summation, we conclude that EHD-RP is based on the electrochemical growth of metals enabled by single-metal ad-ions that are neutralized upon charge transfer from the substrate.

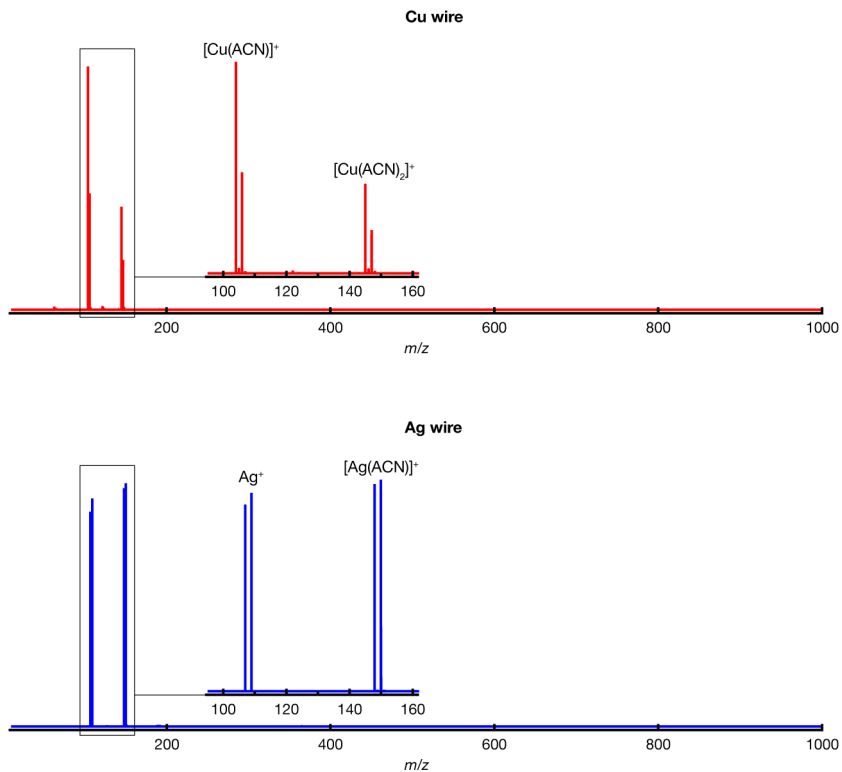


Figure 4.5 – Only single-metal ion clusters are detected in MS. Mass spectra for spraying with a Cu (top) and a Ag electrode (bottom) immersed in acetonitrile (ACN). No significant contributions other than those from single-metal ion clusters are detected up to a m/z ratio of 1000.

4.4.3 Compatibility with conductive, semiconductive and insulating substrates

Electrons are required for the reduction reaction involved in the deposition of metals by EHD-RP. Currently, these electrons need to be supplied via charge transfer from the substrate, although alternative sources could be imagined. Consequently, direct printing of metals is easiest on electrically conductive and semiconductive substrates (Fig. 4.6a). Direct printing on electrically insulating materials is not yet accessible, but printing across insulators between conductive pads is enabled by the as-deposited conductivity of the printed metals (Fig. 4.6b, c).

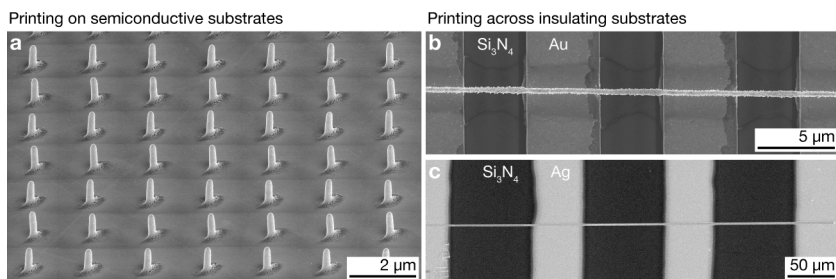


Figure 4.6 – Compatible substrate. EHD-RP enables printing on semiconductive and insulating substrates. **a**, SE SEM micrograph of Cu pillars printed directly onto a single-crystalline Ge substrate (undoped and as-received). **b – c**, Top-view SEM micrographs of Cu lines printed between Ag electrodes across electrically insulating Si_3N_4 substrates: printing from conductive regions onto and across insulating substrates is facilitated by the as-deposited conductivity of the printed lines (SEM signal: a, b: SE, c: BSE).

4.4.4 Range of printable metals

So far, we successfully printed Cu, Ag and Au (Fig. 4.7). In comparison with Cu and Ag, the surface morphology of Au pillars suggests a higher porosity, while the EDX spectrum indicates more pronounced amounts of carbon residue. When printing with Au, unusual clogging of the nozzle is often observed (a problem that is inexistent when using large nozzles of 1 – 2 μm in diameter). Additional to Cu, Ag and Au, we demonstrated first steps towards printing of Zn, Pd, and Fe: Zn was printed, but its deposition is highly irreproducible. Often, Cu instead of Zn is printed using a pure Zn anode wire – apparently, residual Cu contamination on the anode is etched with high preference over Zn. During the deposition of Zn (Fig. 4.8a) in air, the growth rate of Zn was markedly slower than the rate of Cu or Ag. Deposition in Ar atmosphere was not yet

attempted. Additionally, the deposition was unfocused and is presumably heavily contaminated. Clearly, the anodic as well as the cathodic reactions need further attention to enable printing of Zn.

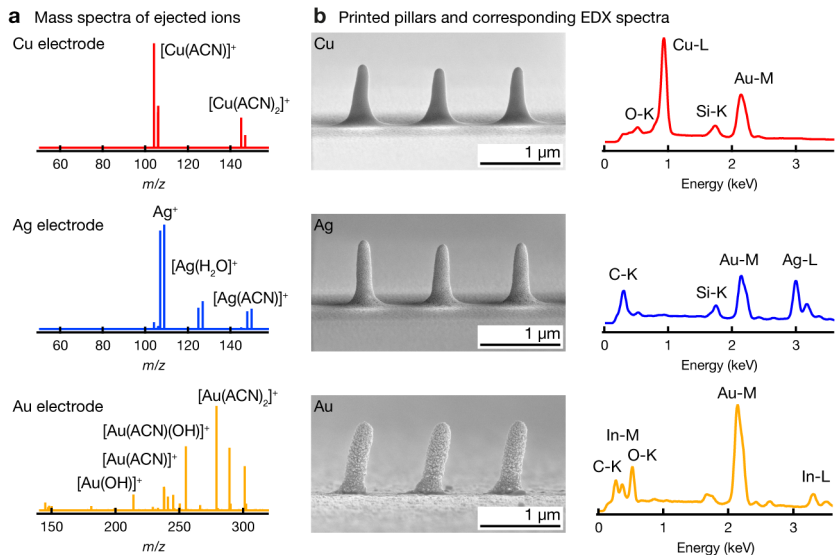


Figure 4.7 – Printing Cu, Ag and Au. **a**, Mass spectra for electrospaying with a Cu, a Ag and a Au wire. **b**, SE micrographs and **c**, corresponding EDX spectra. Cu and Ag were printed on a Au/Si substrate, whereas Au-pillars were printed on an ITO substrate. O-K, In-M and In-L signals originate from the ITO substrate. Image tilt in **b**: 85°.

Furthermore, MS spectra of Pd⁺ and Fe⁺ ions were recorded using Pd or Fe wire anodes in acetonitrile (Fig. 4.8b). However, printing Pd and Fe was unsuccessful so far – mostly organic contaminations and sodium was printed with these metals. Both, Pt and Ir anodes were used in MS, but no respective ions were detected.

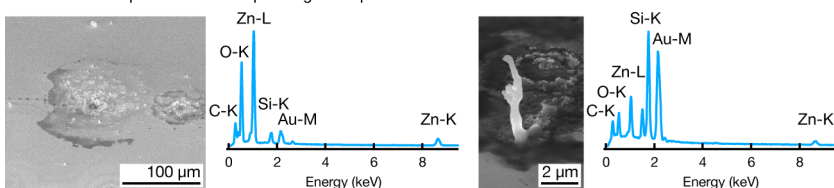
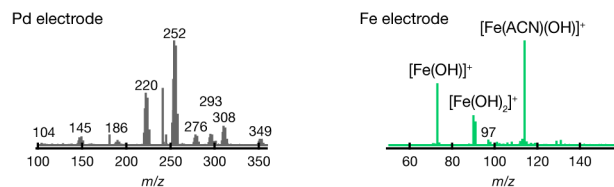
a Printed Zn deposits and corresponding EDX spectra**b** Mass spectra of Pd and Fe

Figure 4.8 – Towards printing Zn, Pd and Fe. **a**, SE micrographs and corresponding EDX spectra of Zn deposits printed on Au substrates in air. Printing of Zn is pronouncedly slower than printing of Cu or Ag. Additionally, the deposits are poorly confined and presumably heavily contaminated. **b**, Mass spectra for electro-spraying with a Pd and Fe electrode. m/z ratios: **Pd**: Pd^+ (104, 105, 106, 108, 110); $[\text{Pd}(\text{ACN})]^+$ (145, 146, 147, 149, 151); $[\text{Pd}(\text{ACN})_2]^+$ (186, 187, 188, 190, 192); $[\text{Pd}(\text{ACN})_2(\text{OH})_2]^+$ (220, 221, 222, 224, 226); $[\text{Pd}(\text{ACN})_2(\text{OH})_2(\text{CH}_3\text{OH})]^+$ (252, 253, 254, 256, 258); $[\text{Pd}(\text{ACN})_3(\text{OH})(\text{CH}_3\text{OH})]^+$ (276, 277, 278, 280, 282); $[\text{Pd}(\text{ACN})_3(\text{OH})_2(\text{CH}_3\text{OH})]^+$ (293, 294, 295, 297, 299); $[\text{Pd}(\text{ACN})_3(\text{OH})(\text{CH}_3\text{OH})_2]^+$ (308, 309, 310, 312, 314); $[\text{Pd}(\text{ACN})_4(\text{CH}_3\text{OH})_2]^+$ (349, 350, 351, 353, 355). **Fe**: $[\text{Fe}(\text{ACN})]^+$ (97).

4.4.5 Geometrical capabilities and spatial resolution

EHD-RP fulfills all stages of geometrical capabilities listed in Section 2.3.1.1 (Fig. 2.14a). Overhangs up to 90° can be printed when synchronizing out-of-plane growth rate and in-plane stage-translation speed (Fig. 4.9a). More complex geometries can be printed with a layer-by-layer strategies. Here, it is important to note that the sine waves in Fig. 4.9b were printed with interrupted trajectories within each layer – EHD-RP thus enables voxel-on-demand printing, which is necessary for most intricate geometries that cannot be printed with continuous trajectories. Out-of-plane wires with aspect ratios of $10^2 - 10^3$ are accessible by continuously retracting the printing nozzle (Fig. 4.9c). The largest aspect ratio printed to date was >1380 (with a diameter of ≈ 260 nm).

Nevertheless, geometrical complexity and fidelity are currently not as high as those offered by some alternative single-metal techniques⁴⁸ – a shortcoming that is shared amongst all EHD-based microprinting techniques. Unwanted growth at edges and corners (Fig 4.10b) and elevated portions of a geometry is favored by the auto-focussing effect of EHD-printing.

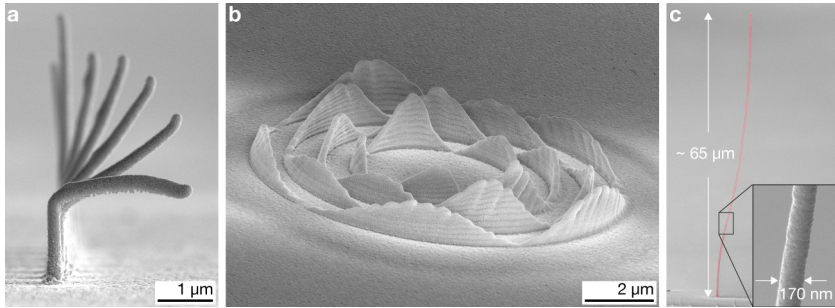


Figure 4.9 – Geometry. **a**, Overhangs formed by a lateral translation of the stage balancing the out-of-plane growth rate. The sequence of pillars was printed by increasing the respective in-plane translation speed towards the front pillar, with a maximum speed of $2.1 \mu\text{m s}^{-1}$. **b**, Concentric, out-of-plane sine waves printed with a layer-by-layer strategy. **c**, Cu wire with an aspect ratio of ≈ 400 . All panels SE-SEM micrographs. Image tilts: a: 85° , b: 34° , c: 82° .

Geometrical features printed by EHD-RP are well within the submicron range. Typical diameters of printed pillars are in the range of 100 – 300 nm (Fig. 4.10a, b). Arrays with a pillar-to-pillar spacing of 500 are printed reproducibly, while a spacing of 250 nm is not yet possible. In-plane features smaller than 100 nm have been printed (Fig. 4.10c). For layer-by-layer printing modes, the spatial resolution is 250 nm (Fig. 4.10d).

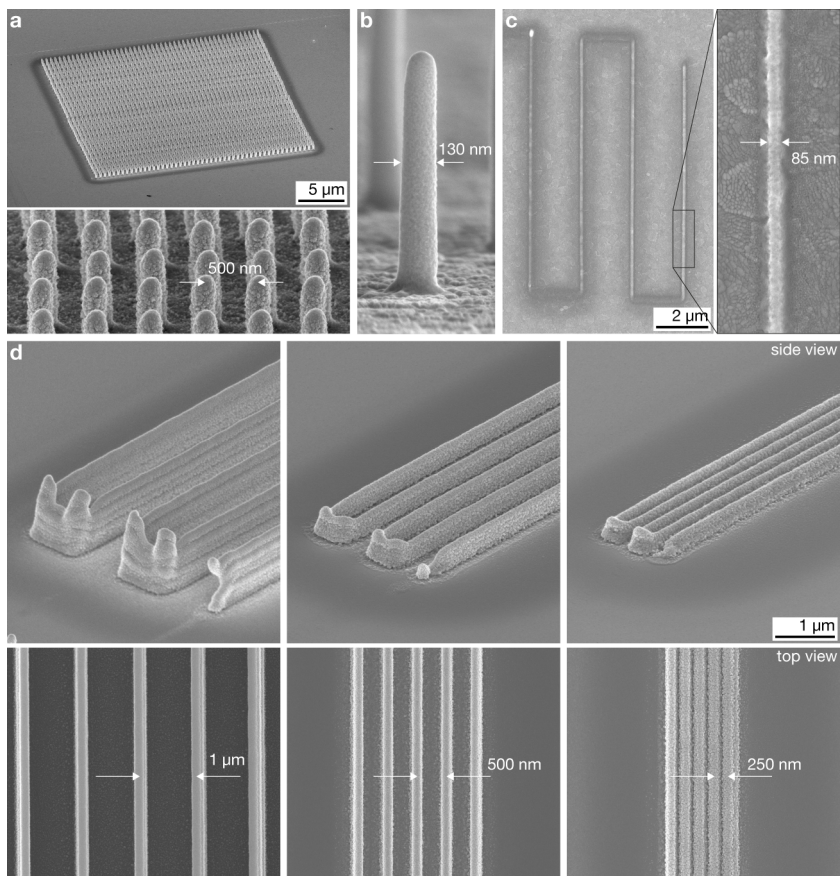


Figure 4.10 – Spatial resolution. **a**, Array of 50×50 Cu pillars printed with a point-to-point spacing of 500 nm. Image tilt: 57° . **b**, Cu pillar 130 nm in diameter. Image tilt: 77° . **c**, Printed Cu line less than 100 nm in width. **d**, Walls printed at decreasing wall-to-wall spacing, with a minimum spacing of 250 nm. Height: ten layers for the leftmost image, three layers for the others. Image tilt top row: 60° . All panels SE-SEM micrographs.

4.4.5.1 Effect of nozzle size on feature size and morphology

The size of the printing nozzle has a pronounced effect on the size and morphology of the printed structures. Three main printing modes are enabled by the use of different nozzles: a so termed spraying mode, a focused mode and a porous mode (Fig. 4.11). While we typically use nozzles that facilitate the focused mode, the other modes can be of interest if either thin but homogeneous films need to be deposited (spraying mode) or high porosity is required, *e.g.* for high surface area or high optical absorption. The focused mode is most suited for high-resolution printing. Here, a nozzle diameter in the range of 160 – 200 nm facilitates focused ejection of ion-loaded solvent. Additionally, solvent flow rates are low enough to allow for prompt evaporation of solvent, resulting in possibly no or only a small sessile solvent droplet on the substrate. Printed features show homogeneous diameters and a dense microstructure, and growth is fast and regular. Highly porous structures are achieved with nozzle diameters much larger than 200 nm. In this mode, a clearly visible, sessile solvent droplet is sustained on the substrate by the increased solvent flow rate. As a downside, the lateral reproducibility is reduced and growth rate is irregular. A defocused, spray-like ejection from nozzles ≤ 100 nm characterizes the third mode. Due to spraying, lateral feature size is increased and pillars show a large base that gradually narrows due to charge-focusing⁹⁹ as pillar growth proceeds.

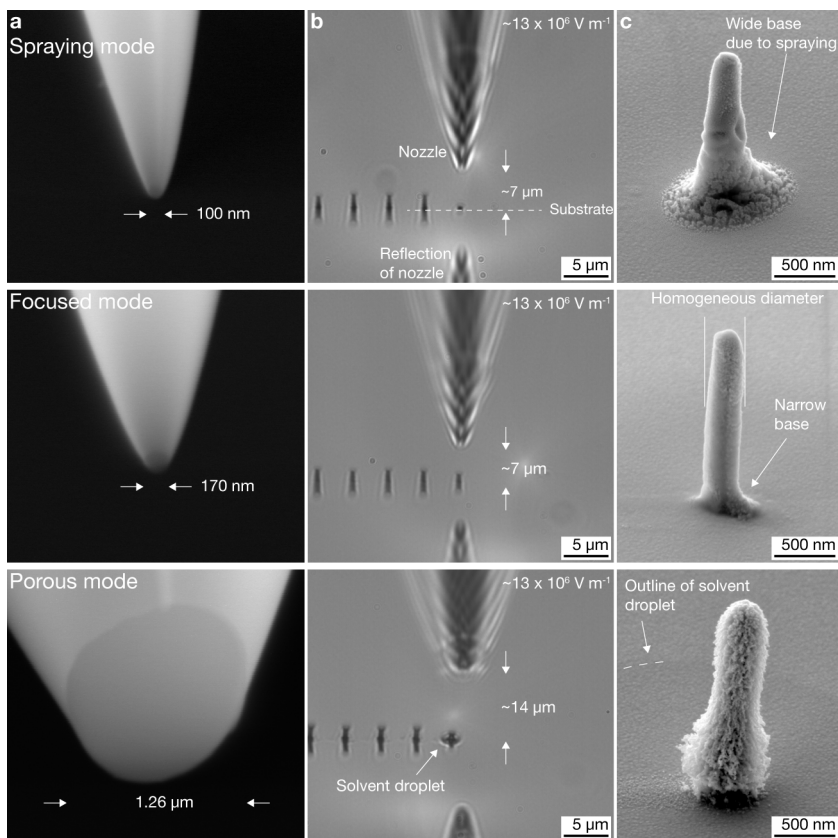


Figure 4.11 – Influence of nozzle diameter on feature size and morphology. Three printing modes are accessed with three different nozzle sizes. **a**, Low-vacuum SE micrographs of nozzles with three characteristic diameters, **b**, optical images of the printing process at a constant electric field, and **c**, SE micrographs of representative pillars printed with the respective nozzles. **Spraying mode:** spraying of the solvent is typically observed for nozzle openings ≤ 100 nm, resulting in pillars with a pronounced base and inhomogeneous diameters. This mode is best applied for spraying of thin films. **Focused mode:** using nozzles of 160 – 250 nm in diameter, the deposition is focused and pillars grow with an almost homogeneous cross section. This mode is used for high-resolution printing. **Porous mode:** For large nozzles with openings on the order of 1 μm , a higher mass flow feeds a sessile solvent droplet during printing. This results in highly porous deposits and poorer lateral resolution. Note: As the growth rate with larger nozzles is faster, the tip-substrate distance is twice the one of the other modes to avoid growth of the pillars into to nozzle. This was compensated by doubling the applied voltage to guarantee a constant electric field. The enlarged distance however has no observable effect on the printed morphology.

4.4.6 Microstructure

Under typical printing conditions, the microstructure of printed Cu is nanocrystalline and dense (Fig. 4.12). For Ag, the density is typically >90%. As suggested by Fig. 4.7, the density of Au is currently lower. The morphology and microstructure are however pronounced functions of several factors. A (presumably incomplete) list: the printing atmosphere, the electric field, the nozzle diameter and the printed metal. Many of these influences have merely been observed up to this point but have not yet been studied in detail. Clearly, further studies will be necessary to expose the relationships and mechanisms of microstructure evolution in EHD-RP.

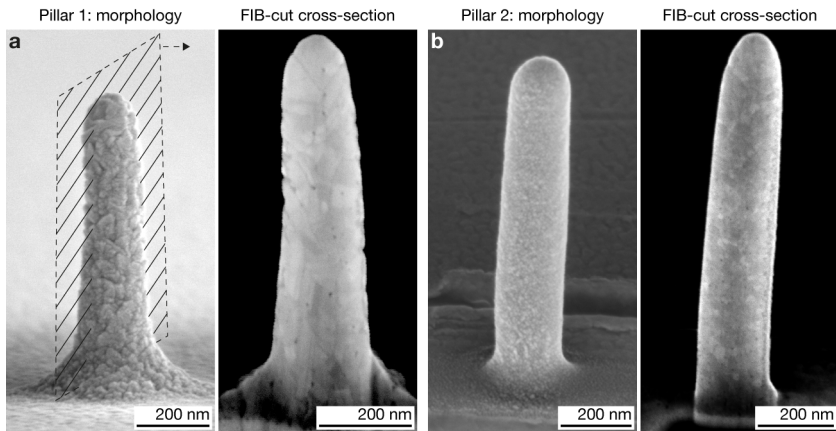


Figure 4.12 – Printing dense Cu. Two different as-printed Cu pillars and corresponding cross-sections showing the dense, polycrystalline microstructure (InLens SE). The cross-sections are tilt-corrected. The pillar in **a**, was printed at a higher voltage than the one in **b**, but also with a different nozzle. Hence, the obvious difference in grain size cannot directly be attributed to the difference in electric field.

In general, printing in Ar-atmosphere (100 – 200 ppm O₂) hinders the formation of unwanted oxide phases that could form when printing in air. No crystalline oxides are detected in the electron diffraction pattern of a pillar printed at ≈ 200 ppm O₂ (Fig. 4.13a). In contrast, additional phases were detected with a pillar printed in air (Fig. 4.13b). However, the additional reflexes could not be correlated to one of the known Cu oxide phases. As a further indication for oxidation in air, the presence of a second phase in Cu observed to evolve in parallel with oxygen content of the printing atmosphere (Fig. D.2). In summation, the presence of an oxygen-containing phase is likely when printing in air, but more detailed studies are required to clarify its nature.

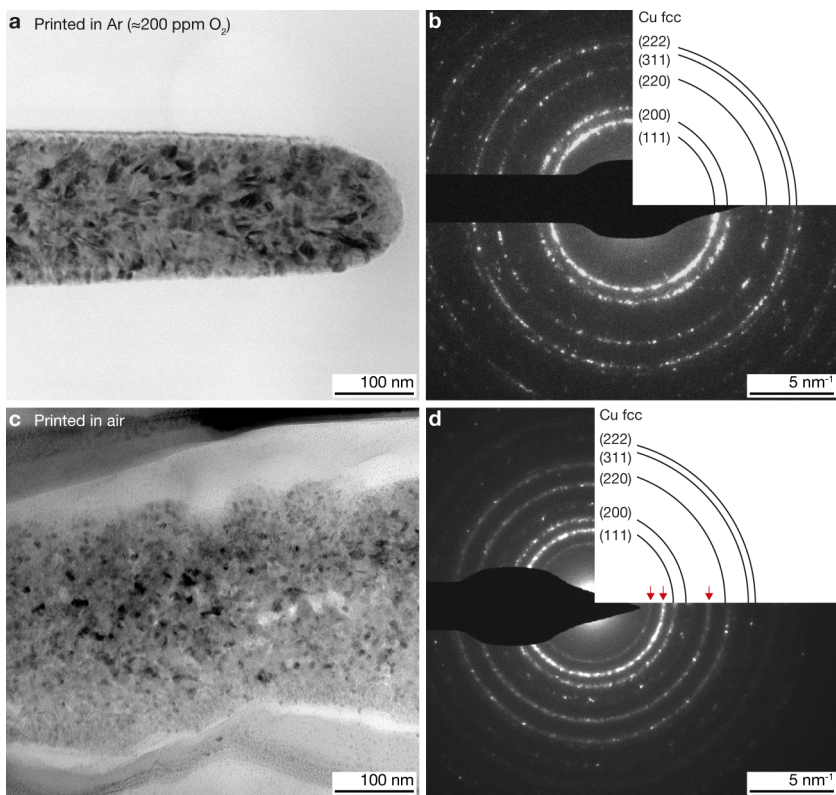


Figure 4.13 – Printing without crystalline oxides. Cu can be deposited without crystalline oxides if printing is performed in oxygen-deficient atmosphere. **a**, BF-TEM and **b**, corresponding diffraction pattern of a Cu pillar printed in Ar atmosphere (≈ 200 ppm O_2). The electron diffraction pattern shows the Cu fcc structure. **c**, **d**, In contrast, printing in air (21 % O_2) promotes the formation of an additional, yet unidentified phase (red arrows).

The grain size and defect density is a function of the electric field applied during printing (Fig. 4.14). At low fields of $1 \times 10^7 \text{ V m}^{-1}$, the grain size is of the order of 20 nm, hence approximately a tenth of a pillar diameter. Additionally, the presence of point defects is pronounced (vacancy clusters or nanometer-sized pores, visible as small, dark areas arranged as chains in the atomic number sensitive HAADF STEM micrograph, arrows in Fig. 4.14a). Printing at higher fields of $4 \times 10^7 \text{ V m}^{-1}$, results in much larger grains, with some grains extending across the whole pillar diameter ($\approx 200 \text{ nm}$ in Fig. 4.14b, c). In addition, a crystallographic correspondence between neighbouring grains, *i.e.* texture, as well as a decrease in point defect density were detected in high-field pillars. The increase in grain size with the electric field as well as the marked decrease in the defect density suggest a pronounced increase of the atomic mobility with the electric field applied during printing.

Due to the effect of the electric field on the grain size, a gradient microstructure were observed in pillars that were grown under conditions of large variations in the electric field strength, for example when a pillar was grown across significantly more than half the gap distance (Fig. 4.15). A sharp instead of a gradual transition from fine to coarse morphology is observed. This suggest a non-linear relation between microstructure and field strength. Presumably, this explains why the microstructure along the pillar axis is typically constant under normal printing conditions, as the low fields used for printing are probably below the threshold for coarse grains (Fig. 4.12, 4.14).

Unfortunately, the effect of increased grain size with increased electric field is not easily translated into layer-by-layer printed structures. At low electric fields, the microstructure of walls or pads (printed from multiple layers with in-plane stage translation) compares to that of pillars (printed with a stationary stage) (Fig. 4.16 a, b). In contrast, a larger electric field results in a pronouncedly increased grain size in pillars but only a moderate (if any) increase of the grain size in walls (Fig. 4.16c, d). Instead, we typically observe columnar growth in walls as well as pads if the ejection voltage is increased.

In all metals, microstructure analyses by EDX and HAADF imaging both indicate the presence of impurities, presumably due to residual solvent and oxides. The presence of carbon residues is more pronounced in Ag and Au (Fig. 4.7). In the case of Cu, the amount of C is typically below the detection limit of EDS SEM. An oxygen peak is typically observed with Cu, but this peak could also originate from the substrate (SiO_2 diffusion barrier).

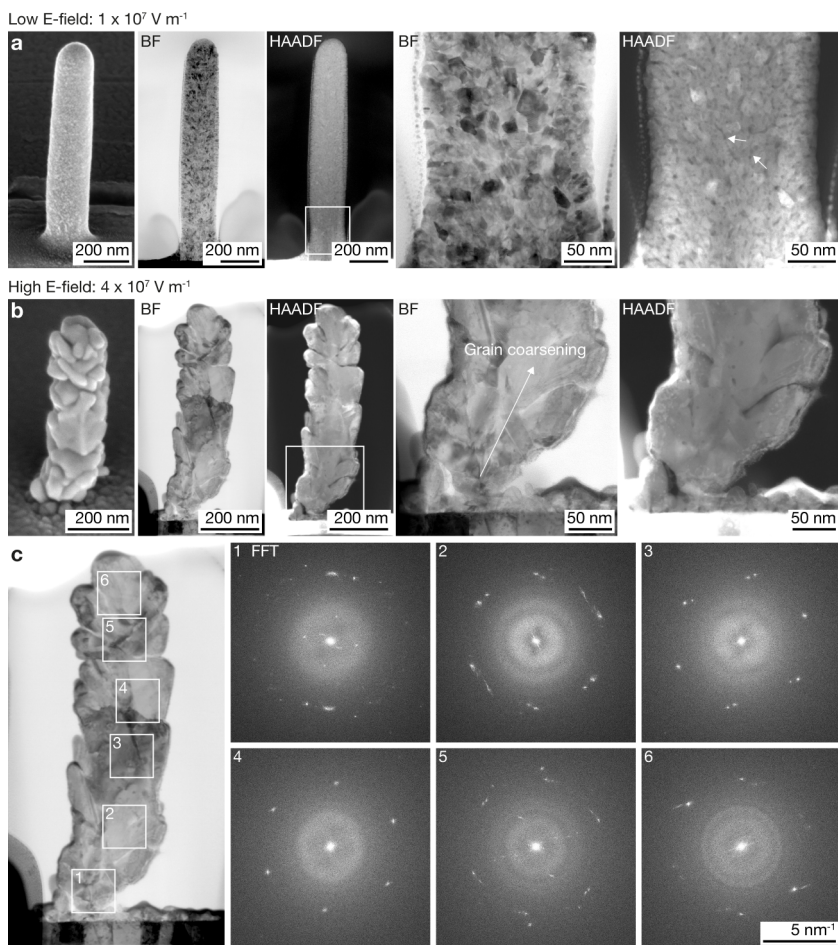


Figure 4.14 – Microstructure as a function of the electric field. SEM and STEM micrographs of a Cu pillar printed in **a**, low and **b**, high electric field conditions. A comparison of the bright field (BF) micrographs acquired from low- and high-field pillars shows that the crystallite size increases with the electric field: pronounced grain coarsening of the crystallites is observed in (b), while the crystallite size is constant in (a). High-angular annular dark field (HAADF) images show dense microstructure. In the low-field pillars, chains of point defects (vacancy clusters or nanoscale pores) are observed (arrows). The HAADF STEM of the high-field pillar show similar defects, but markedly decreased in number. **c**, Fast Fourier transforms (FFT) of high-resolution BF-TEM images taken at the indicated locations 1 – 6 of the high-field pillar (same pillar as in (b)). The crystallographic orientation of individual grains is aligned – the pillar is textured.

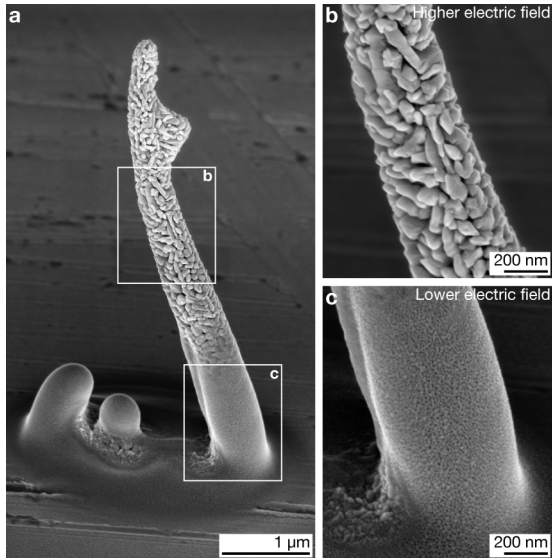


Figure 4.15 – Gradient microstructure due to electric field gradients. InLens SE micrographs of a deposit grown with a constant voltage at a large nozzle-to-substrate distance. To enable a large variation in electric field during growth, the pillar was grown as close to the nozzle as possible (more than half the gap distance). Note the sharp transition from fine to coarse morphology that suggests a non-linear dependence of the microstructure on the electric field.

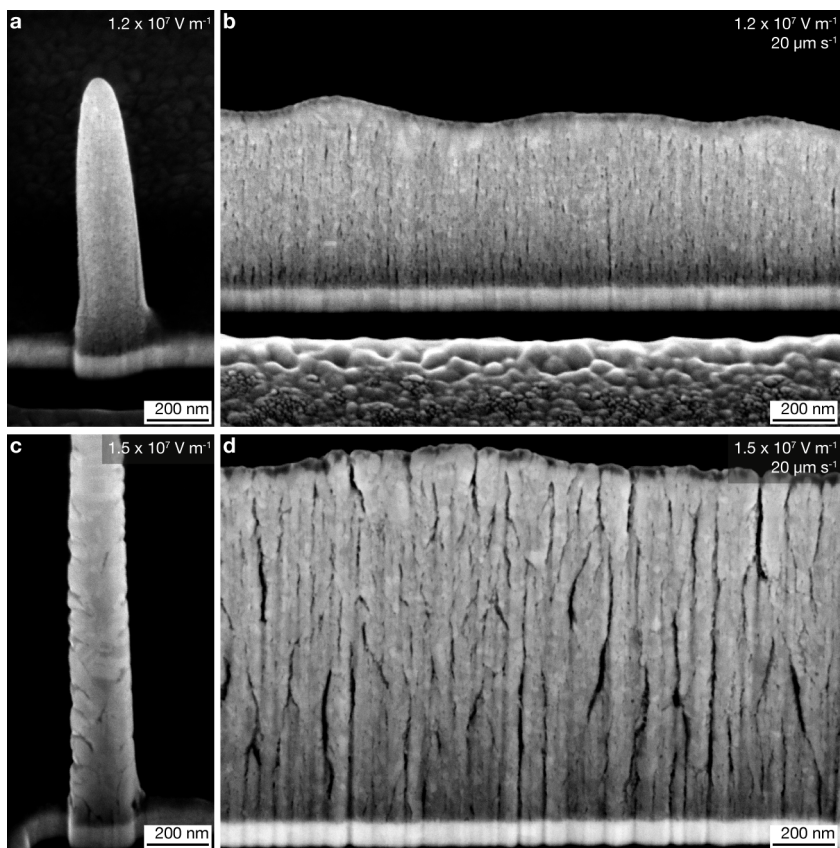


Figure 4.16 – The influence of the printing strategy on the microstructure. InLens SE micrographs of FIB-cut cross-sections of a pillar and a wall printed with an ejection voltage of **a, b**, 90 V and **c, d**, 110 V. While the effect of increased grain size with a higher electric field is observed in pillars, it is not obvious in the walls. Pillars were printed without relative movement of the substrate to the nozzle, whereas walls were printed layer by layer with an in-plane speed of $20 \mu\text{m s}^{-1}$. All structures were printed with the same nozzle in Ar atmosphere ($<40 \text{ ppm O}_2$). Nozzle-substrate distance: $7.5 \mu\text{m}$. All micrographs are tilt-corrected.

4.4.7 Materials properties

The electrochemical growth process offers functional as-deposited materials properties without the need for additional processing. The nanocrystalline microstructure results in excellent mechanical and good electrical properties of as-printed Cu. A flow strength on the order of 1 – 1.5 GPa and a Young's modulus of 81 ± 9 GPa have been determined by micropillar compression (Fig. 4.17). Especially the strength compares well with the highest literature values for nanocrystalline Cu³⁵⁹. The Young's modulus is lower than literature values of 117 – 131 GPa²⁹⁵. The shown compression curves were recorded for printed pillars with their top parts removed and flattened by FIB. For a comparison of cut and uncut pillars, refer to Figure D.3. For a more detailed assessment of the mechanical properties of EHD-RP-printed metals, including compression results for layer-by-layer-printed pillars and nanoindentation of printed pads, see Chapter 3.

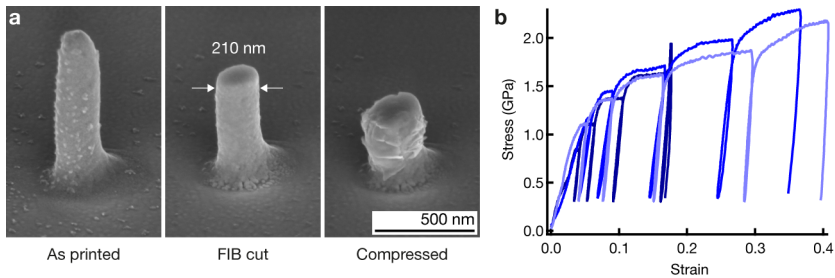


Figure 4.17 – Mechanical properties. **a**, SE SEM micrographs of an exemplary Cu pillar as deposited (left), FIB cut (middle) and compressed (right). Image tilts: 60° . **b**, Stress-strain curves recorded from three FIB-cut pillars. An unloading Young's modulus of 81 ± 9 GPa and a flow stress in the range of 1 – 1.5 GPa is derived from these curves.

The crystalline and percolated as-deposited microstructure renders as-printed materials electrically conductive. As a result, printing across insulating substrates is enabled if printing starts from a grounded pad (Fig. 4.6, 4.18) – as-printed geometries guarantee sufficient charge transport for electrochemical reduction. Best as-deposited electrical conductivities were $\approx 0.1 \times$ bulk conductivity of Cu. As an example, the electrical resistivity of the Cu line in Fig. 4.18 is $(14.4 \pm 2.1) \times 10^{-8} \Omega \text{m}$, corresponding to $\approx 8.4 \times$ bulk resistivity or $0.12 \times$ bulk conductivity of Cu ($1.71 \times 10^{-8} \Omega \text{m}$ at 25°C ³⁶⁰). This value was extracted in a two-point measurement as follows: two Pt-pads for electrical contact were FIB-deposited, once on the grounded Ag electrode (pad 2) and once onto the far end of the line (pad 1). A W-micromanipulator positioned on the

pads was used as the high contact, whereas the Ag electrode was electrically grounded. The resistance of the circuit R_{circuit} (as measured from pad 2) and the resistance of the line plus the circuit $R_{\text{circuit} + \text{line}}$ (measured from pad 1) were derived by averaging all data points from three independent current-voltage curves (Fig. 4.18c): $R_{\text{circuit}} = 61.8 \pm 10.7 \Omega$, $R_{\text{circuit} + \text{line}} = 266.8 \pm 10.4 \Omega$. The resistance of the line was thus calculated as $R_{\text{line}} = R_{\text{circuit} + \text{line}} - R_{\text{circuit}} = 205.0 \pm 14.9 \Omega$. To evaluate a value for the resistivity, we measured the length l of the line in the SEM (Fig. 4.18a), and estimated the average cross-sectional area A of the line from thirteen AFM line profiles recorded at evenly distributed intervals along the length of the line. For $l = 45 \times 10^{-6} \text{ m}$ and $A = (3.16 \pm 0.40) \times 10^{-14} \text{ m}^2$, the above reported resistivity of $\rho_{\text{line}} = (R_{\text{line}} A)/l = (14.4 \pm 2.1) \times 10^{-8} \Omega \text{ m}$ is calculated.

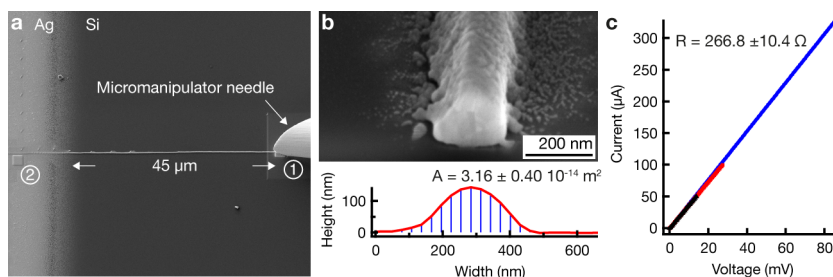


Figure 4.18 – As-deposited conductivity enables printing across electrically insulating substrates. **a**, SE SEM micrograph of a Cu line printed from a Ag electrode onto a Si wafer covered with a 50 nm thermal oxide and 50 nm Si_3N_4 . For resistivity measurements, electrical contact is established using a micromanipulator W needle placed on FIB-deposited Pt pads (1 and 2). **b**, FIB-cut cross section and AFM line profile of the line shown in (a). The cross section was cut just right of pad 1. Channeling contrast reveals a polycrystalline as-deposited microstructure with a grain size <100 nm. Micrograph is tilt-corrected. **c**, Three current-voltage curves measured from pad 1. Subtracting the resistance of the measurement circuit, as recorded from pad 2, derives a resistance of $205.0 \pm 14.9 \Omega$ for the printed line. This corresponds to a resistivity of $\approx 8.4 \times$ the bulk resistivity of Cu.

4.4.8 Printing Speed

Typical out-of-plane printing speeds of EHD-RP are on the order of 3 – 5 voxel/s (normalized by the X-Y feature size) for minimal feature sizes in the range of 100 – 250 nm. Higher growth rates are physically possible when increasing the printing voltage. Up to date, maximum out-of-plane printing speeds that still allowed for a reliable measurement were (10.3 ± 1.8) voxel/s (average pillar diameter (358 ± 25) nm) and highest growth rates that guaranteed dense morphology (5.8 ± 0.6) voxel/s (average pillar diameter: (245 ± 16) nm) (Fig. 4.19a – d). The higher electric field increases the feature size to 300 – 500 nm, and the printed pillars show a coarser topology

due to the influence of the electric field on the microstructure. In plane, printed lines become discontinuous due to insufficient coverage of the deposited material at printing speeds $>5 \mu\text{m s}^{-1}$ when using standard ejection voltages, but continuous multi-layer structures (for example walls) are easily printed at in-plane speeds of $80 \mu\text{m s}^{-1}$. At the other end of the spectrum, lowest growth rates explored were in the range of $0.2 - 0.5 \text{ voxel/s}$ (out-of-plane). For example, a speed of $(0.40 \pm 0.09) \text{ voxel/s}$ was measured for a pillar diameter of $(378 \pm 51) \text{ nm}$. Such decreased rates are of interest if a small out-of-plane chemical voxel size is required.

A speed of $3 - 10 \text{ voxel/s}$ outperforms other electrochemical techniques by at least one order of magnitude, while competing with their very best feature-sizes (Fig. 4.19e). The speed and minimal feature size of EHD-RP are equal to those of ink-based EHD 3D printing. The increased speed facilitates the additive, electrochemical fabrication of structures with at least two dimensions in the sub-millimeter range: a diffraction grating of 300×300 individual Cu pillars printed with a residence time of approximately 200 ms per pillar is printed in a total time of approximately 6 h (Fig. 4.20a, b, Supplementary Movie S2).

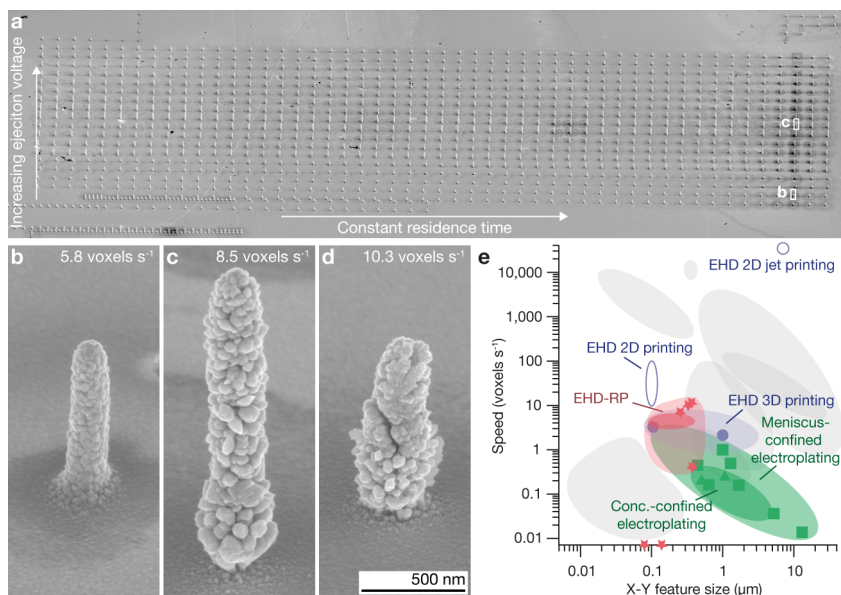


Figure 4.19 – Printing speed. **a**, Measurement of the maximum out-of-plane growth speed. SEM micrograph of an array of Cu pillars printed by increasing the ejection voltage in every second line. Per ejection voltage, the dimensions and residence time of 50 pillars were measured to calculate an out-of-plane voxel speed. **b – d**, Cu pillars printed at average out-of-plane growth speeds of 5.8 to 10.0 voxel/s. Respective residence times: 625, 639, and 257 ms. Image tilt: 57°. **b**, Speed versus X-Y feature size of contemporary small-scale metal AM techniques, with EHD-RP represented in red (dark red: typical speeds used to print the geometries in this chapter). A maximum speed on the order of 10 voxel per second is one order of magnitude faster than previous electrochemical techniques (green). The shaded areas are interpolated from data that link speed and resolution (solid symbols) but are also based on generally reported values for either minimal feature size or speed. Squares: Meniscus-confined electrodeposition^{13,144,147,150}. Triangles: FluidFM¹⁵⁴, SICM¹⁵⁵. Circles: EHD printing^{104,105}. Open circles: EHD 2D printing^{16,108,109}. Stars: EHD-RP (including measurements **a – d**). Stars on the x-axis indicate measured minimal feature sizes that cannot be linked to exact values of growth rate (Fig. 4.10b, c, printed at typical print speeds of $\approx 1 \mu\text{m s}^{-1}$). Grey areas represent alternative small-scale metal AM methods. See Fig. 2.14 for labels.

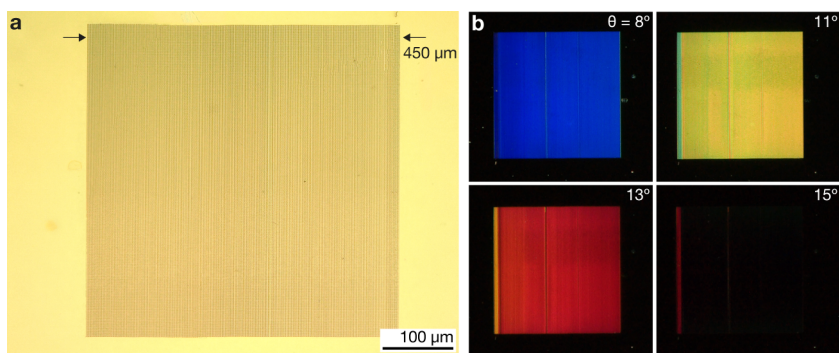


Figure 4.20 – High speed facilitates printing of sub-millimeter-scale objects. **a**, Optical bright field micrograph of a diffraction grating built from 300×300 Cu pillars printed with a residence time of approximately 0.2 s per pillar. Total printing time was approximately 6 h. **b**, Optical dark field micrographs showing the first order of diffraction of the grating in (c). The angles indicate the grating angle θ relative to the position of the grating when light is reflected in zero order.

4.5 Discussion

4.5.1 3D printing with EHD-RP: geometry, resolution and speed

4.5.1.1 Geometry – the need for a feedback

EHD-RP fulfills all stages of geometrical capabilities listed in Section 2.3.1.1 (Fig. 2.14a). Nevertheless, geometrical complexity and fidelity are currently not as high as those offered by some alternative single-metal techniques⁴⁸. The focusing of the electric field at small protrusions and edges of the printed geometries complicate the exact reproduction of designed geometries – a shortcoming that is shared amongst all EHD-based microprinting techniques. As demonstrated by Schneider *et al.*¹⁶, these detrimental effects could be avoided by adjusting the print strategy.

Alternatively, a growth feedback that adjusts the the deposition current *in situ* would be desirable. As the FluidFM approach has shown (Fig. 2.8), a feedback during printing significantly simplifies high fidelity printing of complex geometries. For EHD-RP, such a feedback could in principle be based on the local reduction current which potentially represents the local growth rate. However, preliminary experiments for controlling the local growth rate gave mixed results. On the positive side, the measured current can be related to the deposited volume. In a steady state (voltage plateau in Fig. 4.21), deposition rates of $8.4 \times 10^{-20} \text{ m}^3 \text{ s}^{-1}$ and $1.4 \times 10^{-19} \text{ m}^3 \text{ s}^{-1}$ are measured for currents of 400 and 800 pA, respectively (theoretical rates: $2.9 \times 10^{-20} \text{ m}^3 \text{ s}^{-1}$ and $5.9 \times 10^{-20} \text{ m}^3 \text{ s}^{-1}$ ^a). Yet, two issues raise doubts about whether the measured current can ever represent the local growth rate. First, relating the ion current to the voxel-by-voxel growth rate necessitates that the measured current signal represents the momentaneous reduction in real time. Unfortunately, the EHD-RP circuit reveals significant capacitive elements: upon stepping the current in a current-controlled experiment, the voltage as a function of time t increases proportional to $e^{-t/\tau}$ (Fig. 4.21a, b). Assuming a parallel RC circuit to represent the EHD-RP system in a first approximation, we deduce a capacitance of $(42.0 \pm 1.9) \text{ pF}$ and a time constant $\tau = 5.7 \pm 0.3$ by fitting the voltage transient $V(t)$ of a parallel RC circuit^b to the middle segments of the voltage curves. In the case of this simple equivalent circuit, we assume that only the current across the

^aModified Faraday's law: $V = \frac{m}{\rho} = \frac{ItM}{Fz\rho}$, with V the deposited volume, $\rho = 8960 \text{ kg m}^{-3}$ the density of Cu, I the deposition current, t the deposition time, $M = 63.55 \text{ g mol}^{-1}$ the molar mass of Cu, $F = 96485 \text{ C mol}^{-1}$ the Faraday constant, and $z = 1$ the valency number of Cu^+ in acetonitrile. $\frac{dV}{dt} = \frac{IM}{Fz\rho}$, which results in $\frac{dV}{dt} = 2.9 \times 10^{-20}$ and $5.9 \times 10^{-20} \text{ m}^3 \text{ s}^{-1}$ for $I = 0.4$ and 0.8 nA , respectively.

^b $V(t) = iR + (V_0 - iR) * e^{-t/(RC)}$, with R and C the resistance and capacitance of a parallel resistor and capacitor, and V_0 the voltage across the parallel RC circuit before stepping the current to a new value i .

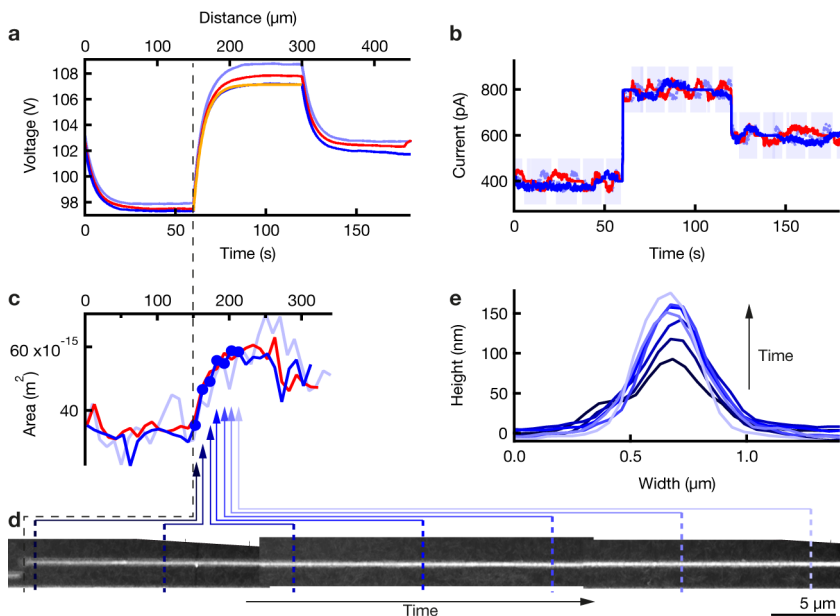


Figure 4.21 – Current-controlled printing and capacitive effects. The measured current is not representative of the deposited volume upon dynamic changes of the system due to capacitive effects. Only in a steady state the current corresponds to the deposited volume. **a**, recorded voltage during printing of three lines while stepping the deposition current as shown in **(b)** in a current-controlled experiment. A capacitance of (42.0 ± 1.9) pF and a time constant $\tau = 5.7 \pm 0.3$ is deduced from fitting the voltage transient $V(t)$ of a parallel RC circuit to the middle segment of the three curves (one fit shown in orange). **c**, The cross-sectional area of lines printed with the current-voltage profile in **(a, b)** versus time shows an increase of the printed volume proportional to the voltage. **d**, AFM height profile of a single line after stepping the current from 400 to 800 pA (corresponds to the blue curve in the graphs). Arrows indicate the corresponding data points in **(c)**. **e**, Cross-sectional line profiles recorded from positions indicated in the AFM profile in **(d)**.

resistor R , i_R represents the deposition current. As i_R is proportional to $V(t)$, the measured volume change of a printed line upon stepping the current also increases proportional to $e^{-t/\tau}$, as measured by AFM of a printed line in Fig. 4.21c. In consequence, a growth feedback based on the current is challenging because the capacitance buffers fast changes in the reduction current. The main contribution to the system's capacitance probably comes from the EHD meniscus (charging of the meniscus by transport of ions), as a severe reduction in anode surface area and hence a drastic decrease of the double layer capacitance on the anode showed no change in recorded current curves. Thus, decreasing the distance between source anode and meniscus could decrease the

capacitance. However, as a second complication for a current-based feedback, ejected ions cannot be assigned to a given voxel. Such a correlation would require a straight path of flight, so that one could assume each ion to land on the voxel just below the nozzle. Unfortunately, it is obvious that ions are deflected by antenna effects.

Consequently, no truly local growth rate can be deduced from the measured ion current, and a growth feedback based on the current is likely not an ideal solution. A feedback that measures the actual physical volume or height printed would be more suitable, as it would represent the true geometry. To enable such a feedback, one could use the printing nozzle as a probe, similar to scanning-probe techniques. However, in contrast to standard scanning probe methods, the measurement of distance should be contact-less, *i.e.* work across a distance of at least a few hundred nanometers, better a few microns, and should not be influenced by the ongoing EHD-ejection. The evaluation of an appropriate mechanism is beyond the goal of this discussion (one could imagine capacitive or eddy-current distance sensing, the integration of far-field interference scanning optical microscopy³⁶¹, a change of the mechanical resonance frequency of the tip as a function of distance, or use hollow AFM probes as printing nozzles and evaluate the attraction of the AFM tip (with the charged meniscus) to the substrate as a function of distance). Nevertheless, I want to stress that work by others has shown that either a feedback¹⁵⁴ or modeling of the growth process^{180,195,196} is necessary to enable the printing of complex geometries with printing techniques that are based on growth of material instead of its mere transfer.

As a final note: the EHD-ejection itself requires a high electric field. Yet, this field is disadvantageous for the geometrical accuracy as it favors growth on protrusions due to field-focusing and hence often provokes inhomogeneous growth. Thus, one should consider options for reducing or removing the electric field on the substrate. One could imagine the installation of an annular extraction cathode between nozzle and substrate that would accommodate the voltage drop but that would let ejected ions pass through a hole aperture. After such an aperture, the ions would travel in a field-free environment and antenna effects on the substrate should be eliminated.

4.5.1.2 Resolution and minimal feature size

A minimal feature size of 80 nm by EHD-RP is among the smallest features demonstrated by small scale AM methods and is equal to the smallest features printed by particle-based EHD-printing, TPL and meniscus-confined electrodeposition. Only electron- and ion-beam-based techniques have demonstrated the growth of more confined deposits.

It is curious to observe that the feature size of EHD-RP is only marginally smaller than the diameter of the printing nozzle. It is well established that droplets or jets ejected by electrohydrodynamic

forces are pronouncedly smaller than the diameter of the used capillaries^{99,107,350,362}. We thus speculate that the ejected droplets are $\ll 200$ nm and that either the wetting of the solvent droplet on the substrate or a badly focused ejection and hence a low accuracy (as observed when spraying with 100 nm wide nozzles, Fig. 4.11). To reduce the size of the sessile solvent droplet (Fig.4.22) and thus potentially reduce the feature size, heating of the substrate to increase the evaporation rate of the solvent should be considered (for example by heating with a laser). To improve the focus of ejection, one should evaluate the use of an ion focussing lens between the nozzle and the substrate or print at notably smaller nozzle-to-substrate distances.

An alternative explanation for the observed resolution might be a charge-transfer-limited reduction reaction. Lets assume the impacting droplets are $\ll 200$ nm, for example 20 nm. If all cations contained in such a droplet are instantaneously reduced upon impact, that is, before the droplet spreads on the surface, a deposit 20 nm in diameter would be formed. However, if the cations cannot be reduced fast enough due to a rate-limitation, the ions would necessarily distribute across a larger area than the cross-section of the impacting droplet before they are reduced – a deposit larger than the droplet would be formed. If we assume that mass transport does not play a role due to the high-speed impact and the small distances involved within the droplet, the speed of the reduction reaction will be limited by the charge transfer rate of electrons from the substrate to the cations. The maximum charge transfer rate cannot be calculated, as it is a function of the potential across the electrode interface, which is unknown in our case. However, we can compare rates estimated from measured deposition currents to maximum charge-transfer rates (that is, current densities) measured in literature and see whether the rates in EHD-RP are far below (hence the deposition would certainly not be charge-transfer limited) or similar (suggesting that the deposition could be charge-transfer limited). Probably the highest current densities for Cu reduction were demonstrated by laser-enhanced jet-plating in aqueous solutions ($10 - 1400 \text{ kA m}^{-2}$ ^{266,363,364}), notably at temperatures of up to 150°C (an enhancement of the charge transfer rate by a factor 10^3 is estimated for an increase of temperature by 50°C ³⁶⁴). At room temperature, jet-plating current densities are $\approx 10 \text{ kA m}^{-2}$ ²⁶⁵. Indeed, estimated current densities for EHD-RP are of the same order of magnitude: an approximate EHD-RP deposition current of 1 nA and a pillar diameter of 200 nm results in an estimated average current density of $\approx 30 \text{ kA m}^{-2}$. For a diameter of only 20 nm, the current density would be 3 MA m^{-2} , surpassing all known literature values. Consequently, a charge-transfer limitation of the resolution is possible. To confirm this hypothesis, the feature size of EHD-RP as a function of substrate temperature should be quantitatively evaluated – if charge-transfer limited, the area of a 1D deposit should decrease with temperature T , as the rate of deposition should follow an Arrhenius-like behavior $\propto e^{-1/RT}$ ^{262,365}.

4.5.1.3 Speed

The speed of EHD-RP outperforms the deposition rate of other electrochemical methods. Nevertheless, compared to other non-electrochemical small-scale AM techniques, the growth rate of EHD-RP is average. Here, parallelization with multi-nozzle printheads (as demonstrated for EHD-printing^{54,57}) or by spraying ions through parallel apertures (as demonstrated for aerosol printing of charged particles³⁶⁶ or electro sprayed ions at larger scales³⁵³) could enhance the throughput.

Nevertheless, the moderate speed raises the question after the limiting factors that cap the maximum attainable speed of EHD-RP. Currently, practical considerations limit the maximum speed, as increased ejection voltages necessary for higher speed show some negative influence on the printed structures: first, a higher ejection voltage seems to increase the width of printed features (Fig. 4.19a). Second, the enhanced grain growth observed at higher fields (Fig. 4.14) increases the roughness of the printed metals and results in pronounced voids between individual crystallites (Fig. 4.19a). Further, the accuracy of the deposition as well as the reproducibility of the growth speed are diminished at higher ejection voltages. We speculate that all these effects are related to the formation of a sessile solvent droplet on the substrate that forms at high ejection voltages due to the increased solvent flow rate (Fig. 4.22). Its presence is the current practical limit to higher growth speeds, although its influence on the growth mode and the resulting morphology and voxel size cannot be pinpointed at the moment. Nevertheless, we already have explored printing with a cone-jet mode, as the increased flow rates promise very high deposition speeds – a speed of 40 000 pixel/s (7 μm line width) has been measured for EHD jet printing of silver inks^{108,109} (Fig. 4.19e). Indeed we measured an increase of the emission current by approximately one order of magnitude for jetting modes compared to the standard printing mode (Fig. 4.22c), but the slow evaporation of the solvent currently hinder the use of this mode. Consequently, increasing the evaporation rate of the solvent to avoid the sessile droplet should be considered when aiming for increased speeds, for example by mild heating of the substrate with a laser or a heating stage.

We cannot predict a single fundamental factor that will ultimately limit the speed of EHD-RP at this stage. Potential candidates for limiting the absolute printing speed are: the ion reduction rate on the substrate (including charge transfer rate and ion transport rate through the sessile solvent), the ion emission rate available from EHD-ejection modes^{107,367} that are suitable for high-resolution printing (focussed modes), the ion transport rate and the maximum solvent flow rate within the nozzle, and the maximum evaporation rate of solvents suitable for printing. A factor that can probably be excluded as rate limiting is the ion generation at the anode, as the surface area of the anode exceeds the area of the cathode by many orders of magnitude (approx. by a factor of 10^8 if

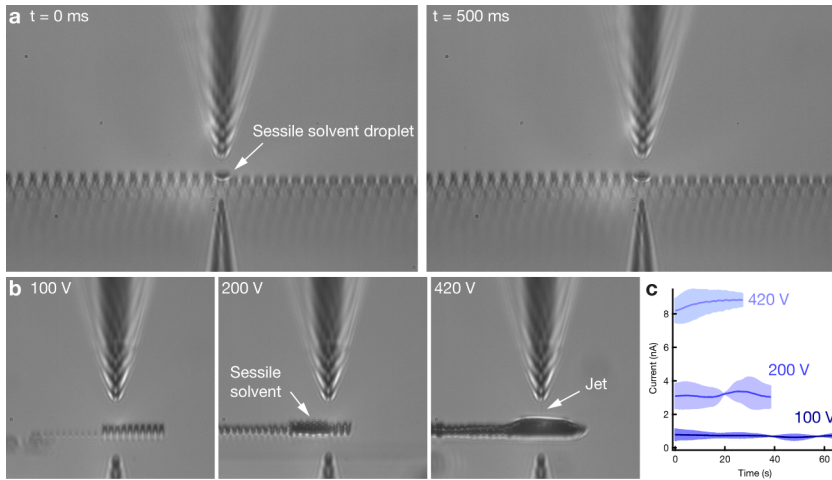


Figure 4.22 – The sessile solvent droplet at high ejection voltages. **a**, Sequential optical images of the printing of pillars at 10 voxel/s (same pillars as in Fig. 4.19a). At high ejection voltages, a sessile solvent droplet is maintained on the substrate. **b**, Optical images of the printing of arrays of pillars at increasing ejection voltages. The tip-substrate gap is approx. $8 \mu\text{m}$. The formation of a jet, accompanied by a high solvent flow rate, is observed at the highest ejection voltage. **c**, Current transients recorded during the printing of the arrays in **b** (raw data (light blue) and smoothed data (dark blue)).

the immersed anode surface is considered, and approx. $10^5 - 10^6$ if only the anode area closest to the nozzle apex is considered).

4.5.2 Microstructure and materials properties

Mechanical and electrical properties of metals synthesized by EHD-RP are similar to those offered by alternative electrochemical techniques. The small grain size and the large density of vacancy clusters of nanometer-sized pores is especially beneficial for the strength of the printed metals. The reason for an elastic modulus 30 – 45 % lower than bulk values of Cu is up for speculation. As also discussed in Chapter 3, the often-observed presence of vacancy clusters or nanopores (for example Fig. 4.14a or Fig. 3.4) or potentially residual oxides could cause the lowered stiffness, but ask for more detailed studies. In contrast, no large amount of organic residues, which would also lower the modulus, were detected by SEM-EDX in printed Cu-structures (Fig. C.4). Nevertheless, a respective chemical analysis with a higher sensitivity should be performed (Atom probe tomography for example).

The grain size of <100 nm is probably a major contribution to the increased electrical resistivity compared to bulk values. If compared to a resistivity of a sputtered and annealed Cu film with a grain size comparable to the printed line ($\rho_{\text{PVD}} \approx 4 \times 10^{-8} \Omega \text{m}$ for a grain size of 50 nm and a film thickness of 50 nm³⁶⁸), the resistivity of the as-printed line is only a factor $\rho_{\text{line}}/\rho_{\text{PVD}} \approx 4$ higher. Additional components that probably contribute to the lowered as-deposited conductivity are the high density of point defects (Fig. 4.14) and possibly residual carbon impurities. If a better conductivity is required, thermal annealing should be considered to reduce the defect density and increase the size of crystallites.

In general, it should be noted that the materials properties reported here are obtained from samples printed with not-yet fully optimized printing parameters. Presently, low fields are employed for printing, because they guarantee lower surface roughness and easier control. Nevertheless, the pronounced dependency of the synthesized microstructure on the electric field offers an excellent handle to control and optimize the microstructure of printed metals. In principle, that is. Currently, the promotion of grain growth with increased electric fields (as observed in pillars) is difficult in layer-by-layer printed geometries (Fig. 4.16). In pillars, the continuous growth seems to enable grain coarsening, resulting in grains as wide as the pillars' diameters. In contrast, the non-continuous out-of-plane growth in layer-by-layer printed structures apparently results in nucleation of new crystallites in every pass of the nozzle – contamination by drying solvent or oxidation in-between two layers might hinder epitaxial growth on previously deposited layers. Additionally, preferred growth at protrusions due to electric field focusing (an effect that is probably more pronounced at higher electric fields) potentially leads to growth instabilities and hence the columnar growth observed. Consequently, these issues need to be solved if the electric field should be used to optimize the microstructure in structures other than pillars. If a solution is found, one could

imagine adjusting global or even local properties to a given application – a possibility that ink-based techniques lack and should be explored, for example for the synthesis of 3D microstructural gradients.

In summary, there is clearly room left to explore despite the good as-deposited performance observed so far. A few open questions that should be tackled are: the exact mechanism that determines the grain size and defect density (electric field or growth rate? Both are currently coupled); the cause for the comparably low ratio of E/H ; the characterization and quantification of contaminants (primarily carbon and oxygen); the influence of thermal annealing; the effect of the print strategy (translation speed and trajectory) on the microstructure of "bulk" structures such as the walls in Fig. 4.16 or the pads in Chapter 3. Furthermore, the highly porous microstructure offered by the use of larger nozzles has not yet been explored for possible applications.

4.5.3 Range of materials and substrates

We have demonstrated the deposition of Cu, Ag, Au and Zn. Of these, the deposition of Cu and Ag is facile and highly reproducible. In contrast, Au deposition requires the use of larger nozzles to avoid unwanted clogging, and Zn deposition is not yet reproducible. The comparably low number of currently printable metals contrasts with the large range of sacrificial metal anodes that have been successfully employed in solution-^{354,355} and spray-based synthesis³⁵⁶. A few examples include metals often used in standard electrochemistry such as Au, Cu^{239,344,345}, Ag, Fe^{345,369}, Co³⁴⁶, Zn^{345,370} and Ni^{345,371,372}, but also highly passivating metals such as Al^{347,348}, W³⁷³, Mo³⁷⁴, Ti³⁷⁵ or Si³⁷⁶. This discrepancy can be interpreted in two ways: first, there is a large potential for extending the range of printable metals, as many different metals have previously been used as sacrificial anodes for the production of solvated metal cations in organic solvents. Second, a closer study of the individual stages of the printing process is necessary to mine this potential.

It is assumed that many issues with metals other than Ag and Cu are related to a lack of control of the anodic and cathodic reactions. In standard electrochemical deposition, the type of chemical reaction is controlled by an appropriate selection of the electrode potential. In contrast, EHD-RP lacks control or even the measurement of these potentials. So far, neither the surface potential of the anode-wire nor the potential of the substrate are known – we only control the overall potential drop across both electrode surfaces, the electrolyte and the nozzle-substrate gap.

If the electrode potentials are not controlled, the respective surface reactions are not controlled either. The cathodic potential is probably less important, as side reactions on the substrate are

more likely related to the the printing atmosphere. In contrast, the anodic electrochemistry should be studied closely. Unfavorable anodic reactions can certainly impede printing and need to be avoided in the future. For example, acetonitrile is known to polymerize and form polymeric films on Pt electrodes at high surface potentials^{377,378}. The coating drastically reduces the anodic current density and, in the case of EHD-RP, would suppress the generation of cations. Further, the clogging of small nozzles when using Au anodes could be caused by products of such a polymerization reaction. In the case of Zn and other metals that form passive oxides (*e.g.* Al, Cr, Ti, Si), the lack of control of the corrosive potential probably results in passivation of the anode and, again, a ceasing of the supply of ions necessary for printing. Only the oxidation in either the active or transpassive potential regime can secure the continuous production of cations. Here, it is important to note the difference in anodic behavior of metals in aqueous and organic media. For example, Fe in pure acetonitrile is passivated across a far larger potential range than in water³⁷⁹. The addition of only 2 % water ensures active corrosion.

It follows that control of the anodic surface potential as well as studies of ideal solvents that promote active dissolution will be essential for extending the range of printable metals. Control of the anodic surface potentials can be ensured by the design of a three-electrode electrochemical cell within the printing nozzle – a task that should have high priority. Guidance for the construction and control of such a cell is available in MS literature: multiple laboratories demonstrated the working principle of two- and three-electrode cells within electrospray emitters for on-line electrochemistry^{380–383}. Thus, I am positive that the number of metals accessible with EHD-RP can be largely extended if unwanted side reactions at the anode and cathode can be avoided.

To further expand the materials range of EHD-RP, printing electrical insulators and semiconductors could be envisioned. Deposition of oxides or nitrides as well as compound semiconductors such as ZnS or ZnO could be synthesized by reactive deposition, for example by printing the respective metal ions in a reactive gas atmosphere for enabling *in-situ* chemical reactions (oxygen-rich atmosphere for oxidation of printed metals that is). Of course, the electron transfer required for printing might limit the thickness of printed insulators to the tunneling-distance of electrons – hence defying the purpose of the printed insulators.

Direct printing on non-conductive substrates is not yet accessible to EHD-RP. Although the as-deposited conductivity of metals printed by EHD-RP enable printing *onto* insulators between conductive pads, direct printing *on* insulators is currently not available. For many applications in microelectronics, this is no drawback, as hardly any metallic components in a circuit need to be floating, *i.e.* not connected to some external circuitry. Further, isolated metallic structures could be constructed by printing sacrificial electrical connections that are removed in post-print processing.

Nevertheless, alternative sources of electrons should be considered to facilitate printing on arbitrary substrates. Here, I would suggest to explore gas plasmas as electron donors. Plasma cathodes (confined plasma jets that impinge the surface of liquid electrolytes) have been shown to drive electrochemical synthesis of metal nanoparticles^{384–387}. Further, such plasma jets can be miniaturized using nanoscale glass capillaries³⁸⁸. Consequently, one could envision the combination of EHD-RP (providing metal cations) with a localized plasma jet (providing the electrons necessary for reduction) to unlock printing metals directly onto insulating substrates.

4.6 Conclusion and outlook

This chapter introduced a novel electrochemical 3D printing technique with submicrometer resolution: EHD-RP. Its development was motivated by the superior materials quality that is provided by the electrochemical approach, but a lack of electrochemical printing methods that reach print speeds that are similar to those of transfer techniques. By combining the mass-transport strategy of a suitable transfer technique – EHD-printing – with electrochemical synthesis concepts we succeeded in speeding up electrochemical 3D printing by one order of magnitude.

As shown, the direct, ink-free process results in excellent mechanical and good electrical properties printed at competitive speeds and ambient pressures – readily permitting applications such as small-scale wire bonding, optical or mechanical metamaterials and printed sensors or actuators. However, a more thorough understanding of the mechanisms that determine the synthesized microstructure will be necessary to optimize the materials properties to a given application. Hence, more systematic studies of the key parameters should be performed. Additionally, the range of metals and materials in general should be studied. Although we focused on three distinct metals, EHD-RP's materials palette can likely be extended by exploring synthesis protocols that grant access to additional metals and potentially non-metals, such as semiconductors, ceramics and polymers. Finally, the basic mechanisms underlying EHD-RP are poorly understood: what are the limiting factors that determine the growth speed or the minimal feature size? Which processes are rate-limiting and thus mostly responsible for the capacitive effects? As this knowledge is needed for effectively improving the technique, any future work should include quantitative studies of the basic working principles.

In summary, EHD-RP combines the best characteristics of transfer and synthesis techniques: it adapts the speed from EHD-printing, but offers high-quality materials due to the synthesis principles of electrochemical methods. While this combination on its own potentially enables a multitude of practical applications, the true advantage of EHD-RP lies somewhere else. As shown in the next chapter, the use of sacrificial anodes for the *in-situ* generation of ions to be printed (as opposed to the use of pre-synthesized metal-salt electrolytes or inks) unlocks a feature unique in the family of small-scale AM methods: multi-metal printing with unprecedented detail.

Chapter 5

Multi-metal electrohydrodynamic redox 3D printing for voxel-by-voxel materials design

The previous chapter introduced electrohydrodynamic redox printing (EHD-RP) and elaborated on its advantages compared to other electrochemical AM methods. However, the most powerful and distinguishing feature of EHD-RP is neither its speed, its resolution nor its materials quality – the most unique aspect is its multi-metal capabilities. The use of a second anode as an additional ion source within the printing nozzle for the first time elevates an electrochemical method into the ranks of multi-material 3D printing techniques. On-the-fly switching and mixing of two metals printed from a single multichannel nozzle facilitates a chemical feature size of <400 nm with a spatial resolution of 250 nm. As shown, the additive control of the chemical architecture of materials provided by EHD-RP unlocks the synthesis of 3D bi-metal structures with programmed local properties and opens new avenues for the direct fabrication of chemically architected materials and devices.

This chapter is based in part on: Reiser, A., Lindén, M., Rohner, P., Marchand, A., Galinski, H., Sologubenko, A. S., Wheeler, J. M., Zenobi, R., Poulidakos, D., Spolenak, R. Multi-metal electrohydrodynamic redox 3D printing at the submicron scale. *Nat. Commun.* **10**, 1853 (2019), licensed under a CC BY 4.0 license.

5.1 Introduction: multi-material 3D printing

In the last decade, mayor efforts have resulted in AM's superior geometrical abilities. Today, one new frontier of AM is the integration of functionality and locally optimized materials properties within a single printed object. Approaches include the incorporation of prefabricated functional devices^{389,390}, multi-material printing^{28,391–393}, bioinspired printing of adaptive⁷ and hierarchically architected structures^{6,394}, and site-specific tuning of a material's local microstructure and chemistry for mesostructure optimization^{395–397}. Of these approaches, multi-material printing is possibly the most versatile and fundamental approach.

The fabrication of heterogeneous material systems offers key advantages: on one hand, heterogeneity is the basis of all functional devices. On the other hand, property gradients boost materials performance in both natural and manmade materials^{398–409}. Multi-material AM may considerably advance the synthesis of such materials by unlocking the fabrication of intricate 3D gradients – due to its temporal and spatial control of materials deposition, AM is superior to today's top-down or self-assembly approaches in terms of deterministic 3D design.

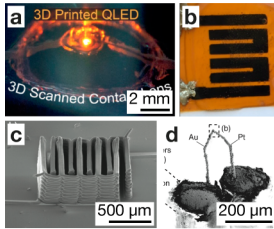
Recent examples of multi-material AM provide a glimpse of the potential of complex, functional 3D gradients (Fig. 5.1): mechanical gradients optimize stress distribution and thus structural performance^{396,405,406}. Further, they are used for non-uniform materials deformation for robotic design⁴¹⁰ or programmed failure³⁹³, and facilitate the design of mechanical metamaterials⁴¹¹. Finally, the combination of conductive, semiconductive and insulating materials enable all-printed, active and passive electronics^{5,392} or even bionic and microphysiological devices that merge tissue engineering and electronic sensing²⁸.

5.1.1 Multi-material 3D printing at small scales

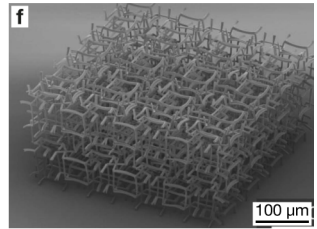
The concept of AM is scale-independent and may be applied across all length scales. Hence, downscaling of multi-material methods aims at integration of functionality and the tuning of local materials properties with microscale resolution. At this scale, printed lattice materials with properties tuned by their geometrical architecture have already opened a wide range of applications, including new classes of mechanical and optical metamaterials^{9,38,43}. Now, emerging microscale AM methods with multi-material capabilities have started to extend the additive control to the local chemical composition, *i.e.* the chemical architecture, paving the way to additively manufactured batteries^{24,414}, thermocouples⁵², bi-material metamaterials⁴¹¹ and materials with locally tailored electrical resistance⁹⁵, chemical reactivity¹³⁰ or microstructure¹⁴⁸.

Multi-material AM

Active and passive electronic devices



Mechanical metamaterials



Mechanical gradients: mesostructure optimisation

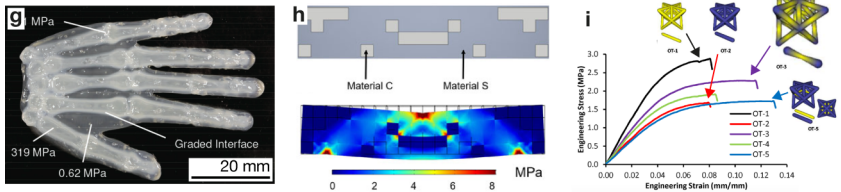


Figure 5.1 – State-of-the-art applications of multi-material AM. Multi-material AM facilitates the synthesis of 3D functional gradients with high complexity. This enables the site-specific printing of active electronic devices, the combination of highly disparate materials, for example living cells and inorganic materials, in a functional manner, or the local design of mechanical stress fields for metamaterials or mesostructure optimization. **a – e**, All-printed, active and passive electronics. **a**, Quantum-dot-LED deposited onto contact lens using five different functional inks³⁹². **b**, Fully packed carbon-nanotube supercapacitor composed of three functional inks⁴¹². **c**, Li-ion battery with a $\text{Li}_4\text{Ti}_5\text{O}_{12}$ and LiFePO_4 anode and cathode, respectively²⁴. **d**, Fully functional Pt-Au thermocouple printed on top of a Pt-Au wire pair⁵². **e**, An all-printed, microphysiological cantilever substrate with embedded strain gauge enables cardiac tissue engineering and sensing of tissue contraction. Optical image: cantilever deflecting upon tissue contraction (cantilever is 4 mm in width). Zoom: z-projection of immunostained laminar tissue on the cantilever surface. Graph: relative resistance changes (left axis) and corresponding calculated tissue twitch stress (right axis) recorded from the printed strain-sensor embedded in a spontaneously beating cantilever²⁸. **f**, Unusual materials properties by multi-material AM: a bi-material mechanical metamaterial with a negative coefficient of thermal expansion⁴¹¹. **g – i**, Gradient mechanical properties for mesostructure optimization. **g**, A 3D gradient structure, resembling a human hand, 3D-printed with polymeric resins of different stiffness³⁹³. **h**, Top: internal structure of a bi-material bending-bar optimized to enhance bending stiffness. Bottom: simulated von Mises stress distribution shows optimized stress concentration in the stiff material⁴⁰⁶. **i**) Stress-strain curves of truss structures with homogeneous, graded, or heterogeneous distribution of two materials. Optimized allocation of materials enhances materials performance (see blue and purple curve)⁴¹³. **a – i**, Reprinted with permission from **a**,³⁹² ©2014 ACS; **b**,⁴¹² 2017 ACS; **c**,²⁴ ©2013 John Wiley and Sons; **d**,⁵² ©2016 John Wiley and Sons; **e**,²⁸ ©2016 Springer Nature. **f**,⁴¹¹ CC BY 4.0 (<https://creativecommons.org/licenses/by/4.0/>); **g**,³⁹³ ©2018 John Wiley and Sons; **h**,⁴⁰⁶ ©2017 Materials Research Society; **i**,⁴¹³ ©2016 ACS.

Yet, to see small-scale AM unfold its full potential for the fabrication of multi-material devices and chemically heterogeneous materials, major challenges need to be addressed. On one hand, common approaches enforce extensive practical limits to the complexity of the 3D chemical architecture due to limited geometrical and chemical resolution^{52,104,130} (Fig. 5.2). The exclusive use of discrete materials-sources, for example multiple printing nozzles, results in low switching frequencies and limited grading between two materials, as well as difficult alignment. Consequently, the spatial resolutions is typically lower than for single-material printing with the same technique. More importantly though, the smallest chemical voxel size, corresponding to the smallest 3D feature of tunable elemental composition, is typically several micrometers, even if the geometrical feature size is pronouncedly smaller^{24,52,104,130,283}. On the other hand, access to high-performance inorganic materials is not available, since all present multi-material methods are transfer methods. Unfortunately, the materials properties of these techniques are often far from those demanded in microfabrication^{45,48} (Chapter 3). Additionally, the thermal post-print processing required for ink-based approaches renders many materials combinations incompatible.

Inorganic multi-material AM at small scales

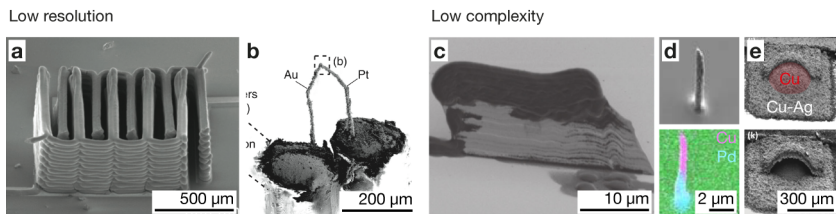


Figure 5.2 – Challenges of inorganic multi-material AM at small scales. **a, b**, Typical techniques used for multi-material deposition are limited to a resolution $\gg 1 \mu\text{m}$. **a**, Li-ion battery printed by DIW²⁴. **b**, Thermocouple deposited by LIFT of Pt and Au melts⁵². **c – e**, More importantly, the complexity of 3D gradients printed by available methods is low because of low switching frequencies between two materials. **c**, Wall of anthracene (black) and Ag printed by EHD-printing¹⁰⁴. **d**, Bi-metal Cu-Pd pillar deposited by aerosol-printing (SEM micrograph and corresponding EDX elemental map)³⁶⁶. **e**, Dome of Cu-Ag alloy (bottom) fabricated by printing and post-print etching of a sacrificial Cu support (top, red)¹³⁰. **a – e**, Reprinted with permission from **a**,²⁴ ©2013 John Wiley and Sons; **b**,⁵² ©2016 John Wiley and Sons; **c**,¹⁰⁴ ©2015 John Wiley and Sons; **d**,³⁶⁶ CC BY 4.0 (<https://creativecommons.org/licenses/by/4.0/>); **e**,¹³⁰ ©2015 John Wiley and Sons.

5.2 Objective of this chapter

This chapter will demonstrate the multi-metal capabilities of EHD-RP. Multi-metal EHD-RP overcomes the above-mentioned limitations of small-scale multi-material AM for the case of metals, as it enables the direct printing and mixing of multiple, high-quality metals from a single nozzle.

Key benefits of EHD-RP are high frequency of switching between two metals, in combination with the as-deposited functionality demonstrated in the previous chapter. I will show that the combination of submicron geometrical feature size and fast modulation of the printed chemistry offers unmatched control of the 3D chemical architecture of printed structures and enables tuning of local properties through local alloying at the submicron scale.

5.3 Methods

This methods section only discusses details that specifically apply to multi-metal printing with EHD-RP. Please refer to Section 4.3 for a general overview of the printing process and details of the setup. Different to single-metal printing, multi-metal EHD-RP employs two-channel nozzles that can accommodate two separate sacrificial anodes and requires additional electronics for switching the anodic voltage between the two electrodes.

5.3.1 Materials

Two-channel printing nozzles were fabricated from quartz capillaries (Sutter Instrument) using the P-2000 micropipette puller system (Sutter Instrument). Pulling parameters for typical nozzle diameters are listed in Table 5.1.

Table 5.1 – Pulling parameters for two-channel nozzles. Pulling parameters for two-channel quartz nozzles. Heat, filament (fil), velocity (vel), delay (del), and pull refer to the five programmable parameters of the P-2000 micropipette puller system. For a description of the parameters, refer to Section 4.3.

| \varnothing [nm] | glass | line | heat | fil | vel | del | pull | loops |
|--------------------|--------------|------|------|-----|-----|-----|------|-------|
| 200 \pm 30 | QT120-90-7.5 | 1 | 800 | 4 | 40 | 130 | 30 | |
| | | 2 | 825 | 3 | 30 | 130 | 100 | 1 |

5.3.2 Printing setup for two sacrificial anodes

To enable switching of the anodic voltage between multiple sacrificial anodes, two high-voltage relays (HE751, Littlefuse) were added to the setup described in 4.3.2 (Fig. 5.3, label 2). These mechanical relays were interfaced via the analog output of the piezo-controller and could hence be synchronized with the stage movement.

5.3.3 Printing parameters

When printing with multiple electrodes, the voltage needed to be adjusted for each electrode in order to match the individual growth rates. In general, it should be noted that all electrodes not in use had to be electrically floating, that is, neither connected to electrical ground nor any of the high voltage outputs. In case multiple electrodes were printed at the same time, all electrodes had to be held at the same voltage. If these guidelines were not followed, parasitic currents between electrodes caused cross-contamination of the electrodes, because individual channels of the nozzle are

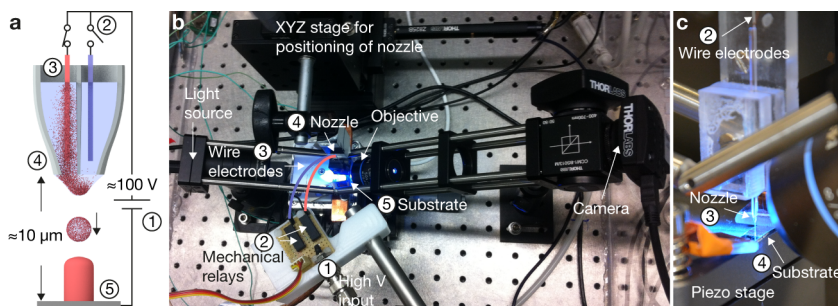


Figure 5.3 – Printing setup for bi-metal printing. **a**, Schematic of the printing process using two source electrodes. Major components of the setup: (1) Voltage source, (2) mechanical relays to switch the voltage between individual electrodes, (3) metal wires used as electrodes, (4) printing nozzle, (5) grounded substrate. **b**, Main components of the printing setup, as described in the methods Section 4.3.2. Numeric labels as in (a). The wire electrodes are schematically drawn in red and blue. **c**, Zoomed image of a two-channel nozzle positioned above the substrate, with a Cu and a Ag wire inserted into the back of the nozzle.

connected across a liquid bridge at the nozzle tip. See Section 5.4.5 for a more detailed discussion of individual growth rates and alignment of the two materials printed from a two-channel nozzle.

5.3.4 Selective etching of Cu

Selective etching of Cu from printed Cu-Ag structures was performed under potential control at 0.25 V vs. a saturated calomel electrode in 10 vol.% aqueous phosphoric acid (puriss. pa, >85%, Sigma Aldrich), using an Autolab PGSTAT12 potentiostat (Metrohm) and a Pt counter-electrode. The etching solution was not agitated. Typical etching times were 45 s for sacrificial Cu support structures and 15 s to generate nanoporous Ag (Fig. 5.11). Samples were briefly immersed in pure deionized water after etching and subsequently blow dried with air.

5.3.5 Analysis

Mass spectrometry. All mass spectrometry (MS) experiments were performed on a Synapt G2S (Waters) instrument in positive ion mode using the time-of-flight mode (ion mobility was not activated). The extraction voltage was set to 150 – 400 V using an external power supply (B2962A, Keysight). The nozzle was positioned at a distance of 2 – 4 mm from the grounded MS cone. Spectra were recorded with an integration time of 1 s and summed over several acquisitions. For transient measurements, spectra were acquired at intervals of 20 ms. All transient MS data correspond to the sum of the ion currents recorded for all species containing Cu^+ and Ag^+ , and is

presented as-recorded. The following peaks were summed if not otherwise noted: Cu: m/z of 104, 106, 145 and 147, Ag: m/z of 107, 109, 125, 127, 148 and 150.

EDX spectroscopy. In general, atomic percentages of Cu and Ag were quantified by EDX and are stated relative to the total Cu-Ag signal to avoid any contributions of signals from the substrates. The EDX spectra in Fig. 5.4e are presented with background subtraction: all spectra of the pillars and of the substrate were normalized by the Au peak originating from the substrate, and the background spectra were subtracted from the spectra of the pillars. The elemental content profiles of Cu-L and Ag-L signals in Fig. 2b are normalized by the summed signal (at.%) of both lines. For the elemental content map in Fig. 5.10b (etched state), the intensity of the Cu-L signal (representing nothing but background noise of the detector) was scaled to match the background signal of the corresponding Ag-L map.

Mechanical tests. Bending of the pillars in Fig. 5.11 was performed by horizontally applying a displacement to the uppermost ≈ 300 nm of the pillars using a sharpened tungsten needle (Pico-probe, GGB industries inc.). The needle was translated by the Alemnis indenter system, and the experiments were observed *in situ* in a LEO 1530 SEM (Zeiss) (see Movie S3 for details). The applied lateral forces were not measured.

5.4 Results

5.4.1 Multi-metal and alloy printing from a single nozzle by EHD-RP

The use of two wire anodes as sources for the deposited ions unlocks simultaneous printing of multiple metals from a single multichannel nozzle by EHD-RP (Fig. 5.4a). To grow two different metals A and B, a wire of A and a wire of B are each placed in one of the compartments of a two-channel nozzle (Fig. 5.4b). If the positive voltage is applied to one of the wire electrodes only, then only one ion species A^{z+} or B^{z+} is created and ejected, and A or B is printed. If both electrodes are biased simultaneously, an alloy A-B is deposited. Figure 5.4d – e demonstrates this principle for a Cu and a Ag electrode: mass spectra of the ejected ions reflect the elemental nature of the biased electrodes (Fig. 5.4d), and energy-dispersive X-ray (EDX) spectroscopy confirms the corresponding chemical composition of the printed structures (Fig. 5.4e).

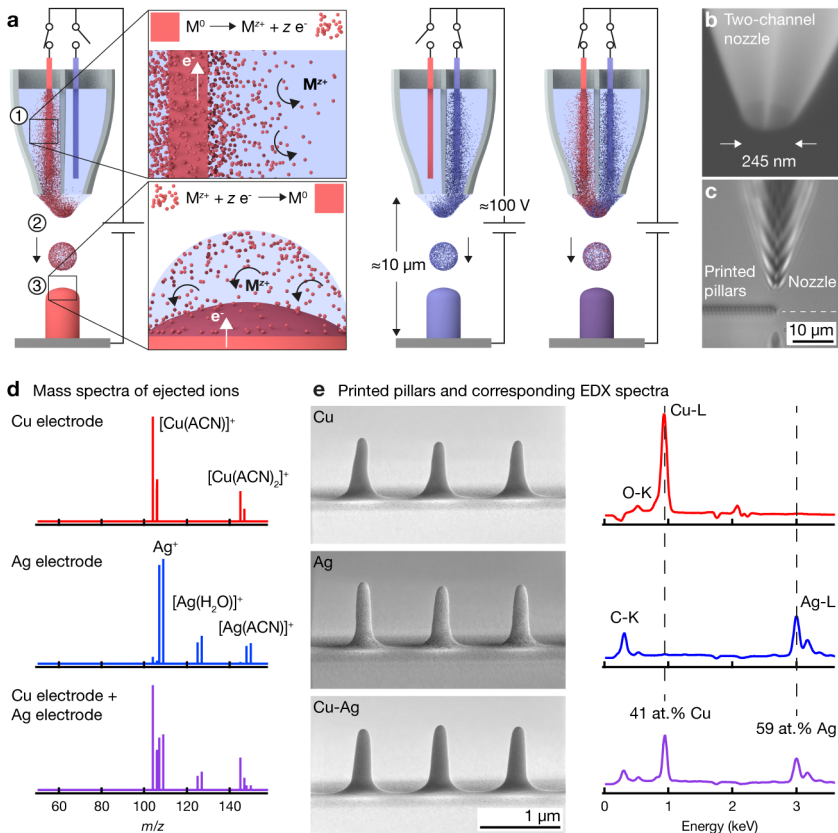


Figure 5.4 – Multi-metal EHD-RP. **a**, Working principle: (1) Solvated metal ions M^{z+} are generated within the printing nozzle via electrocorrosion of a metal electrode M^0 immersed in a liquid solvent. (2) Ion-loaded solvent droplets are ejected by electrohydrodynamic forces. (3) Upon landing, M^{z+} ions are reduced to zero valence metal M^0 through electron transfer from the substrate. Switching the oxidative voltage between different electrodes in a multichannel nozzle enables on-the-fly modulation of the printed chemistry (Schematics not drawn to scale: typical dimensions of the electrode wire are $100\ \mu\text{m} \times 2\ \text{cm}$). **b**, Low-vacuum SE micrograph of a typical two-channel nozzle. **c**, Optical micrograph of the printing process. **d – e**, Printing Cu, Ag and Cu-Ag from a single, two-channel nozzle. **d**, Mass spectra of ejected ions when biasing the Cu electrode, the Ag electrode, or both electrodes immersed in acetonitrile (ACN). **e**, SE micrographs of printed Cu, Ag and Cu-Ag pillars with corresponding energy-dispersive X-ray (EDX) spectra reflecting the chemical nature of the respective source electrode (background subtracted). The C-K and O-K peaks likely originate from residual solvent and minor oxidation respectively. The Cu and Ag contents of the Cu-Ag pillars are given in at.% normalized to the total Cu + Ag signal. Image tilt: 85° .

5.4.2 On-the-fly variation of the printed chemistry

The prompt, on-the-fly control of ion generation facilitates fast variation of the printed chemistry. Figure 5.5a shows MS transient ion currents recorded upon switching the voltage between a Cu and a Ag electrode at different frequencies. Alternating ion-current pulses as narrow as 100 ms are clearly resolved. Selectivity of the ON ion species over the OFF species is high, although a spike of OFF ions ejected at the beginning of each pulse indicates purging of leftover ions (See Section 5.4.5 for more details).

Upon printing, the individual pulses of Cu^+ and Ag^+ ions translate into chemical modulations, and are resolved up to the minimal pulse width of 100 ms (Fig. 5.6b). However, mixing of the individual chemical signals is evident for intervals smaller than one second. Nonetheless, ion pulses of 100 ms were used for printing, and chemical features smaller than 400 nm were printed in practice (Fig. 5.6b).

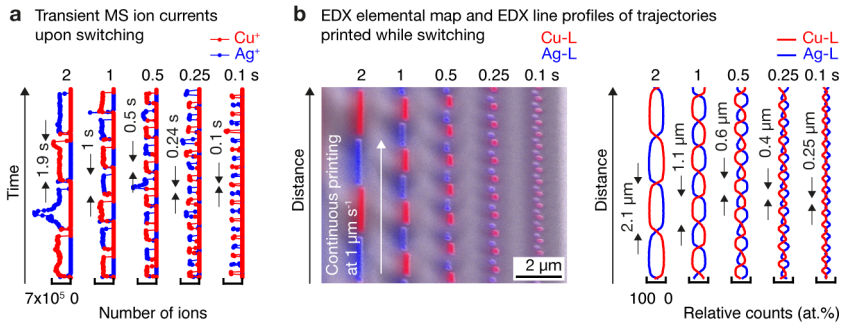


Figure 5.5 – On-the-fly switching of the printed chemistry. Fast switching between two metals printed from a two-channel nozzle: **a**, Summed mass spectrometry (MS) ion currents of Cu^+ (red) and Ag^+ (blue) cations ejected upon switching the anodic voltage between a Cu and a Ag electrode at different intervals. Switching between two ejected ion species is highly selective. **b**, Overlaid SE micrograph and EDX elemental map of trajectories printed with the same switching profile as in (a) (Cu-L signal, red, and Ag-L signal, blue). The corresponding EDX line profiles show that the switching between Cu and Ag is resolved up to the smallest pulse width.

5.4.3 3D printing chemically architected structures

The rapid switching of the printed metals enables the direct synthesis of chemically heterogeneous 3D geometries with high spatio-chemical resolution. As one of two examples, pillars with individual numbers of Cu and Ag segments were grown by alternating the anodic electrode potentials

at intervals of 0.5 – 1 s while printing in a serial, point-by-point manner (Fig. 5.6a). As a second example, a Cu-wall with an embedded chemical image of the letters 'Ag' printed in silver demonstrates the realization of an intricate chemical architecture by switching between two metals upon printing in a layer-by-layer mode (Fig. 5.6b, Movie S1).

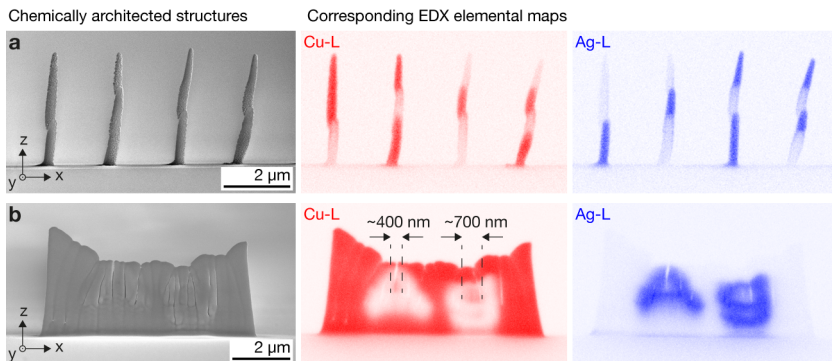


Figure 5.6 – Additive control of the chemical architecture. Examples of chemically heterogeneous structures printed using a single nozzle: SE micrographs and corresponding EDX elemental maps of **a**, a sequence of pillars with different numbers of Cu and Ag modulation periods, and **b**, an out-of-plane Cu wall with the letters 'Ag' embedded in silver, printed with a continuous layer-by-layer printing mode (Movie S1). Image tilts 87°.

5.4.4 Reproducibility and alignment of the chemical switching

Printing two metals from a single, multichannel nozzle mitigates alignment issues considerably. Consequently, printing structures that demand well aligned deposition of two materials, such as the layered pillars shown in Fig. 5.6a, can be printed with high reproducibility (Fig. 5.7). Nevertheless, the asymmetry of a two-channel nozzle can cause some spacial shift of the two materials: in the shown experiment, the alignment upon the Ag-to-Cu switching was ideal, while the switching from Cu to Ag resulted in a slight lateral misalignment of approximately half a pillar-diameter. The in-plane shift for a typical nozzle, as measured in Fig. 5.5b, is on the order of 150 ± 10 nm, with a typical line width of 330 ± 20 nm for each of the individual materials.

Further, an imbalance in deposition rates of the two materials can result in inhomogeneities in height as observed in the wall in Fig. 5.6b and in the line sequence in Fig. 5.5b. In both cases, Ag was printing at a slightly lower rate. Thus, the parts of the wall in Fig. 5.6b that contain Ag layers (middle) are approx. 30% lower in height compared to the sections of the wall that are built from Cu only (sides).

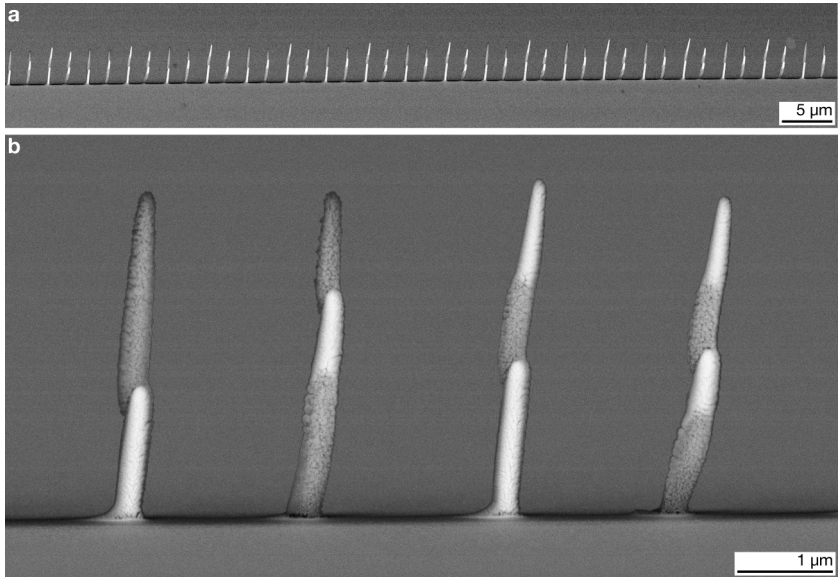


Figure 5.7 – Reproducibility of the chemical switching. **a**, BSE micrograph of a sequence of chemically layered pillars. Bright contrast corresponds to Ag, dark contrast to Cu. Once the growth rates are adjusted for each metal, printing is reproducible. **b**, Zoomed image that shows the repetitive unit of the sequence in (a). This micrograph corresponds to the SE image and the EDX elemental maps shown in Fig. 5.6a.

5.4.5 Switching speed and current output profile

For well defined alternation between the two metals, a square-wave pulse train is the desirable ion current profile upon switching: fast rise and fast drop of the current guarantee a spatially most confined chemical voxel. As we found, the shape of the current output upon switching is pronouncedly influenced by the switching procedure.

The typical electrical setup for printing consists of a polarized electrode connected to the high output of a voltage source, and a grounded substrate (Fig. 5.8a). To stop the ion ejection from the nozzle, the electrode needs to be depolarized. This can be achieved by either setting the electrode to an electrically floating or grounded state. If the electrode is switched into a floating state, the surface charge is removed through further oxidation of the electrode and ejection of ions through the nozzle until the surface potential is equilibrated. Thus, the ejection ceases in a slow and gradual

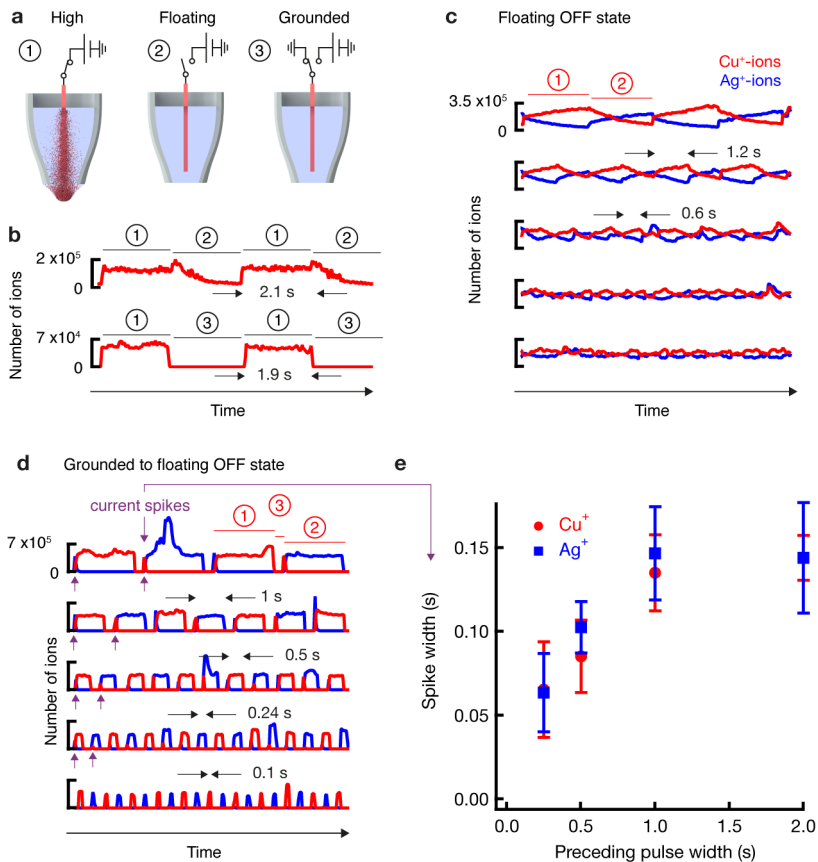


Figure 5.8 – Increased switching speed by active removal of surface charge. **a**, To stop the ejection of ions from a nozzle, the high potential of the electrode (1) needs to be removed. This may either occur by switching the source into an electrically floating (2) or a grounded (3) OFF state. In the floating case, the electrode's remaining charge is removed through extended ion ejection. In the grounded case, the charge is removed through the external circuit. **b**, MS ion currents recorded for a Cu electrode switched from high (1) to floating (2) (top) or from high (1) to grounded (3) (bottom). The numbers indicate the switching-states. **c**, **d**, MS ion currents recorded for switching between a Cu (red) and a Ag (blue) electrode at decreasing intervals, either by switching the sources directly into the floating OFF state (**e**) or only after an intermittent grounded stage (**d**). The numbers indicate the switching-states for the red current transient. Current spikes of the opposite ion species are observed upon switching in (**d**) (purple arrows). **e**, Width of the current spikes (measured at their base) as a function of the preceding ON-time of the respective ion source (Cu^+ : red circles, Ag^+ : blue squares). The error bars indicate the standard deviation of the measurement.

manner (Fig. 5.8b). In contrast, if the electrode is grounded, all surface charge is removed through the external circuitry, and the ejected ion current is quenched rapidly.

If multiple electrodes are used as ion sources, any electrode switched off must be in an electrically floating state to avoid unwanted redox-currents in-between the individual electrodes (the individual channels of the nozzle are connected by the solvent across the meniscus at the orifice). Consequently, the easiest strategy to switch between two electrodes is to alternate the individual sources from high to floating. As described above, this approach results in prolonged ejection of ions after turning off an electrode. Consequently, switching between two elements is blurred (Fig. 5.8c). To obtain a square-wave ion-current output, the electrode to be turned OFF needs to be grounded just long enough to enable complete removal of the surface charge through the external circuit (Fig. 5.8d). Subsequently, this electrode can be switched to a floating OFF state before the other electrode is polarized. This approach necessitates the intermittent off-time of 100 ms between deposition pulses. The interrupted deposition could be corrected for by synchronized pausing of stage translation.

While the switching mode high – grounded – floating enables faster switching, it does not avoid a current spike of the opposite ion species at the onset of each ion pulse (purple arrows in Fig. 5.8d). As suggested by Fig. 5.8e, the width of these spikes is a function of the ON-time of the preceding pulse and possibly plateaus at ≈ 150 ms for ON-times > 1 s (although the two data points are clearly too few data to draw a definite conclusion).

5.4.6 Microstructures of Ag and Cu printed from a single nozzle

In analogy to printing with a single metal, the microstructure of metals printed from a two-channel nozzle is polycrystalline and of high density. Estimation of the pore area fraction of Cu, Ag and Cu-Ag pillars yields densities of $>90\%$ for all materials (Fig. 5.9). We assume that the as-deposited, co-printed Cu-Ag material is in a metastable, solid solution state, since it is deposited at room temperature using relatively high growth rates on the order of $\approx 1 \mu\text{m s}^{-1}$. No evidence for a phase separation of the thermodynamically immiscible Cu-Ag system was detected at length scales accessible with BSE microscopy, but no TEM studies have been performed.

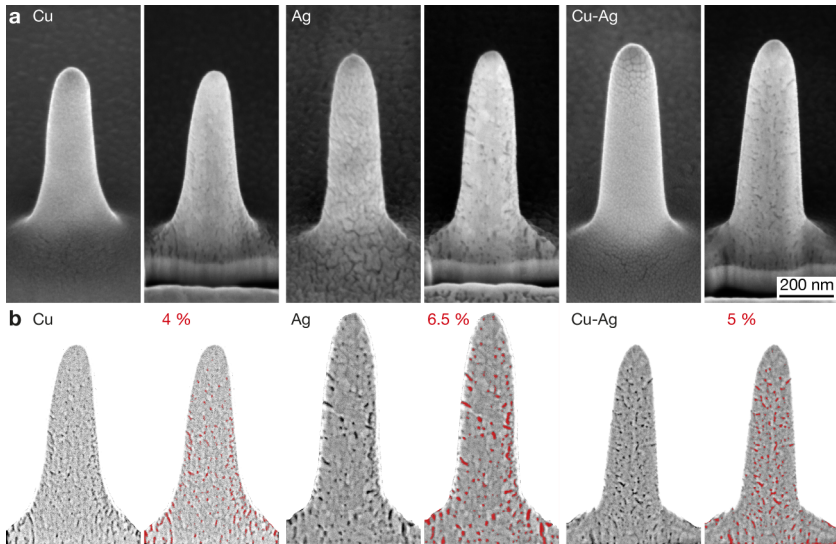


Figure 5.9 – Microstructure and pore fraction. **a**, InLens SEM micrographs and FIB cross sections of as-deposited Cu, Ag and Cu-Ag pillars printed from the same two-channel nozzle (in each case the rightmost pillar of Fig. 5.4e). All pillars are polycrystalline. **b**, The pore area fractions estimated by image contrast analysis are: Cu: 4%, Ag: 6.5%, Cu-Ag: 5%. All images are tilt-corrected.

5.4.7 Tailored local properties via additive design of the local chemical composition

The additive control of the chemical architecture provides the means to extend the classic approach of tuning properties by alloying to the individual portions of a printed structure, enabling the deterministic programming of local materials properties through the architecting of the local composition. Indeed, we demonstrate two examples of chemically heterogeneous structures that express local variations in properties based on tuning of the local electrochemical nobility. In both examples, the combination of two metals of different electrochemical nobility within one printed structure enables applications that are inaccessible with the individual materials.

First, we employ selective etching of printed Cu support structures to extend the range of accessible geometries to bridging structures (Fig. 5.10). Second, we utilize dealloying of co-printed Cu-Ag segments (45 – 50 at.% Cu) to fabricate pillars with local modulations in nanoscale porosity and

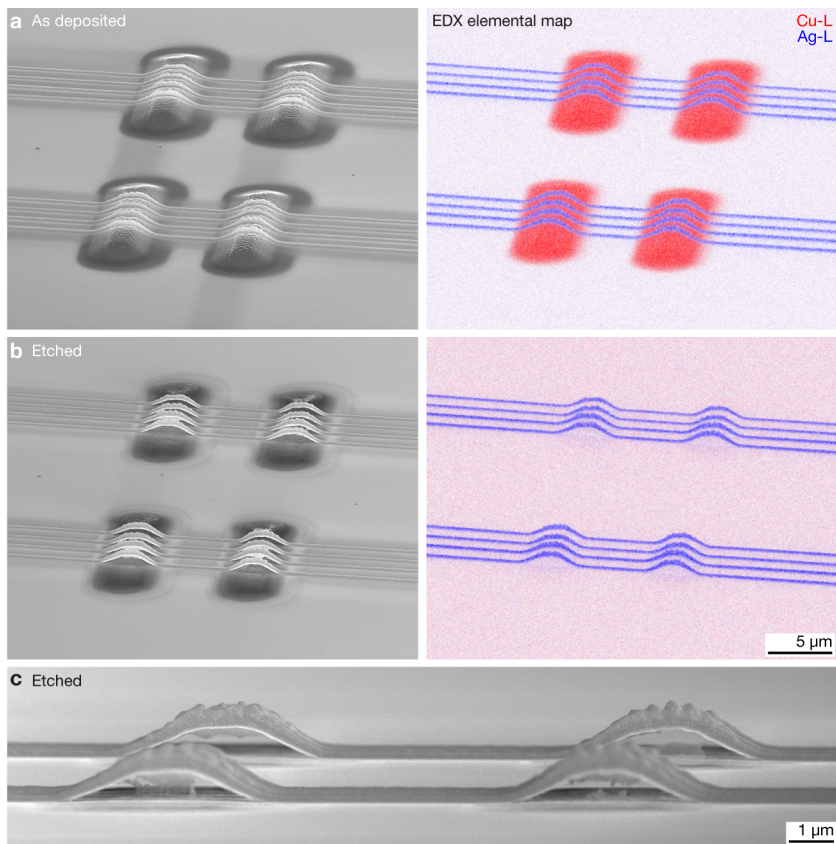


Figure 5.10 – Sacrificial support structures. Exploiting the dissimilar nobility of Cu and Ag for printing of sacrificial support structures. SE micrographs and corresponding EDX elemental maps of **a**, Ag lines printed on top of Cu support structures before and **b, c**, after selective wet etching of Cu. Image tilts: a, b, 60°, c, 82°.

thus a step-function in mechanical strength (Fig. 5.11). The latter is showcased by the significantly increased plasticity within the softer, porous segments upon bending of the pillars (Fig. 5.11c, Movie S3). As this is only a qualitative demonstrator, the changes in modulus and hardness upon dealloying have not been quantified yet.

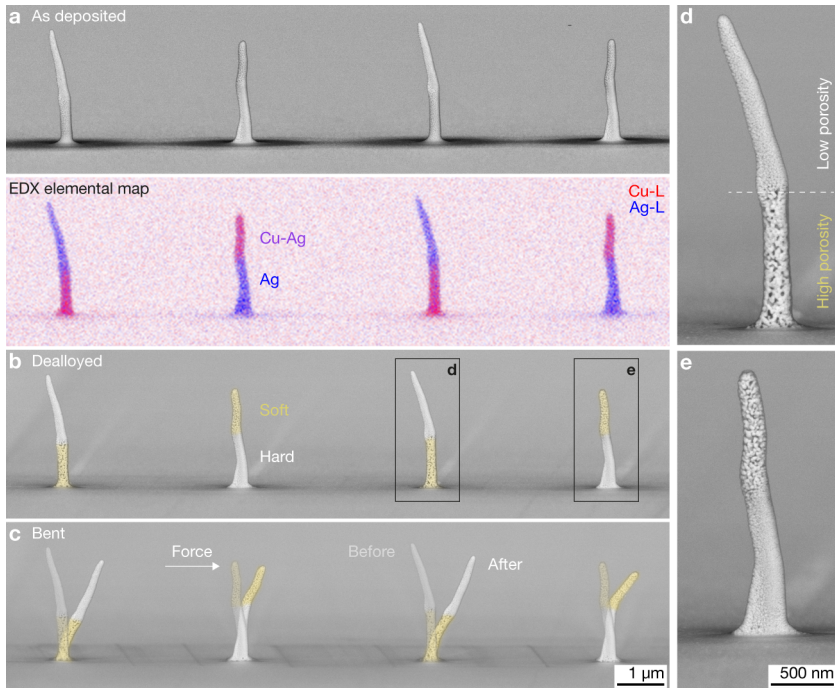


Figure 5.11 – Tailored local materials strength via the design of the chemical architecture. Exploiting the dissimilar nobility of Cu and Ag for tuning of local porosity and thus local mechanical strength. **a**, Bi-metal pillars printed with alternating segments of Ag and Cu-Ag before and **b**, after selective dissolution of Cu. The dealloying of Cu from the Cu-Ag segments renders partially nanoporous Ag pillars with soft (porous, colored in yellow) and hard segments. **c**, The step-function in porosity modulates the local mechanical strength: upon bending of the pillars, the plastic deformation is pronouncedly confined in the porous segments (Movie S3). **d**, **e**, Close-up of the partially nanoporous pillars after dealloying. All micrographs: InLens SE, tilt 87°.

5.5 Discussion

5.5.1 Bi-metal printing from a single nozzle: advantages and challenges

The concept of multi-metal EHD-RP – in-situ generation of the precursors for the material to be printed in a fast and easily controlled way, in combination with ejection from a single nozzle – enables printing of chemical architectures unmatched in complexity by any alternative approach for inorganic materials at comparable length scales (Fig. 5.12). Compared to multi-nozzle systems, the use of a single nozzle facilitates an increase in complexity of the chemical sequence without a penalty in printing speed and added alignment errors. Compared to alternative single-nozzle approaches, the switching speed and hence the steepness of any material gradient is orders of magnitude larger for EHD-RP: all alternative single-nozzle strategies base on mixing and co-extrusion of two inks – an approach that is well suited for printed of smoothly graded materials but cannot access step-function gradients and are limited to chemical voxel sizes \gg the geometrical voxel size⁴¹⁵.

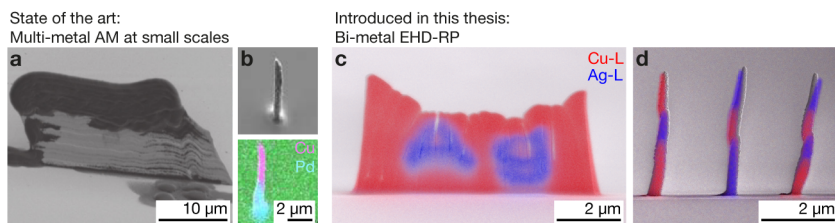


Figure 5.12 – Bi-metal EHD-RP in comparison with the state of the art at comparable length scales. **a, b,** Difficult alignment and switching between two materials at the sub-micrometer scale prevents state-of-the-art multimaterial methods from depositing complex chemical architectures (**a**, EHD printing of two inks, year 2015¹⁰⁴, **b**, aerosol-printing, 2018³⁶⁶). **c, d,** In contrast, the here introduced technique, EHD-RP, enables fast switching between two metals printed from a single print head and thus more complex chemical 3D designs. **a, b,** Reprinted with permission from **a**,¹⁰⁴ ©2015 John Wiley and Sons; **b**,³⁶⁶ CC BY 4.0 (<https://creativecommons.org/licenses/by/4.0/>).

Thus, EHD-RP holds great potential for the synthesis of most complex chemical architectures. However, multiple technical challenges need to be addressed to realize this potential, including the geometrical alignment upon switching, precise control of the atomic fraction of each metal, and of course the currently limited range of metals and materials in general (which is discussed in Section 4.5.3).

5.5.1.1 Spatial alignment

The asymmetry of the presently employed two-channel nozzles causes some lateral misalignment upon switching (Fig. 5.6a, 5.5b). Minimal shifts obtained with best nozzles are of \approx half a line-width. In general, the misalignment is most critical for 2D structures, as the shift is to some extent mitigated by the auto-focussing effect of EHD-deposition⁹⁹ when depositing out-of-plane wires. If a shift occurs, it is typically constant for a given nozzle and could possibly be corrected by translating the stage accordingly. Yet, the magnitude of the lateral shift between two materials varies from nozzle to nozzle, as the asymmetry of the nozzles is not constant due to uncontrollable fluctuations in the fabrication process. In addition, the lateral resolution observed for the two metals printed from a two-channel nozzle often differs. Thus, statistical analysis of the asymmetries during printing, optimization of the nozzle fabrication and development of an alignment procedure should be performed if one intends to continue using these multi-channel nozzles. However, I propose that a re-design of the multi-channel nozzles is more sustainable than difficult optimization and the implementation of artificial corrections. In the best case, this results in a solution that nullifies the observed shift and differences in feature size and does not require calibration of each nozzle.

Quite likely, the shift observed with today's two-channel nozzles is caused by the two separate apertures for each metal – in the end, the used theta-nozzle is merely two individual nozzles mounted in extreme proximity. As with standard multi-nozzle systems, this misalignment of two nozzles causes a misalignment in printed geometries. Consequently, the two-nozzle design needs to be discarded and multiple materials need to be printed from a truly single nozzle. However, preliminary experiments showed that two separate channels are required to avoid cross-contamination of the two sources. Hence, future designs need to fulfill two main design criteria: 1) individual channels for each metal, and 2), all channels ending in a single, circular ejection aperture. While such a design could be microfabricated (FluidFM probes with multiple channels do exist), I would adhere to simpler nozzle fabrication procedures for the time being. To this end, I recommend to explore nested designs of multiple drawn capillaries (Fig. 5.13). Such a design satisfies the two design criteria while at the same time maintaining simplicity – a key advantage of the current EHD-RP technology.

First trials with such nested designs suggest that a large dead volume between the apertures of the inner and outer nozzle results in delayed and gradual switching between Cu and Ag, contrasting with the immediate switching observed for simple two-channel nozzles (Fig. 5.13c, d). Minimization of the dead volume is complicated by the difficult fabrication of outer nozzles – the large diameter of the capillaries and the resulting misalignment of the laser during pulling cause asymmetric tapers. Yet, the fabrication of inner nozzles with long and flexible tapers enables (manual)

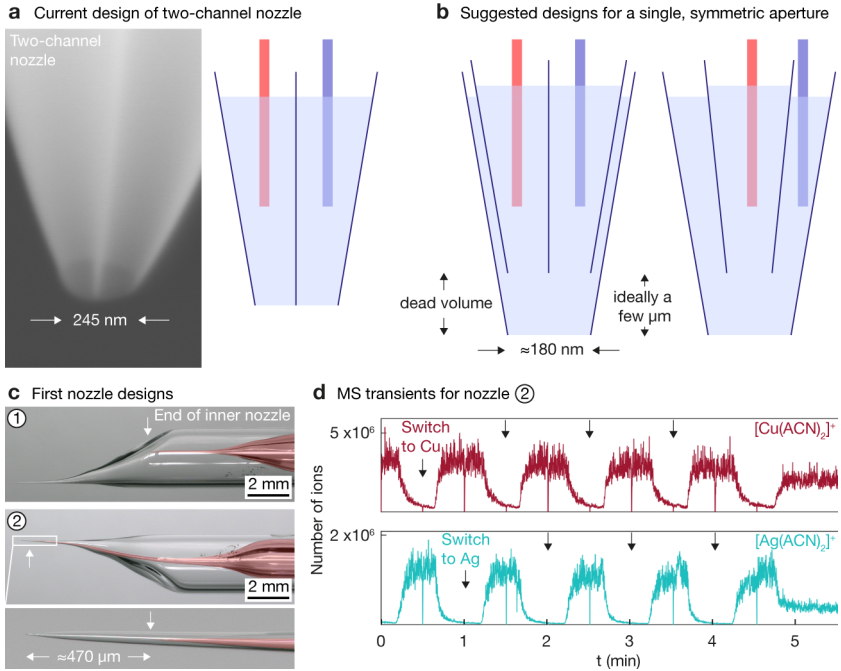


Figure 5.13 – Suggested nested nozzle design. **a**, Low-vacuum SE micrograph and schematic drawing of a theta-nozzle used in today’s bi-metal printing experiments. The asymmetrical aperture with two individual openings probably causes the observed spatial shift of two printed metals upon switching. **b**, I suggest nested capillaries (either a theta-capillary in a single-channel capillary, left, or a single-channel capillary in a single-channel capillary, right) as a simple design approach for printing nozzles with a single, circular aperture but individual channels for each metal. **c**, Optical micrographs of two-channel nozzles (shaded in red) inserted in asymmetric single-channel nozzles. The white arrows mark the position of the aperture of the inner nozzle. (1) Two-channel nozzle with a short taper: the distance to the aperture is several millimeter. (2) Two-channel nozzle with a long, flexible taper: the distance from inner to outer aperture is reduced to $\approx 470 \mu\text{m}$. **d**, MS transients recorded with nozzle (2) (with an empty outer nozzle): $[\text{Cu}(\text{ACN})_2]^+$ and $[\text{Ag}(\text{ACN})_2]^+$ ion currents upon switching between a Ag and a Cu wire at an interval of 30 s. A delay of $\approx 15 \text{ s}$ between switching of the anodic voltage (black arrows) and the increase of the respective ion current is observed (Adapted from the Bachelor Thesis of Andrea Scheidegger).

placement of the inner nozzle at a distance of a few hundred micrometers from the outer nozzle's end, despite the asymmetry (Fig. 5.13c, nozzle (2)). For reducing this distance to a few micrometers, a new nozzle holder that features a micromanipulator stage for positioning has been fabricated but not yet validated. Future experiments should confirm the effectiveness of the suggested design approach – in any case, a print head that facilitates well-aligned and user-friendly multi-material printing will be a decisive advantage over the current technology.

5.5.1.2 Individual growth rates and controlled mixing

A mismatch of the growth rates of two metals printed simultaneously or sequentially results in distorted multi-metal geometries (5.6b). In practice, any operator tries to harmonize the two rates, as they are easily adjusted by tuning the individual ejection voltages. However, perfect matching is impossible during operation, and multiple layers always amplify any imbalance. Thus, a feedback-loop that controls the individual growth speeds based on the electric current through the separate sources should be implemented in the future to improve the geometrical reproduction of the designed features. As discussed previously (Section 4.5.1.1), the ejection current is proportional to the grown volume in steady state. Hence, the individual ejection voltages could be adjusted to match the individual reduction currents for equal growth rates.

Today, EHD-RP supports only three modes of bi-metal printing: printing either one or the other metal, or printing both metals simultaneously. When co-printing two metals, the alloy composition is presumably determined by the individual anodic currents of the sources, which are primarily a function of the applied voltage (and presumably the opening diameter of the two channels). Unfortunately, the potential of the two sources cannot be adjusted individually when polarizing two sources simultaneously, as unequal anodic potentials result in cross-currents between the sources and consequential cross-contamination (as the two channels are connected across a liquid bridge at the aperture of the theta nozzle). Thus, the single growth rates cannot simply be matched by adjusting the individual anodic voltages. As a result, the composition of 1:1 co-printed alloys is rarely 1:1, but usually varies between 40 at.% and 60 at.% of one element because a lever for adjusting the individual growth rates is missing. Similarly, EHD-RP is currently unable to produce alloys that lean towards one side of composition, for example 0.1:1.

Future users should thus need to evaluate ways of controlling individual growth rates while at the same time avoiding cross-currents between the sources in order to deposit extended ranges of compositions and gradient alloys. As the two sources can only be polarized sequentially in the case of differing anodic potentials, I would suggest to pulse the individual sources in an alternating fashion, with duty cycles proportional to the intended atomic fraction of the alloy to be printed.

5.5.1.3 Switching speed

Clear and complete switching between two ejected species of ions is the prerequisite for a small chemical feature size when modulating the chemistry on the fly. As shown by the MS transient currents in Fig. 5.5a, the output current of two different metals upon switching mostly follows a square wave, hence guaranteeing spatially well defined chemical voxels upon continuous printing. Nevertheless, a mixing of the printed Cu-Ag segments in Fig. 5.5b is apparent. This mixing is at least partially attributed to the limited lateral resolution of the EDX line scans, and TEM EDX mapping of lines printed on thin membranes should be performed to quantify the intermixing upon switching with higher resolution.

In any case, the spikes of opposite material ejected upon switching (Fig. 5.8d, purple arrows) probably contribute to some real intermixing and blurred interfaces between two materials. These spikes presumably indicate the purging of ions from the OFF channel of the printing nozzle – ions that were dissolved but not yet ejected during the preceding pulse. This ejection of previously ionized ions limits the sharpness of any interface produced by switching between two metals and will result in a gradient region containing a mixture of both metals. The width of this interface can be estimated by the approximate pulse duration of the current spikes: Fig. 5.8e plots the width of the current spikes, measured at their base, as a function of the preceding ON-time of the respective source. The observed maximum spike width of 0.15 s translates into a width of 100 – 200 nm for a resulting gradient region when assuming a typical printing speed of $1 \mu\text{m s}^{-1}$. As this is on the order of the lateral printing resolution, the purging of the leftover ions does currently not limit the minimal in-plane interface width (as it is simultaneously restricted to the lateral resolution). In contrast, the spike width limits the width of interfaces when printing out of plane. Here, lower out-of-plane growth rates would benefit sharper interfaces between two materials – out-of-plane growth speeds as low as $\approx 150 \text{ nm s}^{-1}$ have been demonstrated, which would reduce the interface width to $\approx 20 \text{ nm}$.

Additionally, sharpest interfaces could be formed during post-print annealing. For immiscible systems, for example Cu-Ag, a post-print heat treatment would result in de-mixing of as-printed metastable solid solutions, thus forming atomically sharp interfaces.

5.5.2 Bi-metal printing – towards voxel-by-voxel control of materials properties

The sacrificial supports utilized for facile printing of arching wires (Fig. 5.10) or the pillars with designed gradients in nanoscale porosity (Fig. 5.11) constitute basic demonstrations of additively

designed local properties in microscale objects (chemical reactivity and stiffness and strength in these cases). In general, a variety of mechanical, optical and reactive properties can be accessed with the three currently printable metals Cu, Ag and Au: optical absorption (through post-print dealloying for nanoporosity), electrical resistance (through porosity, alloying or post-print oxidation), strength and stiffness (pure metals or alloying), or oxidation susceptibility (pure metals or alloying). Once a few more metals are available, magnetic (Fe, Ni, Co) and thermal properties (high melting, *e.g.* W, or low melting, *e.g.* Sn) can be added to this list. Thus, even if EHD-RP remains restricted to metals, a large number of disparate materials properties could be unified within a single printed object.

However, for voxel-by-voxel tuning of properties by EHD-RP, one should account for the fact that many materials properties are a function of not only chemistry also the materials' microstructure (grain size, point-defect density, porosity). For example, solid solution hardening will hardly change the local strength in a nanocrystalline metal, as the Hall-Petch hardening will entirely dominate the strengthening. Likewise, the electrical resistance in the printed metals is probably dominated by the high defect density rather than the chemical nature of the printed metal. Most of the times, local property design will thus require a combination of voxel-by-voxel control of chemistry (as demonstrated in this chapter) and microstructure.

The dependency of the synthesized microstructure on the electric field indicates that the microstructure can be controlled and, more importantly, changed *in situ* for each single voxel (with accompanying difficulties when translating this concept to layer-by-layer printed structures, as discussed in Section 4.5.2). However, it is unclear how the microstructure and the composition couple upon printing. While this relation should certainly be explored and understood in the future, one should also consider microstructure tuning through post-print annealing or etching procedures. Such approaches can build on established knowledge for microstructure design (as demonstrated in Figure 5.11). For example, one could try to use Ag precipitation and segregation to grain boundaries to stabilize the as-printed nanocrystalline microstructure in Ag-Cu alloys. Upon thermal annealing of a printed Cu / Ag-Cu structure, Cu would presumably undergo grain, while Cu-Ag segments might retain their nano grain size. Thereby, one could alter local electrical resistance or strength not directly through chemistry only, but through an interplay of alloying and heat treatment for designing the final microstructure.

5.6 Conclusion and outlook

In summary, EHD-RP markedly advances the state of the art of multi-metal AM at small scales. A chemical resolution of <400 nm in combination with a geometrical resolution of 250 nm and switching intervals as low as 100 ms offer unmatched control of the 3D chemistry of additively synthesized metals. Although we focused on bi-metal printing with Cu and Ag, the approach could be extended to more complex materials combinations by using nozzles with more than two channels and by exploring synthesis protocols that grant access to additional metals and potentially non-metals. As we have shown, control of the local chemistry can be used to control local properties of printed structures. Here, the demonstrations of sacrificial support structures will surely extend the geometric complexity that is accessible with EHD-RP. Yet, most importantly, demonstration of local alloying and accompanying local nanoporosity is a first demonstration towards gradient property design in 3D inorganic materials at the submicron scale.

Thus, EHD-RP holds the potential for unlocking unique routes for the bottom-up fabrication of chemically designed 3D devices and materials with locally tuned properties or a rational use of alloying elements. However, to access this potential, multi-metal EHD-RP must solve multiple technical challenges (additional to those mentioned in the previous chapter). Apart from expanding the range of metals and materials, these mostly center around alignment and growth-rate control of the individual metals: new nozzle designs are necessary to eliminate spatial shifts, and a feedback for the individual metals' growth rate is inevitable for accurate geometrical reproduction of multi-metal structures as well as for precise control of printed alloy composition.

In the future, the control of local alloy composition could be combined with EHD-RP's control over the grain size or porosity (Section 4.4.6) to enable full control of a material's microstructure with submicrometer resolution. This would enable deterministic design of a multitude of local properties, such as reactivity, strength or electrical resistance. Such materials could find application in catalysis, active chemical devices, small-scale robotics, and architected materials that go beyond single-material cellular designs.

Chapter 6

Electrochemical additive deposition with nanosecond voltage pulses in a STM – a route towards smallest feature sizes

Currently, no AM method provides direct and easy 3D fabrication of high-purity metals with a resolution $\ll 100$ nm. To challenge this shortcoming, the present chapter explores a concept originally applied to microscale electrochemical machining⁴¹⁶ for the nanoscale electrochemical deposition of Co on Au. The concept's essence is the localization of electrochemical reactions below a probe during polarization with ns-long voltage pulses. As shown, the strong confinement enables a feature size of < 50 nm for 2D patterning. The chapter presents the designed setup and the associated deposition procedures, verifies the potential for nanoscale in- and out-of-plane deposition and qualitatively illustrates the influence of deposition parameters on the feature size. Finally, it critically discusses issues with the anodic stability of Au tips used for patterning. As an inert probe is the prerequisite for controlled structuring, we scouted for alternative tip materials and experimentally verified the increased resistance of Pt probes against degradation. Consequently, the developed setup and processes are now available for reproducible 2D and possibly 3D patterning of metals at the nanoscale.

6.1 Introduction: Scanning-probe microscopy for electrochemical patterning – potential for smallest feature sizes

None of the current AM methods can easily provide metals of high purity with a resolution <100 nm – standard FEB and FIB deposits grown from conventional precursors contain 10 – 20 at.% metal only, and their purification is challenging²¹⁶. Electrochemical methods could be regarded as the sole candidates with potential to access the 10 nm-regime with pure metals, as not many alternative techniques can possibly reach that length scale at all^a. However, compared to electron- and ion-beam techniques, the minimal feature size offered by contemporary electrochemical methods is still least one order of magnitude larger (≈ 100 nm compared to ≈ 10 – 20 nm).

To evaluate options for decreasing the minimal feature size of electrochemical concepts, it is helpful to consider the technical limitations of state-of-the-art techniques for 2D and 3D patterning, which include nozzle-based methods (all current AM concepts) and tip-based methods (up to date used for 2D patterning only). Of the nozzle-based concepts, concentration-confined electrodeposition is probably unsuitable for nanoscale deposition due to the poor confinement of deposition – the use of apertures as small as 30 – 50 nm merely decreased the feature size to 400 – 600 nm¹⁵⁵, and much smaller apertures are not available. In contrast, other nozzle-based approaches have shown minimal 2D features of 90 nm¹⁵³ (Meniscus-confined electrodeposition, MCED) and 80 nm (EHD-RP, Chapter 4) (Fig. 6.1a – c). In first approximation, the minimal feature size of MCED is proportional to the diameter of the capillary, which necessitates the use of capillaries <100 nm for feature sizes <100 nm (this is a rough approximation, as the meniscus can be smaller than the nozzle). Handling of these probes is challenging due to enhanced evaporation with small capillaries¹⁵¹ and accompanying clogging issues. With EHD-RP, clogging is less an issue as the constant liquid flow probably prevents drying of the solvent. Unfortunately, smaller nozzles ($\varnothing 100$ nm instead of $\varnothing 160$ nm) did not yet result in a decreased feature size (Fig. 4.11), and the current limits to the feature size of EHD-RP are unknown.

In contrast, electrochemical 2D patterning with nanoscale-sharp tips (as those typically used in scanning probe microscopy, SPM) is a viable approach for structuring with a feature size close to 10 nm – the smallest feature size demonstrated was 16 nm for Co deposits⁴¹⁸ (Fig. 6.1f) and

^aThe low transfer accuracy of LIFT likely renders advances towards nanoscale patterning impossible. Further, every technique that necessitates thermal annealing for the creation of pure structures (all ink-based methods and FEBID / FIBID) will struggle to avoid dewetting and thus break-up at line widths $\ll 100$ nm. Additionally, no ink-based method will reach a resolution that is lower than several particle diameters due to clogging issues (DIW writing currently achieves minimal line widths of 1 – 2 μm) and the fact that a line diameter must contain multiple particles should coalescence of particles upon sintering result in a continuous line (dictated by volume conservation). Currently, the smallest line width of annealed inks is 80 nm¹⁶. With smallest particle diameters of a few nanometers, line widths of several tens of nanometers are probably the absolute minimum of inks.

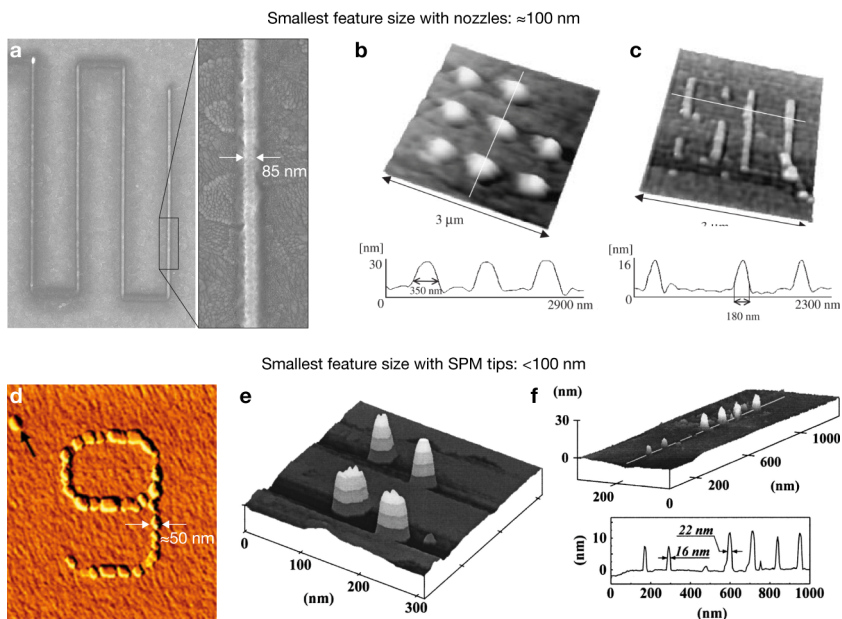


Figure 6.1 – High-resolution electrochemical 2D patterning: nozzle-based vs. tip-based concepts. In electrochemical 2D patterning of metals, smallest feature sizes are achieved with SPM tips. While patterning with capillary-based nozzles demonstrated smallest feature sizes of ≈ 100 nm (a – c), patterning with SPM tips achieved features as small as ≈ 20 nm (d – f). **a**, Top-view SE micrograph of the thinnest Cu line we printed by EHD-RP. **b**, **c**, Shear-force microscope images of Cu patterns grown by MCED using a glass capillary with an aperture of ≈ 200 nm¹⁵³. **d**, Indirect patterning with a SPM tip: AFM micrograph of electrodeposited Cu structure⁴¹⁷. Localization was achieved indirectly, mechanically removing a thin copper-oxide passivation layer with the AFM tip while holding the substrate at a reduction potential. **e**, **f**, Direct patterning with a SPM tip: STM scans of Co dots patterned in an electrochemical STM⁴¹⁸. A locally increased concentration of Co^{2+} ions established with the STM tip initiates confined deposition. Features < 50 nm are achieved by optimizing tip-substrate distance (d) and deposited charge (e). **b – f**, Reprinted with permission from **b**, **c**,¹⁵³ ©2004 JSAP; **d**,⁴¹⁷ CC BY 2.0 (<http://creativecommons.org/licenses/by/2.0>); **e**, **f**,⁴¹⁸ ©2001 ECS.

≈ 10 nm for Cu (Fig. 6.2i). With SPM tips, no clogging limits the minimal dimension of the structuring tools, guaranteeing smallest probes and thus the potential for smallest feature sizes.

6.1.1 Electrochemical lithography with scanning probes

Electrochemical patterning with nanoscale SPM probes offers highest spatial resolution due to the minimal size of the structuring tools. However, the localization of electrodeposition and the supply of ions is less straightforward than with capillary-based printing nozzles. Of the methods suggested in literature, dip-pen lithography^{419,420} is the only technique that works in air, supplying ions through a liquid meniscus between substrate and an atomic force microscope (AFM) tip (similar to the meniscus used in MCED). Localization of deposition in the meniscus is straightforward, but the limited reservoir of ions (metal salts dried on the AFM tip) is not ideal for continuous deposition. As a consequence, the majority of proposed techniques relies on the supply of ions from a bath of electrolyte solution. Immersing the SPM tip and the substrate into a solution of metal salts guarantees an (almost) infinite supply of cations for electrodeposition, but demands more advanced strategies for localization of the electrodeposition.

The proposed concepts for localized growth below a SPM tip immersed in an electrolyte bath can be grouped into two fundamental categories: first, the limitation of the active surface area, and second, a local modification of the factors that govern either the kinetics or the energetics of the electrodeposition reaction. The first group is not suited for 3D deposition, as it merely relies on the local activation of a generally passivated substrate^{417,421} – an approach that is limited to deposition directly on the substrate and offers no means for out-of-plane growth (Fig. 6.1d). In the second group, methods that kinetically favor deposition below the tip suffer from low resolution (a minimal feature size of $2\ \mu\text{m}$ ⁸³ was achieved by using the tip as a local anode upon direct current electrodeposition^{83,86}) or, again, the inability for 3D deposition (all methods based on introducing surface defects for preferential nucleation^{422,423}). The only concepts that guarantee strict localization of the deposition (and thus high resolution) in combination with no need for modifications of the substrate (and thus the possibility to enter the third dimension) are those that energetically limit the spatial extent of cathodic reactions.

Energetic localization of electrochemical deposition is based on a local increase of the activation overpotential η_{ct} for the charge transfer between the solid phase and the cations. This approach guarantees strong confinement, because the cathodic current j (proportional to the growth rate)

increases exponentially with η_{ct} , as described by the Butler-Volmer equation (shown as an approximation which is valid for $\eta_{ct} > 30$ mV only):

$$j = -j_0 e^{\frac{-\alpha z F}{RT} \eta_{ct}}, \quad (6.1)$$

with the exchange current density j_0 , the transfer coefficient α , the Faraday constant F and the valency number z of the cations. Note that the cathodic overpotential is by nomenclature negative, hence j indeed increases with increasing negative η_{ct} .

Two concepts that make use of the exponential confinement have been proposed. The first is based on the manipulation of the local Nernst potential^{418,424,425} (here termed the "Hofmann" approach, after the author of the first paper⁴²⁴, as the authors themselves did not introduce a name), and the second relies on spatially containing the charging of the cathode's double-layer capacitance by nanosecond voltage pulses⁴¹⁶. Both strategies have previously demonstrated deposition of metals with nanometric resolution (Fig. 6.1e, f and Fig. 6.2i). During my thesis, I experimentally evaluated both strategies for nanoscale 2D and 3D deposition, but only succeeded with the second approach. Hence, only the concept of electrochemical localization with nanosecond pulses is introduced in more detail in the next section. For a brief outline of the "Hofmann" approach and our own experimental verification of the concept, refer to Section E.3.

6.1.2 Electrochemical micromachining with nanosecond voltage pulses

Typically, the surface potential of a conductive electrode immersed in an electrolyte solution, that is, the voltage drop across its electrochemical double layer (DL), is constant across the electrode's expanse (given that the electrode's electric resistance is negligible, as in the case of metallic surfaces). Nevertheless, Schuster *et al.*^{416,426,427} showed that the anodic or cathodic overpotential can be confined to finite areas on the electrode. Their concept is illustrated best with the simplified equivalent circuits for two current paths (1) and (2) that connect the immersed tip and substrate in Fig. 6.2a. As will be shown, the application of nanosecond voltage pulses between the tip and the substrate results in an effective confinement of current flow through path (1) and hence a localization of all electrochemical reactions to regions below the tip.

The electrochemical DLs on both electrodes are represented by capacitors C_{DL} , connected by a resistor R (the electrolyte resistance). If a potential U is applied between the tip and the substrate, the resulting voltage across the individual R - C paths is termed U_C . While U_C is equal for every point on the substrate in a steady state, it varies as a function of distance d to the tip in the transient case: upon stepping the potential U , the transient $U_C(t)$ for each current paths is described by the

time constant $\tau = RC$. As R for each point on the substrate is proportional to the resistivity ρ times the variable distance d from the tip, $\tau = RC = \rho d \cdot c_{DL}$ (with the double layer capacity c_{DL}). As c_{DL} and ρ can be assumed to be constant, $\tau(d)$ is directly proportional to the local distance d to the tip: $\tau_1 < \tau_2$. Additionally, $U_C(t)$ becomes a function of not only t but also d .

Let us now consider $U_C(t, d)$ at the end of a voltage pulse of width t_p (Fig. 6.2b). The local polarization $U_C(d)$ reaches significant values if the local $\tau(d)$ is on the order of the pulse width t_p . In contrast, the polarization is negligible at locations with $\tau(d) \gg t_p$. These regions polarize notably only during a longer voltage pulse, drawn in blue (until the DL across the whole substrate is charged equally in steady state). The spatial limitation of significant polarization to regions with $\tau(d) \leq t_p$ enables the effective localization of electrochemical reactions to areas close to the tip. The critical pulse width to limit polarization within a distance d of 1 μm from the tip was estimated by Schuster *et al.*⁴¹⁶ to be 30 ns in aqueous electrolyte solutions^b.

As the rate of electrochemical reactions is an exponential function of the activation overpotential η_{et} (equation 6.1) – which in the present case corresponds directly to U_C , as the resting potential of the surface is potentiostatically adjusted to the $M|M^{z+}$ equilibrium potential – the areal limitation of electrochemical oxidation or reduction is well defined: Figure 6.2c plots calculated polarization U_C and the corresponding anodic etching rate of Cu at the end of a 50 ns pulse applied to a cylindrical tip versus the distance from the edge of the tip. The exponential dependence on $U_C(d)$ results in a drop of the etching rate by a factor of 100 at a distance of $\approx 4 \mu\text{m}$ compared to the etching rate below the tip. Consequently, well defined, local dissolution of metallic surfaces is obtained with short pulse widths (Fig. 6.2d).

The amount of confinement is proportional to the pulse length t_p , because $d \propto \tau \approx t_p$ (Fig. 6.2d, e). It is believed that a confinement distance of $\approx 20 \text{ nm}$, generated with pulse widths of 200 ps, is the practically attainable minimum due to mass transport issues and technical difficulties for applying much shorter pulses⁴²⁸. Yet, this resolution is good enough to enable structuring of submicron-scale features: using a $\varnothing 220 \text{ nm}$ Ir wire, trenches $\approx 260 \text{ nm}$ in width were machined into Au⁴²⁸ (with a resulting gap width of only 20 nm, Fig. 6.2f). Similarly, de Abril *et al.*⁴²⁹ demonstrated milling of 160 nm wide features in a Cu-substrate with a conductive AFM tip (Fig. 6.2g). Finally and most important for the motivation of this chapter, $\approx 10 \text{ nm}$ -wide Cu dots were deposited with a STM tip (Fig. 6.2i).

The experimental setup and procedure introduced by Schuster *et al.*^{416,426,427} are as follows: a bi-potentiostat controls the average potentials of two electrodes – the tip and the substrate – at

^bWith typical values of $\rho=30 \Omega \text{ cm}$, $c_{DL} \approx 10 \mu\text{F cm}^{-2}$ and $d=1 \mu\text{m}$: $t_p = \tau = \rho d \cdot c_{DL} = 30 \text{ ns}$

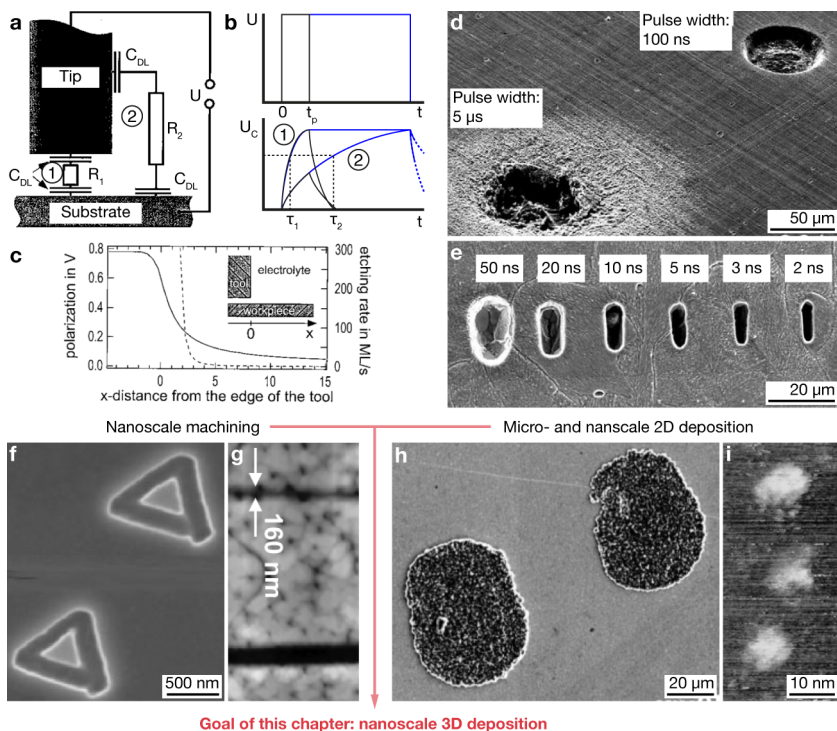


Figure 6.2 – Electrochemical micromachining with nanosecond voltage pulses. Spatially confining the polarization of the substrate’s double layer (DL) during nanosecond voltage pulses strongly localizes electrochemical reactions. **a**, Equivalent circuit formed by tip and substrate immersed in an electrolyte solution, with the DL capacitance C_{DL} and electrolyte resistances R_1 and R_2 for two current paths between tip and the substrate ((1) small distance d to tip; (2) large d)⁴¹⁶. **b**, Upon the application of a short voltage pulse U (black), the transient of the DL polarization of both electrodes is described by $\tau(d)$ and reaches a value $U_C(t_p, d)$ at the end of the pulse of width t_p . For location (1), with $\tau(d_1) \approx t_p$, U_C reaches a significant value. For location (2), with $\tau(d_2) \gg t_p$, polarization is negligible. During a long voltage pulse (blue), U_C of both locations saturate at the same level. **c**, Calculated polarization of the DL on the substrate at the end of a voltage pulse (50 ns, -1.6 V) applied between a cylindrical tip electrode and a Cu substrate as a function of the distance from the edge of the tip (solid line) and corresponding Cu dissolution rate (dashed line)⁴¹⁶. **d, e**, The degree of localization is inversely proportional to the pulse length: **d**, SE micrograph of two holes etched into a Cu substrate with a cylindrical Pt tip ($\varnothing 50 \mu\text{m}$) using different pulse widths: 100 ns (top), 5 μs (bottom)⁴²⁶. **e**, SE micrograph of trenches milled into a Ni-substrate using different pulse widths, but otherwise identical conditions (tip $\varnothing 2 \mu\text{m}$)⁴²⁶. **f, g**, Smaller features can be milled with smaller tips: **f**, Triangular troughs machined with a $\varnothing 220$ nm Ir wire into a Au film (200 ps (lower triangle) and 300 ps pulses (upper triangle), 2.3 V)⁴²⁸. **g**, AFM scans of three trenches milled into a Cu surface with a conductive AFM tip at different tip-scanning speeds of 200 (top), 50 nm s^{-1} (bottom) (20 ns pulses, -3.2 V)⁴²⁹. **h, i**, Inversion of the polarity of the applied pulsed enables deposition instead of dissolution of metals. **h**, SE micrograph of Cu dots deposited on Au with an elliptical Pt-tool (200 ns pulses, 2 V)⁴¹⁶. **i**, Nanoscale Cu dots deposited in an electrochemical STM (50 ns, 3 V)⁴³⁰. **a, c – i**, Reprinted with permission from **a, c, h**,⁴¹⁶ 2000 AAAS; **d, e**,⁴²⁶ ©2003 Elsevier; **f**,⁴²⁸ ©2006 John Wiley and Sons; **g**,⁴²⁹ ©2008 IOP Publishing Ltd; **i**,⁴³⁰ ©1998 APS.

potentials where neither oxidation nor reduction occurs. A pulse generator is used to apply either oxidizing or reductive, nano- to picosecond-long voltage pulses between the tip and the substrate. The separation of tip and substrate is usually less than one micron. Materials such as Cu⁴¹⁶, Ni^{428,431} and p-Si^{416,427} have been machined with micrometer precision, using insulated Pt- or W-wires as tools. Changing the polarity of the voltage pulses further enables the deposition of metallic patterns, so far shown for Cu^{416,430} (Fig. 6.2h, i).

In summary, electrochemical micromachining has demonstrated additive and subtractive electrochemical structuring of metals with a minimal resolution of 10 – 20 nm⁴²⁸. Additionally, the strategy is not limited to 2D deposition (as many other SPM lithography techniques), and could enable 3D growth. Thus, the concept has potential for unrivaled minimal feature sizes in electrochemical AM. However, to our knowledge, no 3D deposition has been attempted so far.

6.2 Objective of this chapter

This chapter explores possibilities for nanoscale 3D deposition with nanosecond voltage pulses (Fig. 6.2), motivated by the promise of achieving smallest feature sizes amongst all electrochemical AM techniques. The stated goal is a minimal feature size that can compete with that of FEBID and FIBID, *i.e.* ≈ 10 nm. This goal should be achieved by the design of an electrochemical STM setup that enables the implementation of Schuster's structuring approach⁴¹⁶ with STM probes as tools for local deposition. The chapter will discuss the sub-100 nm 2D structuring of Co and encountered challenges for 3D deposition and reproducibility, both related to the electrochemical stability of the used metallic STM tips. As tip erosion prevented a stable probe (a problem that is solved at the end of the chapter), no quantitative evaluation of the spatial resolution and the growth mechanism was yet attempted – studies that need to be performed in the future and will be discussed in the outlook.

As a note: I have unsuccessfully tried to use the "Hofmann" approach for nanostructuring. While 1D deposition of Co on Au was achieved (Section E.3), the results were not reproducible and handling of the setup was tedious. Thus, the chapter will focus entirely on local electrodeposition with nanosecond voltage pulses.

6.3 Methods

6.3.1 Electrochemical STM and pulse setup

A schematic of the home-built setup for additive deposition with nanosecond voltage pulses is shown in Fig. 6.3. The setup is composed of three subsystems: a STM (Cypher-AFM in STM-mode, Asylum Research, USA) combined with a home-built electrochemical cell (label 1 in the figure), a bi-potentiostat (PGUmicro, IPS, Germany) and a pulse pattern generator (2x81111A, Agilent, USA). The purpose of the STM is twofold: first, it controls the movement of the substrate relative to the tip in three dimensions during deposition. Second, it provides the tunneling current as a position feedback signal. This feedback allows the positioning of the tip before and during deposition with sub-nanometer precision. The bi-potentiostat controls the average potentials of the tip and the substrate – both immersed in an electrolyte solution – versus the reference electrode and thereby governs global, non-localized electrochemical reactions. Additionally, it monitors the corresponding faradaic currents. In contrast, the pulse generator controls the potential of the tip and the substrate at MHz-rates, inducing localized electrochemical reactions under the tip. The pulse amplitude and the pulse current are monitored with an oscilloscope (6404D, PicoScope, England). It is important to note that the measurement grounds of the three subsystems are held at the same level to avoid leakage currents between the individual instruments. This is achieved on a hardware level by shorting the BNC ground connections of the instruments and by isolating the bi-potentiostat from mains earth using an isolation transformer.

The setup operates in two distinct modes that cannot run simultaneously: the feedback mode and the pulse mode. In feedback mode, the STM tip is connected to the input of the STM current amplifier. This enables the monitoring of the tunneling current and hence precise positioning of the tip. The tunneling voltage is equal to the surface potential of the tip (Working electrode 1, WE1) and the surface potential of the substrate (WE2). In pulse mode, the tip is routed to the output of the pulse generator, so that voltage pulses can be applied to the tip. A mechanical relay switch (Fig. 6.3a, (2)) switches the electrical connection of the tip between the STM current input and the pulse generator as required. In either position of the switch, the potential of the tip is that of measurement ground.

The current circuits for low- (blue) and high-frequency currents (red) are separated by appropriate high- and low-pass filters (Fig. 6.3a, (4, 5)). The low-frequency currents, representing global faradaic reactions, flow between the counter electrode (CE) and the tip (for faradaic reactions at the tip) or between the CE and the substrate connected to the WE2 input of the potentiostat (faradaic reactions at the substrate). The high-frequency current flows from (or into) the output of the pulse

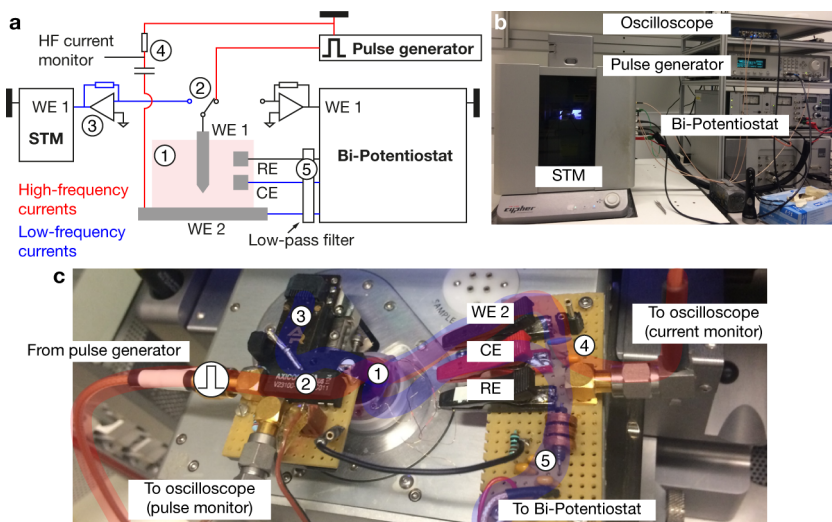


Figure 6.3 – Setup for local deposition in an electrochemical STM. **a**, Schematic of the home-built setup and corresponding photographs of **b**, the three sub-systems that were joined and **c**, the electrochemical cell with corresponding STM and filter electronics. The main components are: STM tip (WE 1) and substrate (WE 2) are immersed in an electrolyte solution contained in an electrochemical cell (1). The surface potentials of WE 1 and 2 are controlled by a bi-potentiostat. The tip is either connected to the current input of the STM (3) or the output of the pulse generator and is switched between the two with a mechanical relay (2). A high-pass filter (4) and low-pass filters (5) separate the high-frequency (red) and the low-frequency (blue) current circuits.

generator through the tip into the substrate and subsequently across a capacitance (high-pass filter, (4)) to ground. In order to minimize the interference of these two circuits, low-pass filters (5) are connected to RE, CE and WE2 in series (see Figure E.2 for a schematic of the electronic circuits).

The setup is computer controlled through a customized software developed in-house and programmed in the Igor Pro software environment (Wavemetrics). The software automates the deposition procedure (described in more detail in Section 6.4.1). It facilitates point-wise or continuous deposition, implements a correction for substrate tilt, and enables recording of out-of-plane growth curves (see Section 6.4.5).

6.3.2 Chemicals and Materials

The electrochemical cell was designed in-house and made from polychlorotrifluoroethylene (PCTFE, Cellpack, Switzerland). O-rings were purchased from Angstrom+Pfister (NORMATEC FKM 70, Switzerland). The counter- and quasi-reference-electrode were plain Au wires (\varnothing 0.1 mm, Möller AG). All constituents of the cell and the electrodes were immersed in fresh piranha solution (3:1 volumetric mixture of H_2SO_4 (conc.) : H_2O_2 (30%)) and subsequently rinsed with MilliQ water and stored in MilliQ water until used. Substrates were either Au single crystals ((111)-out-of-plane $<1\%$, 99.999% purity, Mateck, Germany) or 100 nm thick Au films evaporated onto Si-wafers (including a Cr adhesion layer, 10 nm). The substrates were flame-annealed in a propane-butane flame for 10 min preceding every experiment. After each experiment, the single crystals were cycled in 1 M aqueous H_2SO_4 to remove metallic residues.

Au STM tips were electrochemically etched from Au wires (\varnothing 0.25 mm, 99.999%, Alfa Aesar, Germany) in a 1:1 volumetric solution of HCl (fuming) and ethanol. For etching, we used a potentiostat (PTSTAT12, Metrohm Autolab, Netherlands) to apply a positive DC potential of 2.4 V between a Pt counter-electrode and the Au wire. No current monitor or feedback mechanism to terminate etching was used. After etching, the tips were rinsed with MilliQ water and blow-dried. Pt tips were etched from Pt wires (\varnothing 0.25 mm, 99.997%, Alfa Aesar, Germany) in aq. NaOH solutions. DC or AC voltage profiles with various amplitudes (2 – 10 V) were tested, but no reproducible fabrication procedure could be established. Hence, Pt-20at.%Ir tips were purchased from NugaNeedles (NN-USPtIr-W250, nominal tip radius 25 – 50 nm). All STM tips were coated with a thermoplastic wax (Apiezon, England) to minimize the active surface area of the tips to approximately $50\ \mu\text{m}^2$.

Electrolytes were prepared in glass vials previously cleaned in fresh piranha solution and thoroughly washed with MilliQ water. Typical concentrations were 1 and 2 M of CoSO_4 (Heptahydrate, 99.999%, Alfa Aesar, Germany). The solvent was either MilliQ water or dimethyl sulfoxide (DMSO, analytical reagent grade, Fisher Scientific UK). The electrolyte was handled with sterile plastic Eppendorf pipette tips. All experiments were conducted under atmospheric conditions, without any purging of the electrolytes.

For a qualitative assessment of the anodic stability of Au, Pt, Ir, graphite, Ta, Ti, and ITO, the respective materials were sputter-deposited as thin films and their corrosion behavior was studied upon constant and pulsed (pulse length: 200 ms) polarization at +4.5 V vs. a saturated calomel reference electrode (SCE) (pulse base potential -0.5 V) in three different electrolyte solutions: 1 M aq. Na_2SO_4 , 1 M aq. CoSO_4 , and 1 M $\text{NiNO}_3 \cdot 6\text{H}_2\text{O}$ in DMSO.

6.3.3 Analysis

The dimensions of the deposits were typically assessed *in situ* via STM imaging (typical parameters were: tunneling current: ≈ 1 nA, tunneling voltage: ≈ 200 mV, scan rate: 1 – 2 Hz). Section line profiles were always averaged over a width of 10 scan lines. SEM analysis was performed with a Magellan 400 SEM (FEI, USA). The chemical composition was qualitatively analyzed by SEM EDX spectroscopy (Quanta 200F, FEI, equipped with an Octane Super EDX system, EDAX, software: Genesis, EDAX. Acceleration voltage: 15 kV).

6.4 Results

6.4.1 The principle deposition procedure

Figure 6.4 sketches the basic procedure for localized deposition of Co on a Au substrate utilizing a Au STM tip as a tool for initiating deposition (as inspired by the concept presented in Section 6.1.2). First, it is important to note that the surface potentials of the two working electrodes, Φ_{tip} and $\Phi_{\text{substrate}}$, are continuously controlled by a low-frequency bi-potentiostat (versus a Au quasi-reference electrode, RE). Both electrodes are held at a potential that avoids any faradaic reactions related to the deposition or dissolution of Co. Typically, Φ_{tip} and $\Phi_{\text{substrate}}$ are selected to be in-between the onset potential of Co deposition $\Phi_{\text{Co}^{2+} \rightarrow \text{Co}}$ and Co dissolution $\Phi_{\text{Co} \rightarrow \text{Co}^{2+}}$, as indicated in the cyclic voltammogram of the Au substrate in Fig. 6.4a (Φ_{tip} is ≈ 200 mV positive to $\Phi_{\text{substrate}}$). The rationale for these potentials is simple: $\Phi < \Phi_{\text{Co}^{2+} \rightarrow \text{Co}}$ would result in continuous, non-localized electrodeposition of Co onto the substrate (or the tip); in contrast, $\Phi > \Phi_{\text{Co} \rightarrow \text{Co}^{2+}}$ would lead to the immediate dissolution of any localized deposit.

Prior to any deposition, an image of the substrate is recorded by scanning of the surface with the setup in feedback mode (1, see Section 6.3.1 for an explanation of the two modes). For deposition, the tip is positioned 10 – 100 nm above the substrate by first approaching the surface until a tunneling current is detected (defined as "contact") and then retracting the tip by the respective distance d into its dwell position (2). In this position, the setup is switched into pulse mode, *i.e.* the STM tip is connected to the output of the pulse generator. For deposition, a pulse train of a predefined number of pulses (typically 100 – 100 000 pulses of 10 – 100 ns at a duty cycle of 0.01 – 0.1 and an amplitude of +1 – +6 V) is applied to the tip. As described in detail elsewhere^{416,426,428}, the high-frequency pulses are added to the baseline potential of the tip Φ_{tip} (and with opposite polarity to $\Phi_{\text{substrate}}$), which results in a local decrease of the surface potential $\Phi_{\text{substrate}}$ to values $< \Phi_{\text{Co}^{2+} \rightarrow \text{Co}}$ and initiates local growth (3). After deposition, the system is returned into feedback mode and the deposits are imaged (4). To judge whether the deposited material is Co, the surface potential is lifted to values $\Phi_{\text{substrate}} > \Phi_{\text{Co} \rightarrow \text{Co}^{2+}}$ (5) – if the deposit dissolves, it is assumed to be Co metal. STM scans documenting such a deposition-dissolution cycle are shown in Fig. 6.4c.

6.4.2 2D feature size

A note needs to be made before presenting our observations regarding the influence of various parameters on the minimal feature size: unsatisfactory stability of the STM probes used for deposition makes quantitative analysis of the present data impossible. As we will see in Section 6.4.6,

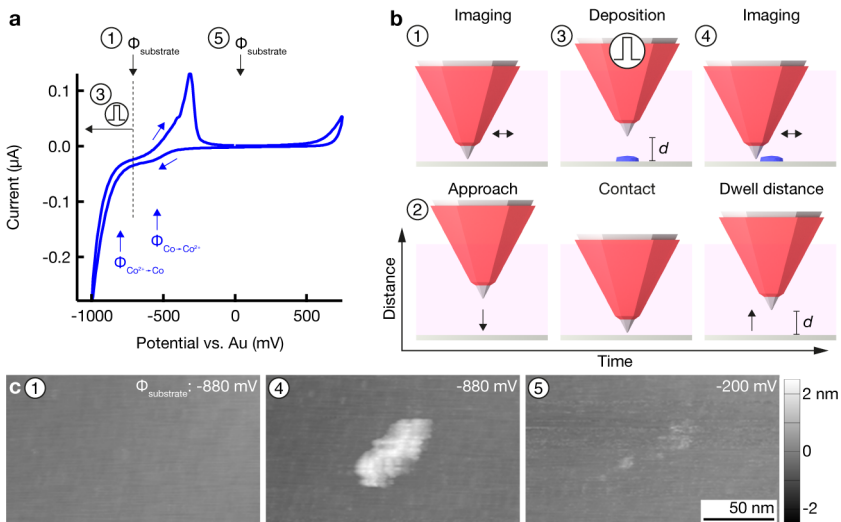


Figure 6.4 – Principle: localized Co deposition by nanosecond voltage pulses. **a**, Cyclic voltammogram of a Au substrate in a solution of 1 M CoSO_4 in DMSO. During and after deposition, the substrate potential $\Phi_{\text{substrate}}$ is potentiostatically set to $\Phi_{\text{Co}^{2+} \rightarrow \text{Co}} < \Phi_{\text{substrate}} < \Phi_{\text{Co} \rightarrow \text{Co}^{2+}}$, preventing delocalized deposition of Co as well as dissolution of local Co deposits (1). Upon application of positive nanosecond voltage pulses to the tip, the substrate is locally polarized towards more negative potentials, initiating local Co deposition (3). **b**, Schematic of the deposition process: Tip and substrate are immersed in a Co^{2+} -containing electrolyte solution. (1) An image of the substrate prior to deposition is acquired. (2) The tip is positioned at a defined distance d from the substrate. (3) Application of nanosecond voltage pulses to the tip locally polarizes the substrate below the tip and initiates local deposition. (4) Deposition is verified by a post-deposition scan. **c**, STM scans of a Au surface before (1) and after (4) local deposition (1 M CoSO_4 in DMSO), and after increasing the surface potential to a value $\Phi_{\text{substrate}} > \Phi_{\text{Co} \rightarrow \text{Co}^{2+}}$ (5). Its dissolution suggests that the deposit was indeed Co. Surface potentials (vs. Au) are stated in the images.

the mostly employed Au STM tips were not sufficiently stable upon anodic polarization and can thus not be considered as inert. This leads to the conclusion that the apex shape and radius cannot be assumed constant, with the consequence that quantitative comparisons of the deposits as a function of deposition parameters cannot be made. Thus, the following trends have qualitative character only. However, more stable probes have been fabricated and evaluated (Section 6.4.7), which should pave the way to quantitative verification of the concepts proposed by Schuster *et al.* ^{416,426,428}

Schuster's theoretical discourse of electrochemical machining and deposition using nanosecond voltage pulses ^{416,426,428} predicts multiple factors that influence the extent of the polarized area on

the substrate and hence the lateral dimension of a milled hole or a deposit. A primary factor is the pulse length (for a given electrolyte resistance). Its influence has been validated multiple times in literature^{416,426,431}, and confirmed in our experiments: decreasing the pulse width from 100 to 20 ns reduces the approximate diameter of single Co deposits from ≈ 500 nm to ≈ 200 nm in an aqueous electrolyte (Fig. 6.5a), and from ≈ 150 nm to ≈ 50 nm in an organic DMSO electrolyte (Fig. 6.5b).

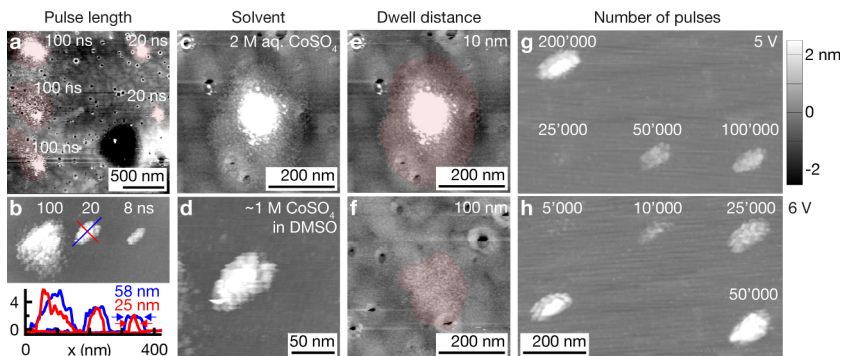


Figure 6.5 – Parameters influencing the 2D feature size. A number of parameters determine the degree of localization of the deposit. The presented post-deposition STM scans compare the influence of the stated parameter on the lateral extent of the deposit grown with otherwise unchanged parameters (unless otherwise stated). As a guide for the eye, the areas of the deposits are shaded in red in (a, e, f). **a, b**, The longer the polarizing pulses, the larger the resulting deposits from aqueous electrolytes (a) as well as DMSO-based electrolytes (b). The line profiles in (b) indicate the width along the long (blue) and the short (red) axes of the ellipsoid deposits. **c, d**, An increase in electrolyte resistance, *i.e.* when using DMSO (d) instead of water (c) as a solvent, increases the confinement for a given pulse length (20 ns. Number of pulses: 500 (water), 50 000 (DMSO)). **e, f**, The lateral size of the deposits decreases with dwell distance (e, 10 nm, f, 100 nm). **g, h**, At initial stages of deposition, *i.e.* at low numbers of pulses, the lateral diameter increases with the amount of pulses. For larger numbers of pulses, the lateral size of the deposits is approximately constant (compare 25 000 and 50 000 pulses in h). The greyscale height scale applies to all STM scans.

Additionally, for a given pulse width, the resolution must be proportional to the electrolyte conductivity ρ , as $\tau \propto \rho$. For otherwise equal parameters, an increase in electrolyte resistance should decrease the size of the polarized area and hence the diameter of the deposit. Figure 6.5c, d shows a corresponding comparison of Co dots deposited from 2 M aq. CoSO_4 (c, diameter ≈ 200 nm) and 1 M CoSO_4 in DMSO (d, diameter ≈ 75 nm) (20 ns pulses). Unfortunately, we have not measured the electrical conductivities of the very electrolytes used in this experiment. At a later stage, we determined the conductivity of aq. 1 M CoSO_4 and 1 M $\text{NiNO}_3 \cdot 6\text{H}_2\text{O}$ in DMSO as 34 and 10 mS cm^{-1} , respectively. While these two values are not directly representative for the experiment

presented in Fig. 6.5c, d, they give an impression of the approximate ratio of conductivity (the conductivities of the pure solvents differ by a factor of ≈ 10 : distilled water $5 \times 10^{-5} \text{ mS cm}^{-1}$, DMSO $2 \times 10^{-6} \text{ mS cm}^{-1}$ ⁴³²).

Further, an increased distance between tip and substrate results in a minor decrease of the lateral size of the deposits and a pronounced decrease of their volume (Fig. 6.5e, f). Lastly, more pulses per deposition event increase the deposited volume (Fig. 6.5h, i). Additionally, at the initial stages of deposition, the lateral feature size is a function of the number of pulses, that is, the total polarization time. However, the few data points presented suggest that the lateral size saturates at larger pulse numbers (compare 25 000 and 50 000 pulses in Fig. 6.5h).

Coarsely optimizing all the mentioned factors resulted in the smallest features obtained up to date: the elliptical deposit in Fig. 6.5b (8 ns), with a FWHM of 25 and 58 nm for the short and long axis, respectively. Note that no tip deconvolution was performed.

6.4.3 2D patterning

2D patterns are easily generated with the point-by-point deposition approach described in Section 6.4.1. A spacing of 100 nm between individual deposition events results in patterns of discrete dots (Fig. 6.6a), while smaller spacings typically derive a seemingly continuous film (b) or lines (d). Note the strong spatial confinement of the grown patterns: two atomically thin terrace edges of the (111) Au substrate are still visible in closest proximity to the deposited film in Fig. 6.6b (arrow).

In contrast to the point-wise strategy, continuous translation of the tip at a fixed distance to the substrate and simultaneous polarization with nanosecond voltage pulses has not resulted in reproducible deposition up to date.

In general, please note that all deposited structures are very much two-dimensional. Typical out-of-plane aspect ratios are $\ll 1$, for example ≈ 0.1 for the line in Fig. 6.6d.

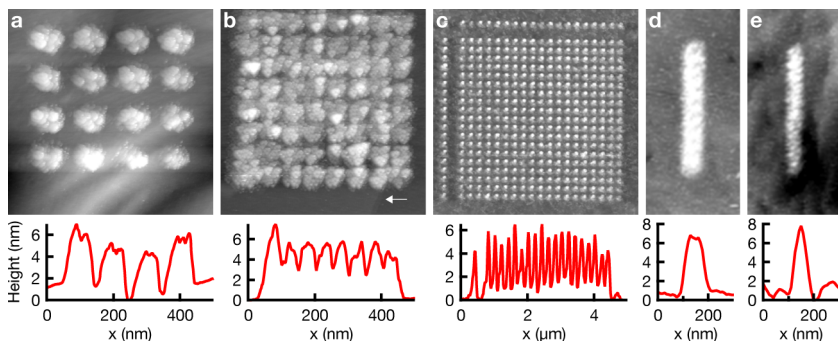


Figure 6.6 – 2D patterning. STM scans of patterns grown with a point-by-point strategy. Point-to-point spacing: **a**, 100 nm, **b**, 50 nm, **c**, 200 nm, **d**, **e**, 50 nm. The arrow in (b) points to two terrace edges of the (111) Au substrate – their visibility illustrates the strong confinement of the Co deposition. Deposition parameters: electrolyte: ≈ 1 M (a – c), 0.5 M (d, e) CoSO_4 in DMSO; pulse length: 100 ns; pulse amplitude: 6 V (a – c), 5 V (d, e); duty cycle: 0.01; pulses per point: 3000 (a – c), 2000 (d, e); dwell distance: 10 nm (a – d), 30 nm (e).

6.4.4 The chemical nature of the deposits

Chemical characterization of the grown patterns has proven difficult due to the low amount of deposited volume. SEM EDX spectroscopy could only be performed on thick deposits that are not representative for high-resolution patterning – thinner, representative structures provide too low electron interaction volume (Fig. 6.7a – c). TEM EDX analysis has not yet been performed.

As an alternative to quantitative EDX analysis, we often settled with a qualitative *in-situ* electrochemical "analysis": it is argued that only Co could be deposited from the electrolyte solution itself, given its composition. Hence, the only alternative source of material would be the STM tip itself (Au). Thus, one could reason that the deposits should either be Co, Au or a mixture of the two. Further, one could hypothesize that pure Co deposits should dissolve at potentials $\Phi_{\text{Co} \rightarrow \text{Co}^{2+}} < \Phi_{\text{substrate}} < \Phi_{\text{Au} \rightarrow \text{Au}^{3+}}$, while pure Au deposits should be inert and mixed deposits should partially dissolve. Two corresponding experiments are presented in Fig. 6.7d, e. In both cases, the patterns only dissolve partially upon stepping the surface potential to oxidative values for Co.

6.4.5 Towards 3D deposition

The height of a dot grown upon a single deposition event, *i.e.* when firing a defined number of pulses while the tip is in its dwell position, must be smaller than the dwell distance. Otherwise, the

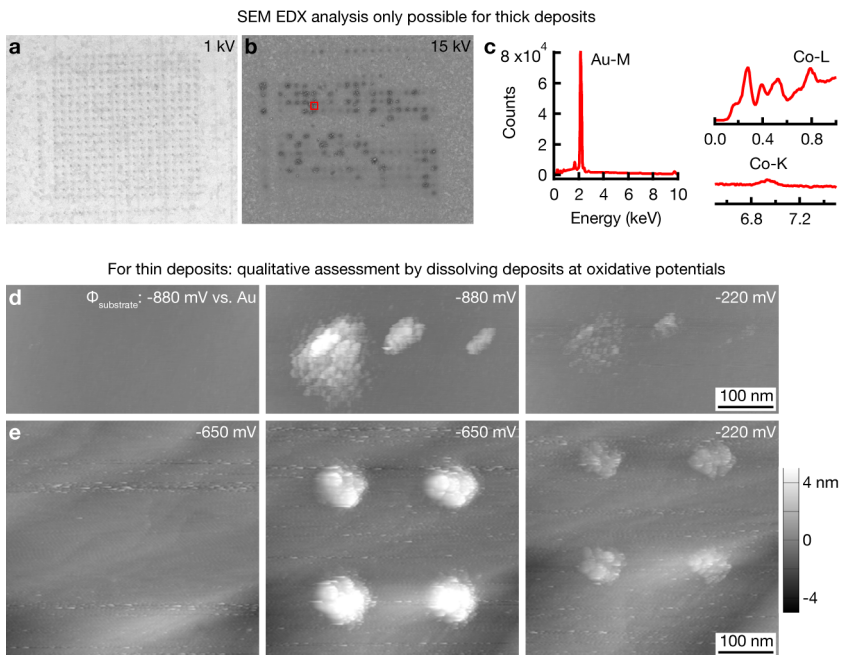


Figure 6.7 – The chemical nature of the deposits: Co from the electrolyte solution or Au from the tip? **a – c**, SEM EDX analysis of printed 2D patterns is not possible, as they are electron-transparent at acceleration voltages needed for analysis. Only thick deposits that are not representative for the high-resolution patterns yield an EDX signal. **a**, SE SEM micrograph of a patterned grid (the grid of Fig. 6.6c) acquired with an acceleration voltage of 1 kV. **b**, BSE SEM micrograph of an array that contains thicker deposits. **c**, EDX analysis of one of the deposits (red square in (b)) confirms the presence of Co. **d, e**, Alternatively, the composition of printed structures is qualitatively assessed *in situ* by ramping the surface potential to a potential $\Phi_{\text{Co} \rightarrow \text{Co}^{2+}} < \Phi_{\text{substrate}} < \Phi_{\text{Au} \rightarrow \text{Au}^+}$. **d, e**, show STM scans of the Au surface before and after deposition as well as after stepping the potential to oxidative values for Co (≈ -200 mV vs. Au). At these potentials, the deposits dissolve partially.

deposit will short-circuit the tip and substrate, which usually results in large and poorly confined deposits as those seen in Fig. 6.7b. Hence, for a typical dwell distance of 10 nm and a lateral feature size of 50 – 100 nm, the maximum aspect ratio of a single deposit is 0.1 – 0.2. Building out-of-plane structures thus requires the sequential stacking of individual deposits. The respective procedure is outlined in Fig. 6.8a: after each dwell, the tip approaches the surface, detects the out-of-plane position of the grown deposit, and retracts by the defined dwell distance d . This routine maintains a constant spacing between tip and growing structure. The out-of-plane growth of the deposit can be tracked by recording the z -position of contact between tip and deposit. Graphs that plot this data are thus termed 'growth curves'.

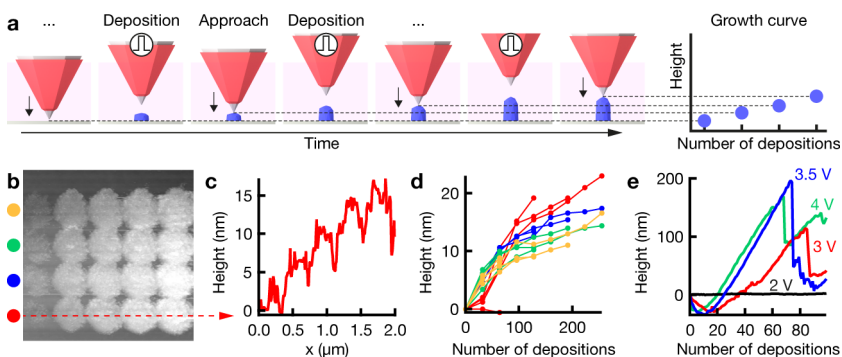


Figure 6.8 – Towards 3D: out-of-plane growth. **a**, Repetition of single deposition events at the same location enables sequential stacking of deposits. The growth of the deposit is monitored by approaching the tip towards the deposit's surface after each deposition event. Recording the position of contact between tip and deposit enables tracking of the growth in a so-termed "growth curve". **b**, STM scan of a grid of dots deposited with an increasing number of consecutive deposition events per point (left to right, from one to nine in steps of two). **c**, Corresponding cross-section line profile (bottom row). **d**, Growth curves for each of the dots in (a). Colors correspond to the labels in (b). **e**, Growth curves for a larger number of deposition events as a function of pulse amplitude. Note the absence of growth for an amplitude of 2 V (black) and the negative growth at the onset of deposition for larger amplitudes. Deposition parameters: ≈ 1 M CoSO_4 in DMSO; pulse length: 100 ns; pulse amplitude: 4 V (b – d); duty cycle: 0.01; num. of pulses: 3000 per deposition event; dwell distance: 10 nm; dwell time, *i.e.* time per deposition event: 0.2 s; tip: Au.

Fig. 6.8b presents "3D" array of dots deposited by increasing the number of deposition events from left to right. Note that the width of the deposits does not increase with height (except after the first deposition event). The corresponding cross-section line profile demonstrates the gradual increase in height of the individual dots (c). Finally, the corresponding growth curves in panel (d) indicate similar heights. Thus, out-of-plane growth is in principle accessible and can be tracked with the growth curves.

However, growth curves for larger numbers of consecutive deposits do not report steady out-of-plane growth, indicating instabilities in the process (Fig. 6.8e). For a pulse amplitude of 2 V, no growth occurs. Increasing the pulse amplitude to 3 – 4 V results in first a dip of the growth curves to height values <0 . Subsequently, the values typically increase, but are interrupted by sudden, pronounced drops. Thus, it is concluded that out-of-plane growth with the setup used to record the data in Fig. 6.8 is reproducible but poorly controlled.

6.4.6 Insufficient stability of Au STM tips under typical deposition conditions

Negative values of the growth curves in Fig. 6.8e indicate either the tip crashing into the substrate, a hole being milled into the substrate, or degradation of the tip. Post-deposition STM scans of the substrate exclude any subtractive machining of the substrate. Repeated tip crashes are also unlikely, as post-deposition SEM analysis of tips do not show any bending of the tip. However, a comparison of a Au STM tip before and after its use in multiple deposition experiments confirms removal of material from the tip apex (Fig. 6.9a), presumably due to anodic dissolution of Au.

To verify the loss of tip material upon anodic pulsing, we designed a straightforward model experiment based on the assumption that any material that is dissolved from the tip would redeposit on the substrate: pulse experiments are conducted in supporting electrolyte solutions containing no metal cations that could be deposited (typically 0.25 M aq. Na_2SO_4). Consequently, all material grown on the substrate after a deposition event must originate from the tip. The used STM tips are imaged prior to and after deposition experiments. Indeed, these experiments confirm loss of tip material (Fig. 6.9b – d). Thus, the following assumption is made and applied to the rest of the result section: any material deposited in Co^{2+} -ion-free electrolyte solutions originates from the utilized tip and thus indicates the tip's degradation. However, this is no quantitative relation, as not all material dissolved from the tip transfers to the substrate: in Fig. 6.9b – d, the estimated volume removed from the tip is $\approx 2 \times 10^7 \text{ nm}^3$, compared to only $\approx 6 \times 10^4 - \text{max. } 1 \times 10^5 \text{ nm}^3$ for the deposit in (c) (Figure E.1).

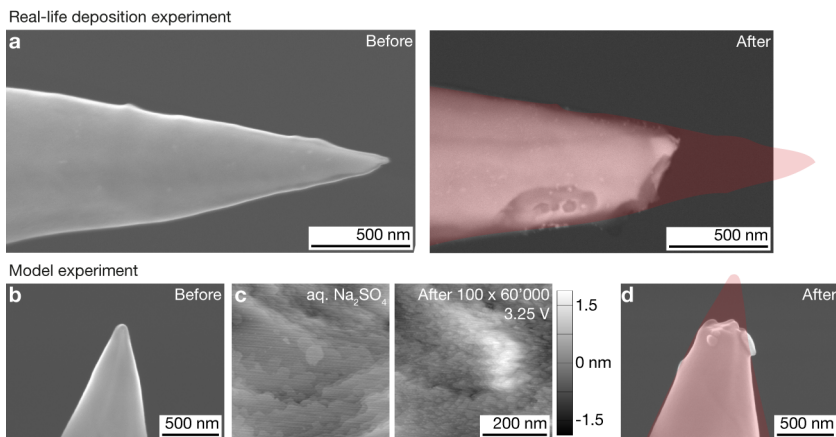


Figure 6.9 – Degradation of Au tips upon deposition. **a**, SE SEM micrographs of a Au STM tip before (left) and after (right) its use as a local electrode for multiple deposition experiments. A length of >500 nm of the original tip apex is missing after experiments. The red shading in the right micrograph indicates the dimensions of the original tip. **b – c**, A model experiment confirms substantial loss of tip material upon pulsing in aq. 0.25 M Na_2SO_4 : as the electrolyte solution is bare of any metal cations that could be reduced onto the substrate, the deposited material in (c) must originate from the STM tip. Note: the deposition in (c) was not the only deposition performed with the respective tip, but it was by far the most extreme (see Figure E.1 for the complete experiment). Deposition parameters in (c): pulse width: 20 ns; pulse amplitude: 3 V; duty cycle: 0.01 ; deposition events \times pulses per deposition event: $100 \times 60\,000$; dwell distance: 50 nm; tip: Au.

6.4.7 Tip stability: Au versus Pt

The anodic instability of Au under typical deposition conditions necessitates a change of tip material. Pt was decided to be the most promising candidate as a replacement for Au after comparing the anodic stability of Au, Pt, Ir, graphite, Ta, Ti, and ITO thin films at potentials up to $+4.5$ V vs. SCE (results not shown). Indeed, a comparison of pulse experiments of Au and Pt tips in a Co^{2+} -free supporting electrolyte suggest a higher stability of Pt (Fig. 6.10): while first clear signs of Au tip degradation, *i.e.* deposited material below the tip, are detected after $1 \times 60\,000$ pulses, similar deposition of Pt is only observed after $100 \times 60\,000$ pulses (although there is minor deposition already after $10 \times 60\,000$ pulses).

The deposition of Pt tip material onto the substrate is minimized if the pulse amplitude is decreased to 2.5 V (Fig. 6.11a). This suggest a sufficient stability of the tip for Co deposition when compared to typical deposition parameters in Co^{2+} -containing electrolyte solutions. Indeed, a deposition experiment in 0.25 M aq. CoSO_4 yielded pronounced deposition already at $1 \times 60\,000$ pulses

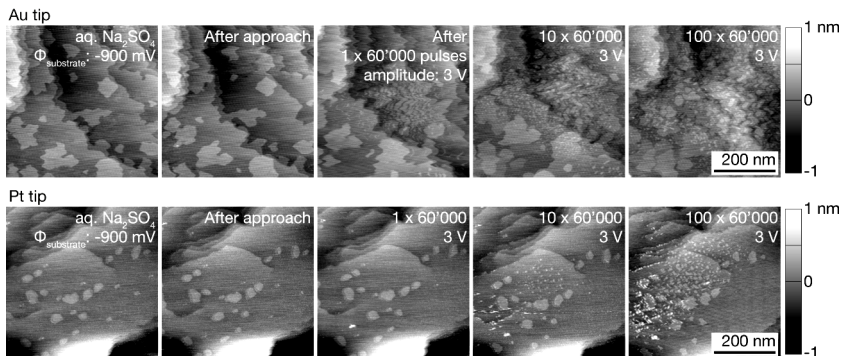


Figure 6.10 – Anodic stability of Au versus Pt tips. STM scans of a Au surface before and after $1 \times$, $10 \times$ and $100 \times 60\,000$ voltage pulses applied to either a Au (top row) or a Pt tip (bottom row) in $0.25\text{ M aq. Na}_2\text{SO}_4$. For the Au tip, deposition is evident already after $1 \times 60\,000$ pulses, indicating dissolution of the tip. In contrast, a similar amount of deposition from the Pt tip is only observed for $100 \times 60\,000$ pulses, suggesting a higher resistance of Pt against anodic oxidation. The label OFF indicates a simple tip approach without pulses. Deposition parameters: pulse width: 20 ns ; pulse amplitude: 3 V ; duty cycle: 0.1 ; dwell distance: 50 nm ; $\Phi_{\text{substrate}}: -900\text{ mV}$; $\Phi_{\text{tip}}: -700\text{ mV vs. Au}$.

(Fig. 6.11b) – a total polarization time that does not deposit any tip material in $0.25\text{ M aq. Na}_2\text{SO}_4$ (a). Additionally, first signs of deposition are already evident after 5000 pulses. Lifting the surface potential to $\Phi_{\text{substrate}} > \Phi_{\text{Co} \rightarrow \text{Co}^{2+}}$ (-200 mV vs. Au), the deposit instantaneously dissolves and only some residues remain (Fig. 6.12a). Smaller dots grown with a lower total polarization time dissolve completely (Fig. 6.12b), indicating no co-deposition of Pt during pulsing.

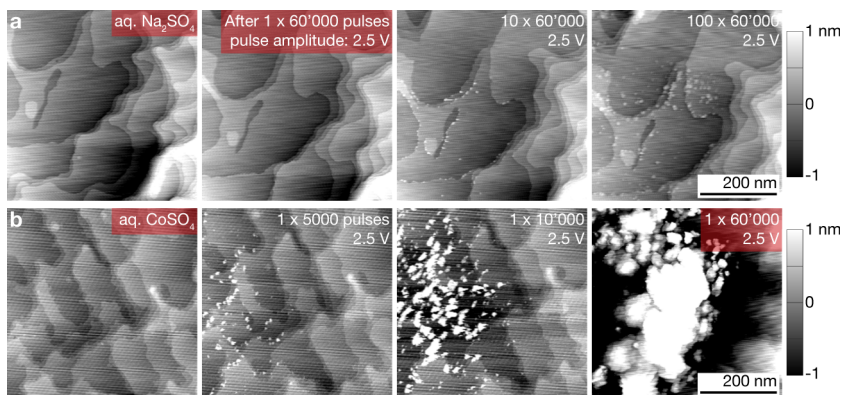


Figure 6.11 – Deposition with Pt tips in aq. Na_2SO_4 and CoSO_4 solutions. A comparison between deposition experiments in Co^{2+} -free and Co^{2+} -containing electrolytes suggest sufficient stability of Pt tips for Co deposition: STM scans of a Au surface before and after deposition with stated number of pulses in **a**, 0.25 M aq. Na_2SO_4 and **b**, 0.25 M aq. CoSO_4 . In the Co^{2+} -containing solution, a significant amount of material is deposited after $1 \times 60\,000$ pulses. In contrast, no deposition is detected with equal parameters in the Co^{2+} -free solution, and only minor deposition is observed after $100 \times 60\,000$ pulses. Note: the deposition in the rightmost scan of (b) was initiated on a previously clean surface, while the deposit in the third scan was grown on top of the one in the second scan. Deposition parameters: pulse width: 20 ns; pulse amplitude: 2.5 V; duty cycle: 0.1; dwell distance: 50 nm; $\Phi_{\text{substrate}}$: -900 mV (a), -1000 mV (b); Φ_{tip} : -700 mV; tip: Pt.

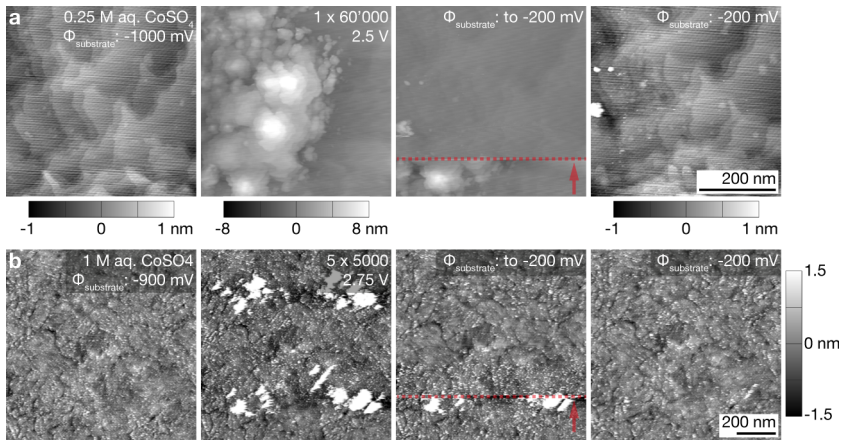


Figure 6.12 – Complete dissolution of deposits. **a**, STM scans of a Au surface before (first scan) and after deposition in 0.25 M aq. CoSO₄ (second scan, same deposit as in Fig. 6.11b). Stepping $\Phi_{\text{substrate}}$ to -200 mV vs. Au (dashed line in the third scan. The arrow denotes the scan direction) results in the instantaneous dissolution of the deposits. Note the different gray scales of the individual panels. **b**, Scans of the surface of a Au thin film before and after the deposition of four dots (only 5×5000 pulses) and after their complete dissolution at -200 mV vs. Au. Deposition parameters: pulse width: 20 ns; pulse amplitude: 2.5 V (a), 2.75 V (d); duty cycle: 0.1; dwell distance: 50 nm; Φ_{tip} : -700 mV. tip: Pt (a), Pt-20at.%Ir (b).

6.4.8 Out-of-plane growth curves with Pt-20at.%Ir tips – increased process stability?

The apparently increased stability of Pt and Pt-20at.%Ir tips suggests the potential for stable and controlled deposition. However, as preliminary results show, the tips' inertness is only guaranteed in a narrow process window. Growth curves recorded for a Pt-20at.%Ir tip in aq. CoSO₄ suggest an increased process stability compared to Au tips – single deposits reach heights of 1 – 3 μm after 150 × 30 000 pulses (3 V), and the number of growth curves that contain drops is decreased compared to experiments with Au tips (Fig. 6.13b). Nonetheless, abrupt collapses still occur with Pt-20at.%Ir tips. These instabilities seem to be a function of pulse amplitude: a pulse amplitude of 2.75 V results in continuous growth, while growth curves for larger voltages are pronouncedly less smooth and feature the well-known drops (Fig. 6.13c). A comparison of pre- and post-deposition micrographs of the utilized tip's apex still indicates loss of material, as expected from the growth curves (Fig. 6.13a, d). It is still to be shown that Pt or Pt-20at.%Ir tips do not degrade with appropriate process parameters.

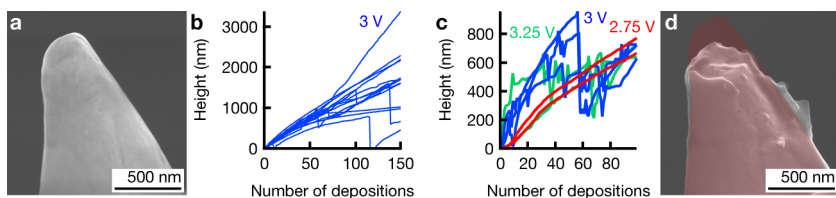


Figure 6.13 – Out-of-plane growth curves with Pt-20at.%Ir tips. a, d, Pre- and post-experiment SE micrograph of the tip used in (b) and (c). b, Growth curves recorded with a Pt-20at.%Ir tip. While stable growth up to a height of 2 – 3 μm can be achieved, the growth curves are not free of instabilities. c, Growth curves recorded for pulse amplitudes of 2.75, 3 and 3.25 V. Low amplitudes enable continuous growth, while larger voltages cause growth instabilities. Deposition parameters: 1 M aq. CoSO₄; pulse width: 20 ns; pulse amplitude: 3 V (a), 2.75 – 3.25 V (b); duty cycle: 0.1; pulses per deposition event: 30 000 (a), 10 000 – 30 000 (b); dwell distance: 50 nm; dwell time: 0.5 s; tip: Pt-20at.%Ir.

6.5 Discussion

We have confirmed that localized deposition from Co^{2+} -containing electrolyte solutions can be initialized by application of nanosecond voltage pulses to a local anode such as a STM probe. Thus, the stated objective of the chapter – exploration of the applicability of Schuster’s micromachining concept for local nanoscale deposition – has been fulfilled. However, although the results are qualitatively reproducible, they lack quantitative character – neither have we been able to confirm the chemical nature of the deposits with certainty, nor did the unstable STM probes allow for a quantitative verification of the localization concept as described in theory^{416,428}. The required experiments to address these shortcomings are discussed in the following – after all, the demonstrated potential of Pt or Pt-20at.%Ir probes for stable operation readies the present setup for eventually realizing true 3D deposition.

6.5.1 The chemical nature of the deposits

We demonstrated that especially Au tips can be a source for material deposition. Thus, it is likely that deposits grown with Au tips contain Au, and that the residues after partial dissolution of the structures in Fig. 6.7 are Au. In contrast, the deposition of presumably pure Co structures is enabled with Pt and Pt-20at.%Ir tips at deposition parameters that prevent tip dissolution (Fig. 6.11a, b) – the complete dissolution of deposits at -200 mV vs. Au in Fig. 6.11d strongly suggests that their major constituent is Co. Nonetheless, this assumption needs to be confirmed with a standard chemical analysis technique *ex situ* (I would suggest TEM EDX or, if larger structures can be printed, SEM EDX).

With the need for this analysis in mind, let us nevertheless list the facts that support the hypothesis of deposits indeed being pure Co: first, the stability of the structures at $\Phi_{\text{substrate}} < \approx 600\text{ mV}$ and their dissolution at $\Phi_{\text{substrate}} > \approx 400\text{ mV}$, as judged by STM scans, matches the behavior of Co predicted by the cyclic voltammogram in Fig. 6.4a. Second, the deposition of any element other than Co from the used electrolyte solutions is unlikely: the high purity of the Co salts (99.999%) and the solvents used, the harsh cleaning of the electrochemical cell and its components, in combination with the high concentration of Co^{2+} ions in the solution render the deposition of mere "contamination" unlikely (although we have seen delocalized deposition of unknown material in an early stage of the project, motivating the present cleaning procedure).

Consequently, we are quite certain that future chemical analysis will confirm the deposition of Co. Nevertheless, all deposition experiments should include pre- and post-print SEM analysis of the tip to confirm (or establish) stable operating conditions that prevent anodic oxidation of the probe.

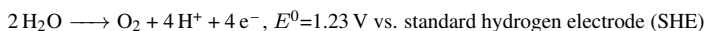
6.5.2 The anodic stability of Pt and Pt-20at.%Ir tips

Prolonged stability of the probe is of utmost importance for the explored concept. Without an inert behavior of the probe, its size and shape and thus the size and shape of the deposits will not be constant, rendering reliable patterning and quantitative analysis of the deposition mechanism unachievable.

The Pourbaix diagram of Pt in water is characterized by large areas of either immunity or passivity – only anodic polarization at lowest pH results in dissolution⁴³³. Nevertheless, anodic etching of the apex of a Pt-20at.%Ir tip is obvious in Fig. 6.13d. While no similar assessment was yet successful for Pt tips, the deposition observed in pure supporting electrolyte in Fig. 6.10 also suggests etching of tip material. While proper selection of process parameters might avoid degradation of the tip, such an approach considerably narrows the process window and hence might have negative effects on maximum speed or resolution of the technique. Additionally, even the most minimal removal of material will add up to notable changes in tip geometry when the size of the pattern and thus the number of depositions is increased sufficiently. Consequently, a strategy that fully protects the tip independent of process parameters is desired.

In electrodeposition, the electrochemical reduction reaction on the cathode requires a complementary oxidation reaction on the anode to guarantee charge neutrality and to enable continuous flow of charge between the two electrodes. Thus, the localized deposition necessitates a simultaneous oxidation, presumably at the tip apex. To guarantee a stable probe, one "simply" needs to ensure that this anodic processes do not involve dissolution of the tip material.

In an aqueous solution, a likely anode reaction at the tip is water oxidation:



An alternative reaction is oxidation of the tip material ($E^0(\text{Pt}|\text{Pt}^{2+})=1.188 \text{ V vs. SHE}$). Note that the standard potential for oxidation of Pt is lower than that for oxidation of water. Yet, as Pt is expected to passivate at moderate pH⁴³³, water will likely oxidize instead. Nevertheless, the protons H^+ produced upon water oxidation are known to decrease local pH values close to the anode⁴³⁴. As Pt is neither stable nor passivated at anodic potentials in highly acidic media, one could argue that a locally decreased pH could establish a corrosive environment for Pt, which eventually leads to the observed dissolution of Pt (although it is unclear whether the local pH would drop sufficiently upon water oxidation).

To securely avoid oxidation of Pt in any case, one should provide an oxidation reaction with a standard potential far negative of that of Pt. Additionally, a decrease of local pH should be avoided. To this end, one should exchange the presently used solvents H₂O and DMSO (which both have high anodic stability) with a solvent that readily oxidizes at moderate anodic potentials. A possible candidate is ethanol, with typical peak-potentials of 0.6 – 0.75 V vs. SHE for oxidation on Pt⁴³⁵.

6.5.3 General advantages and limitations of the concept

Confining substrate polarization during nanosecond voltage pulses is a robust approach for the strong localization of electrochemical reactions at the nanoscale (demonstrated in this chapter for additive patterning, and previously for subtractive machining^{426,428}). In combination with easily available nanometer sized probes, a minimal feature size of 10 – 50 nm is probably within reach (provided the probe is stable). This would outperform the feature size of all small-scale metal AM methods except that of FEBID / FIBID. As the method is based on electrochemical reduction, one could probably expect a materials' performance similar to that of other electrochemical methods. Thus, the concept could be attractive for niche applications that demand high-purity and high-density metals at smallest resolutions. A further advantage is the inherent growth feedback provided by all SPM based printing techniques – as shown in Fig. 2.8, such a feedback can enable controlled deposition of most complex geometries.

Limitations of the concept are similar to those of other electrochemical techniques: on one hand, a growth speed of currently $\approx 5 - 10 \text{ nm s}^{-1}$, corresponding to 0.1 – 0.2 voxel/s for a feature size of 50 nm, is very low (the result of the low duty cycle required for deposition (0.01 – 0.1) and possibly the dependence on diffusive mass transport to re-supply the consumed ions in the tip-substrate gap. Probably, the speed could be increased if the method was combined with concentration-confined electrodeposition, as this method provides high rates of ion supply by pressure-dispensing a concentrated salt solution from a hollow AFM tip). On the other hand, an electrically conductive substrate is always required (although one can easily imagine wiring in-between electrodes, as shown with EHD-RP). Finally, in contrast to other electrochemical methods, the presented concept requires a redox system that is characterized by an irreversible electron transfer, *i.e.* that offers reduction and oxidation potentials that are separated by at least a few tens of mV (otherwise, there is not substrate potential that avoids delocalized deposition but guarantees stability of localized deposits). This is not the case for all metals – prominent exceptions are for example Cu deposition on Cu or Cu on Au in aqueous solutions. Consequently, the number of metals that can be patterned is likely lower than that of established electrochemical AM concepts.

6.6 Conclusion and outlook

This chapter researched the potential of nanoscale additive deposition of metals using nanosecond voltage pulses applied to a nanometer sized tip. To this end, I designed, built and automated a corresponding setup that combines a STM, an electrochemical cell and the necessary electronics to supply nanosecond voltage pulses to the STM probe. The influence of multiple deposition parameters on the feature size was qualitatively verified as predicted, but was not yet quantitatively analyzed. Smallest 2D features ≈ 50 nm in diameter have been deposited, and 2D surface patterning was demonstrated. Most importantly, we identified issues with the stability of Au STM tips, and could demonstrate an improved inertness of Pt or Pt-20at.%Ir probes – a finding that will hopefully improve reproducibility in future experiments.

In the near future, experiments should focus on three topics: first, a tip that is inert in a large process window is needed. Potentially, dissolution of the tip could be avoided by engineering the anodic oxidation reaction accordingly. Second, chemical analysis of the deposits must confirm Co deposition. Third, the localization as a function of various process parameters should be assessed in a quantitative study to elucidate whether nanoscale deposition is in agreement with the theory proposed by Schuster *et al.*⁴¹⁶.

In comparison with other electrochemical small-scale AM methods, the studied concept offers potential for unrivaled minimal feature size. Nevertheless, the slow growth rate, the comparably complex instrumentation and involved experimental procedure will probably prevent a wide dissemination of the technique – all other electrochemical methods, including EHD-RP, are simply easier and faster to use. Thus, any potential application of the concept will be restricted to niche applications that demand highest resolution and higher metal content than that in FEBID and FIBID deposits.

Chapter 7

General discussion, conclusion and outlook

The declared aim of this thesis was twofold: an assessment of the microstructure and mechanical properties of metals printed by modern small-scale AM techniques, and – thereby motivated – the development of new methods that provide high-quality metals at a resolution $\ll 1 \mu\text{m}$. These aims have been fulfilled. Nevertheless, the present work can only be another small step towards implementation of small-scale AM in today's routines for advanced microfabrication. This final chapter will thus review the main findings of this thesis, ask questions that have not been answered by this thesis, and outline the consequences for future studies. Finally, the chapter tries to put the thesis in perspective to other ongoing research in the field of small-scale AM and small-scale fabrication of 3D structures in general. Essentially, the chapter will try to convince the reader of three fundamental (and possibly trivial) insights I earned in my PhD years: conceptual development of new techniques needs to be followed by quantitative studies of underlying processes; not every small-scale AM method is practical and user-friendly – and only those that are will probably leave their laboratory environment; small-scale AM is not the ideal solution for many applications, but for some – AM needs to find its niche in advanced micromanufacturing.

7.1 From qualitative concepts to quantitative understanding

The broad focus of this thesis and the aspiration to scout for novel solutions instead of advancing previous techniques in many respects resulted in a coarse conceptual overview rather than a detailed and quantitative description of mechanisms – I am left with a wealth of insights but an equal amount of open questions. Answering these questions will demand detailed studies of fundamental processes that have been beyond the scope of this thesis. The following two example should underline the need for a transition from developing concepts to theoretically understanding small-scale AM.

7.1.1 Materials properties of additively microfabricated metals – the need for processing-microstructure relationships

Our comparative study of the microstructure and mechanical properties of small-scale printed metals in Chapter 3 has concluded with two major findings: first, the characteristic microstructure and the resulting properties of metals deposited by the different techniques cover a large range, with densest, stiffest and strongest materials synthesized by electrochemical techniques as well as FEBID and FIBID. Second, it was acknowledged that the broad applicability of these very same methods is limited due to a narrow range of accessible chemistries (so far only metals in the case of electrochemistry) and the comparably small build volumes. Because of these limitations of techniques that offer "best" metals, it was argued that the improvement of materials printed by colloid-based methods – providing the broadest range of materials, albeit not at "best quality" – is still necessary if small-scale AM should appeal to a broad range of applications and users.

For the optimization of the microstructure of metals derived from colloids, more quantitative studies of the sintering mechanisms as a function of ink composition (particle size and size distribution, sintering additives etc.) and geometry are necessary. However, these studies will be left to researchers that employ inks, and this thesis will content itself with the suggestions given in Section 3.5.3.1 (brief sintering for a combination of minimal shrinkage and high strength thanks to the ligament size effect, sintering aids and higher temperatures for applications that require densest structures). Whether such an endeavor is the most sensible option towards high-performance materials is critically discussed further below.

In view of the main topic of this thesis – electrochemical small-scale AM – we should briefly review the following statement though: electrochemical techniques provide metals with good mechanical properties. Nothing is wrong about this statement, but it is very general in respect to mechanical performance and at the same time ignores all other materials properties. The high strength

and stiffness compared to metals fabricated by non-electrochemical means is mainly owed to the high density of the electroplated metals. For further increase in performance, an understanding of the relations of processing parameters and resulting microstructure needs to be established – a task that has been approached for the case of meniscus-confined electrodeposition^{148,149,152} but still needs to be initiated for the other techniques. Such fundamental insights are especially required in light of other materials properties, with electrical conductivity clearly leading the way. Here, the optimization of the microstructure and the materials' purity is fundamental for lowest resistivity and will demand the exact opposite microstructural characteristics (lowest defect density, *e.g.* large grain size) than those needed for high strength (high defect density, *e.g.* small grain size). Consequently, electrochemical AM methods should not content themselves with depositing dense metals, but should aim at depositing metals with specific microstructures that serve given applications best.

Unraveling the respective relations between deposition parameters and resulting microstructure will further ready electrochemical AM for voxel-by-voxel tuning of the microstructure. Such an ability should enable the optimization of a structures' overall performance when combinations of properties that request disparate microstructure are needed. For example, in an application that asks for the tolerance of high mechanical loads as well as good electrical conductivity, the microstructure of a 3D geometry could be optimized for highest strength at locations of stress concentration, while the parts of the structure that see low levels of stress are optimized for high conductivity. Such an ability would be unique amongst all techniques currently used in micro- and nanofabrication and would clearly define a niche for AM (introduced in more detail further below).

7.1.2 The fundamental processes involved in EHD-RP

Chapters 4 and 5 have introduced the concept of single- and multi-metal EHD-RP, including some of the underlying principles, for example the growth mechanism based on the reduction of cations. However, most fundamentals are yet to be discovered and described. The following paragraphs list some processes and their relations that I consider important for a comprehensive description of the EHD-RP process but are yet to be understood. An in-depth discussion of the experimental results and more details to the topics mentioned here are given in the respective chapters.

In general, deposition by EHD-RP is the result of three basic processes that are likely coupled and eventually determine the final resolution and speed of printing and set boundaries to the materials and materials' microstructure that can be synthesized: the anodic dissolution, the EHD ejection, and the cathodic deposition.

EHD ejection. The modes of EHD ejection are manifold and mainly a function of the electric field and the flow rate^{367,436}. These parameters determine the focus and stability of the ejection, the size of ejected droplets, the frequency of ejection, and the overall flow rate. Up to date, we have not been able to determine which ejection mode is typically at work in EHD-RP. However, its classification is critical for understanding the deposition: the ejection frequency and flow rate govern the ejection current, possibly the charge per droplet and the amount of solvent on the substrate (and thus the environment in which deposition occurs) – important factors that influence the growth rate and resulting microstructure. Additionally, the size of the impacting droplets, the flow rate or maybe the EHD current could be limiting factors to the minimal spatial resolution. Finally, we showed that the nozzle size influences print modes (focused versus de-focused) and the microstructure – an influence that is most likely also connected to different but yet unclassified EHD ejection modes. Consequently, the process of EHD ejection is related to all deposition processes in a most fundamental manner. Its study and classification is thus of high importance.

Anodic processes. The anodic dissolution of the sacrificial metal sources is at the heart of EHD-RP – without continuous dissolution there is no deposition. Consequently, a main prerequisite for printing a given metal is the ability of maintaining continuous anodic dissolution without passivation of the electrode or the formation of residues that are detached from the electrode and could clog the printing nozzle. Sustaining this reaction is not trivial for many metals, as the nature of the anodic reactions (dissolution versus passivation) is often determined by the anodic surface potential – a potential that we can neither measure nor control at the present stage. It is likely that such control will be crucial for expanding the range of printable metals, as it will determine whether ions of the respective metals can be produced. Additionally, rendering the anodic current the rate-limiting step in deposition could potentially enable lower growth rates and thus higher materials quality. The construction of a three-electrode electrochemical cell that allows for measurement and control of the anode potential inside the printing nozzle should thus be of high priority (Section 4.5.3).

Cathodic processes. We have presented strong evidence that the deposition of metals in EHD-RP occurs via electron-transfer from the substrate and hence is electrochemical in nature. The respective reduction reaction thus must be characterized by an overpotential that drives charge transfer and governs charge-transfer rates, thereby potentially influencing the synthesized microstructure and possibly the spatial resolution. What is the value of this potential? Is it constant or does it oscillate with the same frequency charges arrive at the substrate? These and related questions will have to be tackled theoretically or indirectly, as no reference electrode can be introduced into single droplets on the substrate. Although I feel unable to offer a concrete starting point, I judge a study of these questions worthwhile, given their potential relevance for the synthesized microstructure.

7.2 Is there a future for small-scale AM?

Due to a lack of experience, I do not dare to anticipate the needs and wishes of modern industrial microfabrication. Yet, as a personal opinion, I suggest three profound criteria that a small-scale AM technique needs to fulfill for application in research (the usual playground for any technique before transition into industry): first, it needs to provide the materials as well as the materials' quality offered by techniques it tries to replace or complement. Second, it needs to be practical (which is an objective measure which will differ if you are a practitioner in a research laboratory or an engineer in a microfabrication fab). Third, it has to complement existing methods by occupying a niche that only AM can occupy. These criteria are discussed in the following.

7.2.1 Metals and materials – EHD-RP as a multi-material method?

Lets assume that an application of metal AM in many real-life devices is only realistic if the provided materials properties are equal to those of metals deposited by PVD or electrodeposition (two long-established processes in microfabrication), and let us discuss modern metal AM methods accordingly.

AM techniques based on the transfer of colloids unfortunately deposit metals with porous microstructure. The assumption that this is a no-go for many applications that request materials of highest performance provokes the question whether fully dense metals could be realized from inks? In answer to this question, I offer a highly subjective and personal opinion: no. In my view, ink-based processes are not suitable for the deposition of dense structures attached to rigid substrates – the volume-loss inherent to the concept based on coalescence of discrete particles, in combination with shrinkage that is constrained by a substrate, renders full densification very challenging (purely out-of-plane structures could probably be densified though). In contrast, ink-printing at larger scales obtains high densification thanks to unconstrained sintering of structures detached from substrates and is thus a valid route to high-performance materials.

Electrochemical methods are currently the only additive concepts with potential for the fabrication of pure and dense metals with a resolution $\leq 10 \mu\text{m}$, as metals by standard FEBID and FIBID are far from pure, and LIFT deposits are porous and usually lack smallest feature-sizes. As shown, electrochemical techniques synthesize metals with properties equal to those of PVD thin films (Chapter 3 and 4). It is to be proven whether the current performance suffices for applications that are competitive with the standards of the microelectronics industry. But in any case, it is certain

that the range of metals^a, their microstructure and the compatibility with different substrates needs improvement. These goals should be within reach, as electrochemical deposition is a standard process in microfabrication and recipes for all required metals and strategies for process integration on all substrates exist – but additive techniques need to adapt these.

In the deposition of materials other than metals, electrochemical methods are naturally less versatile. Conductive polymers have been grown by meniscus-confined electrodeposition (oxidative polymerization of anilin)¹⁴³. Additionally, the synthesis of semiconductor films is facilitated by electrodeposition^{437–439}, but has not yet been demonstrated by today's small-scale AM concepts. In contrast, insulators are not directly obtainable by electrodeposition, as the electron transfer required for deposition necessitates conductivity of the material to be deposited. Here post-deposition thermal oxidation of electrodeposited metals could be a feasible route for some applications.

Ultimately, an additive deposition technique that offers direct access to all classes of materials in high quality on any substrate and – importantly, also enables sequential or simultaneous deposition of multiple materials – is desirable. The success and widespread use of PVD sputtering and thermal evaporation for thin-film deposition is owed to the combination of these attributes. In small-scale AM, electrodeposition will probably not be the technique that can fulfill these demands. However, neither are colloid-based techniques – despite the large choice of materials, the properties after thermal sintering will likely be unsatisfactory for many applications, and combinations of multiple material classes are difficult to achieve due to large differences in sintering temperatures.

Thus, novel concepts are needed for accessing a broad range of materials in high quality. Here, I hope that EHD-RP could offer a possible route towards multi-material AM. I propose two strategies for accessing non-metals with EHD-RP: first, providing an alternative source of electrons (an electron beam or a gas plasma) to enable deposition of and onto electrical insulators. Second, enabling in-situ gas-phase reactions of the ions for the synthesis of metal compounds (in analogy to reactive sputtering). Possibly, these measures will render EHD-RP a multi-material instead of a mere multi-metal technique. Alternatively, still-to-be-developed techniques based on the concepts of sputtering or evaporation may be good solutions (ultra-high vacuum and pure source materials are surely beneficial for best materials performance).

^aMetals in microfabrication: Al, Au, Ti, W, Cu, Cr and Ni-Fe alloys, and, less commonly, Zr, Ta, Ir, C, Pt, Pd, Ag, Zn and Nb^{78,268}. Metals by electrochemical AM up to date: Cu, Pt, Ag, Au, see Chapters 2 and 4

7.2.2 Practicability of small-scale AM: the need for a growth feedback

The previous section discussed prerequisites for additive microfabrication techniques regarding materials and their quality. Additionally, with six years of experience as a user in the field of small-scale AM, I realize that no method will disseminate if user-friendliness is low. In an article reviewing 3D structuring by TPL, Hohmann *et al.*⁴⁷ list the following factors that were responsible for easy accessibility of the technique and thus partially its success: a high structuring speed, a large sample volume, and simple pre- and post-processing. For metal-AM, I would like to add the importance of facile reproduction of the intended geometry (a problem especially for synthesis techniques but hardly for TPL).

The individual factors vary in importance depending on the application. Speed might be the main criterion if AM is used as a highly specialized processing step integrated in a larger processing chain for mass fabrication. Here, optimization of pre- and post-processing and the printing parameters to obtain a specific geometry is affordable – the same optimization is necessary for every lithography process. In contrast, there is no room for lengthy optimization in a research environment, as geometries, materials and substrates will change frequently. As research is likely the environment small-scale AM will prove itself in first (as did TPL), I would absolutely stress the importance of a growth feedback for synthesis techniques.

A growth feedback measures the geometry of the printed structure *in situ* and feeds this information to the printing device, which can take necessary adjustments on the fly to produce structures with high fidelity. Transfer techniques can sometimes do without such control, as the knowledge of transferred volume per time in combination with a material transfer that is not influenced by electric fields or growth inhomogeneities typically enables a fair prediction of the printed geometry. In contrast, synthesis techniques invariably need a feedback if structures of strict dimensions are to be printed – growth rates and feature sizes that are often not precisely known and vary as a function of location and time during printing render reproduction of complicated geometries very challenging without feedback. Additionally, parameters typically change in every experiment and necessitate time-consuming calibration procedures if high reproducibility is requested (the effort necessary for calibration is well illustrated by simulation-guided FEBID^{180,195,196} – an approach that facilitates reproducible growth of complex nanoscale 3D geometries by predicting local growth rates based on simulations, but requires most extensive calibration for every precursor, Fig. 2.10).

Two examples for a successful feedback are specimen-current-controlled FIBID¹⁷⁹ and the feedback used in concentration-confined electroplating. While the first is an indirect feedback which still requires calibration, the second is a direct feedback that provides the out-of-plane dimensions

of the grown structure in real time without calibration (Section 2.2.6)^{154,155}. In-plane dimensions are more difficult to obtain, but can be accessed by scanning the probe¹⁵⁵. The enabling character of such a feedback is demonstrated by the complex structures printed by the Exaddon CERES printer (former FluidFM μ 3D printer by Cytosurge) – likely the most advanced geometries printed in metals at these scales up to date (Fig. 7.1d, Fig. 2.8). Consequently, all AM methods should strive after a direct feedback that informs the printing process of the grown geometry in real time (discusses in detail for EHD-RP in Section 4.5.1.1).

7.2.3 AM's niche: a comparison to 3D fabrication via 2D lithography

In the last decade, AM was by far not the only concept evaluated for 3D fabrication at small scales. By now, processes based on established 2D lithography can provide complex 3D geometries in high-quality materials. Especially stress-controlled folding or buckling of structures deposited onto pre-strained elastomeric substrates proved to be a highly versatile approach. By uni- or bi-axial release of the substrates, patterned and partially released films of a large variety of organic or inorganic materials deterministically buckle or fold to form intricate 3D structures (Fig. 7.1). As the process can draw from established microfabrication processes for materials synthesis (PVD and CVD), the range of available materials and their quality is exceptional, enabling straightforward design of microelectronic devices¹⁸, MEMS¹¹, antennas⁴⁴⁰ or sensors^{441,442}. Additionally, parallel processing enables wafer-scale fabrication, and the concept's reproducibility and accuracy is high. These are substantial advantages over the state of the art of additive techniques. Consequently, one has to ask where AM can outperform lithography-based approaches? This question should by no means provoke a competition of the two concepts – ideally they combine in a symbiotic fashion. The question should simply force AM to focus on its strengths and unique characteristics.

In my opinion, AM offers three key advantages. First, lithography-based 3D processing necessitates planar and often special – compliant in the case of buckling – substrates. In contrast, the additive concept can easily accommodate site-specific deposition on a large range of non-planar substrates, such as the tip of an AFM probe⁵¹, the end of a thermocouple⁵² or an optical fiber²⁰, or the surface of nonplanar macroscale components¹²⁸. The direct deposition at the location of interest further avoids the transfer from substrates used for fabrication to substrates requested by the application, which I imagine difficult for geometries of smallest feature sizes.

Second, AM does and probably will always provide the most complex geometries (the concept itself does, not necessarily the individual techniques) that are inaccessible by buckling and folding, for example extreme aspect ratios and filled (a cube) or closed (a hollow but fully closed sphere)

Methods for fabrication of 3D structures in inorganic materials at small scales

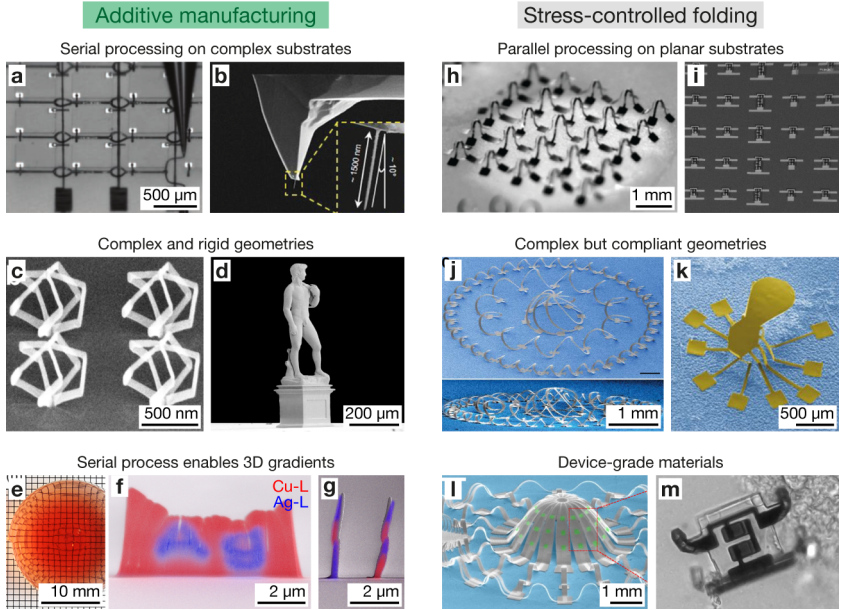


Figure 7.1 – AM vs. lithography for 3D microfabrication. An overview of the key advantages of the two concepts AM and stress-controlled deformation that both enable deterministic fabrication of 3D structures at small scales and some applications. **a – g**, Additive manufacturing: **a**, Patterning of 3D Ag interconnects on a LED chip array¹². **b**, Iron nanowire grown onto the tip of a commercial AFM probe to render a high-aspect-ratio MFM probe⁵¹. **c**, Nanoscale Pt-containing structures¹⁹⁵. **d**, A microscale replica of Michelangelo's David in Cu¹⁵⁶. **e**, Printed SiO₂ structure with a gradient in TiO₂ content (red colorant added for visualization) for the fabrication of a lens with a gradient in refractive index⁴⁴³. **f**, **g**, EDX elemental maps of Cu-Ag bi-metal structures with designed chemical gradients printed by EHD-RP (Chapter 5). **h**, Array of folded "tents"⁴⁴⁴. **i**, Photograph cell-sized robots before release from a Si wafer (no scale bar available). **j**, 3D mesostructure of monocrystalline Si⁴⁴⁴. **k**, Bi-stable structure (SU8)¹⁸. **l**, Colorized SEM image of MoS₂ photodetectors on a hemisphere with 3D interconnects⁴⁴¹. **m**, Cell-sized robot (no scale bar available). **a – e**, **h – m**, Reprinted with permission from **a**,¹² ©2009 AAAS; **b**,⁵¹ ©2014 ACS; **c**,¹⁹⁵ ©2018 ACS; **d**, ©Exaddon¹⁵⁶, **e**,⁴⁴³ ©2018 ACS; **h**, **j**,⁴⁴⁴ ©2015 AAAS; **i**, **m**, ©Marc Miskin, University of Pennsylvania; **k**,¹⁸ ©2018 Springer Nature; **l**,⁴⁴¹ CC BY 4.0 (<http://creativecommons.org/licenses/by/4.0/>).

geometries. Importantly, AM can fabricate these geometries as rigid and dense structures, while buckling necessarily results in compliant and thin-film like geometries.

Third and most distinguishing, AM is a serial process. While the serial nature is typically lamented for causing the low throughput of the concept, one should focus on its unique advantage : building a structure by sequential deposition of discrete units of material (individual voxels) unlocks the possibility to alter chemistry, microstructure or material as a function of spatial position in three dimensions with little effort (given one can control the deposition parameters in each voxel). The thereby enabled point-specific control of a part's internal structure, *i.e.* its distribution of chemical composition and microstructure, facilitates the design of materials with spatially varying properties. Fundamentally, such variation is the basis of all functional devices. Furthermore, heterogeneous materials systems with graded properties are often more efficient under mechanical load than homogeneous counterparts, and enable fine tuning of electrical and optical properties^b. Important for defining this niche of AM, the deterministic fabrication of complex 3D gradients within materials and geometries is only reasonable with a serial concept; with lithography-based approaches, the deposition of intricate gradients quickly amounts to infinitely complex processes^c, while AM methods that tune deposition parameters or deposited chemistries on a voxel-by-voxel basis increases the complexity without extra effort.

For inorganic materials, EHD-RP is currently the only small-scale approach that has demonstrated the potential for such voxel-based multi-material synthesis. Nevertheless, other techniques described in this thesis could surely follow. Additionally, concepts for multimaterial fabrication by TPL have recently been introduced, based on mixtures of wavelength-sensitive photoresists⁴⁴⁵ or a microfluidic system for the sequential supply of different photoresists⁴⁴⁶. Although direct structuring with TPL is limited to organic resists, the concepts can be extended to combine multiple inorganic materials in particle form⁴⁴⁶ – sintering of such multimaterial structures would be even more challenging than that of single-material structures today⁹³, but could be envisioned.

In summary, I see AM as the ideal fabrication concept for microscale structures on non-planar substrates, for the large number of 3D geometries not accessible by folding 2D structures, and chemical or microstructural gradients within materials and structures. While the first two directions were at the focus of the field in the last decade, the latter is in its very early stages – currently,

^b A few examples: tough but strong metals are facilitated by grain size or nano twin gradients,^{398,399} internal gradients of Young's moduli enhance bending stiffness^{405,406} and avoid stress-localization at interfaces⁴⁰⁷, and gradients in strength enable designed failure^{393,397}. Gradient doping enables improved carrier-separation for solar water splitting^{408,409} or optical lenses with spatially varying refractive indices⁴⁴³.

^c As an example, lithography-based fabrication of the Cu-Ag wall in Fig. 7.1 (39 layers) would require ≈ 70 masks and 280 processing steps (70 \times coating of photoresist, exposure, deposition of metal, lift-off). The introduction of gradual transitions between Cu and Ag or non-linear gradients would make a fabrication by any non-serial process completely impossible.

no application demands complex gradients at small scales. Nevertheless, I am convinced that once AM unlocks easy access to local tuning of grain sizes or dopant levels with submicrometer resolution, it will spark a number of applications unthought of today – mirroring the large number of opportunities created by monolithic 3D microfabrication today.

7.3 Consequences: the future of EHD-RP

The development of EHD-RP is a major part of the present thesis. Naturally, I wonder whether this concept will be successful and thus benefit modern microfabrication. Above, I have established three subjective criteria that define a potentially successful AM concept: access to a broad range of high-quality materials and substrates, user friendliness (which, among other features includes a feedback mechanism for reproducible printing without calibration), and a focus on the strengths of AM (direct deposition on non-planar substrates, complex geometries and voxel-by-voxel control of the deposited material). As of today, EHD-RP partially fulfills some of these criteria: a good performance of the synthesized metals in comparison to most other small-scale methods, a fast structuring speed and a simple setup for user-friendliness, and voxel-by-voxel control of the local composition of bi-metal structures. From the persisting obvious mismatch between ideal and reality, one should extrapolate priorities for future work on EHD-RP. The following paragraph suggests a number of key projects that aim at strengthening the strengths of EHD-RP and eliminate some of its weaknesses. The projects are listed by priority.

In general, more fundamental understanding of the processes involved in EHD-RP is required, as this will be the prerequisite for further progress in almost any of the suggested projects. Additionally, a concept for a growth feedback should be introduced as soon as possible – although not fundamentally necessary for application, it would dramatically improve the rate of successful experiments and thus accelerate progress. A priority for extending the capabilities of EHD-RP is an increase of the number of printable metals, as only a minimal selection of metals that offer a range of properties (high chemical resistance, high strength or stiffness, high conductivity, ferromagnetism) will enable real-life applications. Second, mechanisms that determine the printed microstructure should be studied. The general ability of synthesizing a variety of microstructures is a key advantage of electrochemical printing and should be strengthened. Third, one should explore options to access direct printing on non-conductive substrates (by providing an alternative source of electrons), before attempting the ultimate goal of venturing beyond metals and printing semi-conductive or non-conductive materials (possibly by reactive deposition).

Applications that explore EHD-RP's facile and fast electrochemical printing as well as the control of local microstructure are already initiated, targeting interconnects for all-printed electronics or photosensors based on nanoporous metals. The above-mentioned key-projects will further ready EHD-RP for the fabrication of more advanced structures, such as 3D sensors, active chemical devices or electromechanical circuit elements. Most importantly though, they will strengthen EHD-RP's unique capability of voxel-by-voxel control of microstructure and chemistry for the synthesis of high-resolution 3D gradients in inorganic materials – unknown but promising land for microfabrication and materials design that can exclusively be explored by small-scale AM.

Appendix A

Appendix to Chapter 1

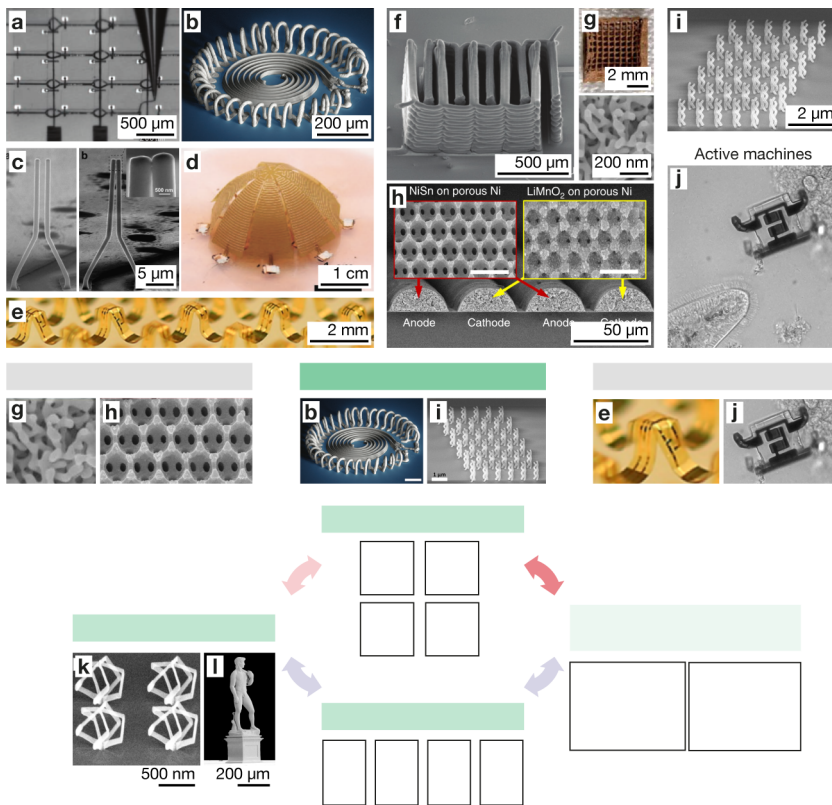


Figure A.1 – Description, references and copyrights for reproduced panels in Fig. 1.1. **a**, Direct ink writing (DIW) of Ag interconnects on 4×4 LED chip array¹². **b**, DIW-printed Ag LC resonator consisting of a 32-turn toroidal inductor and a parallel-plate capacitor¹⁷. **c**, Capacitive MEMS switch based on two printed Cu microwires (left: open, right: closed)³⁰³. **d**, Meanderline-based hemispherical electrically small antenna fabricated by mechanically guided 3D assembly⁴⁴⁰. **e**, Array of 3D piezoresistive Si sensors fabricated by mechanical buckling⁴⁴². **f**, DIW-printed interdigitated Li-ion microbattery architecture²⁴. **g**, Hierarchically porous catalyst architecture fabricated by a combination of DIW printing and self-assembly (dealloying). Top: printed lattice, bottom: SEM micrograph of dealloyed Au¹⁰⁰. **h**, Nanoporous electrodes for Li-ion microbatteries fabricated by self-assembly and electroplating²⁵. **i**, Array of intertwined, Pt-containing helices for chiral photonics grown by focused ion beam-induced deposition (FIBID)¹⁸³. **j**, Microbot that can actively travel in liquid. The bot was fabricated by controlled folding of graphene-glass composites and is powered by standard photodiodes. **k**, Nanoscale Pt-containing icosahedra grown with focused electron beam-induced deposition (FEBID)¹⁹⁵. **l**, A microscale Cu replica of Michelangelo's David printed with the commercial CERES printer (Exaddon). **a – l**, Reprinted with permission from **a**,¹² ©2009 AAAS; **b**,¹⁷ ©2017 John Wiley and Sons; **c**,³⁰³ CC BY 4.0 (<https://creativecommons.org/licenses/by/4.0/>); **d**,⁴⁴⁰ ©2018 John Wiley and Sons; **e**,⁴⁴² ©2019 ACS; **f**,²⁴ ©2013 John Wiley and Sons; **g**,¹⁰⁰ CC BY 4.0; **h**,²⁵ ©2013 Springer Nature; **i**,¹⁸³ ©2016 Springer Nature; **j**, ©Marc Miskin, University of Pennsylvania; **k**,¹⁹⁵ ©2018 ACS; **l**, ©Exaddon¹⁵⁶.

Appendix B

Appendix to Chapter 2

Modifications to reprinted figures

Where needed, the reprinted figures were cropped and retouched to remove original scalebars and labels, without altering the scientific content of the original figures. Furthermore, labels and scalebars were added for a consistent design.

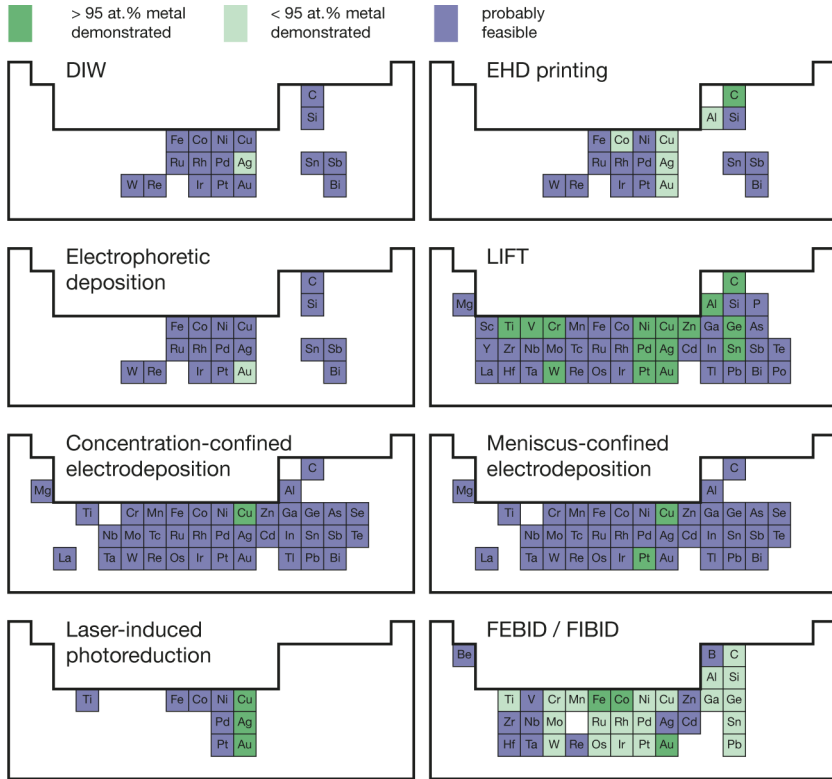


Figure B.1 – Periodic tables of Fig. 2.14 with labels.

Appendix C

Appendix to Chapter 3

C.1 Morphology: LIFT (melt)

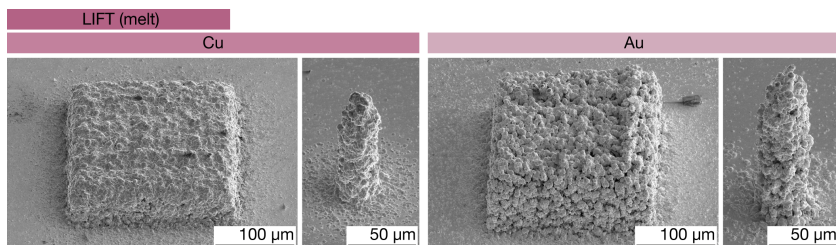


Figure C.1 – Morphology of LIFT-printed Cu and Au. SE micrographs of representative pads and pillars printed from either a Cu (left) or a Au (right) donor thin film. Image tilts: 45° for pads and 55° for pillars.

C.2 Microstructure and chemical composition

Figure C.2 presents cross-sections of pads imaged at low magnification.

Figure C.3 compares the microstructures of annealed inks in different geometries. For each method, the shown pads and pillars were annealed with the same annealing procedures. While some microstructures compare well (DIW (N.), EHDP), others differ between pads and pillars, presumably

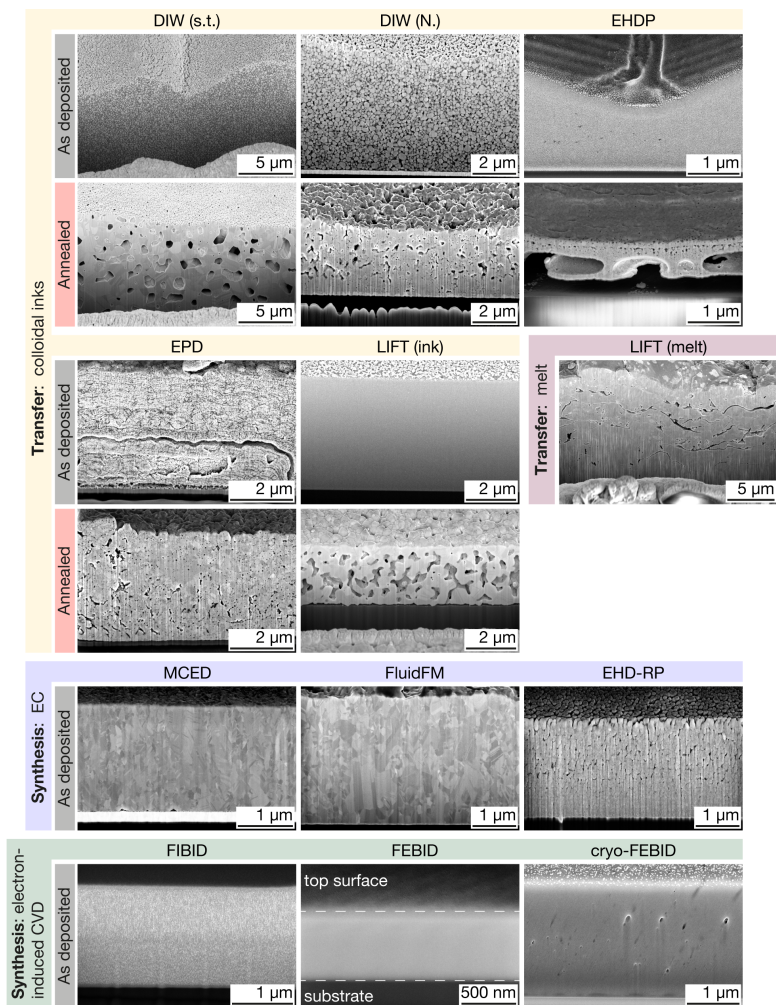


Figure C.2 – Microstructure of printed pads. Representative cross-section micrographs of printed pads at lower magnification. The as-printed and annealed pads of EHDP and LIFT (ink) had different as-deposited thicknesses (hence no shrinkage can be concluded from these images). The cross-section of the as-deposited EHDP pad was made after indentation (hence the triangular indent at its surface). All images are tilt-corrected.

due to differences in local temperatures and local mechanical constraints. All shown pillars feature radial gradients in porosity, with some pillars even being hollow (EHDP, LIFT (ink)). In contrast, the microstructure of pads is typically more homogeneous (at least in the center of the pads, where the cross-sections were cut – we have not studied the edges of the large DIW and LIFT (ink) pads). As an exception, the center of the EHDP pads delaminated upon annealing.

Figure C.4 summarizes the SEM EDX analysis performed on printed pads. EDX spectra were recorded with identical acquisition conditions from a printed pad (blue, same batch of samples presented in Fig. C.2) and the substrate (red). We refrain from a quantitative analysis of the presented data – especially of the carbon and oxygen content – for the following reasons: first, quantification of the light elements (C, N, O in our case) by EDX is unreliable. Second, C is always co-deposited by the electron beam during analysis. Third, the variation in geometry and density of the pads does not allow for a direct comparison between the techniques, and additionally, makes consistent decoupling signals from the printed geometries and the substrates impossible. Nevertheless, we cite some numbers in the following paragraphs – please note that these are at best approximate values and that the signals from the substrate were not subtracted for this analysis.

The following qualitative statements can be made: all as-deposited colloidal inks contain carbon. Upon annealing, this amount is often not significantly reduced (from ≈ 50 at.% to ≈ 40 at.% for both DIW inks annealed at 300 and 450 °C, respectively; from ≈ 70 at.% to ≈ 45 at.% for EHDP pads annealed at 400 °C in O₂ atmosphere; no reduction upon annealing for EPD pads (≈ 50 at.%)). Thus, post-print procedures that specifically target the removal of carbon should be studied if a pronounced reduction in carbon content is desired. Similarly, as-deposited FIBID and FEBID pads contain large amounts of carbon (≈ 55 – 65 at.%). Additionally, FIBID structures contain Ga (≈ 15 at.%), and FEBID pads contain oxygen (≈ 35 at.%). Routines for purification of FEBID and FIBID structures exist²¹⁶ and need to be applied with most precursor compounds if high metal content is required in the final deposits. In contrast, electrochemically grown pads are mostly pure Cu – a C-K peak is detected for pads printed by MCEd, FluidFM and EHD-RP, but in all cases, the same peak is present in the spectra for the substrates, which indicates a general C contamination of the samples rather than a specific contamination of the printed structures.

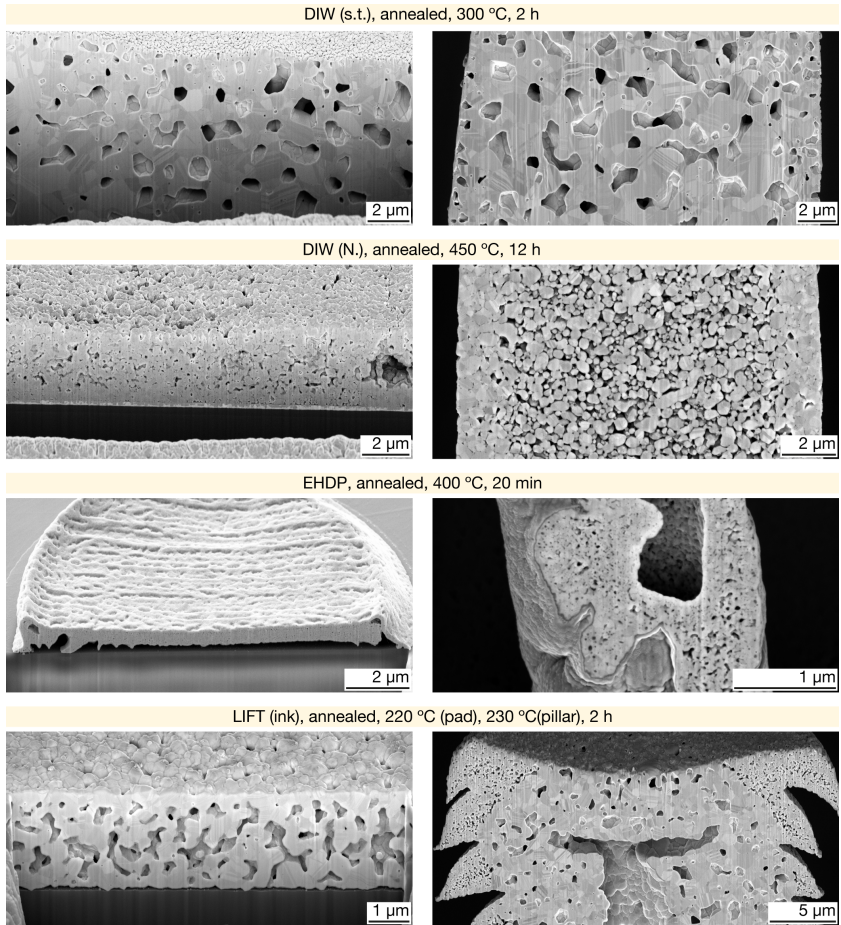


Figure C.3 – Microstructure of annealed pads and pillars printed from colloidal inks / suspensions. FIB-cut cross-sections of representative pads and pillars printed with various colloid transfer techniques. Pads and pillars from the same techniques were annealed with the same annealing procedure.

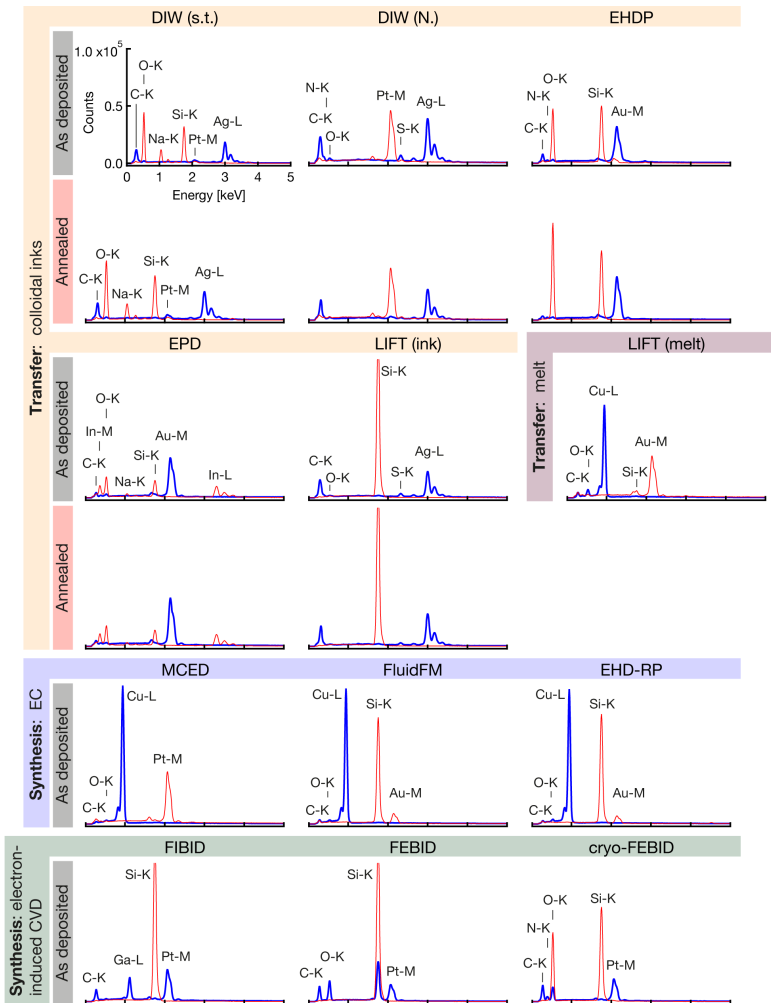


Figure C.4 – EDX analysis of printed pads. EDX spectra of printed pads (blue) and respective substrates (red) acquired with identical imaging conditions. The scale of all graphs is identical to the axes in the DIW (s.t.) graph.

C.3 Mechanical data for all tested samples of all techniques

Table C.1 lists the averaged values of Young's modulus E , hardness H and yield stress $\sigma_{0.07}$ of the metals printed by all studied techniques. In addition, Supplementary Figures C.5 – C.19 summarize the mechanical data collected for all tested AM methods presented in this manuscript. The data is organized as follows (Supplementary Figure C.5): one or two figures per method present all analyzed mechanical data and representative micrographs of the materials' microstructures. In each figure, the data is grouped by annealing state. The left column presents nanoindentation data collected from printed pads, the right column microcompression data from printed pillars. Each graph is accompanied by a representative cross-section micrograph from one of the pads and pillars from the respective batch of samples. The nanoindentation graph shows Young's modulus (red) and hardness (blue) measured as a function of depth. The graph plots an averaged curve (bold line, with the shaded area representing the standard deviation) of all recorded curves (dashed lines). E and H values reported in the manuscript were extracted from the depth range highlighted in the average curves. The microcompression graph displays all measured stress-strain curves (using the average diameter of the deformed portion of the pillars). One representative curve is highlighted for better visibility.

As a deviation from the expected relation of hardness to strength in solids, we measure a pronouncedly higher strength of DIW inks upon microcompression compared to the hardness derived from nanoindentation of the same materials ($\sigma_{0.07}$: 0.256 – 0.315 GPa and H : 0.062 – 0.141 GPa, Supplementary Figures C.5 and C.7). For dense solids, indentation hardness H is ≈ 3 times the yield strength σ ⁴⁴⁷. For porous solids, the constraint factor can reduce to unity, *i.e.* $H = \sigma$, but H never becomes smaller than σ . However, as-printed inks are clearly not solids, but rather granular media, as they are composed of discrete, noncohesive particles. Thus, strength is not necessarily related to plastic deformation of a solid, but rather the flow of individual particles under shear loading. While an analysis of the mechanics of these materials is outside the scope of this paper, we can speculate about the origins of the observed difference. Due to the interlocking of colloids, the necessary yield stresses for deformation is a function of the applied normal stresses⁴⁴⁸. As the stress fields below a flat punch (microcompression) and a sharp pyramid (indentation) are very different, the resulting contact pressures detected with the two methods might differ. Additionally, the probe size in nanoindentation is comparable to the particle size and inter-particle spacing of the probed medium (indenter radius ≈ 50 nm, large particles ≈ 250 nm), whereas it is larger in microcompression (punch diameter $>$ pillar diameter, *i.e.* > 10 μm). Thus, the two methods may potentially probe different deformation mechanisms. Interestingly, this difference is only observed

for DIW inks, hinting towards an influence of the particle shape, the respective binder phase, or size distribution.

Table C.1 – E , H and $\sigma_{0.07}$ data. Averaged values for Young's modulus E , hardness H and yield stress $\sigma_{0.07}$.

| Technique | Nanoindentation | | Microcompression | |
|--|-----------------|-----------------|------------------|-----------------------|
| | E [GPa] | H [GPa] | E [GPa] | $\sigma_{0.07}$ [GPa] |
| DIW (s.t.) | | | | |
| ad. (100 °C, 0.5 h) | 12.6 ± 3.2 | 0.141 ± 0.051 | 33.3 ± 4.1 | 0.265 ± 0.039 |
| 300 °C, 0.5 h | 41.1 ± 9.5 | 0.461 ± 0.181 | 35.7 ± 0.7 | 0.289 ± 0.027 |
| 300 °C, 2 h | 31.1 ± 10.0 | 0.435 ± 0.123 | 42.1 ± 3.8 | 0.168 ± 0.008 |
| DIW (N.) | | | | |
| ad. | 4.62 ± 1.19 | 0.0617 ± 0.0144 | 35.7 ± 2.7 | 0.315 ± 0.015 |
| 450 °C, 12 h | 48.8 ± 13.0 | 0.952 ± 0.239 | 65.7 ± 2.7 | 0.422 ± 0.028 |
| EHDP | | | | |
| ad. | 0.521 ± 0.160 | 0.0480 ± 0.0154 | 1.09 ± 0.14 | 0.0168 ± 0.0017 |
| 400 °C, 20 min | not analyzed | not analyzed | 31.3 ± 0.4 | 0.246 ± 0.058 |
| 400 °C, 20 min, $\varnothing \approx 350$ nm pillars | N/A | N/A | 39.8 ± 8.8 | 0.411 ± 0.057 |
| EPD | | | | |
| ad. | 9.09 ± 5.95 | 0.369 ± 0.321 | 7.29 ± 4.06 | 0.146 ± 0.104 |
| 300 °C, 1 h | 54.2 ± 12.5 | 1.42 ± 0.41 | 47.1 ± 8.5 | 0.366 ± 0.056 |
| LIFT (ink) | | | | |
| ad. | 1.94 ± 0.07 | 0.108 ± 0.004 | 1.16 ± 0.01 | 0.0125 ± 0.0014 |
| 200 °C, 1 h | 36.4 ± 2.5 | 0.661 ± 0.074 | 12.8 ± 0.9 | 0.0880 ± 0.0008 |
| 220 (pads) / 230 °C (pillars), 2 h | 31.0 ± 3.5 | 0.400 ± 0.072 | 26.9 ± 0.4 | 0.118 ± 0.004 |
| LIFT (melt) | | | | |
| Cu | 73.2 ± 10.4 | 1.66 ± 0.37 | 49.8 ± 7.4 | 0.415 ± 0.028 |
| Au | 24.3 ± 10.1 | 0.293 ± 0.235 | 28.3 ± 3.5 | 0.186 ± 0.020 |
| MCED | | | | |
| ad. | 121.8 ± 7.4 | 2.71 ± 0.36 | 114.2 ± 3.6 | 0.774 ± 0.104 |
| FluidFM | | | | |
| ad. | 138.4 ± 18.7 | 2.28 ± 0.45 | 134 ± 11 | 0.962 ± 0.026 |
| EHD-RP | | | | |
| ad. | 80.4 ± 17.9 | 2.22 ± 0.82 | 81.7 ± 8.4 | 1.10 ± 0.12 |
| ad., $\varnothing \approx 170$ nm pillars | N/A | N/A | 88.4 | 1.38 ± 0.06 |
| FIBID | | | | |
| ad. | 140.0 ± 7.9 | 9.42 ± 0.11 | 95.3 ± 9.5 | 2.64 ± 0.25 |
| FEUID | | | | |
| ad. | 75.5 ± 1.6 | 6.01 ± 0.32 | 59.3 ± 3.9 | 2.65 ± 0.04 |
| cryo-FEUID | | | | |
| ad. | 13.8 ± 1.0 | 0.843 ± 0.074 | 3.85 ± 0.93 | 0.100 ± 0.059 |

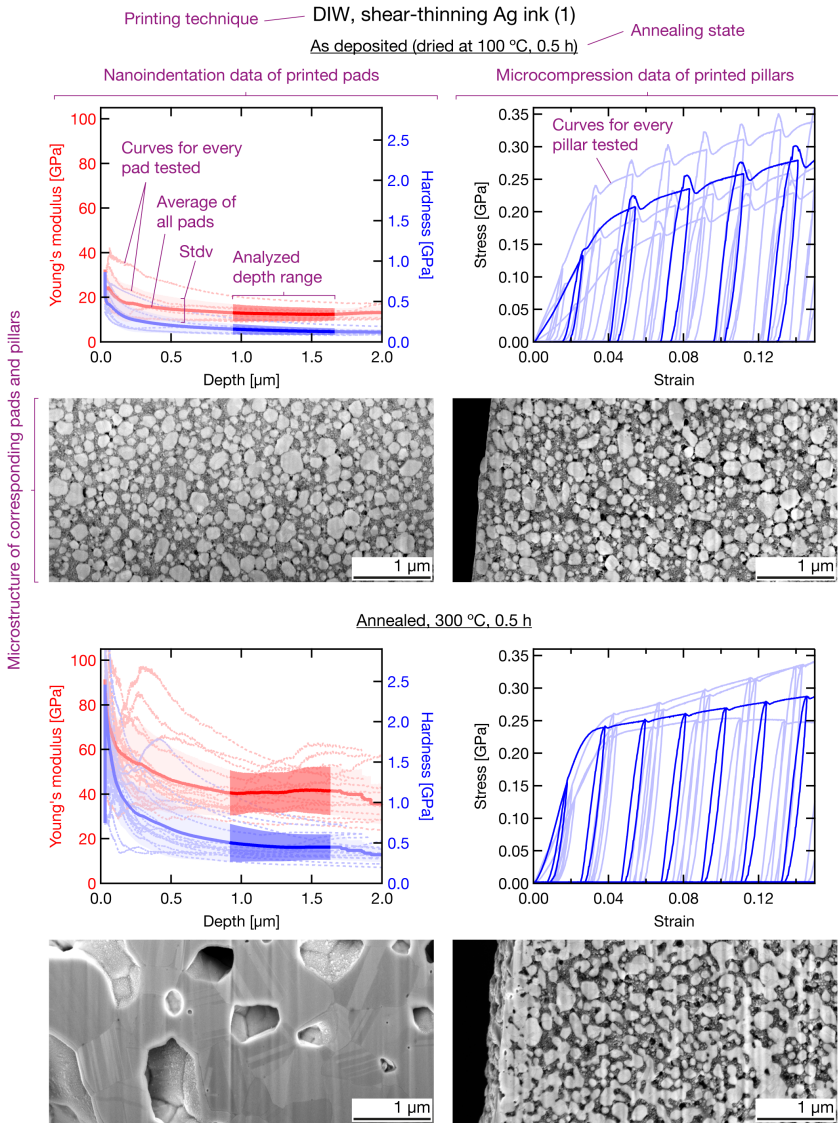


Figure C.5 – Direct ink writing, shear-thinning Ag ink (DIW (s.t.)).

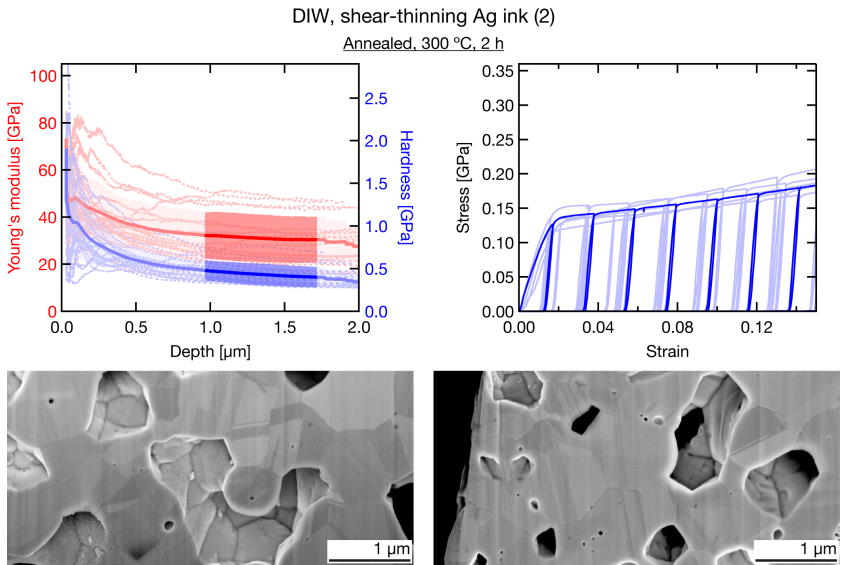


Figure C.6 – Direct ink writing, shear-thinning Ag ink (DIW (s.t.)).

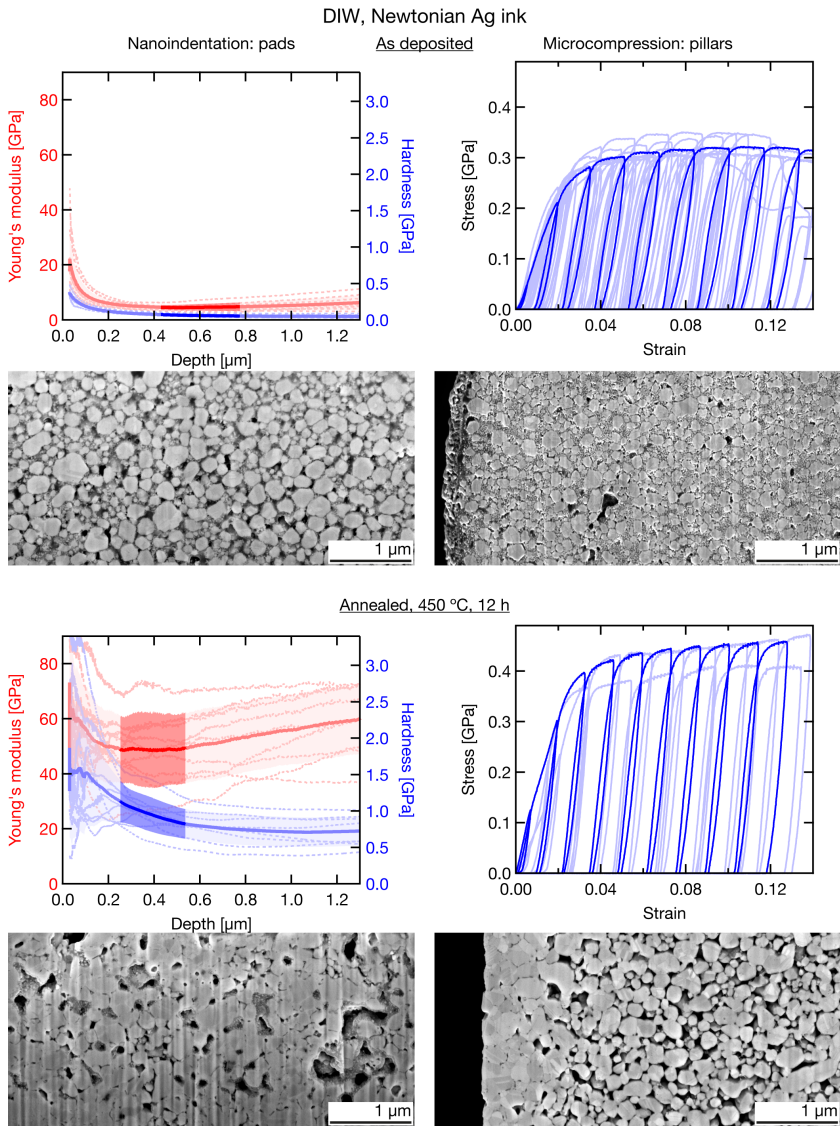


Figure C.7 – Direct ink writing, Newtonian Ag ink (DIW (N.)).

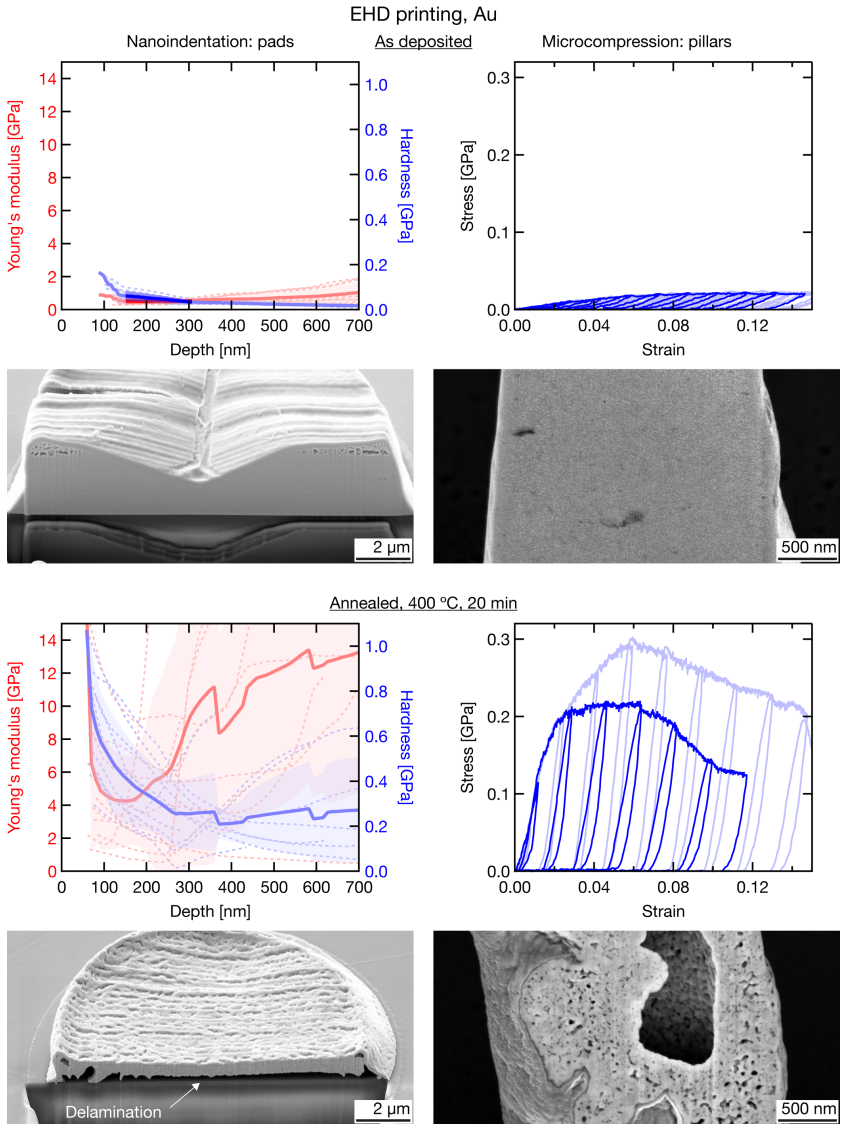


Figure C.8 – Electrohydrodynamic printing, Au ink (EHD). Nanoindentation data of annealed pads was not analyzed, as the large-scale delamination of the pads upon annealing prevented the collection of representative data.

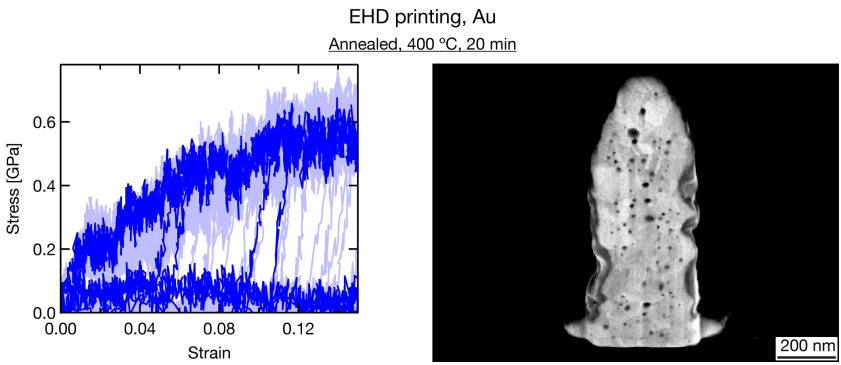


Figure C.9 – Electrohydrodynamic printing, Au ink (EHDP). Microcompression data and representative cross-section of annealed pillars 300 – 350 nm in diameter.

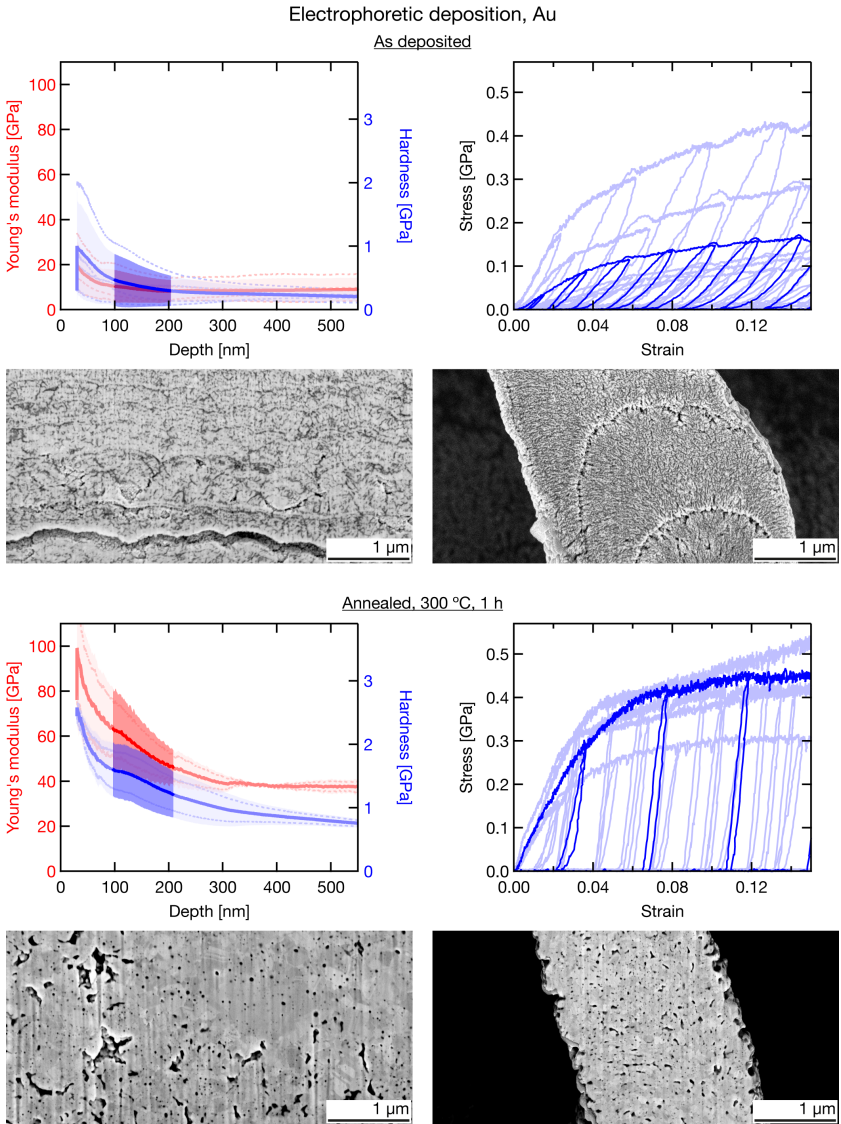


Figure C.10 – Laser-assisted electrophoretic deposition (EPD), Au nanoparticles.

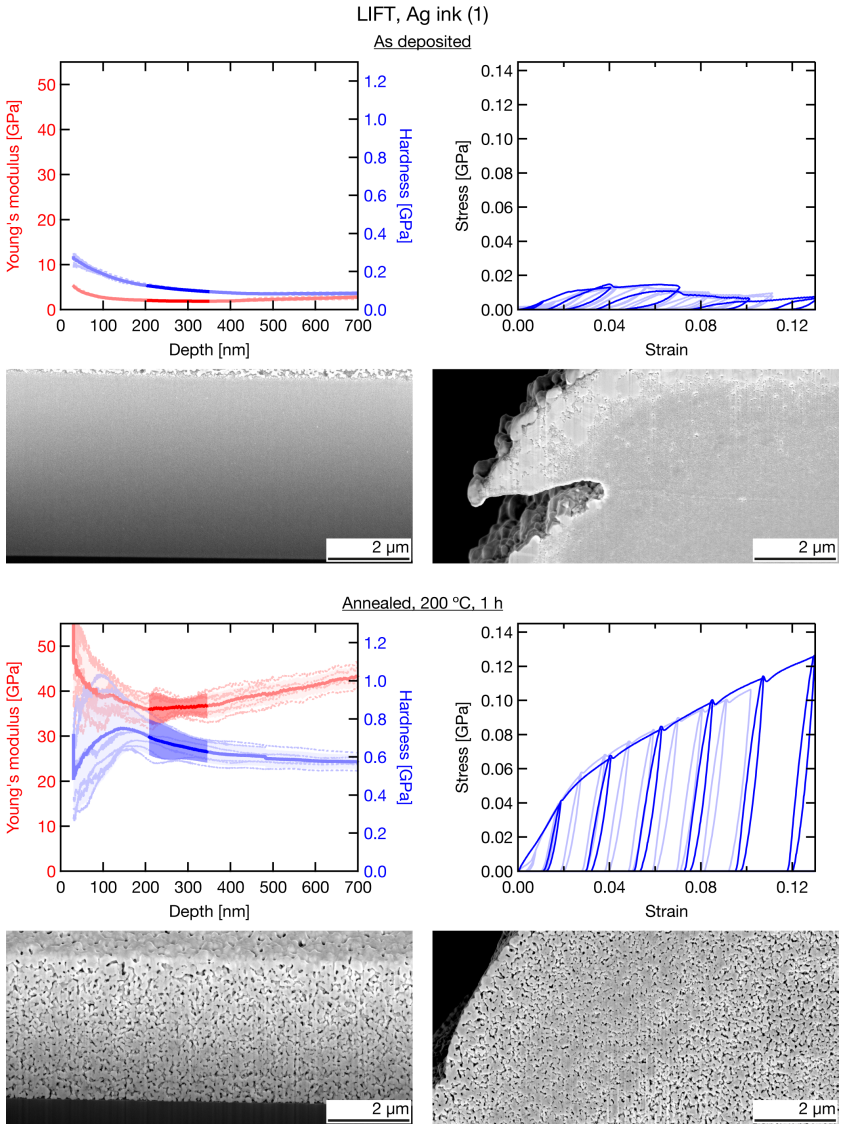


Figure C.11 – Laser-induced forward transfer of Ag ink (LIFT (ink)).

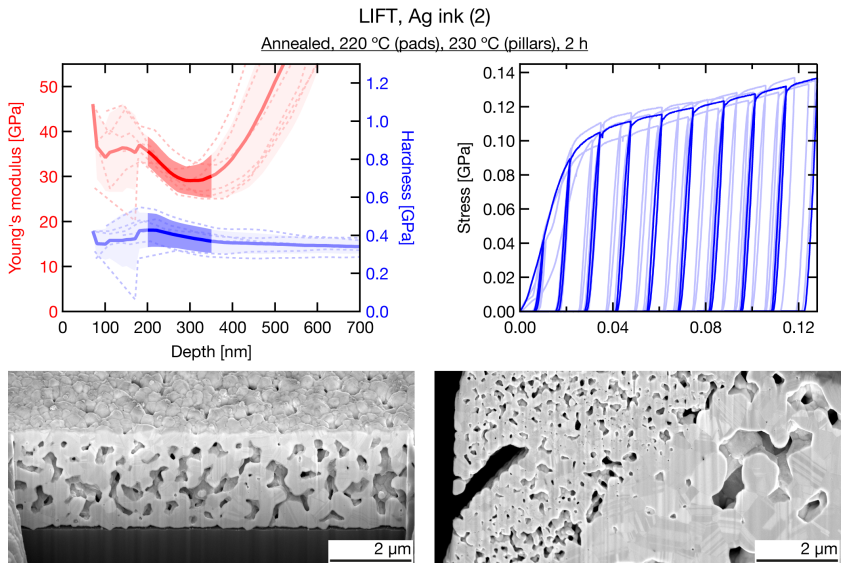


Figure C.12 – Laser-induced forward transfer of Ag ink (LIFT (ink)).

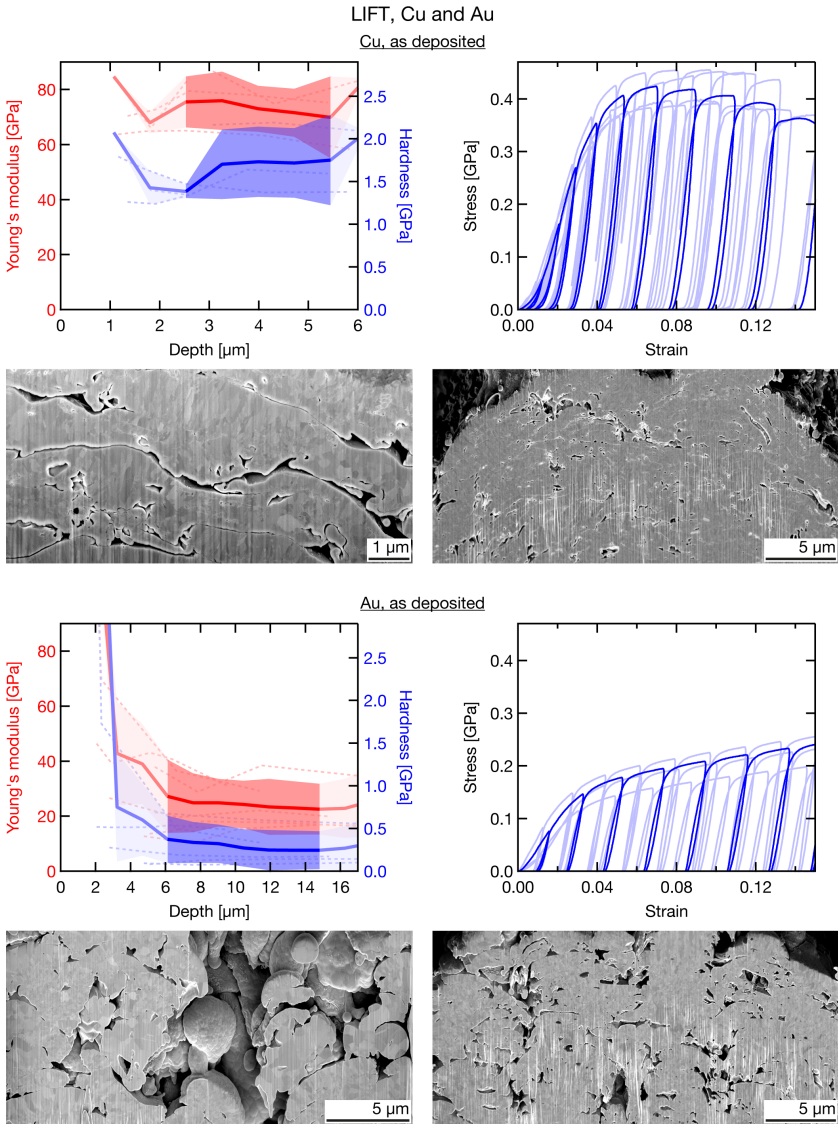


Figure C.13 – Laser-induced forward transfer of Cu and Au (LIFT).

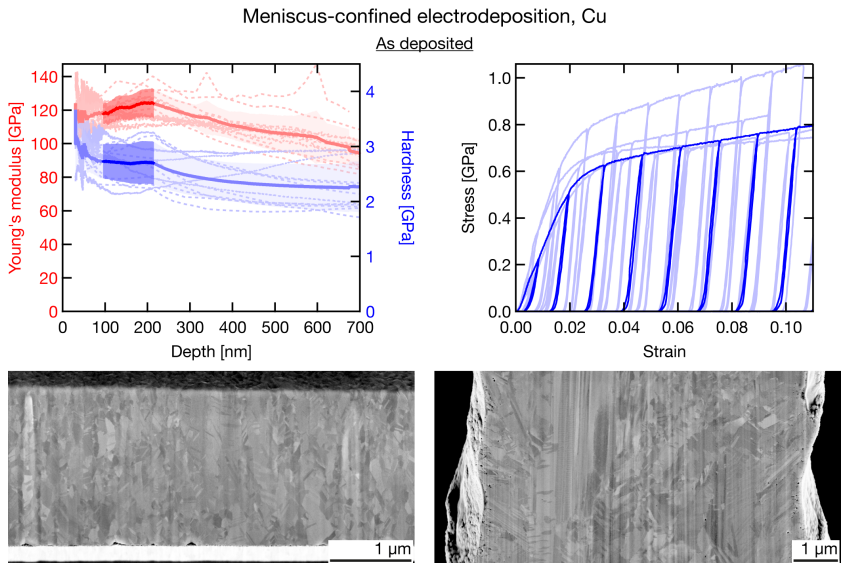


Figure C.14 – Meniscus-confined electrodeposition (MCED) of Cu.

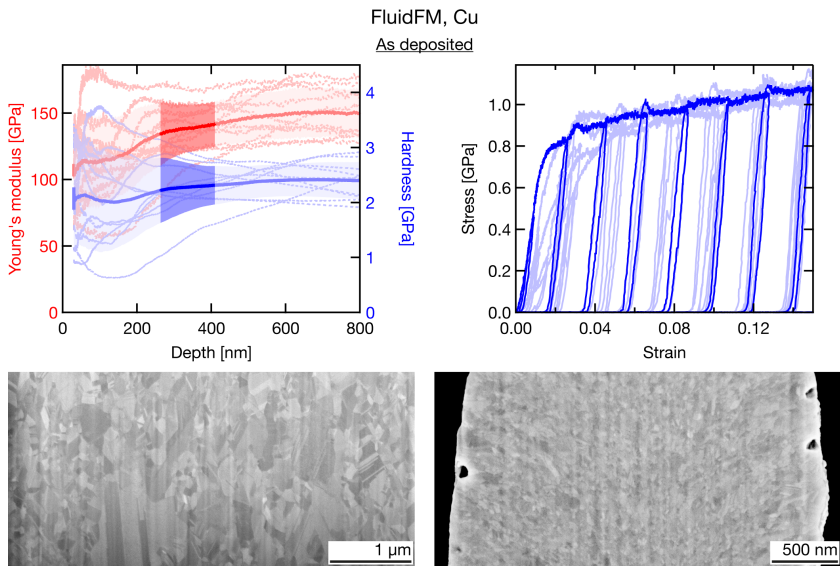


Figure C.15 – FluidFM electrodeposition of Cu.

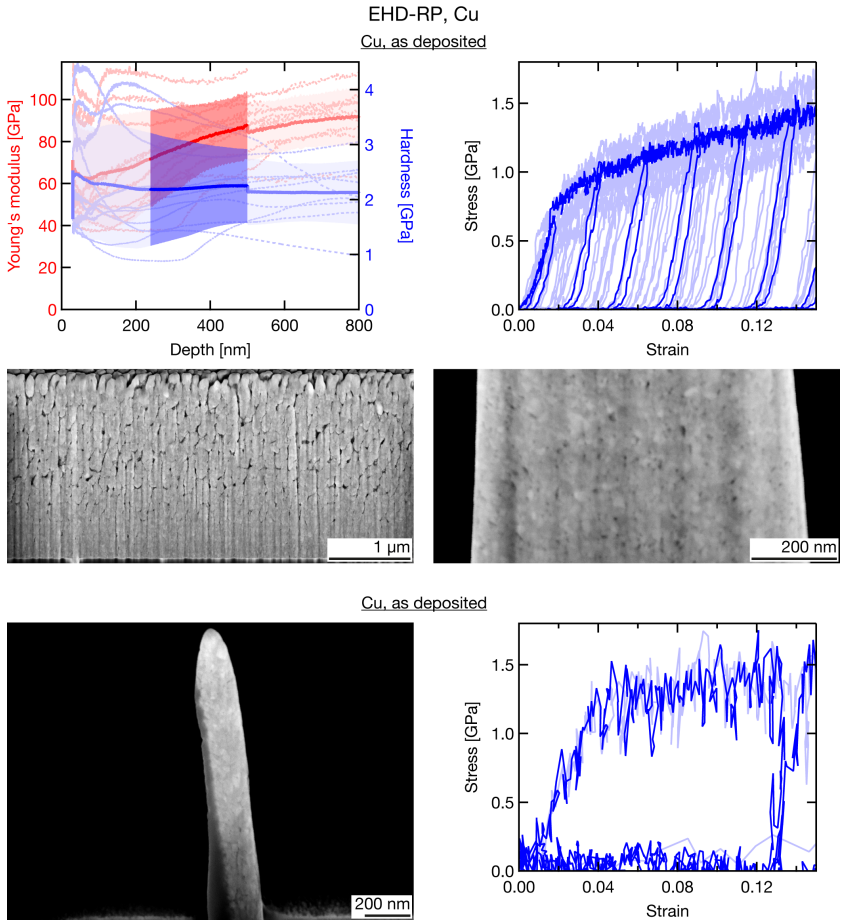


Figure C.16 – Electrohydrodynamic redox printing (EHD-RP) of Cu. Bottom: representative cross-section and microcompression data for two Cu pillars of 160 – 177 nm in diameter.

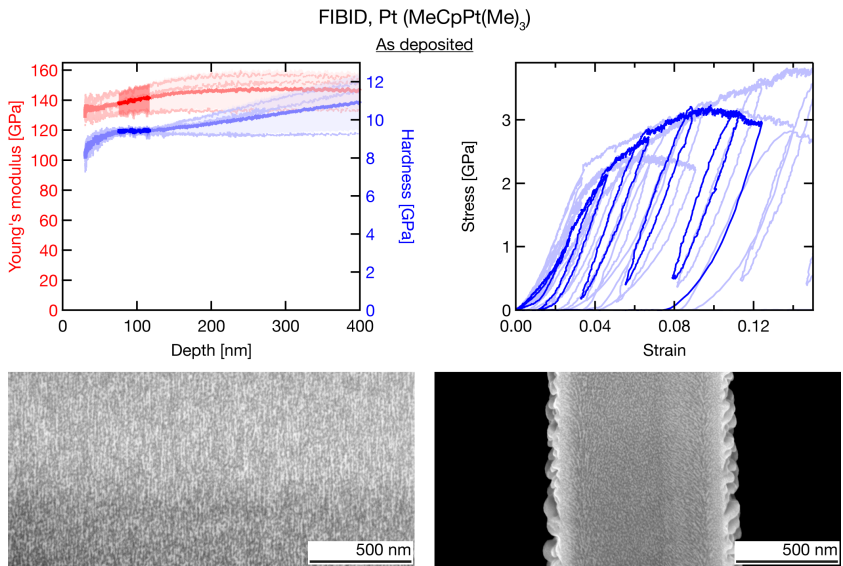


Figure C.17 – Focused ion beam-induced deposition (FIBID) of Pt (MeCpPt(Me)₃).

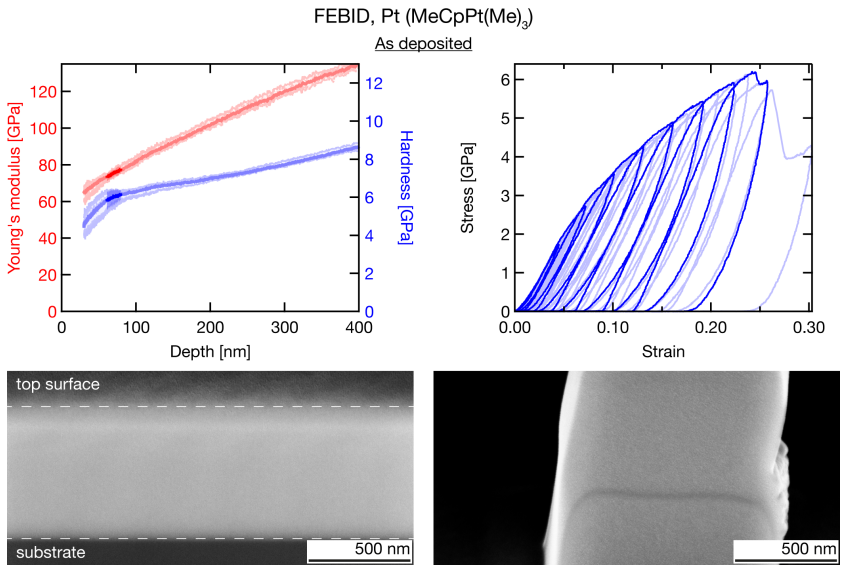


Figure C.18 – Focused electron beam-induced deposition (FEBID) of Pt (MeCpPt(Me)₃).

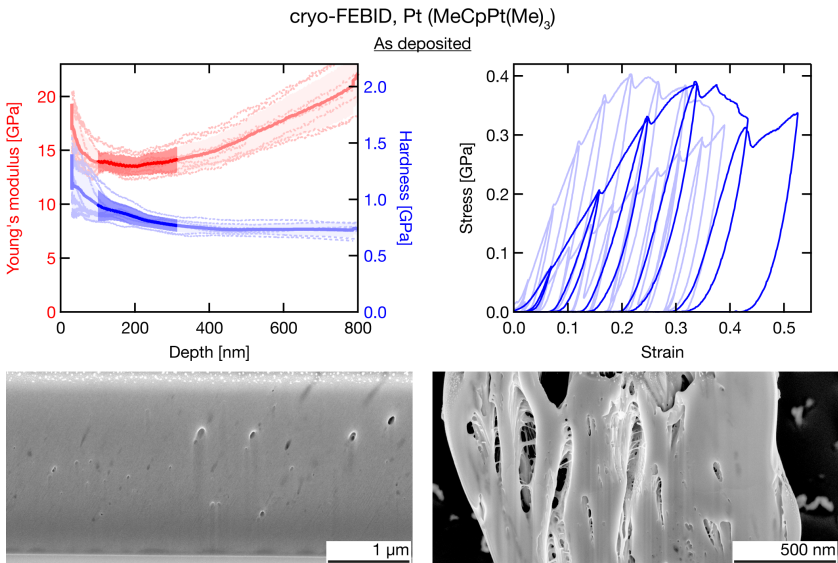


Figure C.19 – Focused electron beam-induced deposition at cryogenic temperatures (cryo-FEBID) of Pt (MeCpPt(Me)₃).

C.4 Mechanical literature data for thin films

Table C.2 – Mechanical literature data for thin films. Literature values for E , H (measured by nanoindentation, Berkovich indenter) and σ_y (measured by microcompression and microtension) of polycrystalline thin films fabricated by traditional deposition techniques (PVD and electrodeposition). The data in the main text was normalized to the values highlighted in **bold**.

| Material | E [GPa] | H [GPa] | σ_y [GPa] |
|--------------------|---|---|-------------------------------|
| Ag | 80.5 ³¹⁵ (bulk), ~ 80 ^{323,324} | 0.7 – 1.5 ^{323,324} , 1.2 | N/A |
| Au | 80.2 ³¹⁵ (bulk), 55 – 88.6 ^{325,326} | 1 – 2 ^{325,326} , 1.2 | 0.04 – 0.8 ^{449–452} |
| Cu | 125 ³¹⁵ (bulk), 88 – 135 ^{295,328,453,454} | 1.6 – 3.5 ^{295,327–329} , 2 | 0.2 – 1.2 ^{455–457} |
| Pt | 174 ³¹⁵ (bulk), 150 – 178 ^{330,458,459} | 1.5 – 8.6 ^{319,320,330} , 4 | N/A |
| amorphous C | 132 (bulk), 40 – 760 ^{341–343} | 5 – 30 ^{341,342} | 7 ³⁴³ |

Appendix D

Appendix to Chapter 4

D.1 Deposition mechanism

Additional arguments that support the hypothesis of an electrochemical growth mechanism are presented in the following: the size of grown crystallites is larger than the theoretical maximum size of particles formed in flight; if charge transfer from the substrate is blocked, no growth occurs.

D.1.1 Maximum theoretical size of crystallites formed in flight

We can estimate a maximum size of particles that could form in flight. If printed structures contain particles or crystallites larger than this critical size, then the features must have grown from the substrate rather than been deposited onto the substrate. To calculate a maximum size, we first assume that a particle will only form from metal cations contained in an individual droplet, *i.e.* that no ions from multiple droplets combine. This assumption is reasonable since droplets of equal sign of charge will fission and repel each other rather than fuse⁴⁶⁰. The maximum charge that can be contained in a droplet of radius r is given by the Rayleigh limit q_R :

$$q_R = 8\pi\sqrt{\epsilon_0\gamma r^3} \quad (\text{D.1})$$

where ϵ_0 is the permittivity of free space and γ is the surface tension of the liquid. The diameter of the largest droplet that could be ejected from a nozzle is assumed to be the diameter of the nozzle itself. For most cases, this is an unrealistic assumption, since actual droplet diameters

are usually a fraction of the nozzle size^{71,99,461}. Nevertheless, the hypothesis is acceptable for the argument presented here, because it will lead to an overestimation of the maximum particle size. For acetonitrile, with $\gamma = 0.0291 \text{ N m}^{-1}$ ⁴³², and a typical nozzle diameter of 200 nm and $r = 100 \text{ nm}$, q_R is

$$\begin{aligned} q_R &= 8\pi \sqrt{8.85 \times 10^{-12} \text{ F m}^{-1} \cdot 0.0291 \text{ N m}^{-1} \cdot (100 \times 10^{-9} \text{ m})^3} \\ &= 4.03 \times 10^{-16} \text{ C} \end{aligned} \quad (\text{D.2})$$

Faraday's law of electrolysis describes the volume V deposited from a charge q as

$$V = \frac{1}{\rho} \left(\frac{q}{F} \right) \left(\frac{M}{z} \right), \quad (\text{D.3})$$

with F the Faraday's constant, ρ the density, M the molar mass, and z the valency number of the cation to be deposited. With ρ and M of Cu, $q = q_R$, and $z = 1$ (see MS in Fig. 1 of the main text), the maximum volume for a spherical particle is

$$\begin{aligned} V &= \frac{1}{8.96 \times 10^3 \text{ kg m}^{-3}} \left(\frac{4.03 \times 10^{-16} \text{ C}}{96485 \text{ s A mol}^{-1}} \right) \left(\frac{63.546 \times 10^{-3} \text{ kg mol}^{-1}}{1} \right) \\ &= 2.96 \times 10^{-26} \text{ m}^3, \end{aligned} \quad (\text{D.4})$$

with a corresponding maximum diameter $d_{\max} = 3.84 \text{ nm}$. This is smaller than the majority of crystallites contained in printed structures (Fig. 4.14). We thus conclude a printing mode based on growth of crystallites upon electro-reduction of cations on the substrate, as opposed to spraying of particles formed in flight.

D.1.2 Blocking charge transfer from the substrate

Electron transfer from the substrate is mandatory for the electrochemical growth mechanism proposed in this report. Thus, blocking the path of electrons from the substrate should interrupt growth. In contrast, interrupting electron transfer from the surface should not affect growth if ions are reduced in flight and deposited as neutralized particles. Figure D.1a outlines a corresponding experiment: a Au substrate is partially covered with an electrically insulating film (1 μm thick alumina). The Au/alumina stack effectively blocks electron transfer while at the same time assuring an unaffected electric field for EHD ejection (with the field defined as voltage applied to the source divided by the nozzle-Au distance).

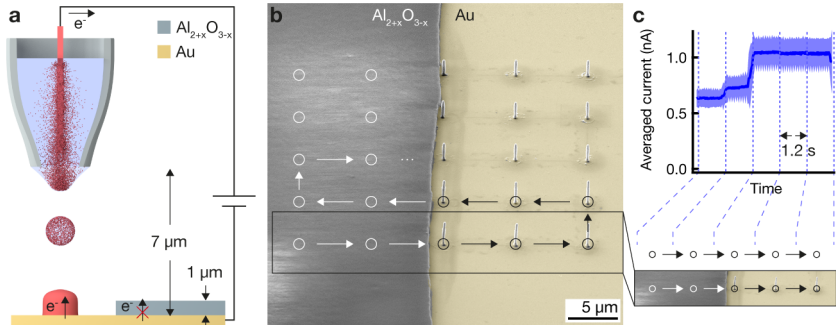


Figure D.1 – Electron transfer from the substrate is essential. Blocking the fast electron transfer from the substrate strongly retards printing – a fact that would not be observed for any deposition modes based on particle formation in air. **a**, A 1 μm thick Al_{2+x}O_{3-x} film deposited onto a Au-substrate presents an effective barrier for electrons from the substrate. Yet, a constant electric field for ejection is maintained by this substrate design. **b**, SE micrograph of an array of Cu pillars printed across the Au-Au/Al_{2+x}O_{3-x} interface. The bare Au surface is false-colored in yellow, the circles mark individual positions of the array, and the arrows indicate printing direction. Although the voltage was held at 110 V during the complete array, Cu only deposits on the conductive surface. **c**, Averaged current through the source electrode during printing of an individual row of the array in (b), averaged over all rows (The solid line is the averaged data, the shading represents the standard deviation). The excerpt of the array at the bottom of (c) indicates the array positions relating to the time axis of the graph. The vertical grid indicates the residence time of 1.2 s used to print each pillar. The uninterrupted ejection current at positions on the oxide indicates ongoing ejection over the oxide.

When printing an array of Cu pillars across the Au-Au/alumina interface, Cu only deposits if fast electron transfer through the bare Au-layer is available (Fig D.1b). No Cu is deposited on the oxide. Figure D.1c shows the corresponding current measured at the high-voltage output of the source: the current decreases whenever ejecting above the oxide, but does not approach zero. Thus, we conclude the EHD ejection is sustained with the nozzle positioned above the oxide. The fact that the individual positions of the array on the oxide are reflected in the current transient support that assumption: the current measured at the positions close to the edge of the oxide is always higher than at the positions at the left end of the array, presumably due to decreased charging and build up of a lower counter field at these positions. The fact that no solvent residues are visible on the oxide is probably owed to charging of the oxide and subsequent deflection of the ejected liquid.

The array shown was printed at a voltage of 110 V, but the same result was obtained in a range from 90 – 140 V. Some insignificant growth is observed for long residence times of >10 s and highest voltages, presumably through charge transfer from the oxide or the atmosphere. It follows that fast charge transfer from the substrate is essential for printing. Further, no neutralized particles are sprayed, else we would detect them on the oxide. In combination with the additional evidence

presented in the above text, even the formation of any charged particles is unlikely, although this experiment does not exclude their formation (as they could be deflected and thus not be detected).

D.2 Influence of oxygen on the microstructure

Fig D.2 shows the evolution of a second phase (dark contrast in the micrographs) parallel to the oxygen content of the atmosphere when printing Cu. A non-quantitative estimate of the areal fraction of the dark phase suggests that it decreases proportional to the oxygen content. The respective EDX spectra indicate that the reduction of areal fraction of the dark phase is accompanied by a reduction of oxygen content in the deposits.

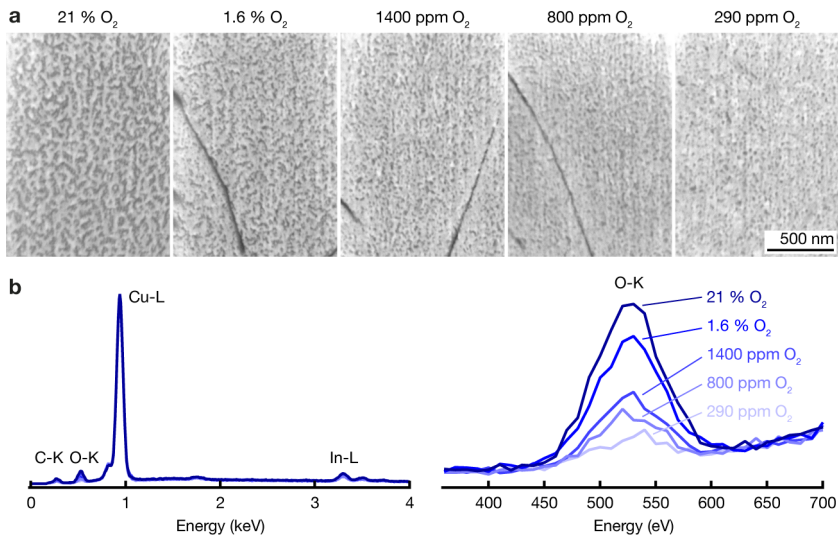


Figure D.2 – Influence of O₂ on the microstructure of Cu. **a**, A second phase forms when printing Cu in air (dark in the InLens SE micrographs). The areal fraction of this phase is proportional to the O₂ content of the printing atmosphere. Please note that these deposits were not yet printed with optimal parameters, hence the large size and the crevices. To exclude an influence of time, the O₂ content in the printing atmosphere was varied in this order: 21 %, 1.6 %, 800 ppm, 1400 ppm, 290 ppm. **b**, EDX spectra recorded from the deposits shown in (a). Counts were normalized to the Cu peak. The zoom shows a correlation of the height of the O-K peak with oxygen content. Note: the deposits were printed on an ITO/glass substrate. As the height of the In-L peak does not change proportionally to the O₂ content, it is concluded that the O-K peak mostly originates from oxides in the deposits and not from the substrate.

D.3 FIB-flattening of pillars for microcompression

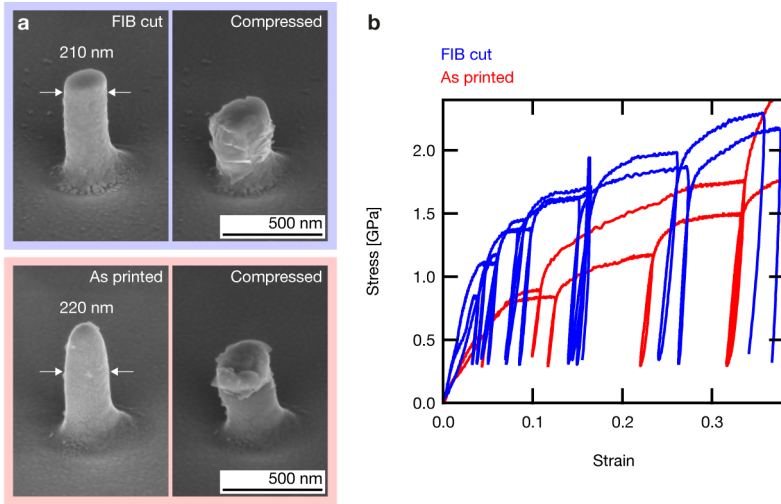


Figure D.3 – FIB-flattening of pillars for microcompression. **a**, SEM micrographs of as-printed (bottom) and FIB-cut pillar before and after microcompression. Image tilts: 60° . **b**, Stress-strain curves recorded from two as-deposited and three FIB-cut pillars. The flat top of the cut pillars result in a more defined yield point. Further, uncut pillars tend to bend (see the slight tilt of the uncut compressed pillar).

Appendix E

Appendix to Chapter 6

E.1 Anodic degradation of the Au tip

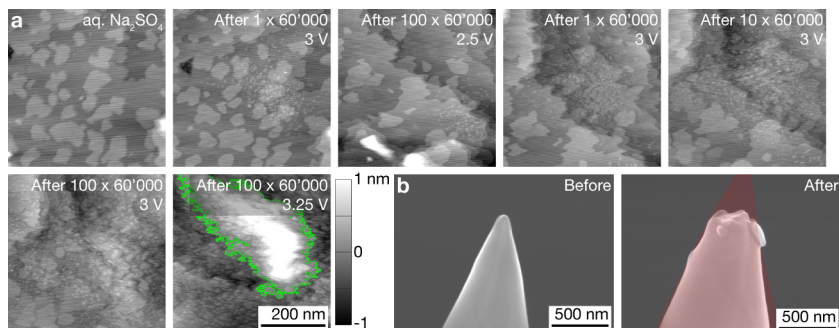


Figure E.1 – Anodic degradation of Au tip. All deposition experiments performed with the Au tip of Fig. 6.9b. **a**, STM scans of a Au surface before (first scan) and after pulsing the Au STM tip in 0.25 M aq. Na₂SO₄ using the parameters stated in the panels. The volume of the outlined deposit in the last scan is $6.3 \times 10^4 \text{ nm}^3$. **b**, SEM micrograph of the Au tip used in (a) before (left) and after (right) the deposition experiments. The estimated volume of the tip material missing after deposition is $\approx 2 \times 10^7 \text{ nm}^3$.

E.2 Setup: circuit diagram

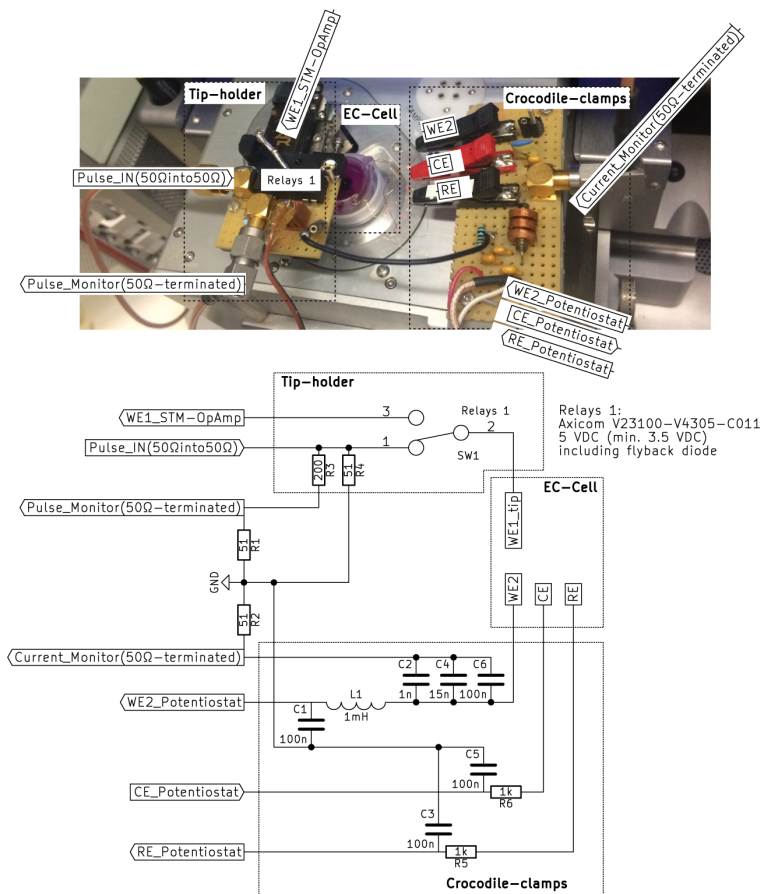


Figure E.2 – Circuit diagram of the electronic components that couple the nanosecond pulses into the electrochemical cell and separate the high- and low-frequency currents. Main in- and outputs as well as some key components are labelled in the photograph.

E.3 Nanoscale deposition with the "Hofmann" approach

The "Hofmann" approach utilizes the fact that the reduction potential is proportional to the the ion concentration above the electrode surface^a – the higher the concentration, the more positive the effective reduction potential. Hoffmann and Schindler *et al.* ^{418,424,425} proposed the increase of the local ion concentration with the help of an STM tip, resulting in a spatially confined lift of the reduction potential and hence deposition: if a substrate is held at a potential some tens of mV positive to the Nernstian reduction potential for a given, global ion concentration in the electrolyte solution, no reduction occurs. However, if the concentration is locally increased until the Nernst-potential exceeds the surface potential, metal-deposition will proceed in that area. Via deposition of Co onto a STM tip and subsequent, burst-like dissolution close to the substrate, Schindler *et al.* demonstrated Co deposits as small as 16 nm (Fig. 6.1e, f). Up to date, Co on Au ^{418,424,425} and Pd deposits on Si substrates ^{462,463} have been fabricated using this method. In principle, the approach could be used fo the growth of out-of-plane features, but according to my knowledge, 3D deposition has not yet been attempted.

E.3.1 Results: 2D patterning with the "Hofmann" approach

Figure E.3 shows our only successful deposition experiment using the approach outlined above: three Co deposits grown on a Au single crystal in an aq. CoSO₄ electrolyte solution, with the first deposition ≈25 nm in width. Stepping the substrate potential $\Phi_{\text{substrate}}$ to $\Phi_{\text{substrate}} > \Phi_{\text{Co} \rightarrow \text{Co}^{2+}}$ results in complete dissolution of the deposits. Although the concept can facilitate highly localized deposition, it proved not to be suitable for 2D or 3D patterning due to its high demands on stability of the surface potential (resulting in low reproducibility with our system) and its extremely slow patterning speed (≈ 10 s per deposit, Fig. E.3c).

^aThe potential E of an electrode M^{z+}/M is a function of the activity a of the M^{z+} ions in solution. This relationship is described by the Nernst equation

$$E = E^0 + \frac{RT}{zF} \ln a_{M^{z+}}, \quad (\text{E.1})$$

where R is the gas constant and T the absolute temperature. The activity $a_{M^{z+}}$ can be related to the concentration $c_{M^{z+}}$ using the activity coefficient γ :

$$a_{M^{z+}} = \gamma c_{M^{z+}}. \quad (\text{E.2})$$

In most cases however it is acceptable to treat activation and concentration as being equal ($\gamma = 1$).

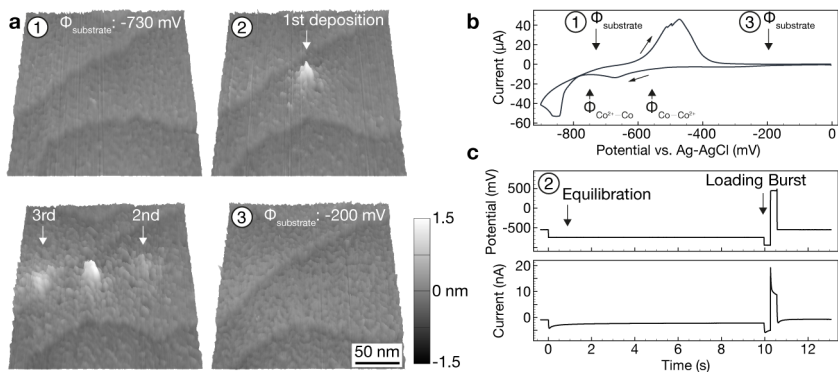


Figure E.3 – Deposition with the "Hofmann" approach. **a**, STM scans of a Au surface before (1) and after (2) deposition in 1 mM aq. $\text{CoSO}_4 + 0.25 \text{ M Na}_2\text{SO}_4$. The third scan was recorded after placing two more deposit left and right of the first one. Stepping the surface potential to $\Phi_{\text{substrate}} > \Phi_{\text{Co} \rightarrow \text{Co}^{2+}}$ fully dissolves the deposits. **b**, Cyclic voltammogram of Au in 1 mM aq. $\text{CoSO}_4 + 0.25 \text{ M Na}_2\text{SO}_4$. For deposition (1), the substrate is held at a potential just above the Co reduction potential (the onset of Co deposition cannot be discerned in the voltammogram as it is screened by oxygen reduction currents). The onset potential of deposition is determined by STM observation of the de-localized deposition). **c**, Potential and current transients of the STM probe during a single deposition event. To initiate deposition, Co is deposited onto the probe (Loading) and subsequently dissolved from the probe at once (Burst). All potentials vs. Ag-AgCl.

Bibliography

- [1] Gibson, I., Rosen, D. W. & Stucker, B. *Additive Manufacturing Technologies* (Springer New York, New York, NY, 2015).
- [2] Thompson, M. K. et al. Design for Additive Manufacturing: Trends, opportunities, considerations, and constraints. *CIRP Ann. - Manuf. Technol.* **65**, 737–760 (2016).
- [3] Kang, H.-W. et al. A 3D bioprinting system to produce human-scale tissue constructs with structural integrity. *Nat. Biotechnol.* **34**, 312–319 (2016).
- [4] Jakus, A. E. et al. Hyperelastic “bone”: A highly versatile, growth factor–free, osteoregenerative, scalable, and surgically friendly biomaterial. *Sci. Transl. Med.* **8**, 358ra127–358ra127 (2016).
- [5] O’Donnell, J., Kim, M. & Yoon, H.-S. A Review on Electromechanical Devices Fabricated by Additive Manufacturing. *J. Manuf. Sci. Eng.* **139**, 010801 (2016).
- [6] Studart, A. R. Additive manufacturing of biologically-inspired materials. *Chem. Soc. Rev.* **45**, 359–376 (2016).
- [7] Sydney Gladman, A., Matsumoto, E. A., Nuzzo, R. G., Mahadevan, L. & Lewis, J. A. Biomimetic 4D printing. *Nat. Mater.* **15**, 413–8 (2016).
- [8] Keating, S. J., Leland, J. C., Cai, L. & Oxman, N. Toward site-specific and self-sufficient robotic fabrication on architectural scales. *Sci. Robot.* **2**, eaam8986 (2017).
- [9] Koschny, T., Soukoulis, C. M. & Wegener, M. Metamaterials in microwaves, optics, mechanics, thermodynamics, and transport. *J. Opt.* **19**, 084005 (2017).

- [10] Rogers, J., Huang, Y., Schmidt, O. G. & Gracias, D. H. Origami MEMS and NEMS. *MRS Bull.* **41**, 123–129 (2016).
- [11] Ning, X. et al. 3D Tunable, Multiscale, and Multistable Vibrational Micro-Platforms Assembled by Compressive Buckling. *Adv. Funct. Mater.* **27**, 1605914 (2017).
- [12] Ahn, B. Y. et al. Omnidirectional Printing of Flexible, Stretchable, and Spanning Silver Microelectrodes. *Science (80-.)*. **323**, 1590–1593 (2009).
- [13] Hu, J. & Yu, M.-F. Meniscus-Confined Three-Dimensional Electrodeposition for Direct Writing of Wire Bonds. *Science (80-.)*. **329**, 313–316 (2010).
- [14] Wang, J., Auyeung, R. C. Y., Kim, H., Charipar, N. A. & Piqué, A. Three-Dimensional Printing of Interconnects by Laser Direct-Write of Silver Nanopastes. *Adv. Mater.* **22**, 4462–4466 (2010).
- [15] Grimm, D. et al. Rolled-up nanomembranes as compact 3D architectures for field effect transistors and fluidic sensing applications. *Nano Lett.* **13**, 213–218 (2013).
- [16] Schneider, J. et al. Electrohydrodynamic NanoDrip Printing of High Aspect Ratio Metal Grid Transparent Electrodes. *Adv. Funct. Mater.* **26**, 833–840 (2016).
- [17] Zhou, N., Liu, C., Lewis, J. A. & Ham, D. Gigahertz Electromagnetic Structures via Direct Ink Writing for Radio-Frequency Oscillator and Transmitter Applications. *Adv. Mater.* **29**, 1605198 (2017).
- [18] Fu, H. et al. Morphable 3D mesostructures and microelectronic devices by multistable buckling mechanics. *Nat. Mater.* **17**, 268–276 (2018).
- [19] Huang, W. et al. Three-dimensional radio-frequency transformers based on a self-rolled-up membrane platform. *Nat. Electron.* **1**, 305–313 (2018).
- [20] Gissibl, T., Thiele, S., Herkommer, A. & Giessen, H. Two-photon direct laser writing of ultracompact multi-lens objectives. *Nat. Photonics* **10**, 554–560 (2016).
- [21] Hsiung, B.-K. et al. Rainbow peacock spiders inspire miniature super-iridescent optics. *Nat. Commun.* **8**, 2278 (2017).
- [22] Fan, Z. et al. Three-dimensional nanopillar-array photovoltaics on low-cost and flexible substrates. *Nat. Mater.* **8**, 648–653 (2009).

-
- [23] Kang, S. M. et al. Moth-Eye TiO₂ Layer for Improving Light Harvesting Efficiency in Perovskite Solar Cells. *Small* **12**, 2443–2449 (2016).
- [24] Sun, K. et al. 3D Printing of Interdigitated Li-Ion Microbattery Architectures. *Adv. Mater.* **25**, 4539–4543 (2013).
- [25] Pikul, J. H., Gang Zhang, H., Cho, J., Braun, P. V. & King, W. P. High-power lithium ion microbatteries from interdigitated three-dimensional bicontinuous nanoporous electrodes. *Nat. Commun.* **4**, 1732 (2013).
- [26] Deng, J. et al. Naturally Rolled-Up C/Si/C Trilayer Nanomembranes as Stable Anodes for Lithium-Ion Batteries with Remarkable Cycling Performance. *Angew. Chemie* **125**, 2382–2386 (2013).
- [27] Leong, T. G. et al. Tetherless thermobiochemically actuated microgrippers. *Proc. Natl. Acad. Sci.* **106**, 703–708 (2009).
- [28] Lind, J. U. et al. Instrumented cardiac microphysiological devices via multimaterial three-dimensional printing. *Nat. Mater.* **16**, 303–308 (2017).
- [29] Li, J. et al. Development of a magnetic microrobot for carrying and delivering targeted cells. *Sci. Robot.* **3**, eaat8829 (2018).
- [30] Montemayor, L., Chernow, V. & Greer, J. R. Materials by design: Using architecture in material design to reach new property spaces. *MRS Bull.* **40**, 1122–1129 (2015).
- [31] Schaedler, T. A. & Carter, W. B. Architected Cellular Materials. *Annu. Rev. Mater. Res.* **46**, 187–210 (2016).
- [32] Walia, S. et al. Flexible metasurfaces and metamaterials: A review of materials and fabrication processes at micro- and nano-scales. *Appl. Phys. Rev.* **2**, 011303 (2015).
- [33] Valentine, J. et al. Three-dimensional optical metamaterial with a negative refractive index. *Nature* **455**, 376–379 (2008).
- [34] Gansel, J. K. et al. Gold Helix Photonic Metamaterial as Broadband Circular Polarizer. *Science (80-.)*. **325**, 1513–1515 (2009).
- [35] Ergin, T., Stenger, N., Brenner, P., Pendry, J. B. & Wegener, M. Three-Dimensional Invisibility Cloak at Optical Wavelengths. *Science (80-.)*. **328**, 337–339 (2010).

- [36] von Freymann, G. et al. Three-Dimensional Nanostructures for Photonics. *Adv. Funct. Mater.* **20**, 1038–1052 (2010).
- [37] Soukoulis, C. M. & Wegener, M. Past achievements and future challenges in the development of three-dimensional photonic metamaterials. *Nat. Photonics* **5**, 523–530 (2011).
- [38] Schaedler, T. A. et al. Ultralight Metallic Microlattices. *Science (80-.)*. **334**, 962–965 (2011).
- [39] Lee, J.-H., Singer, J. P. & Thomas, E. L. Micro-/Nanostructured Mechanical Metamaterials. *Adv. Mater.* **24**, 4782–4810 (2012).
- [40] Zheng, X. et al. Ultralight, ultrastiff mechanical metamaterials. *Science (80-.)*. **344**, 1373–1377 (2014).
- [41] Bückmann, T., Thiel, M., Kadic, M., Schittny, R. & Wegener, M. An elasto-mechanical unfeleability cloak made of pentamode metamaterials. *Nat. Commun.* **5**, 4130 (2014).
- [42] Christensen, J., Kadic, M., Kraft, O. & Wegener, M. Vibrant times for mechanical metamaterials. *MRS Commun.* **5**, 453–462 (2015).
- [43] Bauer, J., Schroer, A., Schwaiger, R. & Kraft, O. Approaching theoretical strength in glassy carbon nanolattices. *Nat. Mater.* **15**, 438–443 (2016).
- [44] Frenzel, T., Kadic, M. & Wegener, M. Three-dimensional mechanical metamaterials with a twist. *Science* **358**, 1072–1074 (2017).
- [45] Zhang, Y. et al. Printing, folding and assembly methods for forming 3D mesostructures in advanced materials. *Nat. Rev. Mater.* **2**, 17019 (2017).
- [46] Lewis, J. A. Direct Ink Writing of 3D Functional Materials. *Adv. Funct. Mater.* **16**, 2193–2204 (2006).
- [47] Hohmann, J. K., Renner, M., Waller, E. H. & von Freymann, G. Three-Dimensional μ -Printing: An Enabling Technology. *Adv. Opt. Mater.* **3**, 1488–1507 (2015).
- [48] Hirt, L., Reiser, A., Spolenak, R. & Zambelli, T. Additive Manufacturing of Metal Structures at the Micrometer Scale. *Adv. Mater.* **29**, 1604211 (2017).
- [49] Esposito, M. et al. Tailoring chiro-optical effects by helical nanowire arrangement. *Nanoscale* **7**, 18081–18088 (2015).

- [50] Jang, D., Meza, L. R., Greer, F. & Greer, J. R. Fabrication and deformation of three-dimensional hollow ceramic nanostructures. *Nat. Mater.* **12**, 893–898 (2013).
- [51] Gavagnin, M. et al. Free-Standing Magnetic Nanopillars for 3D Nanomagnet Logic. *ACS Appl. Mater. Interfaces* **6**, 20254–20260 (2014).
- [52] Luo, J. et al. Printing Functional 3D Microdevices by Laser-Induced Forward Transfer. *Small* **13**, 1602553 (2017).
- [53] Schürch, P., Pethö, L., Schwiedrzik, J., Michler, J. & Philippe, L. Additive Manufacturing through Galvanofarming of 3D Nickel Microarchitectures: Simulation-Assisted Synthesis. *Adv. Mater. Technol.* **1800274**, 1800274 (2018).
- [54] Lee, J.-S. et al. Design and evaluation of a silicon based multi-nozzle for addressable jetting using a controlled flow rate in electrohydrodynamic jet printing. *Appl. Phys. Lett.* **93**, 243114 (2008).
- [55] Post, P. C., Mohammadi-Gheidari, A., Hagen, C. W. & Kruit, P. Parallel electron-beam-induced deposition using a multi-beam scanning electron microscope. *J. Vac. Sci. Technol. B, Nanotechnol. Microelectron. Mater. Process. Meas. Phenom.* **29**, 06F310 (2011).
- [56] Auyeung, R. C. Y., Kim, H., Mathews, S. & Piqué, A. Spatially modulated laser pulses for printing electronics. *Appl. Opt.* **54**, F70 (2015).
- [57] Pan, Y., Chen, X., Zeng, L., Huang, Y. & Yin, Z. Fabrication and evaluation of a protruding Si-based printhead for electrohydrodynamic jet printing. *J. Micromechanics Microengineering* **27**, 125004 (2017).
- [58] Bos, F., Wolfs, R., Ahmed, Z. & Salet, T. Additive manufacturing of concrete in construction: potentials and challenges of 3D concrete printing. *Virtual Phys. Prototyp.* **11**, 1–17 (2016).
- [59] Frazier, W. E. Metal Additive Manufacturing: A Review. *J. Mater. Eng. Perform.* **23**, 1917–1928 (2014).
- [60] Herzog, D., Seyda, V., Wycisk, E. & Emmelmann, C. Additive manufacturing of metals. *Acta Mater.* **117**, 371–392 (2016).
- [61] Körner, C. Additive manufacturing of metallic components by selective electron beam melting — a review. *Int. Mater. Rev.* **61**, 361–377 (2016).

- [62] Murr, L. E. et al. Metal Fabrication by Additive Manufacturing Using Laser and Electron Beam Melting Technologies. *J. Mater. Sci. Technol.* **28**, 1–14 (2012).
- [63] Exner, H. et al. Laser micro sintering: A new method to generate metal and ceramic parts of high resolution with sub-micrometer powder. *Virtual Phys. Prototyp.* **3**, 3–11 (2008).
- [64] Vaezi, M., Seitz, H. & Yang, S. A review on 3D micro-additive manufacturing technologies. *Int. J. Adv. Manuf. Technol.* **67**, 1721–1754 (2013).
- [65] Sugioka, K. & Cheng, Y. Femtosecond laser three-dimensional micro- and nanofabrication. *Appl. Phys. Rev.* **1**, 041303 (2014).
- [66] Kaschke, J. & Wegener, M. Gold triple-helix mid-infrared metamaterial by STED-inspired laser lithography. *Opt. Lett.* **40**, 3986 (2015).
- [67] Zeeshan, M. A. et al. Hybrid Helical Magnetic Microrobots Obtained by 3D Template-Assisted Electrodeposition. *Small* **10**, 1284–1288 (2014).
- [68] Engstrom, D., Porter, B., Pacios, M. & Bhaskaran, H. Additive nanomanufacturing – a review. *J. Mater. Res.* **29**, 1792–1816 (2014).
- [69] Jesse, S. et al. Directing Matter: Toward Atomic-Scale 3D Nanofabrication. *ACS Nano* **10**, 5600–5618 (2016).
- [70] Bert Huis in 't Veld et al. Micro additive manufacturing using ultra short laser pulses. *CIRP Ann.* **64**, 701–724 (2015).
- [71] Onses, M. S., Sutanto, E., Ferreira, P. M., Alleyne, A. G. & Rogers, J. A. Mechanisms, Capabilities, and Applications of High-Resolution Electrohydrodynamic Jet Printing. *Small* **11**, 4237–4266 (2015).
- [72] Piqué, A., Auyeung, R. C. Y., Kim, H., Charipar, N. A. & Mathews, S. A. Laser 3D micro-manufacturing. *J. Phys. D: Appl. Phys.* **49**, 223001 (2016).
- [73] Utke, I., Hoffmann, P. & Melngailis, J. Gas-assisted focused electron beam and ion beam processing and fabrication. *J. Vac. Sci. Technol. B Microelectron. Nanom. Struct.* **26**, 1197 (2008).
- [74] Zhang, B., He, J., Li, X., Xu, F. & Li, D. Micro/nanoscale electrohydrodynamic printing: from 2D to 3D. *Nanoscale* **8**, 15376–15388 (2016).

- [75] Serra, P. & Piqué, A. Laser-Induced Forward Transfer: Fundamentals and Applications. *Adv. Mater. Technol.* **1800099**, 1800099 (2018).
- [76] Farahani, R. D., Chizari, K. & Therriault, D. Three-dimensional printing of freeform helical microstructures: a review. *Nanoscale* **6**, 10470 (2014).
- [77] Hossain, M. M. & Gu, M. Fabrication methods of 3D periodic metallic nano/microstructures for photonics applications. *Laser Photon. Rev.* **8**, 233–249 (2014).
- [78] Saile, V., Wallrabe, U., Tabata, O. & Korvink, J. G., editors. *LIGA and Its Applications*. Advanced Micro and Nanosystems (Wiley-VCH Verlag GmbH & Co. KGaA, Weinheim, Germany, 2008).
- [79] Wendy Gu, X. & Greer, J. R. Ultra-strong architected Cu meso-lattices. *Extrem. Mech. Lett.* **2**, 7–14 (2015).
- [80] Fischer, J. & Wegener, M. Three-dimensional optical laser lithography beyond the diffraction limit. *Laser Photon. Rev.* **7**, 22–44 (2013).
- [81] Kruter, W., Buerle, D. & Fimberger, F. Laser induced chemical vapor deposition of Ni by decomposition of Ni(CO)₄. *Appl. Phys. A Solids Surfaces* **31**, 13–18 (1983).
- [82] Toth, Z. et al. LCVD of tungsten microstructures on quartz. *Appl. Phys. B Photophysics Laser Chem.* **54**, 189–192 (1992).
- [83] Jansson, A., Thornell, G. & Johansson, S. High Resolution 3D Microstructures Made by Localized Electrodeposition of Nickel. *J. Electrochem. Soc.* **147**, 1810 (2000).
- [84] Ciou, Y.-j., Hwang, Y.-r., Lin, J.-c. & Tseng, Y.-t. Fabrication of 3D Microstructure by Localized Electrochemical Deposition with Image Feedback Distance Control and Five-Axis Motion Platform. *ECS J. Solid State Sci. Technol.* **5**, P425–P432 (2016).
- [85] Lin, J., Chang, T., Yang, J., Chen, Y. & Chuang, C. Localized electrochemical deposition of micrometer copper columns by pulse plating. *Electrochim. Acta* **55**, 1888–1894 (2010).
- [86] Madden, J. & Hunter, I. Three-dimensional microfabrication by localized electrochemical deposition. *J. Microelectromechanical Syst.* **5**, 24–32 (1996).
- [87] Said, R. A. Microfabrication by localized electrochemical deposition: experimental investigation and theoretical modelling. *Nanotechnology* **14**, 523–531 (2003).

- [88] Seol, S.-K., Pyun, A.-R., Hwu, Y., Margaritondo, G. & Je, J.-H. Localized Electrochemical Deposition of Copper Monitored Using Real-Time X-ray Microradiography. *Adv. Funct. Mater.* **15**, 934–937 (2005).
- [89] Bäuerle, D. *Laser Processing and Chemistry* (Springer Berlin Heidelberg, Berlin, Heidelberg, 2011), 4th edition.
- [90] Duty, C., Jean, D. & Lackey, W. Laser chemical vapour deposition: materials, modelling, and process control. *Int. Mater. Rev.* **46**, 271–287 (2001).
- [91] Maxwell, J. et al. Growth of normally-immiscible materials (NIMs), binary alloys, and metallic fibers by hyperbaric laser chemical vapor deposition. *Appl. Phys. A* **91**, 507–514 (2008).
- [92] Wanke, M. C. Laser Rapid Prototyping of Photonic Band-Gap Microstructures. *Science (80-.)*. **275**, 1284–1286 (1997).
- [93] Vyatskikh, A. et al. Additive manufacturing of 3D nano-architected metals. *Nat. Commun.* **9**, 593 (2018).
- [94] Oran, D. et al. 3D nanofabrication by volumetric deposition and controlled shrinkage of patterned scaffolds. *Science (80-.)*. **362**, 1281–1285 (2018).
- [95] Skylar-Scott, M. A., Gunasekaran, S. & Lewis, J. A. Laser-assisted direct ink writing of planar and 3D metal architectures. *Proc. Natl. Acad. Sci.* **113**, 6137–6142 (2016).
- [96] Breckenfeld, E. et al. Laser-induced forward transfer of silver nanopaste for microwave interconnects. *Appl. Surf. Sci.* **331**, 254–261 (2015).
- [97] Kaschke, J. & Wegener, M. Optical and Infrared Helical Metamaterials. *Nanophotonics* **0**, 38–51 (2016).
- [98] A. Lifton, V., Lifton, G. & Simon, S. Options for additive rapid prototyping methods (3D printing) in MEMS technology. *Rapid Prototyp. J.* **20**, 403–412 (2014).
- [99] Galliker, P. et al. Direct printing of nanostructures by electrostatic autofocussing of ink nanodroplets. *Nat. Commun.* **3**, 890 (2012).
- [100] Zhu, C. et al. Toward digitally controlled catalyst architectures: Hierarchical nanoporous gold via 3D printing. *Sci. Adv.* **4**, eaas9459 (2018).

-
- [101] Lewis, J. A., Smay, J. E., Stuecker, J. & Cesarano, J. Direct Ink Writing of Three-Dimensional Ceramic Structures. *J. Am. Ceram. Soc.* **89**, 3599–3609 (2006).
- [102] Park, J.-U. et al. High-resolution electrohydrodynamic jet printing. *Nat. Mater.* **6**, 782–789 (2007).
- [103] Lee, D., Hwang, E., Yu, T., Kim, Y. & Hwang, J. Structuring of micro line conductor using electro-hydrodynamic printing of a silver nanoparticle suspension. *Appl. Phys. A* **82**, 671–674 (2006).
- [104] An, B. W. et al. High-Resolution Printing of 3D Structures Using an Electrohydrodynamic Inkjet with Multiple Functional Inks. *Adv. Mater.* **27**, 4322–4328 (2015).
- [105] Richner, P. et al. Printable Nanoscopic Metamaterial Absorbers and Images with Diffraction-Limited Resolution. *ACS Appl. Mater. Interfaces* **8**, 11690–11697 (2016).
- [106] Panagiotakopoulou, M. et al. A Nanoprinted Model of Interstitial Cancer Migration Reveals a Link between Cell Deformability and Proliferation. *ACS Nano* **10**, 6437–6448 (2016).
- [107] Jaworek, A. & Krupa, A. CLASSIFICATION OF THE MODES OF EHD SPRAYING. *J. Aerosol Sci.* **30**, 873–893 (1999).
- [108] Jang, Y., Kim, J. & Byun, D. Invisible metal-grid transparent electrode prepared by electrohydrodynamic (EHD) jet printing. *J. Phys. D: Appl. Phys.* **46**, 155103 (2013).
- [109] Seong, B. et al. Metal-mesh based transparent electrode on a 3-D curved surface by electrohydrodynamic jet printing. *J. Micromechanics Microengineering* **24**, 097002 (2014).
- [110] Mishra, S., Barton, K. L., Alleyne, A. G., Ferreira, P. M. & Rogers, J. A. High-speed and drop-on-demand printing with a pulsed electrohydrodynamic jet. *J. Micromechanics Microengineering* **20**, 095026 (2010).
- [111] Schneider, J. et al. A novel 3D integrated platform for the high-resolution study of cell migration plasticity. *Macromol. Biosci.* **13**, 973–983 (2013).
- [112] Kress, S. J. P. et al. Wedge Waveguides and Resonators for Quantum Plasmonics. *Nano Lett.* **15**, 6267–6275 (2015).
- [113] Galliker, P., Schneider, J. & Poulidakos, D. Dielectrophoretic bending of directly printed free-standing ultra-soft nanowires. *Appl. Phys. Lett.* **104**, 073105 (2014).

- [114] Deng, W. & Gomez, A. The role of electric charge in microdroplets impacting on conducting surfaces. *Phys. Fluids* **22**, 051703 (2010).
- [115] Richner, P., Kress, S. J. P., Norris, D. J. & Poulidakos, D. Charge effects and nanoparticle pattern formation in electrohydrodynamic NanoDrip printing of colloids. *Nanoscale* **8**, 6028–6034 (2016).
- [116] Kress, S. J. P. et al. Near-Field Light Design with Colloidal Quantum Dots for Photonics and Plasmonics. *Nano Lett.* **14**, 5827–5833 (2014).
- [117] Kim, D. S. et al. Drop-on-Demand Direct Printing of Colloidal Copper Nanoparticles by Electrohydrodynamic Atomization. *Mater. Manuf. Process.* **26**, 1196–1201 (2011).
- [118] Rahman, K., Khan, A., Muhammad, N. M., Jo, J. & Choi, K.-H. Fine-resolution patterning of copper nanoparticles through electrohydrodynamic jet printing. *J. Micromechanics Microengineering* **22**, 065012 (2012).
- [119] Kang, D., Lee, M., Kim, H., James, S. & Yoon, S. Electrohydrodynamic pulsed-inkjet characteristics of various inks containing aluminum particles. *J. Aerosol Sci.* **42**, 621–630 (2011).
- [120] Lee, M. W. et al. Effects of pulsing frequency on characteristics of electrohydrodynamic inkjet using micro-Al and nano-Ag particles. *Exp. Therm. Fluid Sci.* **46**, 103–110 (2013).
- [121] Iwata, F. & Metoki, J. Microelectrophoresis deposition using a nanopipette for three-dimensional structures. In *2014 Int. Conf. Manip. Manuf. Meas. Nanoscale*, October, pages 304–307 (IEEE, 2014).
- [122] Takai, T., Nakao, H. & Iwata, F. Three-dimensional microfabrication using local electrophoresis deposition and a laser trapping technique. *Opt. Express* **22**, 28109 (2014).
- [123] Iwata, F., Kaji, M., Suzuki, A., Ito, S. & Nakao, H. Local electrophoresis deposition of nanomaterials assisted by a laser trapping technique. *Nanotechnology* **20**, 235303 (2009).
- [124] Bohandy, J., Kim, B. F. & Adrian, F. J. Metal deposition from a supported metal film using an excimer laser. *J. Appl. Phys.* **60**, 1538–1539 (1986).
- [125] Kuznetsov, A. I., Kiyan, R. & Chichkov, B. N. Laser fabrication of 2D and 3D metal nanoparticle structures and arrays. *Opt. Express* **18**, 21198 (2010).

-
- [126] Visser, C. W. et al. Toward 3D Printing of Pure Metals by Laser-Induced Forward Transfer. *Adv. Mater.* **27**, 4087–4092 (2015).
- [127] Zenou, M., Sa'ar, A. & Kotler, Z. Laser jetting of femto-liter metal droplets for high resolution 3D printed structures. *Sci. Rep.* **5**, 17265 (2015).
- [128] Zenou, M. & Kotler, Z. Printing of metallic 3D micro-objects by laser induced forward transfer. *Opt. Express* **24**, 1431 (2016).
- [129] Feinaeugle, M., Pohl, R., Bor, T., Vaneker, T. & Römer, G.-w. Printing of complex free-standing microstructures via laser-induced forward transfer (LIFT) of pure metal thin films. *Addit. Manuf.* **24**, 391–399 (2018).
- [130] Zenou, M., Sa'ar, A. & Kotler, Z. Laser Transfer of Metals and Metal Alloys for Digital Microfabrication of 3D Objects. *Small* **11**, 4082–4089 (2015).
- [131] Fogel, O., Cohen, S., Kotler, Z. & Zalevsky, Z. Mechanical properties of 3D metallic microstructures printed by laser induced forward transfer. *Procedia CIRP* **74**, 285–289 (2018).
- [132] Röder, T. C. & Köhler, J. R. Physical model for the laser induced forward transfer process. *Appl. Phys. Lett.* **100**, 071603 (2012).
- [133] Zenou, M., Sa'ar, A. & Kotler, Z. Digital laser printing of aluminum micro-structure on thermally sensitive substrates. *J. Phys. D. Appl. Phys.* **48**, 205303 (2015).
- [134] Zenou, M., Sa'ar, A. & Kotler, Z. Digital laser printing of metal/metal-oxide nanocomposites with tunable electrical properties. *Nanotechnology* **27**, 015203 (2016).
- [135] Winter, S., Zenou, M. & Kotler, Z. Conductivity of laser printed copper structures limited by nano-crystal grain size and amorphous metal droplet shell. *J. Phys. D. Appl. Phys.* **49**, 165310 (2016).
- [136] Piqué, A. Digital Microfabrication by Laser Decal Transfer. *J. Laser Micro/Nanoengineering* **3**, 163–169 (2008).
- [137] Mathews, S. A., Auyeung, R. C. Y., Kim, H., Charipar, N. A. & Piqué, A. High-speed video study of laser-induced forward transfer of silver nano-suspensions. *J. Appl. Phys.* **114**, 064910 (2013).

- [138] Piqué, A. et al. Laser transfer of reconfigurable patterns with a spatial light modulator. *Proc. SPIE* **8608**, 86080K–86080K–9 (2013).
- [139] Charipar, K. M. et al. Reusable laser-absorbing layers for LIFT. In G. Račiukaitis, T. Makimura & C. Molpeceres, editors, *Laser Appl. Microelectron. Optoelectron. Manuf. XXIV*, March, page 19 (SPIE, 2019).
- [140] Birnbaum, A. J., Wahl, K. J., Auyeung, R. C. Y. & Piqué, A. Nanoposity-induced effects on Ag-based metallic nano-inks for non-lithographic fabrication. *J. Micromechanics Microengineering* **20**, 077002 (2010).
- [141] Birnbaum, A. J. et al. Laser printed micron-scale free standing laminate composites: Process and properties. *J. Appl. Phys.* **108**, 1–7 (2010).
- [142] Birnbaum, A. J., Zalalutdinov, M. K., Wahl, K. J. & Pique, A. Fabrication and Response of Laser-Printed Cavity-Sealing Membranes. *J. Microelectromechanical Syst.* **20**, 436–440 (2011).
- [143] McKelvey, K., O’Connell, M. A. & Unwin, P. R. Meniscus confined fabrication of multidimensional conducting polymer nanostructures with scanning electrochemical cell microscopy (SECCM). *Chem. Commun.* **49**, 2986 (2013).
- [144] Seol, S. K. et al. Electrodeposition-based 3D Printing of Metallic Microarchitectures with Controlled Internal Structures. *Small* **11**, 3896–3902 (2015).
- [145] Suryavanshi, A. P. & Yu, M.-F. Probe-based electrochemical fabrication of freestanding Cu nanowire array. *Appl. Phys. Lett.* **88**, 083103 (2006).
- [146] Suryavanshi, A. P. & Yu, M.-F. Electrochemical fountain pen nanofabrication of vertically grown platinum nanowires. *Nanotechnology* **18**, 105305 (2007).
- [147] Lin, Y.-p., Zhang, Y. & Yu, M.-f. Parallel Process 3D Metal Microprinting. *Adv. Mater. Technol.* **4**, 1800393 (2019).
- [148] Behroozfar, A. et al. Microscale 3D Printing of Nanotwinned Copper. *Adv. Mater.* **30**, 1705107 (2018).
- [149] Daryadel, S., Behroozfar, A. & Minary-Jolandan, M. Toward Control of Microstructure in Microscale Additive Manufacturing of Copper Using Localized Electrodeposition. *Adv. Eng. Mater.* **21**, 1800946 (2019).

- [150] Morsali, S. et al. Multi-physics simulation of metal printing at micro/nanoscale using meniscus-confined electrodeposition: Effect of nozzle speed and diameter. *J. Appl. Phys.* **121**, 214305 (2017).
- [151] Morsali, S. et al. Multi-physics simulation of metal printing at micro/nanoscale using meniscus-confined electrodeposition: Effect of environmental humidity. *J. Appl. Phys.* **121**, 024903 (2017).
- [152] Daryadel, S. et al. Localized Pulsed Electrodeposition Process for Three-Dimensional Printing of Nanotwinned Metallic Nanostructures. *Nano Lett.* **18**, 208–214 (2018).
- [153] Iwata, F., Sumiya, Y. & Sasaki, A. Nanometer-Scale Metal Plating Using a Scanning Shear-Force Microscope with an Electrolyte-Filled Micropipette Probe. *Jpn. J. Appl. Phys.* **43**, 4482–4485 (2004).
- [154] Hirt, L. et al. Template-Free 3D Microprinting of Metals Using a Force-Controlled Nanopipette for Layer-by-Layer Electrodeposition. *Adv. Mater.* **28**, 2311–2315 (2016).
- [155] Momotenko, D., Page, A., Adobes-Vidal, M. & Unwin, P. R. Write–Read 3D Patterning with a Dual-Channel Nanopipette. *ACS Nano* **10**, 8871–8878 (2016).
- [156] <https://www.exaddon.com/> (2019).
- [157] Hirt, L. et al. Local surface modification via confined electrochemical deposition with FluidFM. *RSC Adv.* **5**, 84517–84522 (2015).
- [158] Meister, A. et al. FluidFM: Combining Atomic Force Microscopy and Nanofluidics in a Universal Liquid Delivery System for Single Cell Applications and Beyond. *Nano Lett.* **9**, 2501–2507 (2009).
- [159] Whitaker, J. D., Nelson, J. B. & Schwartz, D. T. Electrochemical printing: software reconfigurable electrochemical microfabrication. *J. Micromechanics Microengineering* **15**, 1498–1503 (2005).
- [160] Tanaka, T., Ishikawa, A. & Kawata, S. Two-photon-induced reduction of metal ions for fabricating three-dimensional electrically conductive metallic microstructure. *Appl. Phys. Lett.* **88**, 081107 (2006).
- [161] Fan, G. et al. Mechanism for the photoreduction of poly(vinylpyrrolidone) to HAuCl₄ and the dominating saturable absorption of Au colloids. *Phys. Chem. Chem. Phys.* **18**, 8993–9004 (2016).

- [162] Cao, Y.-Y., Takeyasu, N., Tanaka, T., Duan, X.-M. & Kawata, S. 3D Metallic Nanostructure Fabrication by Surfactant-Assisted Multiphoton-Induced Reduction. *Small* **5**, NA–NA (2009).
- [163] Ishikawa, A., Tanaka, T. & Kawata, S. Improvement in the reduction of silver ions in aqueous solution using two-photon sensitive dye. *Appl. Phys. Lett.* **89**, 113102 (2006).
- [164] Stellacci, F. et al. Laser and Electron-Beam Induced Growth of Nanoparticles for 2 D and 3 D Metal Patterning. *Adv. Mater.* **14**, 194–198 (2002).
- [165] Tanaka, T., Ishikawa, A. & Amemiya, T. Three-dimensional two-photon laser fabrication for metals, polymers, and magneto-optical materials. In H. Helvajian, A. Piqué, M. Wegener & B. Gu, editors, *Proc. SPIE 9353, Laser 3D Manuf. II*, volume 9353, page 93530M (2015).
- [166] Xu, B.-B. et al. Flexible Nanowiring of Metal on Nonplanar Substrates by Femtosecond-Laser-Induced Electroless Plating. *Small* **6**, 1762–1766 (2010).
- [167] Hu, Q. et al. Additive manufacture of complex 3D Au-containing nanocomposites by simultaneous two-photon polymerisation and photoreduction. *Sci. Rep.* **7**, 17150 (2017).
- [168] Lu, W.-E. et al. Femtosecond direct laser writing of gold nanostructures by ionic liquid assisted multiphoton photoreduction. *Opt. Mater. Express* **3**, 1660 (2013).
- [169] Xu, B.-B. et al. Fabrication of microelectrodes based on precursor doped with metal seeds by femtosecond laser direct writing. *Opt. Lett.* **39**, 434 (2014).
- [170] Kang, S., Vora, K. & Mazur, E. One-step direct-laser metal writing of sub-100 nm 3D silver nanostructures in a gelatin matrix. *Nanotechnology* **26**, 121001 (2015).
- [171] Vurth, L. et al. Two-photon induced fabrication of gold microstructures in polystyrene sulfonate thin films using a ruthenium(II) dye as photoinitiator. *Appl. Phys. Lett.* **92**, 171103 (2008).
- [172] Vora, K., Kang, S., Shukla, S. & Mazur, E. Fabrication of disconnected three-dimensional silver nanostructures in a polymer matrix. *Appl. Phys. Lett.* **100**, 16–19 (2012).
- [173] Vora, K., Kang, S., Shukla, S. & Mazur, E. Three-dimensional silver nanostructure fabrication through multiphoton photoreduction. In A. Heisterkamp, M. Meunier & S. Nolte, editors, *Front. Ultrafast Opt. Biomed. Sci. Ind. Appl. XII*, volume 8247, page 824710 (2012).

- [174] Maruo, S. & Saeki, T. Femtosecond laser direct writing of metallic microstructures by photoreduction of silver nitrate in a polymer matrix. *Opt. Express* **16**, 1174–1179 (2008).
- [175] Blasco, E. et al. Fabrication of Conductive 3D Gold-Containing Microstructures via Direct Laser Writing. *Adv. Mater.* **28**, 3592–3595 (2016).
- [176] Focsan, M., Craciun, A. M., Astilean, S. & Baldeck, P. L. Two-photon fabrication of three-dimensional silver microstructures in microfluidic channels for volumetric surface-enhanced Raman scattering detection. *Opt. Mater. Express* **6**, 1587 (2016).
- [177] Utke, I., Moshkalev, S. & Russell, P., editors. *Nanofabrication Using Focused Ion and Electron Beams* (Oxford University Press, Oxford, 2012).
- [178] Plank, H., Gspan, C., Dienstleder, M., Kothleitner, G. & Hofer, F. The influence of beam defocus on volume growth rates for electron beam induced platinum deposition. *Nanotechnology* **19**, 485302 (2008).
- [179] Guo, D., Kometani, R., Warisawa, S. & Ishihara, S. Growth of ultra-long free-space-nanowire by the real-time feedback control of the scanning speed on focused-ion-beam chemical vapor deposition. *J. Vac. Sci. Technol. B, Nanotechnol. Microelectron. Mater. Process. Meas. Phenom.* **31**, 061601 (2013).
- [180] Fowlkes, J. D. et al. Simulation-Guided 3D Nanomanufacturing via Focused Electron Beam Induced Deposition. *ACS Nano* **10**, 6163–6172 (2016).
- [181] Utke, I. et al. Focused electron beam induced deposition of gold. *J. Vac. Sci. Technol. B Microelectron. Nanom. Struct.* **18**, 3168 (2000).
- [182] Stanford, M. G., Lewis, B. B., Noh, J. H., Fowlkes, J. D. & Rack, P. D. Inert Gas Enhanced Laser-Assisted Purification of Platinum Electron-Beam-Induced Deposits. *ACS Appl. Mater. Interfaces* **7**, 19579–19588 (2015).
- [183] Tasco, V. et al. Three-dimensional nanohelices for chiral photonics. *Appl. Phys. A* **122**, 280 (2016).
- [184] Höflich, K., Yang, R. B., Berger, A., Leuchs, G. & Christiansen, S. The Direct Writing of Plasmonic Gold Nanostructures by Electron-Beam-Induced Deposition. *Adv. Mater.* **23**, 2657–2661 (2011).

- [185] Mohammadi-Gheidari, A., Hagen, C. W. & Kruit, P. Multibeam scanning electron microscope: Experimental results. *J. Vac. Sci. Technol. B Microelectron. Nanom. Struct.* **28**, C6G5 (2010).
- [186] Wieland, M. J. et al. Throughput enhancement technique for MAPPER maskless lithography. *Proc. SPIE* **7637**, 1–11 (2010).
- [187] Lukaszcyk, T., Schirmer, M., Steinrück, H.-P. & Marbach, H. Electron-Beam-Induced Deposition in Ultrahigh Vacuum: Lithographic Fabrication of Clean Iron Nanostructures. *Small* **4**, 841–846 (2008).
- [188] Luxmoore, I. et al. Low temperature electrical characterisation of tungsten nano-wires fabricated by electron and ion beam induced chemical vapour deposition. *Thin Solid Films* **515**, 6791–6797 (2007).
- [189] Blauner, P. G. Focused ion beam induced deposition of low-resistivity gold films. *J. Vac. Sci. Technol. B Microelectron. Nanom. Struct.* **7**, 1816 (1989).
- [190] Luisier, a. et al. Comparative Study of Cu Precursors for 3D Focused Electron Beam Induced Deposition. *J. Electrochem. Soc.* **151**, C535 (2004).
- [191] Xu, Z. An x-ray photoelectron spectroscopy study on ion beam induced deposition of tungsten using WF6. *J. Vac. Sci. Technol. B Microelectron. Nanom. Struct.* **7**, 1959 (1989).
- [192] Bret, T., Utke, I., Gaillard, C. & Hoffmann, P. Periodic structure formation by focused electron-beam-induced deposition. *J. Vac. Sci. Technol. B Microelectron. Nanom. Struct.* **22**, 2504 (2004).
- [193] Bret, T., Utke, I., Hoffmann, P., Abourida, M. & Doppelt, P. Electron range effects in focused electron beam induced deposition of 3D nanostructures. *Microelectron. Eng.* **83**, 1482–1486 (2006).
- [194] Rack, P. D., Fowlkes, J. D. & Randolph, S. J. In situ probing of the growth and morphology in electron-beam-induced deposited nanostructures. *Nanotechnology* **18**, 465602 (2007).
- [195] Fowlkes, J. D. et al. High-Fidelity 3D-Nanoprinting via Focused Electron Beams: Computer-Aided Design (3BID). *ACS Appl. Nano Mater.* **1**, 1028–1041 (2018).
- [196] Winkler, R., Lewis, B., Fowlkes, J., Rack, P. & Plank, H. High-Fidelity 3D-Nanoprinting via Focused Electron Beams: Growth Fundamentals. *ACS Appl. Nano Mater.* **1**, 1014–1027 (2018).

- [197] Belić, D. et al. Direct-Write Deposition and Focused-Electron-Beam-Induced Purification of Gold Nanostructures. *ACS Appl. Mater. Interfaces* **7**, 2467–2479 (2015).
- [198] Esposito, M. et al. Nanoscale 3D Chiral Plasmonic Helices with Circular Dichroism at Visible Frequencies. *ACS Photonics* **2**, 105–114 (2015).
- [199] Peinado, P., Sangiao, S. & De Teresa, J. M. Focused Electron and Ion Beam Induced Deposition on Flexible and Transparent Polycarbonate Substrates. *ACS Nano* **9**, 6139–6146 (2015).
- [200] Belova, L. M., Hellwig, O., Dobisz, E. & Dan Dahlberg, E. Rapid preparation of electron beam induced deposition Co magnetic force microscopy tips with 10 nm spatial resolution. *Rev. Sci. Instrum.* **83**, 093711 (2012).
- [201] Fernández-Pacheco, A. et al. Three dimensional magnetic nanowires grown by focused electron-beam induced deposition. *Sci. Rep.* **3**, 1492 (2013).
- [202] Shimojo, M., Mitsuishi, K., Tanaka, M., Han, M. & Furuya, K. Application of transmission electron microscopes to nanometre-sized fabrication by means of electron beam-induced deposition. *J. Microsc.* **214**, 76–79 (2004).
- [203] Kometani, R., Kanda, K., Haruyama, Y., Kaito, T. & Matsui, S. Evaluation of Field Electron Emitter Fabricated Using Focused-Ion-Beam Chemical Vapor Deposition. *Jpn. J. Appl. Phys.* **45**, L711–L713 (2006).
- [204] Morita, T. et al. Free-space-wiring fabrication in nano-space by focused-ion-beam chemical vapor deposition. *J. Vac. Sci. Technol. B Microelectron. Nanom. Struct.* **21**, 2737 (2003).
- [205] Igaki, J.-y. et al. Three-dimensional rotor fabrication by focused-ion-beam chemical-vapor-deposition. *Microelectron. Eng.* **83**, 1221–1224 (2006).
- [206] DeMarco, A. J. & Melngailis, J. Lateral growth of focused ion beam deposited platinum for stencil mask repair. *J. Vac. Sci. Technol. B Microelectron. Nanom. Struct.* **17**, 3154 (1999).
- [207] Bret, T., Utke, I. & Hoffmann, P. Influence of the beam scan direction during focused electron beam induced deposition of 3D nanostructures. *Microelectron. Eng.* **78-79**, 307–313 (2005).
- [208] Arnold, G. et al. Fundamental Resolution Limits during Electron-Induced Direct-Write Synthesis. *ACS Appl. Mater. Interfaces* **6**, 7380–7387 (2014).

- [209] Silvis-Cividjian, N., Hagen, C. W. & Kruit, P. Spatial resolution limits in electron-beam-induced deposition. *J. Appl. Phys.* **98**, 084905 (2005).
- [210] van Dorp, W. F., van Someren, B., Hagen, C. W., Kruit, P. & Crozier, P. A. Approaching the Resolution Limit of Nanometer-Scale Electron Beam-Induced Deposition. *Nano Lett.* **5**, 1303–1307 (2005).
- [211] Henry, M. R., Kim, S., Rykaczewski, K. & Fedorov, A. G. Inert gas jets for growth control in electron beam induced deposition. *Appl. Phys. Lett.* **98**, 263109 (2011).
- [212] Henry, M. R., Kim, S. & Fedorov, A. G. High Purity Tungsten Nanostructures via Focused Electron Beam Induced Deposition with Carrier Gas Assisted Supersonic Jet Delivery of Organometallic Precursors. *J. Phys. Chem. C* **120**, 10584–10590 (2016).
- [213] Perentes, A., Sinicco, G., Boero, G., Dwir, B. & Hoffmann, P. Focused electron beam induced deposition of nickel. *J. Vac. Sci. Technol. B Microelectron. Nanom. Struct.* **25**, 2228 (2007).
- [214] Rotkina, L., Lin, J.-F. & Bird, J. P. Nonlinear current-voltage characteristics of Pt nanowires and nanowire transistors fabricated by electron-beam deposition. *Appl. Phys. Lett.* **83**, 4426–4428 (2003).
- [215] Friedli, V., Utke, I., Mølhave, K. & Michler, J. Dose and energy dependence of mechanical properties of focused electron-beam-induced pillar deposits from Cu(C 5 HF 6 O 2) 2. *Nanotechnology* **20**, 385304 (2009).
- [216] Botman, A., Mulders, J. J. L. & Hagen, C. W. Creating pure nanostructures from electron-beam-induced deposition using purification techniques: a technology perspective. *Nanotechnology* **20**, 372001 (2009).
- [217] Rajagopalan, M., Bhatia, M., Tschopp, M., Srolovitz, D. & Solanki, K. Atomic-scale analysis of liquid-gallium embrittlement of aluminum grain boundaries. *Acta Mater.* **73**, 312–325 (2014).
- [218] Brintlinger, T. et al. Electrodes for carbon nanotube devices by focused electron beam induced deposition of gold. *J. Vac. Sci. Technol. B Microelectron. Nanom. Struct.* **23**, 3174 (2005).
- [219] Botman, A., Mulders, J. J. L., Weemaes, R. & Mentink, S. Purification of platinum and gold structures after electron-beam-induced deposition. *Nanotechnology* **17**, 3779–3785 (2006).

- [220] Gazzadi, G. C. et al. Focused Electron Beam Deposition of Nanowires from Cobalt Tricarbonyl Nitrosyl (Co(CO)₃NO) Precursor. *J. Phys. Chem. C* **115**, 19606–19611 (2011).
- [221] Riazanova, A. V., Rikers, Y. G. M., Mulders, J. J. L. & Belova, L. M. Pattern Shape Control for Heat Treatment Purification of Electron-Beam-Induced Deposition of Gold from the Me₂Au(acac) Precursor. *Langmuir* **28**, 6185–6191 (2012).
- [222] Begun, E. et al. Post-growth purification of Co nanostructures prepared by focused electron beam induced deposition. *Nanotechnology* **26**, 075301 (2015).
- [223] Geier, B. et al. Rapid and Highly Compact Purification for Focused Electron Beam Induced Deposits: A Low Temperature Approach Using Electron Stimulated H₂O Reactions. *J. Phys. Chem. C* **118**, 14009–14016 (2014).
- [224] Miyazoe, H. et al. Improving the metallic content of focused electron beam-induced deposits by a scanning electron microscope integrated hydrogen-argon microplasma generator. *J. Vac. Sci. Technol. B, Nanotechnol. Microelectron. Mater. Process. Meas. Phenom.* **28**, 744–750 (2010).
- [225] Lewis, B. B. et al. Electron-stimulated purification of platinum nanostructures grown via focused electron beam induced deposition. *Beilstein J. Nanotechnol.* **6**, 907–918 (2015).
- [226] Wu, H. et al. Focused helium ion beam deposited low resistivity cobalt metal lines with 10 nm resolution: implications for advanced circuit editing. *J. Mater. Sci. Mater. Electron.* **25**, 587–595 (2014).
- [227] Winhold, M. et al. Binary Pt–Si Nanostructures Prepared by Focused Electron-Beam-Induced Deposition. *ACS Nano* **5**, 9675–9681 (2011).
- [228] Porrati, F., Kämpken, B., Terfort, A. & Huth, M. Fabrication and electrical transport properties of binary Co–Si nanostructures prepared by focused electron beam-induced deposition. *J. Appl. Phys.* **113**, 053707 (2013).
- [229] Porrati, F. et al. Room temperature L1₀ phase transformation in binary CoPt nanostructures prepared by focused-electron-beam-induced deposition. *Nanotechnology* **23**, 185702 (2012).
- [230] Porrati, F., Sachser, R., Gazzadi, G. C., Frabboni, S. & Huth, M. Fabrication of FeSi and Fe₃Si compounds by electron beam induced mixing of [Fe/Si]₂ and [Fe₃/Si]₂ multilayers grown by focused electron beam induced deposition. *J. Appl. Phys.* **119**, 234306 (2016).

- [231] Koops, H. et al. Two-dimensional photonic crystals produced by additive nanolithography with electron beam-induced deposition act as filters in the infrared. *Microelectron. Eng.* **57-58**, 995–1001 (2001).
- [232] George, H. C., Orlova, T. a., Orlov, A. O. & Snider, G. L. Novel method for fabrication of nanoscale single-electron transistors: Electron beam induced deposition of Pt and atomic layer deposition of tunnel barriers. *J. Vac. Sci. Technol. B, Nanotechnol. Microelectron. Mater. Process. Meas. Phenom.* **29**, 06FB01 (2011).
- [233] Murakami, K. & Takai, M. Nano electron source fabricated by beam-induced deposition and its unique feature. *Microelectron. Eng.* **132**, 74–82 (2015).
- [234] Bresin, M., Thiel, B., Toth, M. & Dunn, K. Focused electron beam-induced deposition at cryogenic temperatures. *J. Mater. Res.* **26**, 357–364 (2011).
- [235] Bresin, M., Toth, M. & Dunn, K. A. Direct-write 3D nanolithography at cryogenic temperatures. *Nanotechnology* **24**, 035301 (2013).
- [236] Fisher, J. S., Kottke, P. A., Kim, S. & Fedorov, A. G. Rapid Electron Beam Writing of Topologically Complex 3D Nanostructures Using Liquid Phase Precursor. *Nano Lett.* **15**, 8385–8391 (2015).
- [237] Nassaralla, C. Pyrometallurgy. In W. Dennis, editor, *Encycl. Mater. Sci. Technol.*, pages 7938–7941 (Elsevier, 2001).
- [238] L'vov, B. V. Mechanism of carbothermal reduction of iron, cobalt, nickel and copper oxides. *Thermochim. Acta* **360**, 109–120 (2000).
- [239] No Title.
- [240] Matsui, S. et al. Three-dimensional nanostructure fabrication by focused-ion-beam chemical vapor deposition. *J. Vac. Sci. Technol. B Microelectron. Nanom. Struct.* **18**, 3181 (2000).
- [241] Hagen, C. W. The future of focused electron beam-induced processing. *Appl. Phys. A* **117**, 1599–1605 (2014).
- [242] van Oven, J. C., Berwald, F., Berggren, K. K., Kruit, P. & Hagen, C. W. Electron-beam-induced deposition of 3-nm-half-pitch patterns on bulk Si. *J. Vac. Sci. Technol. B Microelectron. Nanom. Struct.* **29**, 06F305 (2011).

- [243] Bruckl, H., Kretz, J., Koops, H. W. & Reiss, G. Low energy electron beam decomposition of metalorganic precursors with a scanning tunneling microscope at ambient atmosphere. *J. Vac. Sci. Technol. B Microelectron. Nanom. Struct.* **17**, 1350 (1999).
- [244] Kent, A. D., Shaw, T. M., von Molnar, S. & Awschalom, D. D. Growth of High Aspect Ratio Nanometer-Scale Magnets with Chemical Vapor Deposition and Scanning Tunneling Microscopy. *Science (80-.)*. **262**, 1249–1252 (1993).
- [245] Pai, W. W. Magnetic nanostructures fabricated by scanning tunneling microscope-assisted chemical vapor deposition. *J. Vac. Sci. Technol. B Microelectron. Nanom. Struct.* **15**, 785 (1997).
- [246] Vasko, S. E. et al. High-field chemistry of organometallic precursors for direct-write of germanium and silicon nanostructures. *J. Mater. Chem. C* **1**, 282–289 (2013).
- [247] Ye, W. et al. Direct Writing of Sub-5 nm Hafnium Diboride Metallic Nanostructures. *ACS Nano* **4**, 6818–6824 (2010).
- [248] Actis, P. et al. Electrochemical Nanoprobes for Single-Cell Analysis. *ACS Nano* **8**, 875–884 (2014).
- [249] Maragò, O. M., Jones, P. H., Gucciardi, P. G., Volpe, G. & Ferrari, A. C. Optical trapping and manipulation of nanostructures. *Nat. Nanotechnol.* **8**, 807–819 (2013).
- [250] Mirkin, C. A. The Power of the Pen: Development of Massively Parallel Dip-Pen Nanolithography. *ACS Nano* **1**, 79–83 (2007).
- [251] Barnes, H. A. Thixotropy—a review. *J. Nonnewton. Fluid Mech.* **70**, 1–33 (1997).
- [252] Grier, D. G. A revolution in optical manipulation. *Nature* **424**, 810–6 (2003).
- [253] Doremus, R. H. Optical Properties of Small Gold Particles. *J. Chem. Phys.* **40**, 2389–2396 (1964).
- [254] He, Y. Q., Liu, S. P. P., Kong, L. & Liu, Z. F. A study on the sizes and concentrations of gold nanoparticles by spectra of absorption, resonance Rayleigh scattering and resonance non-linear scattering. *Spectrochim. Acta Part A Mol. Biomol. Spectrosc.* **61**, 2861–2866 (2005).

- [255] Tong, L., Righini, M., Gonzalez, M. U., Quidant, R. & Käll, M. Optical aggregation of metal nanoparticles in a microfluidic channel for surface-enhanced Raman scattering analysis. *Lab Chip* **9**, 193–195 (2009).
- [256] von Gutfeld, R. J., Tynan, E. E., Melcher, R. L. & Blum, S. E. Laser enhanced electroplating and maskless pattern generation. *Appl. Phys. Lett.* **35**, 651–653 (1979).
- [257] Bockris, J. & Reddy, A. *Modern Electrochemistry, Volume 1*, volume 1 (Kluwer Academic Publishers, New York, 2002), 2nd edition.
- [258] Hinatsu, J. T. Diffusion Coefficients for Copper (II) in Aqueous Cupric Sulfate-Sulfuric Acid Solutions. *J. Electrochem. Soc.* **136**, 125 (1989).
- [259] Quickenden, T. I. Toward a Reliable Value for the Diffusion Coefficient of Cupric Ion in Aqueous Solution. *J. Electrochem. Soc.* **143**, 1248 (1996).
- [260] Moats, M. S., Hiskey, J. & Collins, D. W. The effect of copper, acid, and temperature on the diffusion coefficient of cupric ions in simulated electrorefining electrolytes. *Hydrometallurgy* **56**, 255–268 (2000).
- [261] Gladysz, O., Los, P. & Krzyzak, E. Influence of concentrations of copper, levelling agents and temperature on the diffusion coefficient of cupric ions in industrial electro-refining electrolytes. *J. Appl. Electrochem.* **37**, 1093–1097 (2007).
- [262] Bockris, J. O., Reddy, A. K. N. & Gamboa-Aldeco, M. *Modern Electrochemistry, Volume 2A*, volume 2 (Kluwer Academic Publishers, New York, 2002), 2nd edition.
- [263] Turner, D. R. Modern techniques for electroplating gold contacts. *Thin Solid Films* **95**, 143–149 (1982).
- [264] Walker, C. & Walker, R. Effect of ultrasonic agitation on some properties of electrodeposits. *Electrodepos. Surf. Treat.* **1**, 457–469 (1973).
- [265] Alkire, R. C. High-Speed Selective Electroplating with Single Circular Jets. *J. Electrochem. Soc.* **129**, 2424 (1982).
- [266] von Gutfeld, R. J., Gelchinski, M. H., Romankiw, L. T. & Vigliotti, D. R. Laser-enhanced jet plating: A method of high-speed maskless patterning. *Appl. Phys. Lett.* **43**, 876–878 (1983).

- [267] Schiller, S. & Panzer, S. Thermal surface modification by electron beam high-speed scanning. *Surf. Coatings Technol.* **39-40**, 521–529 (1989).
- [268] Madou J., M. *Fundamentals of microfabrication: The science of miniaturization* (CRC Press, New York, 2002), 2nd edition.
- [269] Lindroos, V., Tilli, M., Lehto, A. & Motooka, T. *Handbook of Silicon Based MEMS Materials and Technologies* (William Andrew Publishing, Boston, 2010).
- [270] Bensebaa, F. Wet Production Methods. In *Interface Sci. Technol.*, volume 19, pages 85–146 (Elsevier B.V., 2013).
- [271] Cushing, B. L., Kolesnichenko, V. L. & O'Connor, C. J. Recent Advances in the Liquid-Phase Syntheses of Inorganic Nanoparticles. *Chem. Rev.* **104**, 3893–3946 (2004).
- [272] Dong, H., Chen, Y.-C. & Feldmann, C. Polyol synthesis of nanoparticles: status and options regarding metals, oxides, chalcogenides, and non-metal elements. *Green Chem.* **17**, 4107–4132 (2015).
- [273] Ohring, M. Front Matter. In *Mater. Sci. Thin Film.*, page iii (Elsevier, 2002), 2 edition.
- [274] Abbott, A. P., Dalrymple, I., Endres, F. & Macfarlane, D. R. Why use Ionic Liquids for Electrodeposition? In *Electrodepos. from Ion. Liq.*, volume 01, pages 1–13 (Wiley-VCH Verlag GmbH & Co. KGaA, Weinheim, Germany, 2008).
- [275] Schwartz, M. Deposition from aqueous solutions: an overview. *Handb. Depos. Technol. Film. ...* pages 506–616 (1994).
- [276] Oster, G. K. & Oster, G. Photoreduction of Metal Ions by Visible Light 1. *J. Am. Chem. Soc.* **81**, 5543–5545 (1959).
- [277] Sakamoto, M., Fujistuka, M. & Majima, T. Light as a construction tool of metal nanoparticles: Synthesis and mechanism. *J. Photochem. Photobiol. C Photochem. Rev.* **10**, 33–56 (2009).
- [278] Pierson, H. O. The CVD of Metals (1999).
- [279] Pierson, H. O. Metallo-Organic CVD (MOCVD). In *Handb. Chem. Vap. Depos.*, pages 84–107 (Elsevier, 1999).

- [280] Kodas, T. T. & Hampden-Smith, M. J. Overview of Metal CVD. In *Chem. Met. CVD*, pages 429–498 (Wiley-VCH Verlag GmbH, Weinheim, Germany, 2007).
- [281] Gas injection system, Kleindiek (2016).
- [282] Modular gas injection system, Alemnis (2016).
- [283] Richner, P. et al. Full-Spectrum Flexible Color Printing at the Diffraction Limit. *ACS Photonics* **3**, 754–757 (2016).
- [284] Jakus, A. E., Taylor, S. L., Geisendorfer, N. R., Dunand, D. C. & Shah, R. N. Metallic Architectures from 3D-Printed Powder-Based Liquid Inks. *Adv. Funct. Mater.* **25**, 6985–6995 (2015).
- [285] Röthlisberger, A., Häberli, S., Spolenak, R. & Dunand, D. C. Synthesis, structure and mechanical properties of ice-templated tungsten foams. *J. Mater. Res.* **31**, 753–764 (2016).
- [286] Lassner, E. & Schubert, W.-D. The Element Tungsten. In *Tungsten*, pages 1–59 (Springer US, Boston, MA, 1999).
- [287] Tóth, Z., Szörényi, T. & Tóth, A. Ar⁺ laser-induced forward transfer (LIFT): a novel method for micrometer-size surface patterning. *Appl. Surf. Sci.* **69**, 317–320 (1993).
- [288] Doraiswamy, A. et al. Excimer laser forward transfer of mammalian cells using a novel triazene absorbing layer. *Appl. Surf. Sci.* **252**, 4743–4747 (2006).
- [289] Birnbaum, A. J., Kim, H., Charipar, N. A. & Piqué, A. Laser printing of multi-layered polymer/metal heterostructures for electronic and MEMS devices. *Appl. Phys. A* **99**, 711–716 (2010).
- [290] Qin, D. et al. Microfabrication, Microstructures and Microsystems. In *Microsyst. Technol. Chem. Life Sci.*, volume 194, pages 1–20 (Springer, Berlin, Heidelberg, 1998).
- [291] McLachlan, D. S., Blaszkiwicz, M. & Newnham, R. E. Electrical Resistivity of Composites. *J. Am. Ceram. Soc.* **73**, 2187–2203 (1990).
- [292] Chookajorn, T., Murdoch, H. a. & Schuh, C. a. Design of Stable Nanocrystalline Alloys. *Science (80-.)*, **337**, 951–954 (2012).
- [293] Trelewicz, J. R. & Schuh, C. A. Grain boundary segregation and thermodynamically stable binary nanocrystalline alloys. *Phys. Rev. B* **79**, 094112 (2009).

- [294] Seol, S. K., Kim, J. T., Je, J. H., Hwu, Y. & Margaritondo, G. Fabrication of Freestanding Metallic Micro Hollow Tubes by Template-Free Localized Electrochemical Deposition. *Electrochem. Solid-State Lett.* **10**, C44 (2007).
- [295] Chang, S.-Y. & Chang, T.-K. Grain size effect on nanomechanical properties and deformation behavior of copper under nanoindentation test. *J. Appl. Phys.* **101**, 033507 (2007).
- [296] Pané, S. et al. The effect of saccharine on the localized electrochemical deposition of Cu-rich Cu–Ni microcolumns. *Electrochem. commun.* **13**, 973–976 (2011).
- [297] Schaedler, T. A., Jacobsen, A. J. & Carter, W. B. Toward Lighter, Stiffer Materials. *Science (80-.)*. **341**, 1181–1182 (2013).
- [298] Lopes, A. J., MacDonald, E. & Wicker, R. B. Integrating stereolithography and direct print technologies for 3D structural electronics fabrication. *Rapid Prototyp. J.* **18**, 129–143 (2012).
- [299] Sarobol, P. et al. Additive Manufacturing of Hybrid Circuits. *Annu. Rev. Mater. Res.* **46**, 41–62 (2016).
- [300] Merlijn van Spengen, W. MEMS reliability from a failure mechanisms perspective. *Microelectron. Reliab.* **43**, 1049–1060 (2003).
- [301] Brown, E. R. RF-MEMS switches for reconfigurable integrated circuits. *IEEE Trans. Microw. Theory Tech.* **46**, 1868–1880 (1998).
- [302] Douglass, M. Lifetime estimates and unique failure mechanisms of the Digital Micromirror Device (DMD). In *1998 IEEE Int. Reliab. Phys. Symp. Proc. 36th Annu. (Cat No 98CH36173) RELPHY-98*, Dmd, pages 9–16 (IEEE, 1998).
- [303] Yi, Z. et al. Vertical, capacitive microelectromechanical switches produced via direct writing of copper wires. *Microsystems Nanoeng.* **2**, 16010 (2016).
- [304] Greer, J. R. & Street, R. A. Mechanical characterization of solution-derived nanoparticle silver ink thin films. *J. Appl. Phys.* **101** (2007).
- [305] Lee, D. J. & Oh, J. H. Inkjet printing of conductive Ag lines and their electrical and mechanical characterization. *Thin Solid Films* **518**, 6352–6356 (2010).
- [306] Dou, R., Xu, B. & Derby, B. High-strength nanoporous silver produced by inkjet printing. *Scr. Mater.* **63**, 308–311 (2010).

- [307] Utke, I. et al. Tensile strengths of metal-containing joints fabricated by focused electron beam induced deposition. *Adv. Eng. Mater.* **8**, 155–157 (2006).
- [308] Ding, W. et al. Mechanics of hydrogenated amorphous carbon deposits from electron-beam-induced deposition of a paraffin precursor. *J. Appl. Phys.* **98**, 014905 (2005).
- [309] Wich, T. Nanostructuring and Nanobonding by EBID. In S. Fatikow, editor, *Autom. Nanohandling by Microrobots*, pages 295–340 (Springer London, London, 2008).
- [310] Lee, S. et al. Three-dimensional Printing of Silver Microarchitectures Using Newtonian Nanoparticle Inks. *ACS Appl. Mater. Interfaces* **9**, 18918–18924 (2017).
- [311] Reiser, A. et al. Multi-metal electrohydrodynamic redox 3D printing at the submicron scale. *Nat. Commun.* **10**, 1853 (2019).
- [312] Zheng, N., Fan, J. & Stucky, G. D. One-step one-phase synthesis of monodisperse noble-metallic nanoparticles and their colloidal crystals. *J. Am. Chem. Soc.* **128**, 6550–6551 (2006).
- [313] Charipar, K. M., Diaz-Rivera, R. E., Charipar, N. A. & Piqué, A. Laser-induced forward transfer (LIFT) of 3D microstructures. In H. Helvajian, A. Piqué & B. Gu, editors, *Laser 3D Manuf. V*, February 2018, page 29 (SPIE, 2018).
- [314] Wheeler, J. M. & Michler, J. Elevated temperature, nano-mechanical testing in situ in the scanning electron microscope. *Rev. Sci. Instrum.* **84**, 045103 (2013).
- [315] Köster, W. & Franz, H. Poisson's ratio for metals and alloys. *Metall. Rev.* **6**, 1–56 (1961).
- [316] Maier, V. et al. Nanoindentation strain-rate jump tests for determining the local strain-rate sensitivity in nanocrystalline Ni and ultrafine-grained Al. *J. Mater. Res.* **26**, 1421–1430 (2011).
- [317] Leitner, A., Maier-Kiener, V. & Kiener, D. Extraction of Flow Behavior and Hall-Petch Parameters Using a Nanoindentation Multiple Sharp Tip Approach. *Adv. Eng. Mater.* **19**, 1600669 (2017).
- [318] Sneddon, I. N. The relation between load and penetration in the axisymmetric boussinesq problem for a punch of arbitrary profile. *Int. J. Eng. Sci.* **3**, 47–57 (1965).
- [319] Mencik, J. & Swain, M. V. Mechanical Properties of Platinum Films on Silicon and Glass Determined by Ultra-Microindentation. *MRS Proc.* **356**, 729 (1994).

- [320] Mall, S., Lee, H., Leedy, K. D. & Coutu, R. A. Interrelationship Between Hardness and Resistivity of Metal Alloy Films as Contact Materials in MEMS Switches. In *Part B Magn. Storage Tribol. Manuf. Tribol. Nanotribology; Eng. Surfaces; Biotribology; Emerg. Technol. Spec. Symp. Contact Mech. Spec. Symp. Nanotribology*, pages 1377–1378 (ASME, 2006).
- [321] Zhang, Z., Chen, D., Han, W. & Kimura, A. Irradiation hardening in pure tungsten before and after recrystallization. *Fusion Eng. Des.* **98-99**, 2103–2107 (2015).
- [322] Abadias, G., Dub, S. & Shmegeera, R. Nanoindentation hardness and structure of ion beam sputtered TiN, W and TiN/W multilayer hard coatings. *Surf. Coatings Technol.* **200**, 6538–6543 (2006).
- [323] Shugurov, A., Panin, A., Hui-Gon, C. & Oskomov, K. Size effects on the mechanical properties of thin metallic films studied by nanoindentation. *Sci. Technol. 2004. KORUS 2004. Proceedings. 8th Russ. Int. Symp.* **3**, 168–172 vol. 3 (2004).
- [324] Panin, A., Shugurov, A. & Oskomov, K. Mechanical properties of thin Ag films on a silicon substrate studied using the nanoindentation technique. *Phys. Solid State* **47**, 2055–2059 (2005).
- [325] Okuda, S., Kobiyama, M. & Inami, T. Mechanical Properties and Thermal Stability of Nanocrystalline Gold Prepared by Gas Deposition Method. *Mater. Trans. JIM* **40**, 412–415 (1999).
- [326] Volinsky, A. A., Moody, N. R. & Gerberich, W. W. Nanoindentation of Au and Pt/Cu thin films at elevated temperatures. *J. Mater. Res.* **19**, 2650–2657 (2004).
- [327] Beegan, D., Chowdhury, S. & Laugier, M. T. A nanoindentation study of copper films on oxidised silicon substrates. *Surf. Coatings Technol.* **176**, 124–130 (2003).
- [328] Lu, L. et al. Nano-sized twins induce high rate sensitivity of flow stress in pure copper. *Acta Mater.* **53**, 2169–2179 (2005).
- [329] Beegan, D., Chowdhury, S. & Laugier, M. T. Comparison between nanoindentation and scratch test hardness (scratch hardness) values of copper thin films on oxidised silicon substrates. *Surf. Coatings Technol.* **201**, 5804–5808 (2007).

- [330] Nili, H., Walia, S., Bhaskaran, M. & Sriram, S. Nanoscale electro-mechanical dynamics of nano-crystalline platinum thin films: An in situ electrical nanoindentation study. *J. Appl. Phys.* **116**, 163504 (2014).
- [331] Song, C., Wang, P. & Makse, H. a. A phase diagram for jammed matter. *Nature* **453**, 629–632 (2008).
- [332] Podsiadlo, P. et al. The role of order, nanocrystal size, and capping ligands in the collective mechanical response of three-dimensional nanocrystal solids. *J. Am. Chem. Soc.* **132**, 8953–8960 (2010).
- [333] Yan, C., Arfaoui, I., Goubet, N. & Pileni, M. P. Soft supracrystals of Au nanocrystals with tunable mechanical properties. *Adv. Funct. Mater.* **23**, 2315–2321 (2013).
- [334] Hashin, Z. Analysis of Composite Materials—A Survey. *J. Appl. Mech.* **50**, 481 (1983).
- [335] Roberts, A. P. & Garboczi, E. J. Elastic properties of model porous ceramics. *J. Am. Ceram. Soc.* **83**, 3041–3048 (2000).
- [336] Hodge, A. M. et al. Scaling equation for yield strength of nanoporous open-cell foams. *Acta Mater.* **55**, 1343–1349 (2007).
- [337] Taylor, S. L., Jakus, A. E., Shah, R. N. & Dunand, D. C. Iron and Nickel Cellular Structures by Sintering of 3D-Printed Oxide or Metallic Particle Inks. *Adv. Eng. Mater.* (2016).
- [338] Calvo, M., Jakus, A. E., Shah, R. N., Spolenak, R. & Dunand, D. C. Microstructure and Processing of 3D Printed Tungsten Microlattices and Infiltrated W-Cu Composites. *Adv. Eng. Mater.* **20**, 1800354 (2018).
- [339] Kenel, C., Casati, N. P. M. & Dunand, D. C. 3D ink-extrusion additive manufacturing of CoCrFeNi high-entropy alloy micro-lattices. *Nat. Commun.* **10**, 904 (2019).
- [340] Huth, M., Porrati, F. & Dobrovolskiy, O. Focused electron beam induced deposition meets materials science. *Microelectron. Eng.* **185-186**, 9–28 (2018).
- [341] Jiang, X., Reichelt, K. & Stritzker, B. The hardness and Young's modulus of amorphous hydrogenated carbon and silicon films measured with an ultralow load indenter. *J. Appl. Phys.* **66**, 5805–5808 (1989).
- [342] Weiler, M. et al. Preparation and properties of highly tetrahedral hydrogenated amorphous carbon. *Phys. Rev. B* **53**, 1594–1608 (1996).

- [343] Cho, S., Chasiotis, I., Friedmann, T. A. & Sullivan, J. P. Young's modulus, Poisson's ratio and failure properties of tetrahedral amorphous diamond-like carbon for MEMS devices. *J. Micromechanics Microengineering* **15**, 728–735 (2005).
- [344] Van Berkel, G. J. & Kertesz, V. Redox buffering in an electrospray ion source using a copper capillary emitter. *J. Mass Spectrom.* **36**, 1125–1132 (2001).
- [345] Rohner, T. C. & Girault, H. H. Study of peptide on-line complexation with transition-metal ions generated from sacrificial electrodes in thin-chip polymer microsprays. *Rapid Commun. Mass Spectrom.* **19**, 1183–1190 (2005).
- [346] Al-Abdallah, M. & Al-Omari, M. Anodic behaviour of cobalt in methanol-, ethanol- and acetonitrile-water in the presence of HCl and NaClO₄. *Anti-Corrosion Methods Mater.* **37**, 4–11 (1990).
- [347] Levitin, G., Tel-Vered, R., Yarnitzky, C. & Licht, S. Analytical Determination of Water Effects on the Anodic Dissolution of Aluminum in Nonaqueous Electrolytes. *Rev. Anal. Chem.* **19**, 329–333 (2000).
- [348] Licht, S., Tel-Vered, R., Levitin, G. & Yarnitzky, C. Solution Activators of Aluminum Electrochemistry in Organic Media. *J. Electrochem. Soc.* **147**, 496 (2000).
- [349] Bechelany, M., Elias, J., Brodard, P., Michler, J. & Philippe, L. Electrodeposition of amorphous silicon in non-oxygenated organic solvent. *Thin Solid Films* **520**, 1895–1901 (2012).
- [350] Zeleny, J. The Electrical Discharge from Liquid Points, and a Hydrostatic Method of Measuring the Electric Intensity at Their Surfaces. *Phys. Rev.* **3**, 69–91 (1914).
- [351] Park, J.-U. et al. Nanoscale, Electrified Liquid Jets for High-Resolution Printing of Charge. *Nano Lett.* **10**, 584–591 (2010).
- [352] Berkel, G. J., Asano, K. G. & Schnier, P. D. Electrochemical processes in a wire-in-a-capillary bulk-loaded, nano-electrospray emitter. *J. Am. Soc. Mass Spectrom.* **12**, 853–862 (2001).
- [353] Li, A. et al. Using Ambient Ion Beams to Write Nanostructured Patterns for Surface Enhanced Raman Spectroscopy. *Angew. Chemie Int. Ed.* **53**, n/a–n/a (2014).
- [354] Tuck, D. G. Direct electrochemical synthesis of inorganic and organometallic compounds. *Pure Appl. Chem.* **51**, 2005–2018 (1979).

- [355] Vecchio-Sadus, A. M. The electrochemical synthesis of inorganic and organometallic complexes in non-aqueous media. *J. Appl. Electrochem.* **23**, 401–416 (1993).
- [356] Prudent, M. & Girault, H. H. Functional electrospray emitters. *Analyst* **134**, 2189 (2009).
- [357] Li, A., Luo, Q., Park, S.-J. & Cooks, R. G. Synthesis and Catalytic Reactions of Nanoparticles formed by Electrospray Ionization of Coinage Metals. *Angew. Chemie Int. Ed.* **53**, 3147–3150 (2014).
- [358] Jaworek, A. & Sobczyk, A. Electro spraying route to nanotechnology: An overview. *J. Electrostat.* **66**, 197–219 (2008).
- [359] Chen, J., Lu, L. & Lu, K. Hardness and strain rate sensitivity of nanocrystalline Cu. *Scr. Mater.* **54**, 1913–1918 (2006).
- [360] Bass, J. 1.2.1 Pure metal resistivities at $T = 273.2$ K. In K.-H. Hellwege & J. L. Olsen, editors, *Electr. Resist. Kondo Spin Fluct. Syst. Spin Glas. Thermopower*, pages 5–13 (Springer-Verlag, Berlin/Heidelberg, 1983).
- [361] Decombe, J.-b. et al. Living cell imaging by far-field fibered interference scanning optical microscopy. *Opt. Express* **19**, 2702 (2011).
- [362] Collins, R. T., Jones, J. J., Harris, M. T. & Basaran, O. a. Electrohydrodynamic tip streaming and emission of charged drops from liquid cones. *Nat. Phys.* **4**, 149–154 (2008).
- [363] Puippe, J. C. Investigation of Laser-Enhanced Electroplating Mechanisms. *J. Electrochem. Soc.* **128**, 2539 (1981).
- [364] Von Gutfeld, R. J. & Vigliotti, D. R. High-speed electroplating of copper using the laser-jet technique. *Appl. Phys. Lett.* **46**, 1003–1005 (1985).
- [365] VETTER, K. J. The Theory of Overvoltage. In *Electrochem. Kinet.*, volume 337, pages 104–395 (Elsevier, 1967).
- [366] Jung, W. et al. Three-dimensional nanoprinting via charged aerosol focusing. *arxiv.org* pages 1–31 (2018).
- [367] Lee, A., Jin, H., Dang, H. W., Choi, K. H. & Ahn, K. H. Optimization of experimental parameters to determine the jetting regimes in electrohydrodynamic printing. *Langmuir* **29**, 13630–13639 (2013).

- [368] Rossnagel, S. M. & Kuan, T. S. Alteration of Cu conductivity in the size effect regime. *J. Vac. Sci. Technol. B Microelectron. Nanom. Struct.* **22**, 240 (2004).
- [369] J. Van Berkel, G. Electrolytic corrosion of a stainless-steel electrospray emitter monitored using an electrospray–photodiode array system. *J. Anal. At. Spectrom.* **13**, 603–607 (1998).
- [370] Sousa-Pedrares, A. et al. Electrochemical synthesis and crystal structure of cobalt(II), nickel(II), copper(II), zinc(II) and cadmium(II) complexes with 2-pyridinecarbaldehyde-(2-aminosulfonylbenzoyl)hydrazone. *Polyhedron* **27**, 3391–3397 (2008).
- [371] Ercolano, L., Monetta, T. & Bellucci, F. Anodic dissolution and passivation of Ni IN acid organic aprotic solvents. *Corros. Sci.* **35**, 161–167 (1993).
- [372] Franklin, T. C. & Parsons, C. R. The Anodic Dissolution of Nickel in Acetonitrile. *J. Electrochem. Soc.* **109**, 641 (1962).
- [373] Kelsey, G. S. The Anodic Behavior of Group Six Metals in Methanolic Solution. *J. Electrochem. Soc.* **124**, 927 (1977).
- [374] Habeeb, J. J., Oldham, C. & Tuck, D. G. The electrochemical oxidation of anodic molybdenum into non-aqueous solutions of halogen. *J. Inorg. Nucl. Chem.* **43**, 2087–2088 (1981).
- [375] Zotti, G. Anodic Dissolution of Titanium in Acetonitrile to Ti(IV) Perchlorate and Subsequent Reductive Electrodeposition of Amorphous TiO₂ Films. *J. Electrochem. Soc.* **146**, 637 (1999).
- [376] Propst, E. K. The Electrochemical Oxidation of Silicon and Formation of Porous Silicon in Acetonitrile. *J. Electrochem. Soc.* **141**, 1006 (1994).
- [377] Tourillon, G., Lacaze, P.-C. & Dubois, J.-E. Electrochemical formation of thin polyacetonitrile films on a Pt surface. *J. Electroanal. Chem. Interfacial Electrochem.* **100**, 247–262 (1979).
- [378] Cassidy, J., Khoo, S. B., Pons, S. & Fleischmann, M. Electrochemistry at very high potentials: the use of ultramicroelectrodes in the anodic oxidation of short-chain alkanes. *J. Phys. Chem.* **89**, 3933–3935 (1985).
- [379] Li, F.-B., Bremner, D. H. & Burgess, A. E. Dissolution and passivation of iron in acetonitrile and acetonitrile–water mixtures. *Corros. Sci.* **41**, 2317–2335 (1999).

- [380] Xu, X., Lu, W. & Cole, R. B. On-Line Probe for Fast Electrochemistry/Electrospray Mass Spectrometry. Investigation of Polycyclic Aromatic Hydrocarbons. *Anal. Chem.* **68**, 4244–4253 (1996).
- [381] Van Berkel, G. J., Asano, K. G. & Granger, M. C. Controlling Analyte Electrochemistry in an Electrospray Ion Source with a Three-Electrode Emitter Cell. *Anal. Chem.* **76**, 1493–1499 (2004).
- [382] Kertesz, V., Van Berkel, G. J. & Granger, M. C. Study and Application of a Controlled-Potential Electrochemistry/Electrospray Emitter for Electrospray Mass Spectrometry. *Anal. Chem.* **77**, 4366–4373 (2005).
- [383] Kertesz, V. & Berkel, G. J. Expanded use of a battery-powered two-electrode emitter cell for electrospray mass spectrometry. *J. Am. Soc. Mass Spectrom.* **17**, 953–961 (2006).
- [384] Richmonds, C. & Sankaran, R. M. Plasma-liquid electrochemistry: Rapid synthesis of colloidal metal nanoparticles by microplasma reduction of aqueous cations. *Appl. Phys. Lett.* **93**, 131501 (2008).
- [385] Richmonds, C. et al. Electron-Transfer Reactions at the Plasma–Liquid Interface. *J. Am. Chem. Soc.* **133**, 17582–17585 (2011).
- [386] Brettholle, M. et al. Plasma electrochemistry in ionic liquids: deposition of coppernanoparticles. *Phys. Chem. Chem. Phys.* **12**, 1750–1755 (2010).
- [387] Ghosh, S. et al. Quantitative Study of Electrochemical Reduction of Ag⁺ to Ag Nanoparticles in Aqueous Solutions by a Plasma Cathode. *J. Electrochem. Soc.* **164**, D818–D824 (2017).
- [388] Morimatsu, D. et al. Development of a scanning nanopipette probe microscope for fine processing using atmospheric pressure plasma jet. *Jpn. J. Appl. Phys.* **55**, 08NB15 (2016).
- [389] MacDonald, E. & Wicker, R. Multiprocess 3D printing for increasing component functionality. *Science (80-.)*. **353**, aaf2093–aaf2093 (2016).
- [390] Valentine, A. D. et al. Hybrid 3D Printing of Soft Electronics. *Adv. Mater.* **29**, 1703817 (2017).
- [391] Vaezi, M., Chianrabutra, S., Mellor, B. & Yang, S. Multiple material additive manufacturing – Part 1: a review. *Virtual Phys. Prototyp.* **8**, 19–50 (2013).

-
- [392] Kong, Y. L. et al. 3D Printed Quantum Dot Light-Emitting Diodes. *Nano Lett.* **14**, 7017–7023 (2014).
- [393] Kokkinis, D., Bouville, F. & Studart, A. R. 3D Printing of Materials with Tunable Failure via Bioinspired Mechanical Gradients. *Adv. Mater.* **30**, 1705808 (2018).
- [394] Li, X. & Gao, H. Smaller and stronger. *Nat. Mater.* **15**, 373–374 (2016).
- [395] Dehoff, R. R. et al. Site specific control of crystallographic grain orientation through electron beam additive manufacturing. *Mater. Sci. Technol.* **31**, 931–938 (2015).
- [396] Hofmann, D. C. et al. Developing Gradient Metal Alloys through Radial Deposition Additive Manufacturing. *Sci. Rep.* **4**, 5357 (2015).
- [397] Raney, J. R. et al. Rotational 3D printing of damage-tolerant composites with programmable mechanics. *Proc. Natl. Acad. Sci.* **115**, 1198–1203 (2018).
- [398] Fang, T. H., Li, W. L., Tao, N. R. & Lu, K. Revealing Extraordinary Intrinsic Tensile Plasticity in Gradient Nano-Grained Copper. *Science (80-.)*. **331**, 1587–1590 (2011).
- [399] Lu, K. Making strong nanomaterials ductile with gradients. *Science (80-.)*. **345**, 1455–1456 (2014).
- [400] Yang, L., Tao, N. R., Lu, K. & Lu, L. Enhanced fatigue resistance of Cu with a gradient nanograined surface layer. *Scr. Mater.* **68**, 801–804 (2013).
- [401] Huang, H. W., Wang, Z. B., Yong, X. P. & Lu, K. Enhancing torsion fatigue behaviour of a martensitic stainless steel by generating gradient nanograined layer via surface mechanical grinding treatment. *Mater. Sci. Technol.* **29**, 1200–1205 (2013).
- [402] Wu, X., Jiang, P., Chen, L., Yuan, F. & Zhu, Y. T. Extraordinary strain hardening by gradient structure. *Proc. Natl. Acad. Sci.* **111**, 7197–7201 (2014).
- [403] Wei, Y. et al. Evading the strength–ductility trade-off dilemma in steel through gradient hierarchical nanotwins. *Nat. Commun.* **5**, 3580 (2014).
- [404] Wegst, U. G. K., Bai, H., Saiz, E., Tomsia, A. P. & Ritchie, R. O. Bioinspired structural materials. *Nat. Mater.* **14**, 23–36 (2015).
- [405] Yu, H. Z., Cross, S. R. & Schuh, C. A. Mesostructure optimization in multi-material additive manufacturing: a theoretical perspective. *J. Mater. Sci.* **52**, 4288–4298 (2017).

- [406] Garcia, D., Jones, M. E., Zhu, Y. & Yu, H. Z. Mesoscale design of heterogeneous material systems in multi-material additive manufacturing. *J. Mater. Res.* **33**, 58–67 (2018).
- [407] Libanori, R. et al. Stretchable heterogeneous composites with extreme mechanical gradients. *Nat. Commun.* **3**, 1265 (2012).
- [408] Abdi, F. F. et al. Efficient solar water splitting by enhanced charge separation in a bismuth vanadate-silicon tandem photoelectrode. *Nat. Commun.* **4**, 2195 (2013).
- [409] Wang, M. et al. N Doping to ZnO Nanorods for Photoelectrochemical Water Splitting under Visible Light: Engineered Impurity Distribution and Terraced Band Structure. *Sci. Rep.* **5**, 1–13 (2015).
- [410] Bartlett, N. W. et al. A 3D-printed, functionally graded soft robot powered by combustion. *Science (80-.)*. **349**, 161–165 (2015).
- [411] Qu, J., Kadic, M., Naber, A. & Wegener, M. Micro-Structured Two-Component 3D Metamaterials with Negative Thermal-Expansion Coefficient from Positive Constituents. *Sci. Rep.* **7**, 40643 (2017).
- [412] Chen, B., Jiang, Y., Tang, X., Pan, Y. & Hu, S. Fully Packaged Carbon Nanotube Supercapacitors by Direct Ink Writing on Flexible Substrates. *ACS Appl. Mater. Interfaces* **9**, 28433–28440 (2017).
- [413] Peterson, G. I. et al. Production of Materials with Spatially-Controlled Cross-Link Density via Vat Photopolymerization. *ACS Appl. Mater. Interfaces* **8**, 29037–29043 (2016).
- [414] Kim, H., Auyeung, R. C. & Piqué, A. Laser-printed thick-film electrodes for solid-state rechargeable Li-ion microbatteries. *J. Power Sources* **165**, 413–419 (2007).
- [415] Ortega, J. M. et al. Active Mixing of Disparate Inks for Multimaterial 3D Printing. *Adv. Mater. Technol.* **1800717**, 1800717 (2019).
- [416] Schuster, R., Kirchner, V., Allongue, P. & Ertl, G. Electrochemical Micromachining. *Science (80-.)*. **289**, 98–101 (2000).
- [417] Obermair, C., Kress, M., Wagner, A. & Schimmel, T. Reversible mechano-electrochemical writing of metallic nanostructures with the tip of an atomic force microscope. *Beilstein J. Nanotechnol.* **3**, 824–830 (2012).

- [418] Schindler, W., Hofmann, D. & Kirschner, J. Localized electrodeposition using a scanning tunneling microscope tip as a nanoelectrode. *J. Electrochem. Soc.* **148**, C124—C130 (2001).
- [419] Maynor, B. W., Li, Y. & Liu, J. Au “Ink” for AFM “Dip-Pen” Nanolithography. *Langmuir* **17**, 2575–2578 (2001).
- [420] Li, Y., Maynor, B. W. & Liu, J. Electrochemical AFM “Dip-Pen” Nanolithography. *J. Am. Chem. Soc.* **123**, 2105–2106 (2001).
- [421] Jakob, S. & Schindler, W. Electric field assisted electrochemical “writing” of Co nanostructures onto n-Si(111):H surfaces. *Surf. Sci.* **612**, L1–L4 (2013).
- [422] LaGraff, J. R. & Gewirth, A. a. Nanometer-Scale Mechanism for the Constructive Modification of Cu Single Crystals and Alkanethiol Passivated Au(111) with an Atomic Force Microscope. *J. Phys. Chem.* **99**, 10009–10018 (1995).
- [423] Xia, X. H., Schuster, R., Kirchner, V. & Ertl, G. The growth of size-determined Cu clusters in nanometer holes on Au(111) due to a balance between surface and electrochemical energy. *J. Electroanal. Chem.* **461**, 102–109 (1999).
- [424] Hofmann, D., Schindler, W. & Kirschner, J. Electrodeposition of nanoscale magnetic structures. *Appl. Phys. Lett.* **73**, 3279–3281 (1998).
- [425] Schindler, W., Hofmann, D. & Kirschner, J. Nanoscale electrodeposition: A new route to magnetic nanostructures? *J. Appl. Phys.* **87**, 7007–7009 (2000).
- [426] Kock, M., Kirchner, V. & Schuster, R. Electrochemical micromachining with ultrashort voltage pulses—a versatile method with lithographical precision. *Electrochim. Acta* **48**, 3213–3219 (2003).
- [427] Allongue, P., Jiang, P., Kirchner, V., Trimmer, A. L. & Schuster, R. Electrochemical micromachining of p-type silicon. *J. Phys. Chem. B* **108**, 14434–14439 (2004).
- [428] Schuster, R. Electrochemical microstructuring with short voltage pulses. *ChemPhysChem* **8**, 34–39 (2007).
- [429] de Abril, O., Gündel, a., Maroun, F., Allongue, P. & Schuster, R. Single-step electrochemical nanolithography of metal thin films by localized etching with an AFM tip. *Nanotechnology* **19**, 325301 (2008).

- [430] Schuster, R., Kirchner, V., Xia, X. H., Bittner, a. M. & Ertl, G. Nanoscale Electrochemistry. *Phys. Rev. Lett.* **80**, 5599–5602 (1998).
- [431] Trimmer, A. L., Hudson, J. L., Kock, M. & Schuster, R. Single-step electrochemical machining of complex nanostructures with ultrashort voltage pulses. *Appl. Phys. Lett.* **82**, 3327–3329 (2003).
- [432] Smallwood, I. *Handbook of Organic Solvent Properties* (Elsevier, 1996).
- [433] Pourbaix, M. J. N., Muylder, J. V. & De Zoubov, N. Electrochemical Properties of the Platinum Metals. *Platin. Met. Rev.* **3**, 47–53 (1959).
- [434] Yang, Y.-f. & Denuault, G. Scanning electrochemical microscopy (SECM) study of pH changes at Pt electrode surfaces in Na₂SO₄ solution (pH 4) under potential cycling conditions. *J. Chem. Soc. Faraday Trans.* **92**, 3791 (1996).
- [435] Lai, S. C. S. & Koper, M. T. M. Electro-oxidation of ethanol and acetaldehyde on platinum single-crystal electrodes. *Faraday Discuss.* **140**, 399–416 (2009).
- [436] Collins, R. T., Harris, M. T. & Basaran, O. a. Breakup of electrified jets. *J. Fluid Mech.* **588**, 75–129 (2007).
- [437] Li, L. et al. Direct Electrodeposition of ZnO Nanotube Arrays in Anodic Alumina Membranes. *J. Phys. Chem. C* **111**, 7288–7291 (2007).
- [438] Munisamy, T. & Bard, A. J. Electrodeposition of Si from organic solvents and studies related to initial stages of Si growth. *Electrochim. Acta* **55**, 3797–3803 (2010).
- [439] Rakhshani, A. Preparation, characteristics and photovoltaic properties of cuprous oxide—a review. *Solid. State. Electron.* **29**, 7–17 (1986).
- [440] Liu, F. et al. High Performance, Tunable Electrically Small Antennas through Mechanically Guided 3D Assembly. *Small* **15**, 1804055 (2019).
- [441] Lee, W. et al. Two-dimensional materials in functional three-dimensional architectures with applications in photodetection and imaging. *Nat. Commun.* **9**, 1417 (2018).
- [442] Won, S. M. et al. Multimodal Sensing with a Three-Dimensional Piezoresistive Structure. *ACS Nano* page acsnano.9b02030 (2019).

- [443] Dudukovic, N. A. et al. Predicting Nanoparticle Suspension Viscoelasticity for Multimaterial 3D Printing of Silica–Titania Glass. *ACS Appl. Nano Mater.* **1**, 4038–4044 (2018).
- [444] Xu, S. et al. Assembly of micro/nanomaterials into complex, three-dimensional architectures by compressive buckling. *Science (80-.)*. **347**, 154–159 (2015).
- [445] Bialas, S. et al. Access to Disparate Soft Matter Materials by Curing with Two Colors of Light. *Adv. Mater.* **31**, 1807288 (2019).
- [446] Mayer, F. et al. Multimaterial 3D laser microprinting using an integrated microfluidic system. *Sci. Adv.* **5**, eaau9160 (2019).
- [447] Tabor, D. The hardness of solids. *Rev. Phys. Technol.* **1**, 145–179 (1970).
- [448] Jaeger, H. M., Nagel, S. R. & Behringer, R. P. Granular solids, liquids, and gases. *Rev. Mod. Phys.* **68**, 1259–1273 (1996).
- [449] Emery, R. D. & Povirk, G. L. Tensile behavior of free-standing gold films. Part I. Coarse-grained films. *Acta Mater.* **51**, 2067–2078 (2003).
- [450] Emery, R. D. & Povirk, G. L. Tensile behavior of free-standing gold films. Part II. Fine-grained films. *Acta Mater.* **51**, 2079–2087 (2003).
- [451] Chen, C. Y. et al. Pulse electroplating of ultra-fine grained Au films with high compressive strength. *Electrochem. commun.* **67**, 51–54 (2016).
- [452] Yanagida, S. et al. Microelectronic Engineering Tensile tests of micro-specimens composed of electroplated gold. *Microelectron. Eng.* **174**, 6–10 (2017).
- [453] Fang, T.-H. & Chang, W.-J. Nanomechanical properties of copper thin films on different substrates using the nanoindentation technique. *Microelectron. Eng.* **65**, 231–238 (2003).
- [454] Hong, S. H. et al. Characterization of elastic moduli of Cu thin films using nanoindentation technique. *Compos. Sci. Technol.* **65**, 1401–1408 (2005).
- [455] Dao, M., Lu, L., Shen, Y. F. & Suresh, S. Strength, strain-rate sensitivity and ductility of copper with nanoscale twins. *Acta Mater.* **54**, 5421–5432 (2006).
- [456] Jang, D., Cai, C. & Greer, J. R. Influence of homogeneous interfaces on the strength of 500 nm diameter Cu nanopillars. *Nano Lett.* **11**, 1743–1746 (2011).

- [457] Mieszala, M. et al. Orientation-dependent mechanical behaviour of electrodeposited copper with nanoscale twins. *Nanoscale* **8**, 15999–16004 (2016).
- [458] Darling, A. S. The Elastic and Plastic Properties of the Platinum Metals. *Res. Lab. Johnson Matthey Co Ltd.* pages 14–19 (1966).
- [459] Merker, J., Lupton, D., Töpfer, M. & Knake, H. High temperature mechanical properties of the platinum group metals: Elastic properties of platinum, rhodium and iridium and their alloys at high temperatures. *Platin. Met. Rev.* **45**, 74–82 (2001).
- [460] Duft, D., Achtzehn, T., Müller, R., Huber, B. A. & Leisner, T. Rayleigh jets from levitated microdroplets. *Nature* **421**, 128–128 (2003).
- [461] Fernández de la Mora, J. The Fluid Dynamics of Taylor Cones. *Annu. Rev. Fluid Mech.* **39**, 217–243 (2007).
- [462] Schindler, W., Hugelmann, P., Hugelmann, M., Körtner, F. X. & Ka, F. X. Localized electrochemical nucleation and growth of low-dimensional metal structures. *J. Electroanal. Chem.* **522**, 49–57 (2002).
- [463] Lorenz, W. J., Staikov, G., Schindler, W. & Wiesbeck, W. The role of low-dimensional systems in electrochemical phase formation and dissolution processes. *J. Electrochem. Soc.* **149**, K47—K59 (2002).

Declaration

All contributors other than the author are gratefully acknowledged and listed by chapter and in alphabetical order. In addition, the author's contribution (**A.R.**) are specified at the end of each section.

- **Ralph Spolenak** is a professor at ETH Zürich and head of the Laboratory for Nanometallurgy. R.S. supervised this doctoral thesis.

Chapter 2

- **Luca Hirt** is a former PhD student at ETH Zürich in the Laboratory of Biosensors and Bioelectronics. L.H. and A.R. share first authorship of the original review article that formed the basis of the updated text in the chapter.
- **Tomaso Zambelli** is a principle investigator in the Laboratory of Biosensors and Bioelectronics at ETH Zürich. He and R.S. supervised the compilation of the before-mentioned review article and reviewed the manuscript.
- **A.R.** contributed equally with L.H. to the original review article and updated the present chapter to the state of the art.

Chapter 3

- **Lukas Koch** is a Master's thesis student in the Laboratory for Nanometallurgy and printed all the EHD-RP samples.

- **Jeffrey Wheeler** is a senior scientist in the Laboratory of Nanometallurgy. He performed all microcompression tests (together with A.R.) and advised on the mechanical analysis of the samples. Additionally, he reviewed and discussed the results and the chapter text / the manuscript.
- The **contributors that supplied samples** for the different small-scale AM methods were: Kathleen A. Dunn (SUNY Polytechnic Institute, USA, cryo-FEBID); Toshiki Matsuura and Futoshi Iwata (Shizuoka University, Japan, electrophoretic deposition); Ofer Fogel and Zvi Kotler (Orbotech, Israel, LIFT (melt)); Qikun Shi, Nanjia Zhou (Westlake University, China) and Jennifer Lewis (Harvard University, USA, DIW (s.t.)); Kristin Charipar and Alberto Piqué (Naval Research Laboratory Washington, USA, LIFT (ink)); Patrik Rohner and Dimos Poulikakos (Federal Institute of Technology (ETH) Zürich, Switzerland, EHDP); Sanghyeon Lee and Seung Kwon Seol (Korea Electrotechnology Research Institute (KERI), Republic of Korea, DIW (N.) and MCED); Gerhard Bürki and Ivo Utke (Empa Thun, Switzerland, FEBID and FIBID); Cathelijan van Nisselroy and Tomaso Zambelli (ETH Zürich, Switzerland, FluidFM).
- **A.R.** suggested the study and identified and initiated the relevant collaborations. A.R. coordinated the research efforts. A.R. contributed all microstructural and all nanoindentation analysis to the project, analyzed and visualized all data and wrote the chapter / the manuscript.

Chapters 4 and 5

- **Henning Galinski** is a senior scientist in the Laboratory of Nanometallurgy. He designed the printing setup (together with A.R. and M.L.). All authors discussed, reviewed and commented the draft.
- **Marcus Lindén** is a former Master's student at ETH Zürich. He contributed to the development of EHD-RP during a Master's project, his Master's thesis and as a full-time scientific assistant in the Laboratory of Nanometallurgy. M.L. built the printing setup (together with A.R. and H.G.), and wrote the printing software. M.L. designed (with A.R.) and performed the majority of printing experiments reported in this thesis, and performed preliminary feasibility studies with P.R.. M.L. contributed SEM analysis to the project. All authors discussed, reviewed and commented the draft.

- **Adrien Marchand** is a PostDoc at ETH Zürich in the Laboratory of Organic Chemistry. A.M. designed (together with A.R. and M.L.) and performed MS experiments. A.M. analyzed the MS data. All authors discussed, reviewed and commented the draft.
- **Dimos Poulidakos** is a professor at ETH Zürich and head of the Laboratory of Thermodynamics in Emerging Technologies. Prof. Poulidakos supervised P.R.'s contribution to the work. Preliminary feasibility experiments were performed in D.P.'s laboratory. All authors discussed, reviewed and commented the draft.
- **Patrik Rohner** is a former PhD student at ETH Zürich in the Laboratory of Thermodynamics in Emerging Technologies. P.R. provided know-how on the general setup and basics of EHD printing. P.R. also performed preliminary feasibility studies (together with M.L.). All authors discussed, reviewed and commented the draft.
- **Alla Sologubenko** is a senior scientist at the Scientific Center for Optical and Electron Microscopy at ETH Zürich. A.S. performed TEM analysis. All authors discussed, reviewed and commented the draft.
- **Jeffrey Wheeler** performed micromechanical analysis (together with A.R.). All authors discussed, reviewed and commented the draft.
- **Renato Zenobi** is a professor at ETH Zürich and head of the Laboratory of Organic Chemistry. All MS experiments were conducted in his laboratory. All authors discussed, reviewed and commented the draft.
- The following students contributed to the project in the form of a **Bachelor's thesis** (BT), **Master's thesis** (MT) or **Master's project** (MP) or as a part-time assistant (A), and some of their results are used in one of the two chapters (listed in alphabetical order): Willem Aarents (A), Ramón Frey (A), Sophia Ganzeboom (MP), Lukas Koch (MT), Andrea Scheidegger (BT), Vladimír Vojtěch (A), Pascal Zehnder (A).
- **A.R.** and Ralph Spolenak devised the concept. A.R. coordinated the project and supervised M.L.'s thesis. A.R. (with M.L. and H.G.) built the printing setup. A.R. (with M.L.) designed and performed printing experiments reported here. A.R. (with A.M. and M.L.) designed and performed MS experiments. A.R. provided all SEM analysis shown here and all FIB analysis. A.R. (with J. W.) performed micromechanical analysis. A.R. wrote the original paper draft and visualized the data. A.R. supervised all student projects.

Chapter 6

- **Mark Aarts** is a PhD student at the AMOLF institute (Netherlands) and suggested to engineer the oxidation reaction at the STM probe – respective experiments have not yet been performed, but the idea is discussed in the chapter. Further, he printed the lines shown in Fig. 6.6.
- **Rolf Schuster** is a professor at the Karlsruhe Institute of Technology (KIT). Prof. Schuster introduced me to the experimental details of electrochemical micromachining with nanosecond voltage pulses (hosting me in his group for two weeks) and advised the design of the setup built at ETH Zürich. Additionally, we discussed many of the results.
- The following students contributed to the project in the form of a **Master's thesis** (MT) or a **Master's project** (MP) or as a part-time assistant: Johannes Gabl (A), Steffen Geisel (MP), Avinash Kandalam (MT), Vladimír Vojtěch (MP).
- **A.R.** built the setup (with major input of R. Schuster), wrote the control software and performed most of the deposition experiments shown in this chapter. A.R. supervised all student projects.

Acknowledgements

I would like to take this opportunity to express my gratitude to all the people who supported me during the past six years – this thesis would not have been possible without you.

First and foremost, I would like to thank my supervisor Prof. Ralph Spolenak. Ralph, I could hardly imagine a better place for my PhD studies, both on a professional and a personal level. Your continuous support and your trust, your encouragement of independent work and thinking, your enthusiasm, your critical input but also your ability to discuss on an equal level, have made my PhD a wonderful experience – it was very long, but it was exciting. I am most grateful for your personal support and advice in better and worse times. I am looking forward to the next year of our joint project and coming years that hopefully bring numerous opportunities to keep in touch.

Furthermore, I would like to thank my co-examiners Prof. Julia Greer and Prof. Markus Niederberger for reading and evaluating this thesis.

I also acknowledge the financial support from ETH Zürich through grant No. ETH 47 14-2.

I also want to gratefully acknowledge the input of all our collaborators on the EHD-RP project. Prof. Dimos Poulidakos, Patrik, Prof. Renato Zenobi and Adrien, thank you for your help – this thesis would not have been possible without your input. Adrien, thank you for your enthusiasm, I enjoyed our MS sessions a lot.

I extend a big thank you to all our collaborators on the mechanical study, listed in the Declaration. Thank you for the opportunity to study all the materials, and thank you for your extended patience – it was a very challenging project for me. I hope it will be of use to us all.

Additionally, I want to thank Prof. Schuster for his big support of the STM-project. Without you, this project would not have worked at all. Thank you for hosting me in your laboratory, and thank

you for sharing your in-depth knowledge of the process – I am still amazed by its elegance. At this stage, I also want to acknowledge the work of Mark Aarts, who started to collaborate on the project. Thank you for all your valuable input and fresh ideas.

I would further like to extend a big thank you to the team of Tomaso Zambelli of the Laboratory of Biosensors and Bioelectronics. Luca, it was a lot of fun. Thank you for our collaboration, for your personal support and your very realistic view of small-scale AM. Also, I am impressed by the path FluidFM printing takes. Cathelijm, thank you for our recent collaboration, and Dmitry, thank you very much for your input and advice. I hope there will be future joint projects.

Also, I want to acknowledge the work by the team of Prof. Lars Jeurgens at Empa Dübendorf. Although our joint project did not make it into this thesis, you taught me a lot. Thank you Thomas, and thank you Patrik.

Six years in the Laboratory of Nanometallurgy leaves me with a lot of people to thank for the countless help and support. Thus, I begin with a big thank you to everybody that is or was part of the group. Most of the times, the lab felt like a second home. I am very happy to call you all my doctor-siblings (I stole this line from Andi, but I like it). Of the LNM team, Alla Sologubenko deserves a special mention. Alla, you are a major reason I joined this group. In my view, you live and speak science, and your supervision of my student projects was inspiring. Thank you for always having an open ear for and often an answer to questions big and small. TEM is amazing! Further, I want to thank in particular: Andi, your enthusiasm was a great motivator. I was very happy when I learned that you also start a PhD in the group, and I missed you after you finished two years earlier. Ming, you were the best office mate ever. I hope you will get your fish at some point. Stefano, thank you so much for your support in the last years, experimentally as well as personally. Your excitement and your critical input was very valuable. Jeff, thank you for welcoming me in your office, but most importantly, thank you for the scientific advice and all the feedback. Microcompression rules! Henning, your enthusiasm was almost overwhelming. Thank you for bouncing ideas back and forth (also the many unrealistic ones) and your input on my writing. Matteo, thank you for making sure I pursued a PhD by supervising my Master's thesis in the LNM group.

Six years also mean supervision of a lot of students. To everybody I had the luck to work with: thank you very much, you taught me a lot. Also, of course, many of the results in this thesis would not have been possible without your work. Thank you all for your exquisite work. I hope the numerous failures were not too frustrating. Please excuse me not mentioning everybody by name. Very special thanks go to Marcus: Marcus, I think EHD-RP as it is would not exist without you. It was a lot of fun, and I will always remember the frog with its little ears.

For all the technical support, a big thank you goes to Till, Fabio and Wägi as well as Martin's (ever smaller) team in the mechanical workshop. None of the projects in this thesis would have been possible without your help. Also, I would like to acknowledge the work of the ScopeM team: Karsten, Joakim and Stephan, thank you for the teaching and the help.

Last, but most importantly, I am grateful for the support of my wife, Sabine. Bino, mir wüßed beidi, wie kitschig ich so öppis a dere Stell find, aber es stimmt nunmal: ich bin unendlich froh, dass du da bisch und da gsi bisch. Danke für dini Sorg um mich, danke für's Grenze Ufzeige, und eifach nomal danke dass du da bisch – ich chännt nöd ohni dich.

Curriculum Vitae

Personal Information

| | | | |
|-----------------------|--------------|--------------------------|---|
| Name | Alain Stefan | Address | Konradstr. 18, 8005 Zürich |
| Surname | Reiser | Email | alainreiser@gmail.com |
| Date of birth | 11.11.1987 | ORCID ID | 0000-0001-9980-7434 |
| Nationality | Swiss | Google Scholar ID | wskv6ukAAAAJ |
| Marital status | married | | |

Education

- PhD studies**
2013 – 2019
- Laboratory for Nanometallurgy, ETH Zürich, CH.
PhD supervisor: Prof. Dr. Ralph Spolenak
Additive manufacturing of metals at small length scales – microstructure, properties and novel multi-metal electrochemical concepts
Website: <http://www.met.mat.ethz.ch/research/small-scale-3d-printing.html>
- MSc in Materials Science**
Feb 2011 – Oct 2012
- ETH Zürich, CH.
Major: Materials Analysis and Properties & Nanoscience and -technology.
Overall grade point average: 5.66 (grade point average of the degree programme: 5.38)
Master's Thesis, ETH Zürich, CH & Bar Ilan University, IL
"Thin-film microstructure engineering and effects on carbon nanotube growth"
Supervisors: Dr. Matteo Seita, Prof. Dr. Ralph Spolenak, Prof. Dr. Gilbert Daniel Nessim
- BSc in Materials Science**
Oct 2007 – Jan 2011
- ETH Zürich, CH.
Overall grade point average: 5.20 (grade point average of the degree programme: 4.94)
Bachelor's Thesis, ETH Zürich, CH
"Resistive switching and pulse testing of LSCF thin films and STO single crystals"
Supervisors: Prof. Dr. Jennifer Rupp, Prof. Dr. Ludwig Gaukler

Employments

| | |
|--|--|
| PhD student since May 2013 | Laboratory for Nanometallurgy, ETH Zürich, CH. Advisor: Prof. Dr. Ralph Spolenak |
| Civil service Nov 2012 – Mar 2013 | Laboratory of Materials for Renewable Energy, EMPA Dübendorf, CH. Advisor: Prof. Dr. Andreas Züttel |
| Research internship July – Dec 2010 | Division of Materials Science and Engineering, CSIRO, Clayton, AUS. Advisor: Dr. Laurence Meagher |
| Research Assistant June 2009 – July 2010 | Laboratory for Complex Materials, ETH Zürich, CH. Advisor: Prof. Dr. André Studart |

Supervision of students

In the course of my PhD studies, I have so far supervised a total of fourteen Bachelor's and Master's students. This includes several Master's projects, one Bachelor project, one Bachelor's and four Master's theses, and multiple research assistants.

Teaching activities

| | |
|--|---|
| Fall semester 2016 – Fall semester 2017 | Laboratory course , 1st year Bachelor's students, Materials Science, ETH Zürich. Topic: Young's modulus Head of Lab Courses: Dr. Martin Willeke |
|--|---|

Prizes, awards, fellowships

| | |
|---|--|
| SNSF Early PostDoc Mobility Fellowship | <i>"Supersonic micro- and nanoparticle impact printing – a technology for the bottom-up synthesis of high-quality, inorganic gradient materials with nanoscale resolution"</i> |
| ETH Medal 2013 | Awarded for outstanding Master's thesis. |

Publications in peer-reviewed scientific journals

ORCID profile: <https://orcid.org/0000-0001-9980-7434>
Google Scholar profile: <https://scholar.google.ch/citations?user=\wskv6ukAAAAJ>

1. **A. Reiser**, M. Lindén, P. Rohner, A. Marchand, H. Galinski, A. S. Sologubenko, J. M. Wheeler, R. Zenobi, D. Poulidakos, R. Spolenak. Multi-metal electrohydrodynamic redox 3D printing at the submicron scale. *Nat. Commun.*, **2019**, 10, 1853. <https://www.nature.com/articles/s41467-019-09827-1>
2. **A. Reiser**, L. Hirt (Hirt and Reiser contributed equally), R. Spolenak, T. Zambelli. Additive Manufacturing of Metal Structures at the Micrometer Scale. *Adv. Mater.*, **2017**, 29, 1604211. <http://onlinelibrary.wiley.com/doi/10.1002/adma.201604211/abstract>
3. L. Hirt, S. Ihle, Z. Pan, L. Dorwling-Carter, **A. Reiser**, J. M. Wheeler, R. Spolenak, J. Vörös, T. Zambelli. Template-Free 3D Microprinting of Metals Using a Force-Controlled Nanopipette for Layer-by-Layer Electrodeposition. *Adv. Mater.*, **2016**, 28, 2311. <http://onlinelibrary.wiley.com/doi/10.1002/adma.201504967/abstract>
4. A. C. Kandemir, D. Erdem, H. Ma, **A. Reiser**, R. Spolenak. Polymer nanocomposite patterning by dip-pen nanolithography. *Nanotechnology*, **2016**, 27, 135303. <http://iopscience.iop.org/article/10.1088/0957-4484/27/13/135303/meta>
5. A. Röthlisberger, M. Seita, **A. Reiser**, E. Shawat, R. Spolenak, G. D. Nessim. Investigating the mechanism of collective bidirectional growth of carbon nanofiber carpets on metallic substrates. *Carbon*, **2013**, 63, 498. <https://www.sciencedirect.com/science/article/pii/S0008622313006477>
6. M. Seita, **A. Reiser**, R. Spolenak. Ion-induced grain growth and texturing in refractory thin films – A low temperature process. *Appl. Phys. Lett.*, **2012**, 101, 251905. <http://aip.scitation.org/doi/abs/10.1063/1.4772640>
7. R. Libanori, R. M. Erb, **A. Reiser**, H. Le Ferrand, M. J. Süess, R. Spolenak, A. R. Studart. Stretchable heterogeneous composites with extreme mechanical gradients. *Nat. Commun.*, **2012**, 3, 1265. <https://www.nature.com/articles/ncomms2281>

Contributions to international conferences

1. **A. Reiser**, M. Lindén, R. Spolenak. Redox-Based EHD-Printing – Chemically Architected Metals with Submicron Chemical Resolution. Oral presentation. MRS Fall Meeting, November 25 – 30, **2018**, Boston, USA. <https://www.mrs.org/fall-2018-symposium-sessions/symposium-sessions-detail?code=PM01>
2. **A. Reiser**, P. Rohner, M. Lindén, D. Poulikakos, R. Spolenak. Electrochemical Electrohydrodynamic Printing: Speeding up Electrochemical Microscale Additive Manufacturing. Oral presentation. MRS Sprint Meeting, April 2 – 6, **2018**, Phoenix, USA. <https://mrsspring2018.zerista.com/event/member/468379>
3. **A. Reiser**, R. Frey, V. Schnabel, R. Spolenak. Synthesis of Graded, Nanoporous Coatings by Chemical Dealloying of Electrodeposited CuZn Thin Films and Their Microstructural and Mechanical Properties. Oral presentation. MRS Sprint Meeting, April 2 – 6, **2018**, Phoenix, USA. <https://mrsspring2018.zerista.com/event/member/463906>
4. **A. Reiser**, J. M. Wheeler, R. Spolenak. A Comparative Study of Microstructures and Mechanical Properties of Microscale 3D Printed Metals. Poster presentation. MRS Sprint Meeting, April 2 – 6, **2018**, Phoenix, USA. <https://mrsspring2018.zerista.com/event/member/468645>
5. **A. Reiser**, J. M. Wheeler, R. Spolenak. 3D Printing Graded Microstructures and Properties with Micrometer Resolution: a Universal Strategy for Electrochemical Microscale Additive Manufacturing. Poster presentation. MRS Sprint Meeting, April 2 – 6, **2018**, Phoenix, USA. <https://mrsspring2018.zerista.com/event/member/465089>
6. **A. Reiser**, J. M. Wheeler, R. Spolenak. Microscale Additive Manufacturing of Metal – Mechanical Properties. Oral presentation. ECI, Nanomechanical Testing in Materials Research and Development VI, Oct 1 – 6 **2017**, Dubrovnik, Croatia.
7. **A. Reiser**, L. Hirt, J. Wheeler, S. Küchler, T. Zambelli, R. Spolenak. Metal Additive Manufacturing at the Microscale: Mechanical Properties in Comparison. Poster presentation. MRS Fall Meeting, Nov 27 – Dec 2, **2016**, Boston, USA.
8. **A. Reiser**, S. Pané, R. Spolenak. Electrochemical bottom-up patterning of Co on HOPG at the nanoscale. Poster presentation. Fischer Symposium, June 7 – 11, **2015**, Lübeck, Germany.

Unpublished work

1. **A. Reiser**, L. Koch, K. A. Dunn, F. Iwata, O. Fogel, Z. Kotler, N. Zhou, Q. Shi, J. Lewis, K. Charipar, A. Piqué, P. Rohner, D. Poulidakos, S. Lee, S., S. K. Seol, I. Utke, C. van Nis-selroy, T. Zambelli, J. M. Wheeler, R. Spolenak. Metals by micro additive manufacturing: a comparison of microstructures and mechanical properties. To be submitted to *Small*.
2. **A. Reiser**, R. Frey, V. Schnabel, R. Spolenak. Synthesis of Graded, Nanoporous Coatings by Chemical Dealloying of Electrodeposited CuZn Thin Films and Their Microstructural and Mechanical Properties. In preparation.
3. **A. Reiser**, M. Aarts, E. Alacron Llado, R. Schuster, R. Spolenak. 3D deposition of metals via nanosecond voltage pulses in an electrochemical scanning-transmission microscope. In preparation.
4. P. Rohner, **A. Reiser**, F. T. Rabouq, A. Sologubenko, D. J. Norris, R. Spolenak, D. Poulidakos. Electrohydrodynamically printed gold nanowalls with electrical resistivities close to bulk. In preparation.

List of Figures

| | | |
|------|---|-----|
| 1.1 | Small-scale AM of inorganic materials | 3 |
| 2.1 | State-of-the-art microscale metal AM techniques | 14 |
| 2.2 | Direct ink writing (DIW) | 15 |
| 2.3 | Electrohydrodynamic (EHD) printing. | 18 |
| 2.4 | Laser-assisted electrophoretic deposition. | 22 |
| 2.5 | Laser-induced forward transfer (LIFT) of metal melts. | 25 |
| 2.6 | LIFT: laser decal transfer of inks | 28 |
| 2.7 | Meniscus-confined electrodeposition | 30 |
| 2.8 | Concentration-confined electrodeposition | 33 |
| 2.9 | Laser-induced photoreduction | 36 |
| 2.10 | FEBID / FIBID | 39 |
| 2.11 | cryo-FEBID | 43 |
| 2.12 | Carbothermal reduction of organic-inorganic composites | 45 |
| 2.13 | Implosion Fabrication | 47 |
| 2.14 | Small-scale methods in comparison: fabrication capabilities | 50 |
| 2.15 | Small-scale methods in comparison: microstructure and properties | 67 |
| 3.1 | Study of mechanical properties: small-scale metal AM methods included | 77 |
| 3.2 | Study of mechanical properties: morphology of printed pads | 88 |
| 3.3 | Study of mechanical properties: microstructure of pads | 90 |
| 3.4 | Study of mechanical properties: microstructure of pillars | 91 |
| 3.5 | Study of mechanical properties: mechanical testing | 93 |
| 3.6 | Study of mechanical properties: E , H and $\sigma_{0.07}$ | 94 |
| 4.1 | Colloidal-ink-based AM versus electrochemical AM | 109 |
| 4.2 | Background: electrospraying | 112 |
| 4.3 | EHD-RP: setup | 116 |

| | | |
|------|---|-----|
| 4.4 | EHD-RP: working principle | 120 |
| 4.5 | EHD-RP: Mass spectra of single-metal ion clusters | 122 |
| 4.6 | EHD-RP: compatible substrates | 123 |
| 4.7 | EHD-RP: printing Cu, Ag and Au | 124 |
| 4.8 | EHD-RP: towards printing Zn, Pd and Fe | 125 |
| 4.9 | EHD-RP: geometry | 126 |
| 4.10 | EHD-RP: spatial resolution | 127 |
| 4.11 | EHD-RP: influence of nozzle size | 129 |
| 4.12 | EHD-RP: density of Cu | 130 |
| 4.13 | EHD-RP: avoiding oxidation | 131 |
| 4.14 | EHD-RP: microstructure as a function of the electric field. | 133 |
| 4.15 | EHD-RP: Gradient microstructure due to electric field gradients | 134 |
| 4.16 | EHD-RP: influence of the printing strategy on the microstructure. | 135 |
| 4.17 | EHD-RP: mechanical properties | 136 |
| 4.18 | EHD-RP: electrical properties | 137 |
| 4.19 | EHD-RP: printing speed | 139 |
| 4.20 | EHD-RP: diffraction grating | 140 |
| 4.21 | EHD-RP: capacitances | 142 |
| 4.22 | EHD-RP: sessile solvent droplet | 146 |
| | | |
| 5.1 | Multi-material AM | 155 |
| 5.2 | Challenges for multi-material AM at small scales | 156 |
| 5.3 | Multi-metal EHD-RP: Printing setup | 159 |
| 5.4 | Multi-metal EHD-RP: Principle | 162 |
| 5.5 | Multi-metal EHD-RP: On-the-fly switching of the printed chemistry | 163 |
| 5.6 | Multi-metal EHD-RP: Additive control of the chemical architecture | 164 |
| 5.7 | Multi-metal EHD-RP: reproducibility of the chemical switching | 165 |
| 5.8 | Multi-metal EHD-RP: switching speed | 166 |
| 5.9 | Multi-metal EHD-RP: microstructure and pore fraction | 168 |
| 5.10 | Multi-metal EHD-RP: Sacrificial support structures | 169 |
| 5.11 | Multi-metal EHD-RP: Tailored local materials strength via the design of the chemical architecture | 170 |
| 5.13 | Multi-metal EHD-RP: future nozzle designs | 173 |
| | | |
| 6.1 | High-resolution electrochemical 2D patterning: nozzle-based vs. tip-based concepts | 181 |
| 6.2 | Electrochemical micromachining with nanosecond voltage pulses | 185 |
| 6.3 | EC-STM deposition: setup | 188 |
| 6.4 | EC-STM deposition: principle | 192 |
| 6.5 | EC-STM deposition: 2D feature size | 193 |
| 6.6 | EC-STM deposition: 2D patterning. | 195 |
| 6.7 | EC-STM deposition: nature of the deposit | 196 |

| | | |
|------|--|-----|
| 6.8 | EC-STM deposition: towards 3D | 197 |
| 6.9 | EC-STM deposition: loss of tip material upon deposition | 199 |
| 6.10 | EC-STM deposition: Anodic stability of Au versus Pt tips. | 200 |
| 6.11 | EC-STM deposition: Co deposition with Pt tips | 201 |
| 6.12 | EC-STM deposition: Complete dissolution | 202 |
| 6.13 | EC-STM deposition: growth curves with Pt-20at.%Ir tips. | 203 |
| 7.1 | AM vs. lithography for 3D microfabrication | 217 |
| A.1 | Small-scale AM of inorganic materials | 222 |
| B.1 | Periodic tables with labels | 224 |
| C.1 | Study of mechanical properties: LIFT-printed Cu and Au | 225 |
| C.2 | Study of mechanical properties: microstructure of pads | 226 |
| C.3 | Study of mechanical properties: microstructure of pads vs. pillars printed from colloids | 228 |
| C.4 | Study of mechanical properties: EDX analysis | 229 |
| C.5 | Study of mechanical properties: DIW (s.t.) | 232 |
| C.6 | Study of mechanical properties: DIW (s.t.) | 233 |
| C.7 | Study of mechanical properties: DIW (N.) | 234 |
| C.8 | Study of mechanical properties: EHDP | 235 |
| C.9 | Study of mechanical properties: EHDP | 236 |
| C.10 | Study of mechanical properties: EPD | 237 |
| C.11 | Study of mechanical properties: LIFT (ink) | 238 |
| C.12 | Study of mechanical properties: LIFT (ink) | 239 |
| C.13 | Study of mechanical properties: LIFT | 240 |
| C.14 | Study of mechanical properties: MCED | 241 |
| C.15 | Study of mechanical properties: FluidFM | 242 |
| C.16 | Study of mechanical properties: EHD-RP | 243 |
| C.17 | Study of mechanical properties: FIBID | 244 |
| C.18 | Study of mechanical properties: FEBID | 245 |
| C.19 | Study of mechanical properties: cryo-FEBID | 246 |
| D.1 | EHD-RP: electron transfer from the substrate | 251 |
| D.2 | EHD-RP: influence of O ₂ on the microstructure of Cu | 252 |
| D.3 | EHD-RP: FIB-flattening of pillars for microcompression | 253 |
| E.1 | EC-STM deposition: Anodic degradation of Au tip | 255 |
| E.2 | EC-STM deposition: Schematic of electronic circuit | 256 |
| E.3 | EC-STM deposition: Results "Hofmann" approach | 258 |

List of Tables

| | | |
|-----|---|-----|
| 2.1 | Collection of published data | 51 |
| 4.1 | EHD-RP: Pulling parameters for single-channel nozzles | 114 |
| 5.1 | Multi-metal EHD-RP: Pulling parameters for two-channel nozzles | 158 |
| C.1 | Study of mechanical properties: Measured E , H and $\sigma_{0.07}$ | 231 |
| C.2 | Study of mechanical properties: mechanical literature data for thin films | 247 |

